DOKUZ EYLÜL UNIVERSITY

GRADUATE SCHOOL OF NATURAL AND APPLIED SCIENCES

INVESTIGATIONS ON SYNTHESIS AND CHARACTERIZATIONS OF CARBON NANOTUBES FOR BIOSENSOR APPLICATIONS

by

Hazal GERGEROĞLU

October, 2022

İZMİR

INVESTIGATIONS ON SYNTHESIS AND CHARACTERIZATIONS OF CARBON NANOTUBES FOR BIOSENSOR APPLICATIONS

A Thesis Submitted to the
Graduate School of Natural and Applied Sciences of Dokuz Eylül University
In Partial Fulfillment of the Requirements for the Degree of Doctor of Philosophy in Nanoscience and Nanoengineering

by

Hazal GERGEROĞLU

October, 2022

İZMİR

PH.D. THESIS EXAMINATION RESULT FORM

We have the read the thesis entitled **''INVESTIGATIONS ON SYNTHESIS AND CHARACTERIZATIONS OF CARBON NANOTUBES FOR BIOSENSOR APPLICATIONS''** completed by **Hazal GERGEROĞLU** under supervision of **ASSOC.PROF.DR. MEHMET FARUK EBEOĞLUGİL** and we certify that in our opinion it is fully adequate, in scope and in quality, as a thesis for the degree of Doctor of Philosophy.

Assoc. Prof. Dr. Mehmet Faruk EBEOĞLUGİL

Supervisor

Prof. Dr. Sedat AKKURT	Assoc. Prof. Dr. Metin YURDDAŞKAL
Thesis Committee Member	Thesis Committee Member
Prof. Dr. Mücahit SÜTÇÜ	Prof. Dr. Osman ÇULHA
Examining Committee Member	Examining Committee Member

Prof. Dr. Okan FISTIKOĞLU

Director

Graduate School of Natural and Applied Sciences

ACKNOWLEDGMENTS

First of all, I would like to extend my sincere thanks to my advisor Assoc. Prof. Dr. Mehmet Faruk EBEOĞLUGİL for his guidance and contributions during my Ph.D. research. I would also like to thank my committee members, Prof. Dr. Sedat AKKURT and Assoc. Prof. Dr. Metin YURDDAŞKAL for reviewing my work and offering valuable suggestions and sharing their visions about the content of my thesis.

I wish to express my deep sense of gratitude to Assoc. Prof. Dr. Mustafa EROL, Assoc. Prof. Dr. Fethullah GÜNEŞ, Assist. Prof. Dr. Ahmet AYKAÇ, Assoc. Prof. Dr. Tuncay DİKİCİ for their constructive ideas, help, and constant support. I want to express my gratitude to Evren EGESOY, Dr. Sibel OĞUZLAR, Defne ÖZTÜRK, Abdülvahid ÇELEBİ for their collaboration in the laboratory studies and sharing their valuable experiences with me. In addition, I want to thank to all my lecturers in the department who encouraged me to afford this work. I would also like to express my genuine gratitude to each of people, although it would be impossible for me to name all.

I would like to thank Merve CENGİZ, Assist. Prof. Dr. Hamed Ghorpanhoor, Esra AKKULAK, İzel OK, Kemal Bartu AYDIN, Şule BAYRAK for their invaluable assistance and kind friendship who are my collegues in my department. I would also like to express my genuine gratitude to Dr. Çiğdem KURT, Dr. Zeliha DURAN, Ayşe KARAOĞLU, Merve KARATAŞ, Mert Tuğrul SAĞSÖZ who are the friends of mine contributed to my success with their mental and physically support during my work. Gülperi Feyza YAVUZ, whom I see as my laboratory partner and also my spiritual younger sister, deserves the greatest thanks for helping complete this work and the other studies without any problems. This thesis would not have reached this point without her help, kindness, calmness, and suggestions. I offer my most sincere love and thanks to her.

I would also like to thank the institutions that supported me through my Ph.D. work, including the Research Center of Fabrication and Application of Electronic Materials (EMUM) in Dokuz Eylül University, the Central Research Laboratories and Application (MERLAB) in Izmir Kâtip Çelebi University, and the İzmir Biomedicine

and Genome Center. I am so grateful for all skills and knowledge I earned that helped me to address the challenges of my study.

I was funded by Council of Higher Education 100/2000 Priority Areas Micro-nanotechnology program between 2018 and 2022, and Scientific and Technological Research Council of Turkey with BIDEB 2211/A National Ph.D. Scholarship Program between 2020 and 2022. Moreover, this research was funded by Dokuz Eylül University Rectorate Scientific Research Projects Unit with the project number 2019.KB.FEN.032 between 2019 and 2022. Due to fact that I would like to thank the Council of Higher Education, Scientific and Technological Research Council of Turkey and Dokuz Eylül University Rectorate for their economical and infrastructural supports.

Finally, a special thank goes to my mother Leyla ÇALIŞKAN, and my elder sister Gizem ELMAS, and my lovely cats CUKA and TİTA for their concern, confidence, and support. The successful completion of this study would not have been possible without their constant love, belief, and encouragement.

Last word, I dedicate my study which focused on develop a cancer-detecting biosensor transducer platform for my grandmother Nesibe ÇALIŞKAN who passed away from breast cancer. I hope you're there watching me with a smile.

Hazal GERGEROĞLU

INVESTIGATIONS ON SYNTHESIS AND CHARACTERIZATIONS OF CARBON NANOTUBES FOR BIOSENSOR APPLICATIONS

ABSTRACT

In this thesis, production optimizations of CNTs were carried out with the CVD method, which is a practical and cost-effective method. In the CVD method, a cause-effect relationship was established between the properties and process parameters that determine the final morphology, such as substrate type, catalyst type, catalyst concentration, growth time, and processing temperature. In the first stage, five different catalysts, four different substrate types, three different growth times, **t**hree different catalyst concentrations, and three different growth times were applied. As a result, the most efficient tubular performance was obtained on the Si wafer substrate at one thousand degrees Celsius processing temperature by applying growth times of three, five, and seven minutes with the help of iron-based catalysts.

Data from SEM samples showed that the lowest tube diameter was acceptable nanoscale. With EDX analysis, it has been shown that as the catalyst concentration increases, the carbon efficiency decreases, confirming the results of the SEM analysis. The highest carbon percentage was determined in the sample with the lowest catalyst concentration. The specific peak attributed to sp^2 hybridization of CNT carbon in FT-IR analysis was observed in all sample. CNTs, which are targeted for use in biosensor applications, are desired in terms of their high defect structure and faster interaction with chemical and bioactive species. The Raman spectra confirmed that this goal was achieved with the $\boldsymbol{I_D/I_G}$ ratio of the obtained CVD-based CNTs. XRD graphs showed that the expected graphitic peak for an ideal CNT was obtained for all samples. In XPS spectra, it was observed that the sp^3/sp^2 ratio increased with increasing catalyst concentration. The current-voltage characterizations revealed that all measurements were close and consistent, as well as high potential in a biosensor application. As a result, it has been proven that the properties of CNTs, which are the output of this thesis, can be improved for use in biosensors by controlling the production parameters.

Keywords: Carbon nanotube, chemical vapor deposition, process optimization, biosensor applications

BİYOSENSÖR UYGULAMALARI İÇİN KARBON NANOTÜPLERİN SENTEZİ VE KARAKTERİZASYONLARI ÜZERİNE ARAŞTIRMALAR

ÖZ

Bu tezde, pratik ve uygun maliyetli bir yöntem olan KBB yöntemi ile KNT'lerin üretim optimizasyonları gerçekleştirilmiştir. KBB yönteminde altlık tipi, katalizör tipi, katalizör konsantrasyonu, büyüme süresi işlem sıcaklığı gibi nihai morfolojiyi belirleyen proses parametreleri ile özellikler arasında neden sonuç ilişkisi kurulmuştur. İlk etapta beş farklı katalizör, dört farklı altlık tipi, üç farklı büyüme süresi, üç farklı katalizör konsantrasyonu, üç farklı büyüme süresi uygulanmıştır. Sonuç olarak en verimli tübüler performans demir bazlı katalizörler yardımıyla üç, beş ve yedi dakikalık büyüme süreleri uygulanarak bin santigrat derece işlem sıcaklığında silikon altlık yüzeyinde elde edilmiştir.

SEM örneklerinden elde edilen veriler, en düşük tüp çapının kabul edilebilir nano ölçekli olduğunu göstermiştir. EDX analizi ile katalizör konsantrasyonu arttıkça karbon veriminin düştüğü gösterilmiş ve SEM analizinin sonuçlarını doğrulamıştır. En yüksek karbon yüzdesi, en düşük katalizör konsantrasyonuna sahip numunede belirlenmiştir. FT-IR analizinde KNT karbonunun sp^2 hibridizasyonuna atfedilen spesifik zirve, tüm numunelerde elde edilmiştir. Biyosensör uygulamalarında kullanılması hedeflenen KNT'ler, yüksek kusurlu yapıları ve kimyasal ve biyoaktif türlerle daha hızlı etkileşime girmeleri açısından arzu edilmektedir. Raman spektrumları, elde edilen KBB tabanlı KNT'lerin I_D/I_G oranı ile bu hedefe ulaşıldığını doğrulamıştır. XRD grafikleri, ideal bir CNT için beklenen grafit tepe noktasının tüm numuneler için elde edildiğini göstermiştir. XPS spektrumlarında, artan katalizör konsantrasyonu ile sp^3/sp^2 oranının artışı gözlenmiştir. Akım-voltaj karakterizasyonları, tüm ölçümlerin yakın ve tutarlı olduğunu ve ayrıca bir biyosensör uygulamasında yüksek potansiyel olduğunu ortaya çıkarmıştır. Sonuç olarak bu tezin çıktısı olan KNT özelliklerinin üretim esnasında uygulanan değişkenler ile kontrol edilerek biyosensör uygulama alanına yönelik geliştirilebileceği kanıtlanmıştır.

Anahtar kelimeler: Karbon nanotüp, kimyasal buhar biriktirme, proses optimizasyonu, biyosensör uygulamaları

CONTENTS

Page

Ph.D. THESIS EXAMINATION RESULT FORM ii
ACKNOWLEDGMENTS iii
ABSTRACT v
ÖZ vi
LIST OF FIGURES xi
LIST OF TABLES xv
ACRONYMS AND ABBREVIATIONS xvi

CHAPTER ONE - INTRODUCTION 1

1.1 Background 1
1.2 Objective of the Study 1
1.3 Organization of the Thesis 2

CHAPTER TWO - CARBON NANOTUBES: INTRODUCTION, SYNTHESIS TECHNIQUES, FEATURES, AND APPLICATIONS 3

2.1 Discovery and Brief History of Carbon Nanotubes 3
2.2 Carbon Nanotubes Forms 3
2.2.1 Single Walled Carbon Nanotubes 4
2.2.2 Multi Walled Carbon Nanotubes 7
2.2.3 Difference Between Multi Walled and Single Walled Carbon Nanotubes 8
2.2.4 Difference Between Carbon Nanotubes and Carbon Nanofibers 9
2.3 Carbon Nanotubes Synthesis Techniques 10
2.3.1 Arc Discharge 11
2.3.2 Laser Ablation 12
2.3.3 Chemical Vapor Deposition 13
2.3.3.1 Historical Development 14
2.3.3.2 Chemical Vapor Deposition Technique Types 16
2.3.3.3 Growth Mechanisms of CNTs 22

2.3.3.4 System Parameters 25
2.4 Extraordinary Features of Carbon Nanotubes 34
2.4.1 Carbon Nanotubes Physical Properties 34
2.4.2 Carbon Nanotubes Chemical Properties 41
2.4.3 Carbon Nanotubes Biological Properties 44
2.5 Applications of Carbon Nanotubes 45

CHAPTER THREE - CARBON NANOTUBES BASED ELECTROCHEMICAL BIOSENSORS 49

3.1 Introduction 49
3.2 Historical Background 49
3.3 Desirable Properties in an Ideal Biosensor 51
3.4 Biosensor Types 54
3.4.1 Biosensors by Bioreceptors 55
3.4.1.1 Enzyme-based Biosensors 56
3.4.1.2 Antibody-based Biosensors 57
3.4.1.3 DNA-based Biosensors 58
3.4.1.4 Cell-based Biosensors 59
3.4.1.5 Biomimetics 59
3.4.2 Biosensors by Transducers 60
3.4.2.1 Physical Transducers 61
3.4.2.2 Chemical Transducers 64
3.5 Functionalization of CNTs with Bioreceptors 66
3.5.1 Methods for Functionalizing CNTs 67
3.5.2 The Roles of Functionalized CNTs 69
3.6 Electrochemistry Behind CNT-based Biosensors 70

CHAPTER FOUR - DESIGN AND METHODOLOGY 73

4.1 Introduction to Experimental Design and Studies 73
4.2 Raw Materials and Chemicals Used in Experimental Studies 73

4.2.1 Substrates 73
4.2.2 Catalysts 74
4.2.3 Gas precursors 74
4.3 Equipments Used in Experimental Studies 75
4.3.1 Precision Balance and Ultrasonic Bath 75
4.3.2 The Oven 75
4.3.3 Chemical Vapor Deposition System 76
4.4 Experimental Studies 78
4.4.1 Substrate Cleaning Route 78
4.4.2 Preparation of Catalyst-Containing Solutions 78
4.4.3 Integration of Catalyst and Substrate 79
4.4.4 Chemical Vapor Deposition Process 80
4.4.5 Nomenclature of Samples 81
4.5 Characterization Techniques 83
4.5.1 Scanning Electron Microscopy (SEM) 83
4.5.2 Energy Dispersive X-Ray Analysis (EDX) 86
4.5.3 Fourier Transform Infrared Spectroscopy (FTIR) 87
4.5.4 Raman Spectroscopy 88
4.5.5 X-Ray Diffraction Analysis (XRD) 89
4.5.6 X-Ray Photoelectron Spectroscopy (XPS) 90
4.5.7 Current-Voltage Characterizations 92

CHAPTER FIVE- RESULT AND DISCUSSION 94

5.1 Introduction to shaping experimental outputs according to optimization 94
5.2 Scanning Electron Microscopy (SEM) 94
5.2.1 Group 1 94
5.2.2 Group 2 99
5.2.3 Group 3 106
5.2.4 Group 4 110
5.2.5 Group 5 112
5.2.6 Group 6 114

5.2.7 Group 7 114
5.2.8 Group 8 116
5.2.9 Group 9 118
5.2.10 Group 10 119
5.2.11 Group 11 119
5.3 CNT Formation by Catalysts Type 121
5.4 CNT Morphology by Catalysts Concentration and Growth Time 124
5.5 Energy Dispersive X-Ray Analysis (EDX) 125
5.6 Fourier Transform Infrared Spectroscopy (FTIR) 128
5.7 Raman Spectroscopy 134
5.8 X-Ray Diffraction Analysis (XRD) 140
5.9 X-Ray Photoelectron Spectroscopy (XPS) 145
5.10 Current-Voltage Characterizations 150

CHAPTER SIX - CONCLUSION AND RECOMMENDATIONS 152

6.1 Conclusion 152
6.2 Future Works and Recommendations 154

REFERENCES 155

LIST OF FIGURES

Page

Figure 2.1 Different carbon nanostructures 4
Figure 2.2 Schematic representation of rolled-up graphene layer to form SWNT 5
Figure 2.3 An unrolled graphene sheet from which SWCNT is formed by joining the PQ and OA sides of the OAQP rectangle 5
Figure 2.4 Different types of SWCNT 6
Figure 2.5 Different forms of carbon nanotubes 8
Figure 2.6 The nano-carbon family according to their average diameters 10
Figure 2.7 Schematic representation of the CNTs synthesis using arc discharge technology 11
Figure 2.8 Schematic representation of the CNTs synthesis via laser ablation method 12
Figure 2.9 Important dates of the CVD timeline 15
Figure 2.10 Various CVD technologies 16
Figure 2.11 Schematic representation of catalytic CVD process 17
Figure 2.12 Schematic representation of plasma enhanced CVD process 18
Figure 2.13 Schematic representation of WACVD process 20
Figure 2.14 Growth mechanisms of CNTs via CVD 23
Figure 2.15 Schematic representation of band gaps of single- and double-walled CNTs 35
Figure 2.16 Energy-level structure based on nanotube HOMO and LUMO 38
Figure 2.17 Magnetic susceptibility of different carbons measured experimentally . 39
Figure 2.18 Young's modulus is plotted against tensile strength for many engineering materials in an Ashby plot. 40
Figure 2.19 A carbon atom’s hybridization types 42
Figure 2.20 Hybridization of carbon structures and schematic representation of bond structure of CNT 43
Figure 2.21 Change of carbon nanotube research developments by years in terms of published articles 45
Figure 2.22 Pie chart showing the distribution of CNTs in different application areas. 46

Figure 3.1 Biosensor development timeline 50
Figure 3.2 Schematic representation of biosensors 52
Figure 3.3 Biosensor types 55
Figure 3.4 Techniques of biosensing use diverse biological signaling mechanisms . 56
Figure 3.5 SWCNTs with different chirality for enhanced optical biosensing 62
Figure 3.6 Illustrations of functionalized CNTs with different nanomaterials 67
Figure 3.7 Chemical functionalization techniques for CNTs 68
Figure 3.8 Electrochemistry of carbon nanotubes is similar to that of graphite 71
Figure 4.1 Images of the substrates……..……..74
Figure 4.2 (a) Precision balance, (b) Ultrasonic bath 75
Figure 4.3 Oven used in the preparation of catalyst supported substrates to be sent to the CVD system. 76
Figure 4.4 The CVD system 77
Figure 4.5 The solutions containing different percentages by weight of catalysts 79
Figure 4.6 (a) Catalyst supported substrates, (b) Placing catalyst supported substrates on quartz rod, (c) Insertion of the quartz rod into the CVD system, (d) Appearance of substrates after CVD treatment 80
Figure 4.7 CVD process for CNT growth 81
Figure 4.8 Devices used in SEM characterization 85
Figure 4.9 Device used in EDX characterization 87
Figure 4.10 FT-IR spectrometer 88
Figure 4.11 Raman spectrometer device 89
Figure 4.12 X-Ray diffractometer. 90
Figure 4.13 X-Ray photoelectron spectroscopy 91
Figure 4.14 Current-voltage characterization device 92
Figure 5.1 SEM images of samples 1 and 2 96
Figure 5.2 SEM images of samples 5 and 6 98
Figure 5.3 Images of samples 7 and 8 after CVD process at 1000^{o}C 99
Figure 5.4 SEM images of samples 9 and 10 101
Figure 5.5 SEM images of samples 11 and 12 103
Figure 5.6 SEM images of samples 13,14,15 and 16 105
Figure 5.7 Iron-carbon equilibrium diagram 106

Figure 5.8 Diagram illustrating Fe_2o_3–CH_4 solid stability in equilibrium with the gas phase as a function of temperature and mole fraction of CH_4 107
Figure 5.9 SEM images at x5k magnification of samples applied 6 wt.% catalysts and 3 min growth time. 109
Figure 5.10 SEM images at x5k magnification of samples applied 4 wt.% catalysts and 3 min growth time. 111
Figure 5.11 SEM images at x5k magnification of samples applied 2 wt.% catalysts and 3 min growth time. 113
Figure 5.12 SEM images at x5k magnification of samples applied 6 wt.% catalysts and 5 min growth time. 115
Figure 5.13 SEM images at x5k magnification of samples applied 4 wt.% catalysts and 5 min growth time. 116
Figure 5.14 SEM images at x5k magnification of samples applied 2 wt.% catalysts and 5 min growth time. 117
Figure 5.15 SEM images at x5k magnification of samples applied 6 wt.% catalysts and 7 min growth time. 118
Figure 5.16 SEM images at x5k magnification of samples applied 4 wt.% catalysts and 7 min growth time. 120
Figure 5.17 SEM images at x5k magnification of samples applied 2 wt.% catalysts and 7 min growth time. 121
Figure 5.18 EDX spectrum of samples 38 and 39 126
Figure 5.19 EDX spectrum of samples 44 and 45 127
Figure 5.20 EDX spectrum of samples 50 and 51 128
Figure 5.21 FT-IR spectra of the 3-minute samples 130
Figure 5.22 FT-IR spectra of the 5-minute samples 131
Figure 5.23 FT-IR spectra of the 7-minute samples 133
Figure 5.24 Raman spectrum of the 3-minute samples. 136
Figure 5.25 Raman spectrum of the 5-minute samples. 137
Figure 5. 26 Raman spectrum of the 7-minute samples. 139
Figure 5.27 X-Ray diffraction (XRD) graph of the 3-minute samples 141
Figure 5.28 X-Ray diffraction (XRD) graph of the 5-minute samples 142
Figure 5.29 X-Ray diffraction (XRD) graph of the 7-minute samples 144

Figure 5.30 XPS survey spectra and the deconvoluted C1s spectra of the 3-minute samples. 146
Figure 5.31 XPS survey spectra and the deconvoluted C1s spectra of the 5-minute samples. 147
Figure 5.32 XPS survey spectra and the deconvoluted C1s spectra of the 7-minute samples. 148

LIST OF TABLES

Page

Table 2.1 Comparison of CVD with other CNT production techniques 14
Table 2.2 Some physical characteristics of MWCNTs and SWCNTs..... 36
Table 4.1 Experimentally applied parameters for CNT production..... 82
Table 5.1 Morphological features of CNTs 125
Table 5.2 Chemical composition of the investigated samples 125
Table 5.3 Raman shifts of the peaks of the samples and intensity ratios of D-band to G-band. 135
Table 5.5 Chemical composition, FWHM and sp^3 /sp^2 ratio on the samples surface calculated from XPS spectra..... 149
Table 5.6 Electrical features of samples 150

ACRONYMS AND ABBREVIATIONS

$\mathbf{I_D}$	: Density of D band
$\mathbf{I_G}$	: Density of G band
0-D	:Zero dimensional
1-D	:One dimensional
2-D	:Two dimensional
3-D	:Three dimensional
AA-CVD	:Aerosol assisted CVD
at.%	:Atomic percent
CB	:Carbon black
CDs	:Carbon dots
C_h	: Chiral vector
CNFs	:Carbon nanofibers
CNOs	:Carbon nano-onions
CNSs	:Carbon nanospheres
CNTs	:Carbon nanotubes
CVD	:Chemical Vapor deposition
DNA	:Deoxyribonucleic acid
DsDNA	:Double-stranded DNA
EDX	:Energy Dispersive X-Ray Analysis
EIS	:Electrical impedance spectroscopy
FT-IR	:Fourier Transform Infrared Spectroscopy
FWHM	:Full width at half maximum
GPa	:Gigapascal
HCl	:Hydrochloric acid
HF-CVD	:Hot Filament CVD
HOMO	:Highest occupied molecular orbital
HOPG	:Highly oriented pyrolytic graphite
IR	:Infrared
LACVD	:Laser-assisted CVD

LUMO	:Lowest unoccupied molecular orbital
minute	:Minute
MPa	:Megapascal
M-PECVD	:Microwave Plasma Enhanced CVD
MWCNTs	:Multi-walled carbon nanotubes
NDs	:Nanodiamonds
NIR	:Near infrared
Nm	:Nanometer
NPs	:Nanoparticles
PECVD	:Plasma-enhanced CVD
RF-PECVD	:Radio Frequency Plasma Enhanced CVD
sccm	:Standard cubic centimeters per minute
SCCNTs	:Stacked up carbon nanotubes
SEM	:Scanning electron microscopy
ssDNA	:Two single-stranded DNA
SWCNTs	:Single-walled carbon nanotubes
VLS	:Vapor-liquid-solid
WACVD	:Water-assisted CVD
wt.%	:Weight percent
XPS	:X-Ray photoelectron spectroscopy
XRD	:X-Ray diffraction analysis
π-bond	:Pi bond
ρ	:Resistivity
σ	:Electrical conductivity
σ-bond	:Sigma bond

CHAPTER ONE

INTRODUCTION

1.1 Background

CNTs have emerged fascinatingly among the academic community. Since their discovery in 1991, academics and researchers in industry have made great efforts to understand more about the material with unusual structural, electronic, optoelectronic, semiconductor, mechanical, and chemical properties. CNTs are viewed as a cylindrical roll of a two-dimensional graphene or a one-dimensional fullerene. CNTs with lengths of several microns and diameters on the nanometric scale are also referred to as hollow tubular materials. CNTs have different types according to their structural properties and can be produced by various methods. While all these extraordinary properties of carbon nanotubes open up a new horizon in nanotechnology, nanoengineering, and industry, they have been widely used in the field of biosensor applications because they meet the expected characteristics of an ideal biosensor, such as higher sensitivity and selectivity, real-time measurement, and a high signal to noise ratio.

1.2 Objective of the Study

The aim of this study is to synthesize CNT material by the CVD method and to investigate and examine its usability in biosensor applications. This research can be divided into two parts; the first section examines the effect of the most important CVD parameters for the production of CNTs, such as substrate type, catalyst type, catalyst concentration, growth time, growth temperature, on the final structure and properties; the second part is about the relationship between the parameters considered to be the most efficient and suitable tubular structure and the potential in the application area. Based on the relationship of differences in morphological, structural, physical, and chemical properties with catalyst type, concentration, substrate type, growth time, and growth temperature, CVD-based CNTs were produced. The electrical properties of the CNTs that were made were looked at, and their use as biosensors was talked about.

1.3 Organization of the Thesis

The synthesis of CVD-based carbon nanotubes is discussed in this thesis, which has a total of six chapters but focuses mostly on two topics: process improvements and possible biosensor applications. In Chapter 2, a complete look is taken at the history of the discovery of CNTs as well as the background literature, the structures of carbon nanotubes, their characteristics, manufacturing techniques, and uses. The material presented in Chapter 3 pertains to CNT-based biosensors, and it is based on the research that has been conducted on the historical development, categorization, and fundamental processing mechanism of biosensors. The equipment, chemical initiators, experimental procedures, manufacturing stages, and characterization instruments that were employed in this work to generate CVD-based CNTs are discussed in Chapter 4. Chapter 5 discusses in detail the morphological, structural, chemical, electrical, and crystallographic results of successfully synthesized CVD-based CNTs and examines the various applied catalyst types, catalyst concentrations, substrate types, growth times, and processing temperatures using a variety of characterization techniques. This chapter also examines the different applied catalyst types and substrate types. The cause-and-effect link between fabrication, characteristics, and application is laid out in Chapter 6. This chapter talks about the results of CVD-based CNTs and how they could be used in biosensors. It also talks about the big problems we face when making these materials.

CHAPTER TWO

CARBON NANOTUBES: INTRODUCTION, SYNTHESIS TECHNIQUES, FEATURES, AND APPLICATIONS

2.1 Discovery and Brief History of Carbon Nanotubes

Although it is about 30 years old that carbon nanotubes are seen as a new material group, considering that scientific developments are based on successive processes, the concept of carbon nanotubes probably dates to earlier times historically.

The first nanotubes were probably synthesized as carbon nanofilaments in 1952 by Radushkevich and Lukyanovich (Radushkevich and Lukyanovich 1952). Following this, Hillert and Lange, in 1959, reported the dense bamboo structure of carbon filaments (Hillert and Lange 1959). Subsequently, the synthesis of graphite in cylindrical form by Bollman and Spreadborough in 1960 was a significant breakthrough for the definition of carbon nanotubes (Bollmann and Spreadborough 1960). 16 years after this process, Oberlin and colleagues reported the synthesis of carbon nanofibers due to the decomposition of benzene by the chemical vapor deposition technique in 1976 (Oberlin, Endo, and Koyama 1976).

By 1991, Iijima's extraordinary discovery, producing and defining double and multi-walled carbon nanotubes and his work that revealed the relationship between crystal structure and properties, opened a critical window that inspired new scientific research (Iijima 1991). Later, with the synthesis of single-walled carbon nanotubes (SWCNTs) by Ichihashi with the help of metal catalyst particles (Ichihashi 1993), the birth of an advanced promising novel material was completed in terms of materials science and nanoscience.

2.2 Carbon Nanotubes Forms

Among the various nanomaterials, carbon nanotubes as promising materials for many advanced applications since their discovery by Iijima in 1991 due to their outstanding physical and chemical features (Karousis, Tagmatarchis, and Tasis 2010).

Due to their length (up to a few microns) and small diameters (nanometers), CNTs that provide a wide aspect ratio can be viewed as an approximately one-dimensional form of fullerene (Figure 2.1). They are cylindrical molecules containing a hexagonal arrangement of sp^2 hybridized carbon atoms. They are also called hollow tubular materials composed of carbon atoms with nanometric scale diameters and lengths. CNTs can be described as graphene sheets rolling into continuous cylinders, and two forms of these cylindrical structures are called SWCNTs and multi-walled carbon nanotubes (MWCNTs) (Gergeroglu, Yildirim, and Ebeoglugil 2020).

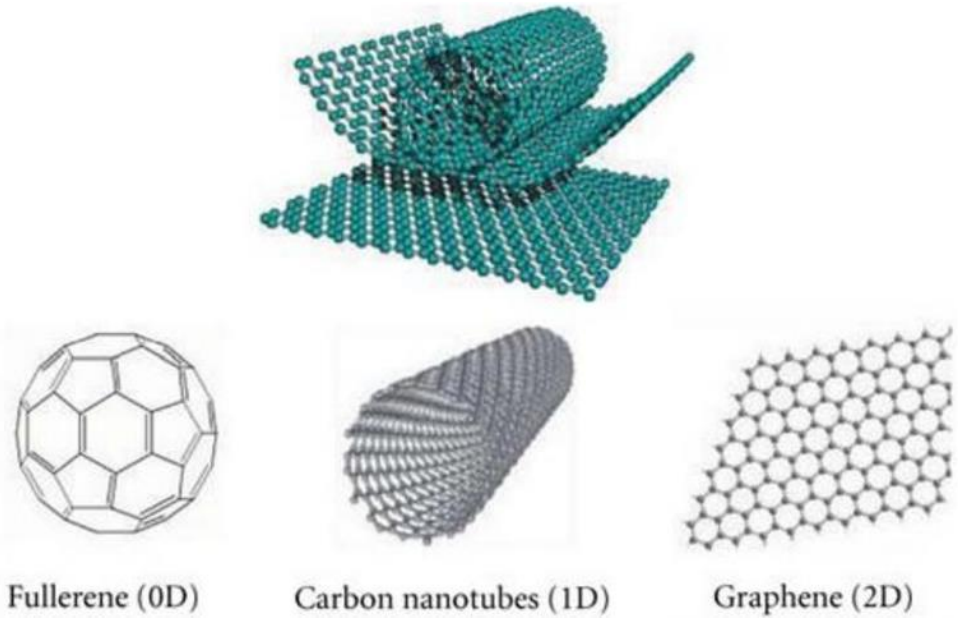


Figure 2.1 Different carbon nanostructures (R. P. Singh 2011)

2.2.1 Single Walled Carbon Nanotubes

SWCNTs are formed by rolling a single graphite sheet (called graphene) into a continuous cylinder, shown schematically in Figure 2.2. In general, SWCNTs range in diameter from 0.7 nm to 2.5 nm, and aspect ratios can be as high as 104-105 (Garg et al., 2021). An SWCNT consists of two separate parts with different physical and chemical features. The first section is the sidewall of the tube, and the second is the end cap of the tube. The end cap shows similar properties to another carbon allotrope, fullerene. On the other hand, the side walls introduce the concept of chirality, which gives the nanotube different chemical and physical properties according to the rolling of the graphene layers in different directions (Mathur, Singh, and Pande 2016)

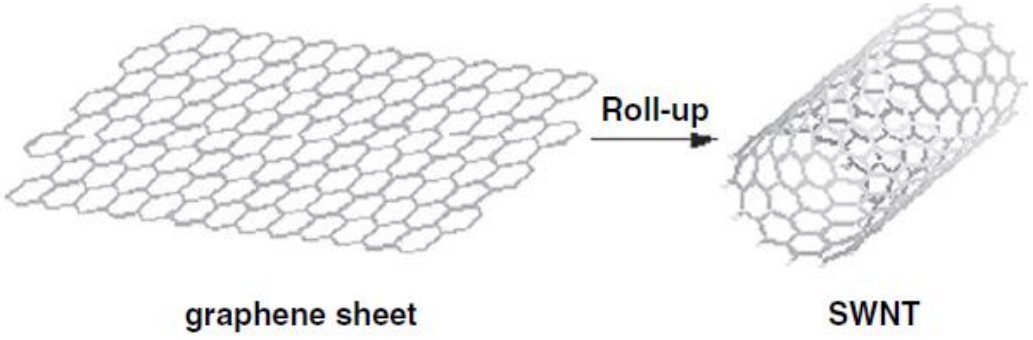


Figure 2.2 Schematic representation of rolled-up graphene layer to form SWNT (Odom et al., 2000)

Figure 2.3, which represents an unrolled graphene sheet, clearly reveals that SWCNT is formed by rolling a graphene sheet. The carbon atoms are arranged in a honeycomb lattice in a graphene sheet. The lattice cell is defined with the help of two primitive vectors, a_1 and a_2 (Neto et al., 2009). To denote the chiral vector C_h and the translational vector T of the nanotube, the rectangle OAQP is formed by joining the edges OA and QP. Also, vector R is an asymmetry vector. C_h denotes the two carbon atoms of the graphene layer governing the nanotube formation, and it is calculated with Equation 2.1 (Dinadayalane and Leszczynski 2007; Garg et al., 2021):

$$\boldsymbol{C_h = na_1 + ma_2 \equiv (n,m)\ 0 \leq n \leq m} \qquad (2.1)$$

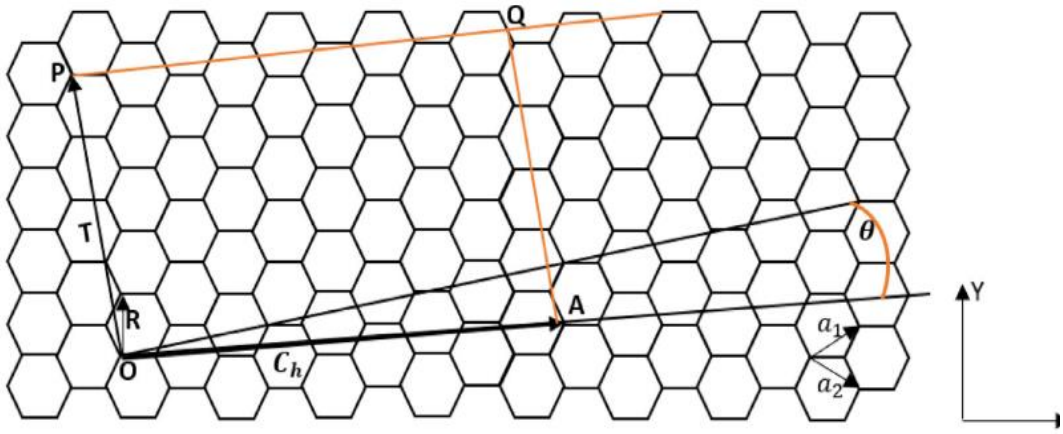


Figure 2.3 An unrolled graphene sheet from which SWCNT is formed by joining the PQ and OA sides of the OAQP rectangle (Garg et al., 2021)

In Equation 2.2, n and m define integers called chiral indexes when denoted as (n, m). The amount of "twist" in the nanotube is determined by the chiral angle (θ), which

is defined as the angle between the $\vec{C}_h$ and the zigzag direction (n, 0). Angle θ is used to determine the electrical properties of the SWCNT and is calculated by Equation 2.2 (Dinadayalane and Leszczynski 2007; Garg et al., 2021):

$$\cos\theta = \frac{C_h.a_1}{|C_h|.|a_1|} = \frac{2n+m}{2\sqrt{n^2+m^2+mn}} \quad (2.2)$$

Depending on chirality, SWCNTs are classified in three different ways: (1) m = n is the armchair nanotube, (2) m = 0 is the zig-zag nanotube, and (3) n> m and if m = 0 is the chiral nanotube (Figure 2.4). Armchair, zig-zag, and chiral carbon nanotubes are generally denoted by (n, n), (n, 0), and (n, m), respectively (Dinadayalane and Leszczynski 2007).

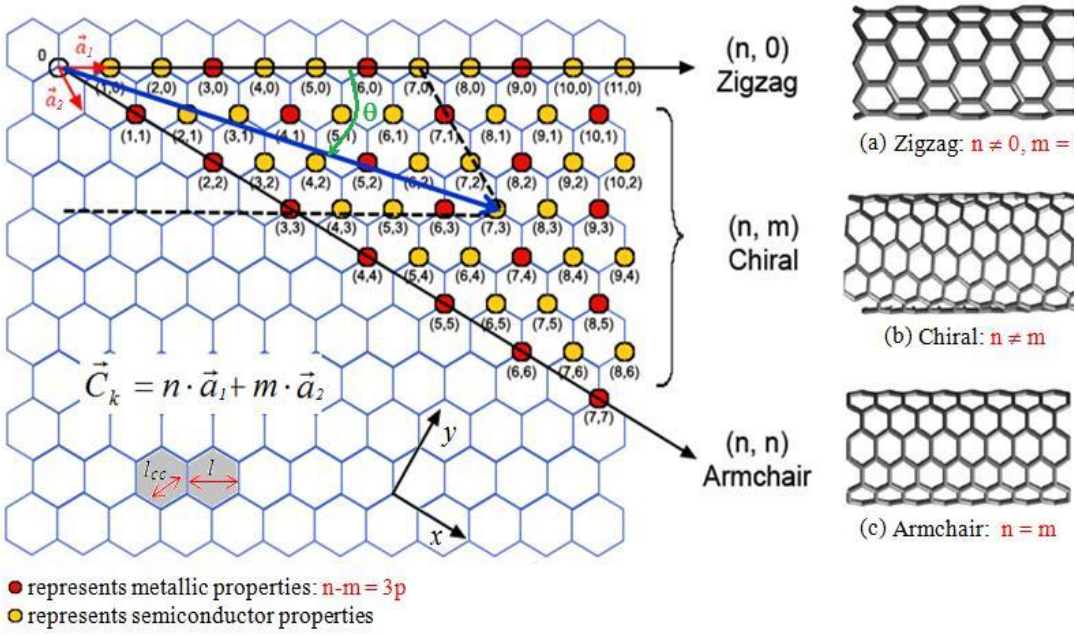


Figure 2.4 Different types of SWCNTs (Attaf 2015)

The value of the chiral angle is 0 and 30, respectively, for zigzag and armchair carbon nanotubes. The chiral angle of all achiral nanotubes is $0^o<\theta<30^o$. If the integers (n, m) are known, the diameter (d_t) and chiral angle(θ) of the nanotube can be measured. To measure the diameter of the nanotube, it is also necessary to know the nearest neighboring carbon atom distance (a_{cc}). However, value 1.421Å is generally used for a_{cc}. Mathematical formula defined for an ideal SWCNT (n, m) diameter is given in Equation 2.3 (Dinadayalane and Leszczynski 2007):

$$d_t = \frac{a_{cc}\sqrt{3\,(n^2+nm+m^2)}}{\pi} \quad (2.3)$$

In this case, the chiral angle (θ) can be defined in Equation 2.4:

$$\boldsymbol{\theta = tan^{-1}\left[\frac{\sqrt{3}m}{2n+m}\right]} \quad (2.4)$$

The diameter and wrapping angle determine the physical features of the CNTs (Kataura et al., 1999; Odom et al., 2000; Wilder et al., 1998). For instance, the calculation of the electronic energy band structure shows that CNTs can be classified as metal or semiconductor according to the (n, m) index (G. Dresselhaus and Riichiro 1998; Mildred S Dresselhaus, Dresselhaus, and Eklund 1996; Hamada, Sawada, and Oshiyama 1992; Mintmire, Dunlap, and White 1992). CNTs have a semi-conducting in nature, but for a given (n, m) SWNTs, when (2n+m) /3 is an integer, the CNTs will be metallic. Thus, it can be claimed that all armchair nanotubes are metallic. Theoretical studies have shown that CNT's electronic and magnetic features are diameter dependent(Mildred S Dresselhaus, Dresselhaus, and Eklund 1996). Moreover, it has been reported that the mechanical features of SWNTs are controlled by the chirality of nanotubes (B I Yakobson, Samsonidze, and Samsonidze 2000; Boris I Yakobson, Brabec, and Bernholc 1996). Therefore, it can be suggested that the physical features of CNTs are dependent on the chiral vector (n, m). Thus, in cases where chirality can be controlled, changes in morphological properties will lead to changes in the magnetic, electronic, mechanical, and optic features of CNTs.

2.2.2 Multi Walled Carbon Nanotubes

Unlike SWCNTs formed by rolling a single graphene sheet, MWCNTs consist of concentric approximately 50 sheets of rolled graphene (Figure 2.5). MWCNTs can be easily distinguished from SWCNTs based on their diameter and characterizations, such as Raman spectroscopy (Ganesh 2013; Garg et al., 2021; Mathur, Singh, and Pande 2016).

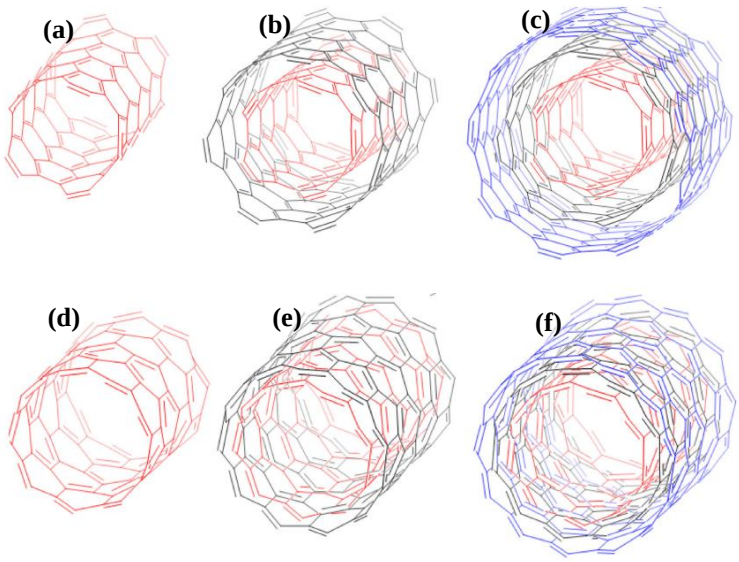


Figure 2.5 Different forms of carbon nanotubes; Armchair nanotubes of (a) single walled, (b) two-walled, (c) multi-walled, Zigzag nanotubes of (d) single walled, (e) two-walled, (f) multi-walled (Garg et al., 2021)

Simply put, MWCNTs are assemblies of several SWCNTs arranged in a coaxial Russian doll structure. Each SWCNT corresponds to a wall of the MWCNTs. These concentric tubes are held together by a cloud of delocalized electrons along the walls due to sp^2 hybridization of carbon atoms, and the inter-wall distance has been reported to be about 0.340 nm (Kukovecz, Kozma, and Kónya 2013; Mathur, Singh, and Pande 2016).

2.2.3 Difference Between Multi Walled and Single Walled Carbon Nanotubes

Although MWCNTs are just concentric SWCNTs, there are significant distinctions between the two nanostructures that directly impact the final attributes and performance in the application region, as previously stated(Gergeroglu, Yildirim, and Ebeoglugil 2020; Thostenson, Ren, and Chou 2001). MWCNTs, for example, have more structural defects than SWCNTs; this may result in less flexibility for the desired field of application (Vajtai 2013).

However, claiming that one tube type is entirely excellent and the other wholly negative is incorrect. Depending on the application, MWCNTs or SWCNTs should be selected. SWCNTs are chosen in drug delivery applications because of their ultra-high

surface area and better drug loading capacity than MWCNTs. Furthermore, SWCNTs are preferable in structural engineering applications because of their higher rigidity (Garg et al., 2021; Vajtai 2013).

SWCNTs may display metallic or semiconductor behavior depending on their diameters and the chiral angle between hexagons and the tube axis, but the MWCNTs have a current-carrying capacity of up to 109 A cm^{-2}, are always metallic, and have zero bandwidth. Additionally, the open end of the MWCNTs has a rapid electron transfer rate comparable to graphite electrodes, whereas the SWCNTs have a significantly slower electron transfer rate. The MWCNTs have a structural complexity and current-carrying capability similar to the metallic/semiconductor SWCNTs. However, unlike SWCNTs, there are different parameters for each tube layer in MWCNTs. Besides, MWCNTs offer greater prospects than SWCNTs, as \sthey are simpler to synthesize owing to reduced product cost per unit, enhanced thermal and chemical stability, and easier control of the development process (Gergeroglu, Yildirim, and Ebeoglugil 2020; Mallakpour and Khadem 2016; Mathur, Singh, and Pande 2016; Rana et al., 2017).

2.2.4 Difference Between Carbon Nanotubes and Carbon Nanofibers

Although CNTs and carbon nanofibers (CNFs) are both hollow and of nanoscale dimensions and have similar manufacturing processes, there are major distinctions that impact their performance and ability to be processed. The first distinction is based on their morphology. CNFs, also known as stacked cup CNTs (SCCNTs), have a distinctive shape in that graphene planes are canted from the fiber axis resulting in exposed edge planes on the interior and external surface of the fiber (Mathur, Singh, and Pande 2016). On the other hand, MWCNTs are generally an assemblage of concentric cylinders constructed of the sheet. Another variation is based on their sizes. CNTs generally have diameters ranging from 1 to 100 nm, while CNFs or SCCNTs have diameters from 50 to 200 nm depending on the kind of \sCNF and synthesis process. Figure 2.6 displays a comparative structure and size of several types of these carbons (Gergeroglu, Yildirim, and Ebeoglugil 2020; Mathur, Singh, and Pande 2016).

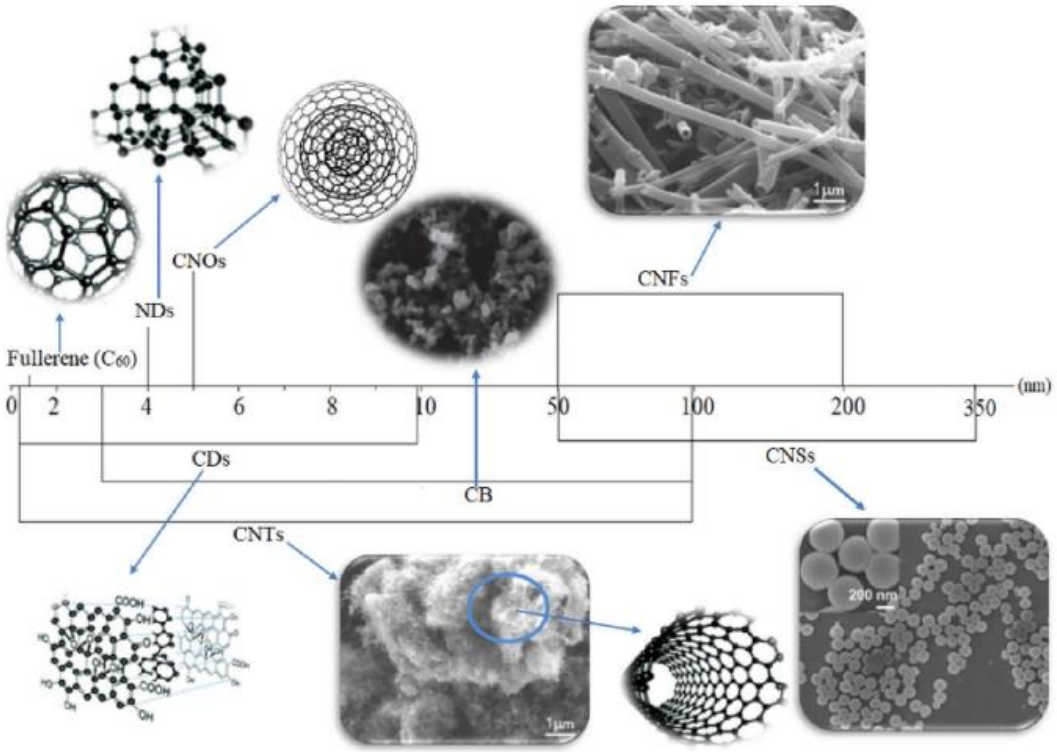


Figure 2.6 The nano-carbon family according to their average diameters; Fullerene (1.4 nm), Nanodiamonds (NDs) (4–5 nm), Carbon nano-onions (CNOs) (5–6 nm), Carbon dots (CDs) (below 10 nm), Carbon black (CB) (3 to 100 nm), CNTs (1 to 100 nm) , CNFs (50 to 200 nm), Carbon Nanospheres (CNSs) (50 to 350 nm) (Gergeroglu, Yildirim, and Ebeoglugil 2020)

2.3 Carbon Nanotubes Synthesis Techniques

MWCNTs and SWCNTs are often manufactured via comparable procedures. Numerous procedures have been developed in the previous 25 years, and presently synthesis of MWCNTs has been well established, and several firms are manufacturing them on a wide scale(Jia and Wei 2019; Qiang Zhang et al., 2011). The most economically feasible technology for manufacturing CNTs is chemical vapor deposition (CVD) and is being followed by most commercial producers with minor changes (Aykaç et al., 2021; Shukrullah et al., 2014). Besides CVD, arc discharge and laser ablation are two more effective approaches for producing CNTs (Lawal 2016; Manawi et al., 2018; Shoukat and Khan 2021).

2.3.1 Arc Discharge

Arc discharge is the electrical breakdown of a gas to form the plasma. The chamber consists of two electrodes: one of which is called anode, which is filled with powdered carbon precursor, generally graphite particles, along with the catalysts; and the other electrode is called cathode, which is usually a pure graphite rod. The chamber is normally filled with a gas or occasionally with liquid environment. An electric field is placed between the two electrodes, which are brought near enough to form an arc, and a gap of 1 to 2 mm is maintained to obtain a continuous discharge. The arc current creates plasma of extremely high temperature ~4000°C, which sublime the carbon precursor within the arc and form the CNTs (Arora and Sharma 2014). A schematic of a typical arc discharge equipment is given in Figure 2.7.

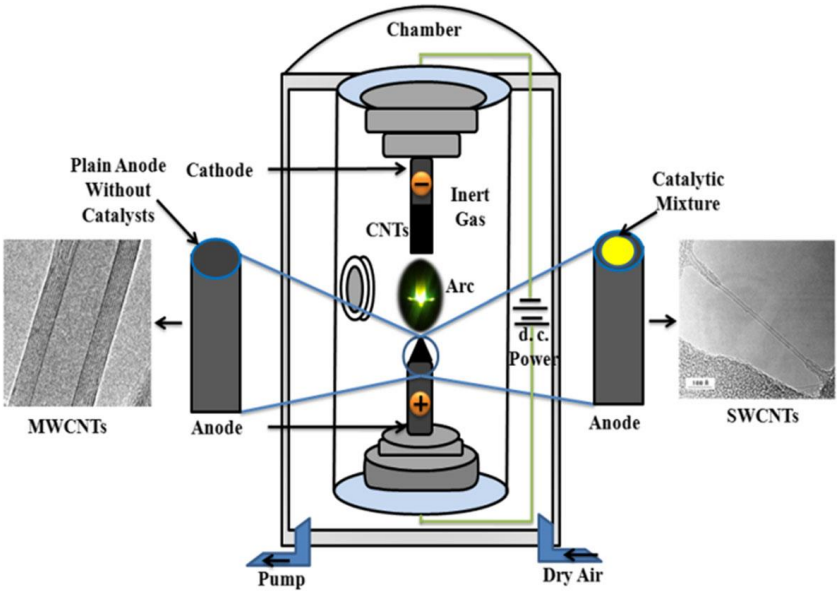


Figure 2.7 Schematic representation of the CNTs synthesis using arc discharge technology (R. Das et al., 2016)

Generally arc discharge is employed for the synthesis of SWCNTs, MWCNTs, and fullerenes (Ando and Zhao 2006; Arora and Sharma 2014; Bogdanov, Deininger, and Dyuzhev 2000). The operating parameters, carbon precursor, and catalyst in the arc chamber influence the kind and purity of carbon nanomaterials. It has been shown that high current density and low gas pressure leads into the development of fullerenes whereas at low current density, and high-pressure nanotubes are created (Ando and Zhao 2006; Farhat and Scott 2006).

There are essentially two deposits in the arc discharge technique: One is the chamber deposits, where the growth takes occur in the presence of catalysts and the result is in the form of webs of SWCNT ropes. The second is the cylindrical mass dubbed the cathode deposit, which comprises predominantly MWCNTs in its core. Interestingly this does not include any metallic contaminants (Mathur, Singh, and Pande 2016). However, there are still several hurdles for the practical uses of the arc synthesized CNTs, such as poor efficiency of catalysts, and the uncontrollability of nucleation process and growth mechanism (Su and Zhang 2015). Therefore, although the arc discharge approach provides the option of utilizing acceptable catalysts and gas phases, manufacturing uniform and pure CNTs has remained a lengthy difficulty (R. Das et al., 2016).

2.3.2 Laser Ablation

Laser ablation is quite comparable to the arc discharge method due to a very similar reaction situation and because both reactions presumably occur with the same mechanism. It was first employed to produce fullerenes, later used for synthesizing nanometer-scale nano carbons such as CNOs, NDs, and CNTs (Guo, Nikolaev, and Rinzler 1995; M. Kim et al., 2017).

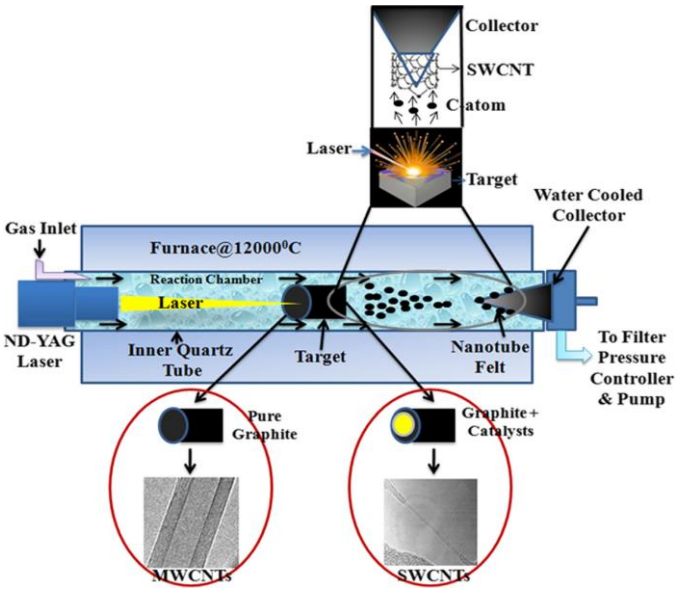


Figure 2.8 Schematic representation of the CNTs synthesis via laser ablation method (R. Das et al., 2016)

In a typical laser ablation experiment (Figure 2.8), the laser pulse is focused onto a graphite target containing a metal catalyst. The target is maintained in the inert gas flow, and the system is heated at roughly 1000°C by an electric furnace. The laser evaporates the target into plasma, in which CNTs are created (Rafique and Iqbal 2011; Terrones 2003). In this technique, the features of final CNTs synthesized are highly reliant on many parameters, including such: the laser properties, the operating pressure and the chemical characteristics, the shape and compositional composition of the target material, the substrate and ambient temperature, flow, and pressure of the buffer gas, and the distance between the target and the substrates (Prasek et al., 2011). Even though this technique provides high purity of CNTs (>90%) and smaller size dispersion than arc discharge and CVD technology, is not suited for the mass manufacture of CNTs (Mathur, Singh, and Pande 2016).

2.3.3 Chemical Vapor Deposition

Chemical vapor deposition (CVD) is one of the most effective means of CNT production up to now, where the final morphology is most effectively managed against the uncontrolled nucleation and growth kinetics in the arc discharge method (M. Kumar and Ando 2010). Moreover, compared to laser ablation, it is regarded as an economically feasible approach for large-scale as well as very pure CNT synthesis. The primary benefits of CVD are the simple control of the reaction course and the relatively high purity of the produced material (Mirabootalebi and Akbari 2017; Y. Zhu et al., 2006). A comparative evaluation of three commonly recommended techniques for CNT production is summarized in Table 2.1.

Table 2.1 Comparison of CVD with other CNT production techniques (X.-D. Wang, Vinodgopal, and Dai 2019)

Method	CVD	Laser Ablation	Arc-Discharge
Condition	Low pressure inter gas	High temperatures (500-1000ºC) at high energy laser beam	Argon or nitrogen
Yield	High (60-90%)	Low (up to 70%)	Low (20-100%)
Purity	Medium to high	Low	Medium
Temperature	500-1200ºC	25-1000ºC	4000ºC
Product	SWCNTs long tubes (0.6 to 4 nm)	SWCNTs long bundles of tubes (1-2 nm)	SWCNTs short tubes (0.6-1.4 nm)
	MWCNTs long tubes (20 to 240 nm)	MWCNTs not very much interest in this method	MWCNTs short with inner diameter of 1-3 nm and outer diameter of 10 nm

2.3.3.1 Historical Development

CVD is not a novel procedure. As indicated in Powell, Oxley, and Blocher's work (C. F. Powell et al., 1966), its first practical usage was developed in the 1880s in the manufacturing of incandescent lights to strengthen the strength of filaments by coating them with carbon or metal. In the same decade, the carbonyl method was invented by Ludwig Mond and colleagues for the synthesis of pure nickel. Several patents were granted during that era addressing the foundation of CVD (H O Pierson and Lieberman 1975).

CVD grew slowly in the following fifty years and was restricted largely to extraction and pyrometallurgy to manufacture high-purity refractory metals such as zirconium (Cameron and George 1999; Fix, Gordon, and Hoffman 1991), titanium (Kurtz and Gordon 1986; Siefering and Griffin 1990), and tantalum (Fix, Gordon, and Hoffman 1993; Tsai et al., 1995). Numerous fundamental CVD approaches were created at that time including the Mond process (the carbonyl cycle) (AUSTEN 1899), the de Boer-Van method (the iodide decomposition) (Loonam 1959), and the Kroll process (the magnesium-reduction reaction) (Wartman et al., 1954).

After World War II, CVD improved fast as researchers understood its potential to synthesize coatings and extraordinary morphologies (Hugh O Pierson 1999). Its relevance has been expanding ever since. Other crucial dates in the evolution of CVD history are indicated in Figure 2.9.

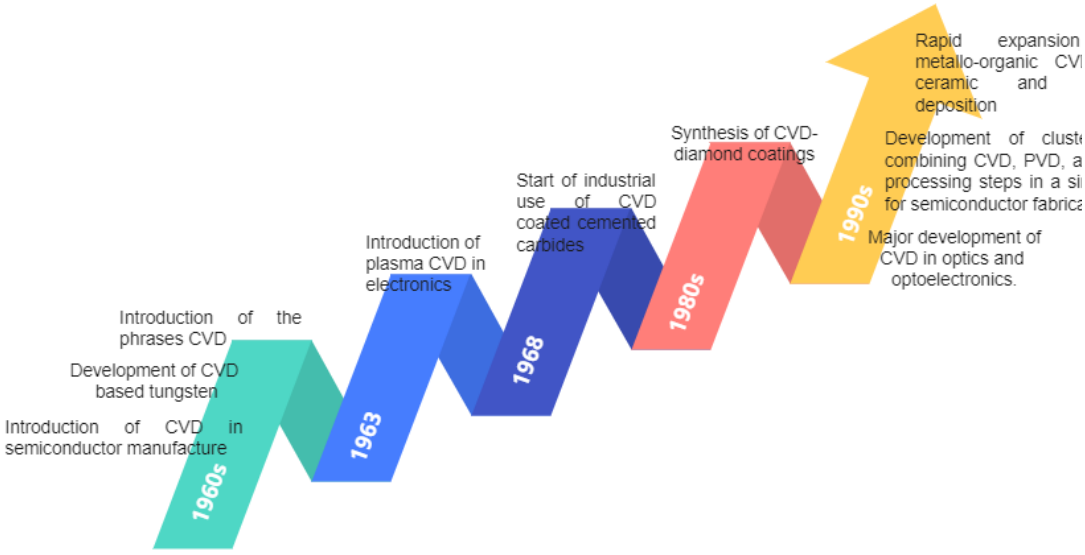


Figure 2.9 Important dates of the CVD Timeline, Redesigned based on (H O Pierson and Lieberman 1975; Hugh O Pierson 1999; C. F. Powell et al., 1966; Q. H. Powell, Kodas, and Anderson 1996)

Since carbon nanomaterials are extensively employed in many applications due to their unique chemical and physical characteristics, the necessity for large-scale manufacturing has been met with the CVD process as the most effective option. Since the early 2000s, major members of the nanocarbon family, such as fullerenes (Chow et al., 1995; X. Wang et al., 2006), CNTs (Colomer et al., 2000; Kong, Cassell, and Dai 1998), CNFs (Merkulov et al., 2001; Todankar et al., 2021; Yoon and Baik 2001), graphene (Kidambi et al., 2012; X. Zhang et al., 2014; Y. I. Zhang, Zhang, and Zhou 2013), and CNOs (C. He et al., 2006; Ruan et al., 2020; C. Zhang et al., 2011), have been synthesized by different CVD processes.

Nowadays, technology is growing at an extremely fast pace. However, to preserve the appropriate viewpoint, it should be recognized that it took almost a century of constant and continuous scientific and technical endeavors to attain the current state. Nevertheless, despite this development, several daunting obstacles remain, such as the accurate estimation of a given CVD composition and its structure and characteristics.

In reality, even while the knowledge of the theory and mechanism of CVD has made enormous gains, the procedure is still frequently regarded as much an art as a science, and progress continues to depend for a big part on experimental breakthroughs.

2.3.3.2 Chemical Vapor Deposition Technique Types

CVD technique is known as simple manner using gas precursor that contained hydrocarbons, and temperature range of CVD reaction of 350-1000^{o}C. Different factors affect CNT synthesis, such as duration and temperature of the reaction, the diameter of catalyst, volume, and type of reactant gas(J.-H. Park and Sudarshan 2001). Classification methods of CVD, depending on energy source and categorization in many kinds; for instance, when the heat source is thermal resistance, the flame of infrared lamps this CVD termed thermal CVD and mechanism and catalyst of process influential in the development of CVD (Mirabootalebi and Akbari 2017). Standard methods of synthesis CNTs are: Catalytic CVD (Magrez et al., 2010; Öncel and Yürüm 2006), Plasma enhanced-CVD (Yanase et al., 2019), Water-Assisted CVD (Y. Zhao et al., 2015), Oxygen-Assisted CVD, Aerosol-Assisted CVD, Alcohol Assisted CVD, Laser CVD, Hot Filament CVD. Figure 2.10 demonstrates the significant approaches CVD for synthesizing CNTs.

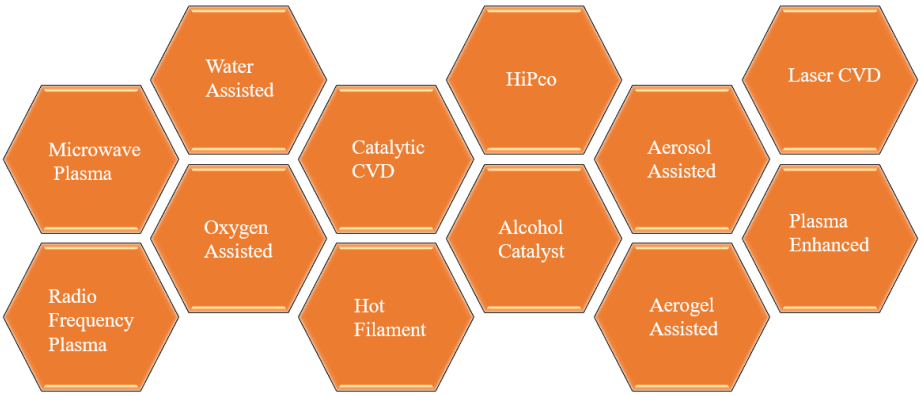


Figure 2.10 Various CVD Technologies

In traditional CVD, the hydrocarbon precursor is decomposed on the metal catalyst particle present in the substrate in the inert atmosphere (Figure 2.11). The hydrocarbon might be in liquid form as toluene, benzene, xylene and ethanol or gaseous form as acetylene and ethylene. The catalyst may be any transition metal such as Ni, Co and

Fe(Mathur, Singh, and Pande 2016). Catalytic chemical vapor deposition (CCVD) is presently the most suited technology for producing carbon nanotubes and utilizes the foundations of the classic CVD method (Magrez et al., 2010). Many research groups have successfully performed to properly regulate the manufactured carbon nanotubes' physical shape(W. Q. Chen et al., 2021; Danafar et al., 2009; S.-H. Lee et al., 2021; Maruyama et al., 2020; Qiang Zhang et al., 2019). For many scientific research groups synthesizing carbon-based nanomaterials, the attractiveness of obtaining CCVD-based CNTs is based on the following facts: lower reaction temperature, lower cost, higher purity product, effective process control to determine final morphology, high product efficiency, adaptability to mass production (Danafar et al., 2009; Mamalis, Vogtländer, and Markopoulos 2004; Teo et al., 2003; Vahlas et al., 2006; Y. Yao et al., 2004). It is well known that CCVD-based CNTs are currently obtained with high quality compared to other methods (Girun et al., 2007). However, different CVD methods have been developed for high CNT production based on the CCVD working mechanism due to the limited production.

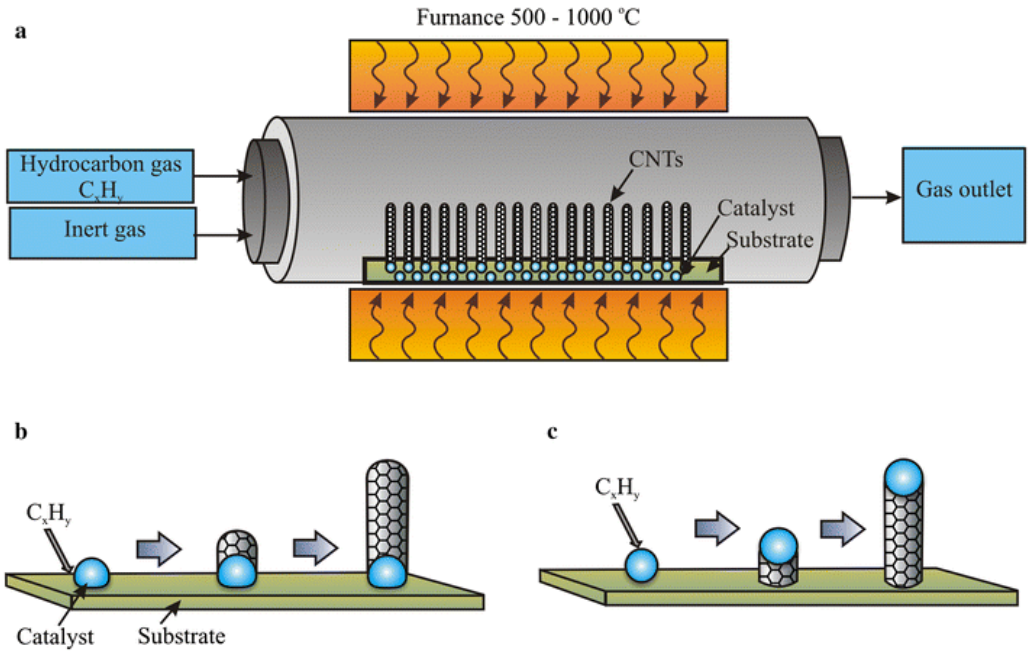


Figure 2.11 Schematic representation of Catalytic CVD process (Zaytseva and Neumann 2016)

Plasma-enhanced CVD (PECVD) is based on the production of activated carbon species by applying a high-energy plasma (Figure 2.12) Thus, it produces reduced catalyst demand for CNT manufacturing compared to other CVD procedures.

However, the main benefit of PECVD-based CNT synthesis has been described as giving a unique capacity for chirality control for SWCNTs (Ghorannevis et al., 2010; Kato and Hatakeyama 2010). Moreover, numerous early and pioneering investigations have recommended the PECVD approach for low temperature aligned CNT production (Abdi et al., 2008; Cole and Milne 2013; Hofmann et al., 2004; Hugh O Pierson 1999; Shoukat and Khan 2022; Qi Wang et al., 2021). However, the catalytic activity yield of graphitization in the PECVD process and its influence on the final morphology still need to be clarified (Yanase et al., 2019). On the other hand, different plasma sources have been applied for CNT production, and different names have been taken in terminology according to the plasma production methods in the PECVD process. These methods include DC discharge (Di Gianfrancesco 2017; Lieberman and Lichtenberg 2005; Nageswaran, Jothi, and Jagannathan 2019), RF discharge (J. Park et al., 2001), and microwave excitation (Klinbumrung et al., 2018) for CNT synthesis.

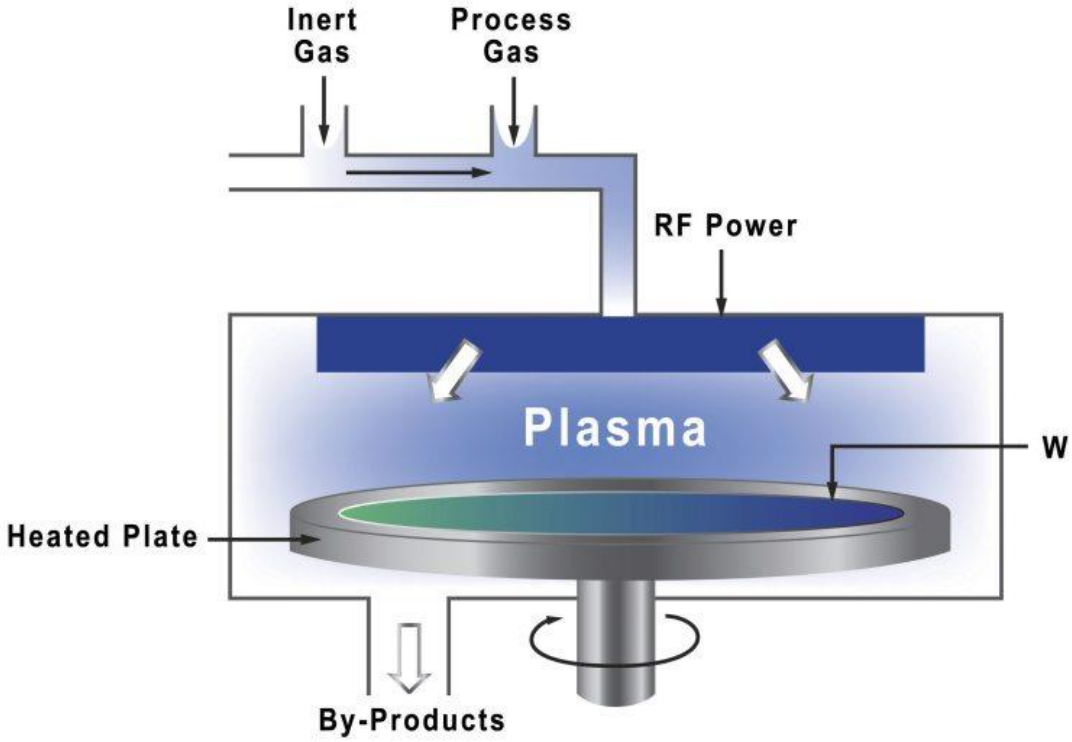


Figure 2.12 Schematic representation of Plasma Enhanced CVD process

Compared to other plasma sources, Radio Frequency Plasma Enhanced CVD (RF-PECVD) an produce homogeneous CNTs in a large area due to the very stable and homogeneous plasma (Yabe et al., 2004). However, the CNTs synthesized by the RF-

PECVD method have undesirable product quality degradation, such as coating a large amount of carbon with soot and obtaining a low aspect ratio in the final morphology (Ho et al., 2001; Valentini et al., 2002). Unlike RF-PECVD, Microwave Plasma Enhanced CVD (M-PECVD) provides high purity CNT production owing to the lack of internal electrodes in the microwave plasma generator itself. In addition, the approach provides benefits such as high reactivity, quick heating, and strong controllability (Croslyn, Smith, and Winefordner 1997; Jauberteau et al., 1998; Schulz, Munzert, and Kaiser 2001; Tatarova et al., 2017). However, the ability to increase the quality of CNTs generated by the approach for the actual use of final CNTs compared to the traditional CVD method of CNT development using the M-PECVD method is yet not established. Furthermore, the final CNTs generated by this process under the atmospheric pressure or low temperature sought for industrial applications are of poor quality(Y. Liu et al., 2021).

Some studies have hypothesized that the encapsulating of the catalyst particle with graphite in the CVD process may lead to catalyst poisoning and hinder the synthesis of CNTs. It is vital to retain the catalyst activity and lifespan, particularly for the systematic development of orientated CNT structures. For this reason, a mild oxidizing ingredient such as water or oxygen is added to the CVD process, hence boosting the catalyst activity and lifespan (Futaba et al., 2005; Hata et al., 2004; Yasuda et al., 2009). Here, the main mechanism is based on the oxidizer eliminating the by-products from carbon pyrolysis and Ostwald's ability to prevent the creation of catalyst particles for the continuation of catalytic activity (Cho, Schulz, and Shanov 2014; Yasuda et al., 2009). For instance, in the water-assisted CVD (WACVD) approach (Figure 2.13 the administration of a tiny and regulated quantity of water throughout the process prolongs the life of the catalyst particles and has also been found to boost the activity (Futaba et al., 2005, 2006). The ultimate height of the morphology produced in CNT synthesis with traditional CVD is between 100-200 micrometers (Dupuis 2005). This length is inadequate and problematic for light and high-strength material applications. Moreover, by regulating the water level in the reaction media in the WACVD approach, 7 mm high CNT synthesis was feasible in a 12-hour timeframe (Chakrabarti et al., 2006). Additionally, altogether the produced CNTs have an average height of 2.5 mm (Hata et al., 2004), and the effectiveness of the WACVD process leads to the

development of densely packed, defect-free, vertically aligned CNT forests, defined as super growth (Nihei et al., 2004; L. Zhu et al., 2005).

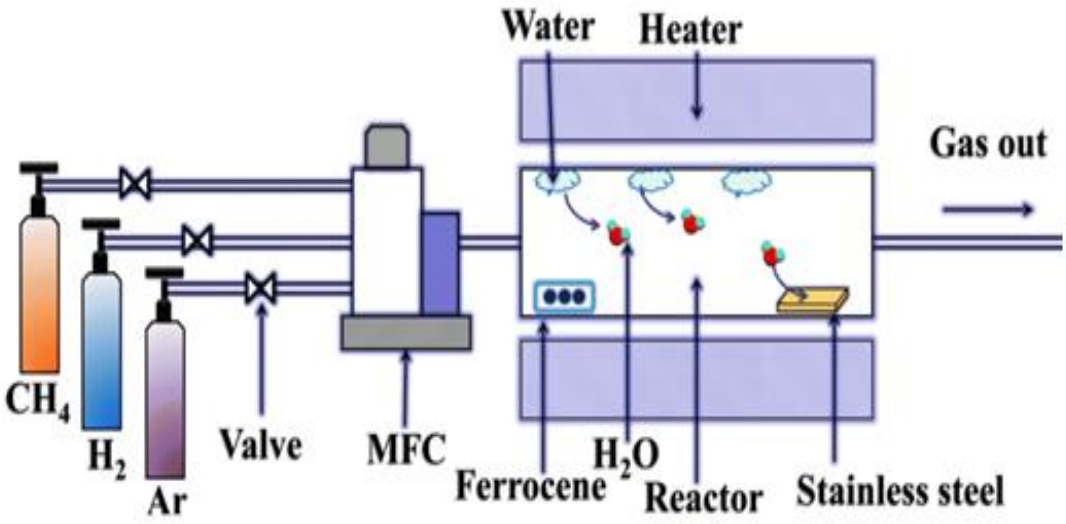


Figure 2.13 Schematic representation of WACVD process (F. Wu et al., 2019)

Similar to WACVD, ethanol, which may degrade into hydroxyl-related groups at high temperatures, can operate as a moderate oxidant (Yu et al., 2006) to prevent catalysts from coating with amorphous carbon (Yu et al., 2006). In the alcohol-assisted CVD approach, methanol or ethanol is evaporated over the surface of a ceramic substrate that contains a metallic catalyst, generating a carbon source for CNT synthesizing on the catalyst particles (Mirabootalebi and Akbari 2017). This technology provides low process temperature, high purity, cheap production cost, and excellent efficiency compared to other conventional CVD methods (Y. Li et al., 2015; Unalan and Chhowalla 2005). Oxygen is utilized as a mild oxidizing component, in the oxygen-assisted CVD technique, oxygen gas is introduced in addition to the system gases used (W. Chen et al., 2015; Liang et al., 2017), and high-efficiency SWCNTs may be produced using this method (Byon et al., 2007). The fundamental benefit of the technology is that by adding oxygen gas to the hydrogen utilized throughout the process, greater control is acquired in the management of the process. Additionally, oxygen may efficiently eliminate carbon impurities such as amorphous carbon and stop the damaging role of gas precursors during CNT manufacturing. Thus, CNTs with excellent purity and efficiency may be produced by oxygen-assisted CVD. However,

it has been observed that this approach is not suited for certain kinds of catalysts such as iron nanoparticles owing to the carbothermal reaction (Mirabootalebi and Akbari 2017). Furthermore, there has not been enough research analyzing optimization parameters for super-growing CNTs using the alcohol, water and oxygen-assisted CVD techniques (Patole et al., 2008; Y. Yun et al., 2006; G. Zhang et al., 2005).

A version of the traditional CVD process, the aerosol assisted CVD (AA-CVD) technique employs aerosol droplets to transport precursors with the help of inert or reactive carrier gases. In the AA-CVD process, the chemical precursors do not necessarily need to be volatile; they only need to be soluble in any solvent from which the aerosol may be formed (X. Hou and Choy 2006). Compared to conventional CVD techniques, AA-CVD technology is highly affordable and gives a well-defined nanotube diameter distribution (Palgrave and Parkin 2006). It is also an adjustable technology for the mass manufacture of CNTs. AA-CVD is now extensively employed to manufacture aligned MWCNTs (Mayne et al., 2001; Vivekchand et al., 2004), and partly metal-filled MWCNTs (Andrews et al., 1999; Glerup et al., 2003; R. P. Singh 2011). However, it has been claimed that this approach in some-specific situations may produce SWCNTs (X. Hou and Choy 2006). Moreover, several inorganic porous materials have also been studied by researchers as support materials in the manufacture of single- and multi-walled CNTs using AA-CVD (M. Kumar and Ando 2005, 2010). However, for the manufacturing of AA-CVD-based CNTs, the approach entails a more complicated deposition mechanism than standard CVD since it comprises atomization and evaporation processes of solvent and precursor gases. Therefore, further studies are required to understand better and apply the AA-CVD technique (X. Hou and Choy 2006).

The laser-assisted CVD (LACVD) technique is a modification of conventional CVD in which the global heat source for the furnace is replaced with a small spot heated by a laser. There are two forms of laser CVD, pyrolytic and photolytic (Bondi et al., 2006). Pyrolytic laser-assisted CVD has comparable features to conventional CVD in that it comprises the heating of thermal energy by the laser, the transfer of energy from the heated point to the reactive, the separation of reactive molecules, and lastly the realization of deposition(Duty, Jean, and Lackey 2001). However, the key feature that separates LACVD from traditional CVD is that the laser beam may be

concentrated on a tiny patch of the substrate. Thus, the substrate is not harmed and allows better control over the synthesis settings for users (Mirabootalebi and Akbari 2017). The synthesis of most materials that can be generated by conventional CVD on diverse substrate surfaces is also valid for LACVD (Alexandrescu et al., 2003; Rohmund et al., 2002). However, there is limited study on the synthesis of CNT production using LACVD, and additional studies are required to clarify the arguments regarding the mechanism of CNT generation with this approach (Bondi et al., 2006; De Heer, Chatelain, and Ugarte 1995; Shi et al., 2006).

The Hot Filament CVD (HF-CVD) is a conventional method for the deposition of diamond sheets from a combination of hydrocarbon and hydrogen(Matsumoto et al., 1982). In CNT manufacturing using HF-CVD, unlike the usual CVD approach, there is a metallic filament near the substrate. The filament is a thermal source for the decompose of the hydrocarbon gas precursor and is responsible for heating the substrate. The essential feature of HF-CVD is its applicability to mass production owing to the potential of generating big area films. It is also relatively inexpensive cost and has simple equipment (Chaisitsak, Yamada, and Konagai 2004; Yilmaz et al., 2017). However, the filaments employed during the process are mainly metallic materials like tantalum, tungsten, and molybdenum, which might lead to undesired contaminations such as amorphous carbon, which will lead to a loss in the purity and quality of the end product (C. J. Lee et al., 2002).

The efficiency and purity of the final product, and mass production were considered in the development of each CVD method. In this context, although the methods have different advantages and disadvantages, as explained above, it should be noted that they apply the principles of the traditional CVD method.

2.3.3.3 Growth Mechanisms of CNTs

In the traditional CVD, a catalyst material is heated to high temperatures in a tube furnace while precursor hydrocarbon gas flows through the tube for a while (M. Kumar and Ando 2010; Mathur, Singh, and Pande 2016). Here, the basic mechanism is to break up a hydrocarbon gas flowing continuously over the catalyst material with the help of heat to form carbon atoms in the desired morphology and then to grow CNT

on the surface of the catalyst, the substrate on the catalyst's surface, or both. For this, the carbon source is passed through a reactor in a tubular form during the synthesis, and the process is carried out at a sufficiently high temperature (Khurshed A Shah and Tali 2016).

Although studies on the growth mechanism to obtain CVD-based CNTs have been controversial, two widely accepted mechanisms consider the relationship between catalyst and substrate. When the hydrocarbon gas passes through the CVD reactor when it meets the catalyst material heated to the desired temperatures, it decomposes into hydrocarbon precursor carbon and hydrogen. A carrier gas or reducing gas is usually used to remove the hydrogen here. The dissociated carbon dissolves in the catalyst. At this point, the carbon solubility of the catalyst and, therefore, the characteristics of the catalyst are of great importance. Because when the catalyst reaches the limit of carbon solubility with temperature, the decomposed carbon begins to precipitate and thus crystallizes to form the CNT structure. Hydrocarbon decomposition is an exothermic process, while carbon crystallization is endothermic, and the thermal gradient continues this process. Therefore, the difference arising from the interaction between the catalyst and the substrate has brought forward two growth mechanisms and has led to acceptance among the scientific communities (Saleh and El-Sheikh 2019).

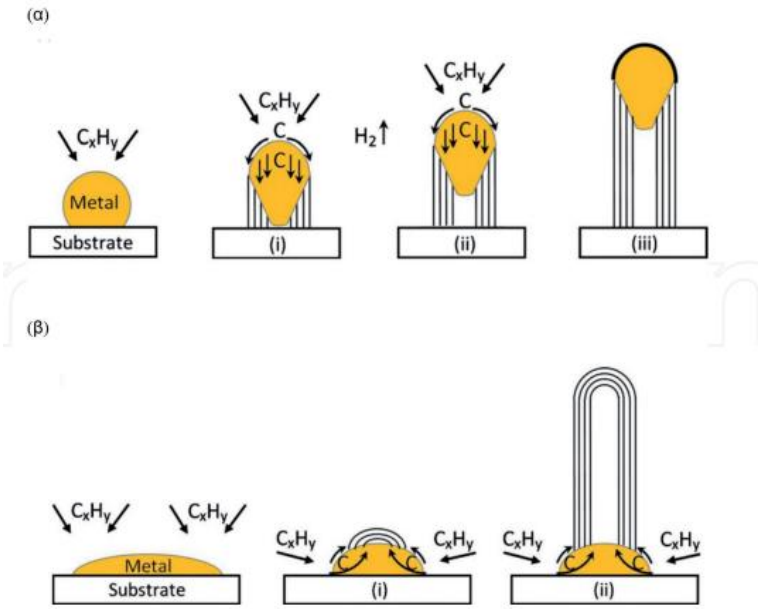


Figure 2.14 Growth Mechanisms of CNTs via CVD

The first of the growth mechanisms is called tip-growth (Figure 14a). The interaction between the metal catalyst and the substrate is weak when the catalyst has a narrow contact angle with the substrate. In such a case, hydrocarbon decomposition begins to occur on the top surface of the catalyst, and then carbon diffuses through the catalyst. When CNT begins to form, the carbon of the CNT begins to accumulate under the catalyst by taking advantage of the weak relationship of the catalyst with the substrate and thus pushes the catalyst upwards on the substrate surface in the opposite direction. Meanwhile, a concentration gradient remains in the catalyst until the top of the catalyst is freed for new hydrocarbon decomposition. Therefore, the diffusion of carbon continues. Thus, the precipitated carbon in the form of CNT continues to lengthen the CNTs, making them larger. When the catalyst is completely covered with carbon, it is saturated with carbon so that no further concentration gradient can exist, and the catalytic activity ceases. CNTs stop growing (Baker et al., 1972; Mathur, Singh, and Pande 2016; X.-D. Wang, Vinodgopal, and Dai 2019).

The other accepted mechanism is called base growth (Figure 2.14b), in which there is a large contact angle between the catalyst and the substrate, in contrast to type-growth. In this mechanism, the interaction between the catalyst and the substrate is strong. However, when the hydrocarbon begins to decompose, a type-growth-like trend is observed first. CNT precipitation for carbon diffusion fails due to the strong interaction between catalyst and substrate. Therefore, the hydrocarbon is forced out of the top of the catalyst in areas with minimal interaction with the substrate to precipitate. Therefore, the crystallization of carbon takes place in the form of a closed carbon network on the most suitable surface of the catalyst, unlike type growth. The CNT structure is formed by the continuous elongation of the carbon network in the form of a graphitic cylinder. The successive decomposition of the hydrocarbon precursor must take place on the lower side surfaces of the catalyst. Thus, the carbon dissolved in the catalyst begins to diffuse upwards. Therefore, the carbon that makes up the CNT grows with the catalyst in the substrate and is rooted in the substrate (Baker and Waite 1975; Mathur, Singh, and Pande 2016; X.-D. Wang, Vinodgopal, and Dai 2019)

2.3.3.4 System Parameters

The key phases of growing CNTs using CVD technique are as follows:

1) Insert the substrate on which CNTs are to be generated

2) Heat the system to the appropriate temperature in an inert gas environment

3) Send etching gas such as hydrogen, or nitrogen to produce catalyst nanoparticles

4) Feed the hydrocarbon gas into the system, and then breakdown the hydrocarbon gas on the catalyst nanoparticles.

5) Perform development of CNTs on catalyst nanoparticles (NPs)

6) Cool the system to ambient temperature in an inert gas atmosphere (Ivanov et al., 1994).

Therefore, during the synthesis of CNTs, many parameters affect the final morphology and properties of CNTs, such as carbon source, catalyst, reactor temperature, system pressure, flow rate of carrier gas, deposition time, reactor type, the geometry of reactor, catalyst support, active metal components in catalyst, and so on. In this section, a complete review of the parameters which regulate the final CNT morphology, indicated in the literature to be most relevant for growth mechanisms is presented.

Catalyst Type

The catalyst material is one of the most critical parameters affecting CNT growth. Many articles in the literature point out that catalysts are essential materials for well-defined shapes and structures of CNTs in a relatively short period (Ando et al., 2004; Laurent et al., 1998; C. J. Lee et al., 2001). The catalyst material has been considered one of the indispensable parameters affecting CNT's growth and kinetics since it is the substance responsible for having either SWCNTs or MWCNTs and either with the tip-growth or base growth mechanisms(Mathur, Singh, and Pande 2016). The catalyst nanoparticle produces nucleation sites for CNT formation and may thus be considered the father of the synthesized nanotube (Khurshed A Shah and Tali 2016). The size of the catalyst dictates the single-walled or multi-walled structure of the final CNTs. For instance, SWCNTs may be generated with catalyst particles a few nm in size, whereas

particles a few tens of nm in size can lead to the MWCNTs (Dupuis 2005; Kukovitsky et al., 2002). Moreover, it has been observed that it is feasible to manufacture MWCNTs without catalyst assistance in some situations (Lipert et al., 2010). However, the major role of the catalyst is to establish nucleation sites where the hydrocarbon precursor to being decomposed by heat would precipitate at a lower temperature to form CNTs (Rashid et al., 2015). Because of the initial necessity for a catalyst for SWCNTs nucleation, significant emphasis has been dedicated to the role of the catalyst in the literature. For MWCNTs, however, these experiments did not go further than hydrocarbon decomposition at the catalyst surface. There is still a contradictory argument in the literature about the role of catalysts. For example, it is now commonly accepted that the diameter, length, and chirality of CNTs and the role of the catalyst in nanotube nucleation and development are not well understood, and consequently, enough control is not given considering a single CVD procedure (Bajwa et al., 2008; Baker and Waite 1975; Hasanzadeh and Eskandari 2020; Moshkalev and Verissimo 2007; Rashid et al., 2015).

In CVD manufacturing of CNTs commonly transition metal nanoparticles\sare utilized as catalysts. In the recent decade, researchers over the world have made considerable efforts to examine the influence of catalyst types on CNT synthesis by CVD (Esteves, Oliveira, and Passos 2018; Hoecker et al., 2016, 2017; Rashid et al., 2015). In this regard, it can be mentioned that the most usually proposed catalyst is iron-based, owing to metals with limited d-vacancies, such as Fe, having restricted carbon solubility in certain temperature ranges (M. He et al., 2016; X.-D. Wang, Vinodgopal, and Dai 2019). Additionally, research have showed that carbon has a greater solubility for Fe at high temperatures, which leads to the production of metal-carbon solid solutions (H. Dai 2002a; J.-B. Park et al., 2002). Hence, Fe demonstrates substantial carbon solubility and diffusion at higher temperatures and produces excellent CNT yields (F. Ding et al., 2008). Like Fe, Co and Ni transition metals are catalysts utilized in creating practical CNTs for reasons such as high carbon solubility at high temperatures and high diffusion rate of carbon in these metals (Bistamam and Azam 2014; Rashid et al., 2015; Tatarova et al., 2017; N. Zhao et al., 2022). In addition, the low equilibrium vapor pressure and high melting point of these metals give the benefit of the CNT synthesis via CVD process over a wide range of

temperatures for a wide variety of carbon sources. It has also been revealed that Fe, Co and Ni exhibit better adhesion to the synthesized CNTs compared to other transition metals.(Sohn et al., 2001; W.-C. Yang, Yang, and Yew 2007; J. Zhang, Tu, and Goto 2011)

On the other hand, 3d and 4d metals with multiple d-vacancies (such as Ti and Nb) may establish strong chemical interactions with carbon to produce very stable carbides (Arthur and Cho 1973). Furthermore, in previous systematic studies of catalyst materials, Al (Ghai, Chatterjee, and Agnihotri 2021), Cu (R. Cui et al., 2010; Khorrami and Lotfi 2016; P. Li and Zhang 2016), Co(S. Ahmad et al., 2019; Esteves et al., 2021), Ni(J. Lin et al., 2018; Z. Ma et al., 2021), Mg (X. Li et al., 2020), Mn (B. Liu et al., 2008), Mo (Yahyazadeh and Khoshandam 2017), Cd (Qian, Lu, and Gao 2011), Cr (C. J. Lee et al., 2000; Pasha, Shafiekhani, and Vesaghi 2009), Ag (Yazyev and Pasquarello 2008), Au (Homma 2014), Sn (Kanada et al., 2008), Pt (Jiajun Wang et al., 2008) and Pd (Wong et al., 2004) have also been reported to have the capacity to catalyze the breakdown of hydrocarbon precursors for CNT formation. Besides metallic catalysts, CNTs have also been synthesized by utilizing diamond (Takagi, Kobayashi, and Homma 2009) and semiconductor (Si and Ge) nanoparticles (Takagi et al., 2007) as catalysts and on sapphire (Takagi et al., 2007) and scraped thin SiO_2 sheets (Huang et al., 2009).

In selecting catalysts, it should be considered that the final CNTs to be obtained should have properties for the application area depending on their structural and morphological properties. Structural features are produced by the catalyst from the production parameters with a dominant mechanism. However, many studies involve motivations such as lowering the process temperature and thus consuming less energy (M. Ahmad and Silva 2020; Diao et al., 2018). Another factor affecting production is the distribution of catalysts on the substrate surface (Hu et al., 2018; X. Yang et al., 2016). Nanoparticles, prone to agglomeration, are commonly used to produce CVD-based CNTs. However, lithography is recommended as the most effective technique to minimize agglomeration, ensure a homogeneous distribution of catalysts on the substrate surface, and generally orient the CNTs (Khurshed A Shah and Tali 2016). In summary, the type, size, amount, and distribution of the catalyst used to control the

diameter and crystallinity of the final CNT to be obtained, is one of the most critical process parameters for efficient synthesis in the CVD method.

Substrate

It is essential to consider all possible chemical and mechanical interactions that could occur during the CVD system's CNT production. Therefore, each interaction should be understood separately, and their combined effects should be assessed (Hart and Slocum 2006). Although catalysts typically have a significant impact on the structural characteristics of CNTs, the regulation and activity of the catalytic sites, as well as CNT-CNT and CNT-substrate interactions, determine whether they are synthesized in an isolated, complex, or directed configuration (Duchamp et al., 2010; Veronese et al., 2007).

To produce CVD-based CNTs, a suitable substrate must be chosen after an appropriate catalyst has been chosen. Because the substrate material can directly affect the surface morphology, rheology, and structural properties of the CNTs to be produced, it is vital to consider the substrate material and type when evaluating its interactions with the catalyst for the final CNT quality and yield. The substrate serves as more than just catalyst support in this situation. It can also have a say on CNT morphology by interacting with catalysts and growth mediums. Therefore, the interaction between catalyst and substrate needs to be carefully studied (Duchamp et al., 2010; Guellati et al., 2018; H. Liu et al., 2008). These interactions can be handled physically and chemically. Examples of physical interactions that can prevent the catalysts on the substrate surface from moving during the process include Van-der-Waals and electrostatic forces. Additionally, thermally accelerating and/or reducing expected diffusion can lessen the sintering of catalysts on the substrate surface. As a result, during the CVD process, the physical interactions between the catalyst and substrate result in the stabilization of the CNTs concurrent with the catalyst particle size distribution. Moreover, chemical interactions between substrates and catalysts can decrease agglomeration in the production of CNTs and maintain the size distribution of catalysts (Ghaemi et al., 2019; Khurshed A Shah and Tali 2016).

There are numerous and intricate interactions between catalyst and substrate materials. A substrate material's thermal and chemical stability is a general prerequisite

for growth of CNTs by CVD. Because it has been discovered that direct growth on silicon (de los Arcos et al., 2002) or metal substrates (Nessim et al., 2009; Talapatra et al., 2006) is challenging due to the diffusion of the catalyst material into the substrate and the formation of silicide or alloys upon heating to CNT temperature (Chhowalla et al., 2001; Melechko et al., 2005). The suitable selection of substrate is therefore essential for the achievement of CNTs. The most common substrate materials with proper catalysts for CNT growth include alumina (Adewumi et al., 2021; Hongo et al., 2002; Mochen Li et al., 2021), silicon (Hata et al., 2004; M. Kumar et al., 2004), and magnesium oxide(Ago et al., 2004; Ward, Wei, and Ajayan 2003). Besides these substrates, clay (Aodkeng et al., 2022), graphite (Baker et al., 1972, 1973), calcium carbonate(Couteau et al., 2003), quartz (Kitiyanan et al., 2000; M. Kumar and Ando 2003; Q. Wu et al., 2021), sodium chloride (Szabó et al., 2003), silicon carbide (SiC) (D. Ding et al., 2003; Murakami et al., 2004), silicon wafer (Simionescu et al., 2022; X. Zhao et al., 2021), silica (Mattevi et al., 2008), and zeolite (Willems et al., 2000) are some of the substrates used in CVD for the growth of CNT. However, the most common discussion among researchers about the synthesis of CNTs by CVD focuses on Si and SiO_2 substrates. According to some researchers, CNTs will preferentially grow on silicon rather than silica (Snow et al., 2003), while others claim the contrary (Delzeit et al., 2002). The substrates became safe tools for synthesizing CNTs due to the discrepant results of catalyst materials and the growth environment, and they have been then widely used to obtain the oriented tubular form of carbon.

Hydrocarbon source

The carbon source's molecular structure significantly impacts the morphology of the CNTs manufactured, and the catalyst life can be prolonged by carefully choosing the CNT precursor and its vapor pressure (H. B. Abdullah et al., 2017). For instance, as they thermally decompose into atomic carbons, linear dimers or trimers of carbon, linear hydrocarbons such as acetylene, ethylene, and methane create flat hollow CNTs. In contrast, cyclic hydrocarbons such as fullerene, benzene, cyclohexene, and xylene generate comparatively curved CNTs with cross-linked tube walls frequently inside(Pant et al., 2021).

Of most hydrocarbons, MWCNTs are more accessible to grow than SWCNTs. Since SWCNTs have higher formation energies than MWCNTs due to their small diameter, high curvature bearings, and high strain energy, it can be inferred that higher temperatures are needed to produce SWCNTs (M. Kumar and Ando 2010). However, MWCNTs' effective carbon sources (benzene, acetylene, etc.) can lose their high-temperature stability and typically become unstable at higher temperatures, causing large amounts of carbonaceous compounds to accumulate outside the nanotubes(H. B. Abdullah et al., 2017; Ahmed et al., 2009). In contrast, SWCNTs can be grown by methane and carbon monoxide without losing high-temperature stability (Guéret, Daroux, and Billaud 1997; Q. Li et al., 2004; Shaikjee and Coville 2012). Thus, the hydrocarbon gas used directly correlates with the temperature in the CVD process, and optimization is essential.

Generally, it is the widely accepted hypothesis that in the CVD mechanism, the precursors decompose into C or C_2 units before precipitating into the metal (Q. Li et al., 2004). Based on this hypothesis, researchers worldwide have demonstrated that they can obtain efficient CNTs by using hydrocarbons such as ethane (Sen, Govindaraj, and Rao 1997), methane (Esteves et al., 2021; Gubernat and Zambrzycki 2021), acetylene (Redina, Avramenko, and Lyanguzov 2021; Songyan Wang et al., 2022), ethylene (Bronikowski 2022; Mochen Li et al., 2021), ethanol (McLean, Mitchell, and Ding 2022; Sawant et al., 2022), carbon monoxide (X. Zhao et al., 2021), xylene(Huseynov et al., 2022; Mitra et al., 2022), isobutane(B. Hou et al., 2011).

Processing Temperature

The characteristics of the hydrocarbon precursor used, as well as the type and size of the catalyst particles, are influenced by the process temperature. As mentioned above, due to the higher energy requirement, single-walled carbon nanotubes (SWCNT) are typically processed at higher temperatures than multi-walled ones, and high-temperature stable hydrocarbons are preferred in this case (Colomer et al., 2000; Min et al., 2005). However, hydrocarbon precursors that produce MWCNTs should be preferred at lower processing temperatures. Therefore, the relationship between hydrocarbon and processing temperature is examined before deciding what morphology should be synthesized (Ganesh 2013; Shudin et al., 2021).

The average radius of the structure that will be formed is another effect of the process temperature. The temperature-dependent formation and morphological characteristics of multi-walled carbon nanotubes may differ depending on the catalyst used in the CVD process. With catalyst support, the general process temperature to produce CNTs can range from 550°C to 1000°C (Ducati et al., 2002). Depending on the rise in processing temperature, sintering is seen in the catalyst nanoparticles used in the case of MWCNT. The small catalyst particle agglomerates form larger particles because of the sintering that takes place in the catalyst (Kukovitsky et al., 2002). To expand a little further, it seems that an increase in reaction temperature tends to raise the reduction temperature, which in turn causes the catalyst particles to clump together and the growth of MWCNTs with larger diameters (C. N. He et al., 2008).

Growth Time

The growth time directly affects the morphological and structural features of the CNTs to be obtained; the growth time mentioned here is when the carbon precursor is applied. Additionally, the literature uses a variety of expressions, including synthesis time, deposition time, and exposure time (Ghoranneviss and Elahi 2016; Mathur, Singh, and Pande 2016; Khurshed A Shah and Tali 2016). The growth time first decides whether the final CVD-based product will be nanotubes or nanofibers. Depending on the increase of the growth period, the product's average diameter may rise steadily and eventually reach nanofiber levels. The long-term feeding of the hydrocarbon precursor to the system will result in thicker and longer tubular structures, as has been repeatedly demonstrated in earlier studies (Altay and Eroglu 2012; Qing Zhang et al., 2002). However, the recommended growth time for efficient CNT synthesis is usually between 15-60 min (Khurshed A Shah and Tali 2016).

The structural characteristics of the final CNTs are another factor that is influenced by the growth time. These structural characteristics are frequently linked to crystal defects and quality. Even if the CNT structure is created through prolonged exposure to the hydrocarbon precursor, carbonaceous impurities may still be incorporated into CNTs. With longer growth times, CNTs lose their crystallinity and quality (Ghoranneviss and Elahi 2016; Jourdain and Bichara 2013). Furthermore, it has been demonstrated that although the CVD system has a wide range of process parameters,

the amount of carbonaceous impurities solely depends on the total time spent exposed to the carbon source(Yasuda et al., 2009).

Other factors

A characteristic limit temperature value is required in each chemical vapor deposition methodology stage for optimized synthesis. However, with changes to every step, the processing conditions must be optimized for the highest possible yield. Reproducibility of the high quality and quantity of CNT produced is, therefore, an important standard for subsequent studies. The following parameters are crucial determinants of the product's final quality, along with some constant variables for repeatability.

- Pretreatment: Because impurities in the organic source would reduce the overall yield, pre-treatment the organic source is necessary before use. To maintain the consistent component chemistry of the organic sources, the preprocessing can be either physical or chemical (Pant et al., 2021).
- Alloying catalysts: Previous CNT experiments took place individually with Ni, Co, and Fe metal catalysts. Although there were higher CNT deposits due to iron's high catalytic effect on hydrocarbon decomposition, those CNTs had poor graphitization (Hernadi, Fonseca, Nagy, Bernaerts, et al., 1996). On the other hand, a cobalt catalyst led to CNTs that were better graphitized but had a lower yield (Hernadi, Fonseca, Nagy, Bemaerts, et al., 1996). Thus, it was tried to bring together the unique advantages of the two metals, and it was productive for producing well-graphitized MWCNTs in massive amounts. Another benefit of using the bimetallic catalyst was that CNTs could be grown at 550^{o}C, at a much lower temperature. It is so because the melting point of Co and Fe combined has a lower melting point than either metal's independent melting point (Coquay et al., 2005; Lobiak et al., 2015). Additionally, alloys have a reputation for being superior catalysts to pure metals. These patterns imply that tri-metallic catalysts should also produce intriguing outcomes, albeit with a more challenging interpretation.
- Catalyst concentration: The concentration of the catalyst is also crucial for CNTs growth. For instance, in the study, where the catalyst concentration in

the zeolite varies in a wide range (1–50 wt.%), CNT is not formed for a catalyst concentration lower than 2.4% by weight in the zeolite, and SWCNTs is obtained with catalyst concentrations 2.4-5%. Results have been reported that higher concentrations lead to MWCNTs growth(M. Kumar and Ando 2010). Another study revealed that MWCNTs structure was obtained with increasing concentrations of Thiophene and Ferrocene catalysts, while SWCNT formation was supported at low concentrations(Y. Jung et al., 2013). In another study, a combined Fe + Co concentration of 40% was also shown to produce the highest yield of MWCNTs with the least amount of metal contamination(M. Kumar and Ando 2008). These studies have shown that SWCNTs or MWCNTs can be grown in a selective manner by carefully choosing the catalyst materials concentrations.

- Combination process for the catalyst and substrate: The right placement of the catalysts on the substrate surface can enable the formation of regions where the CNTs will nucleate to orient the final CNTs. Prior to CVD, catalysts can be applied to the substrate surface using techniques like lithography(Man et al., 2015), electrospray (Vicentini et al., 2019),spraying sol-gel solutions (Terrado et al., 2006), and spin coating(G. S. Choi et al., 2003); this not only promotes the formation of oriented CNTs but also effectively prevents the agglomeration of catalyst particles.
- Vapor pressure of applied gases: Another crucial factor in the controlled growth of CNTs by CVD is the vapor pressure of the hydrocarbon in the reaction zone. However, a limited gas flow rate and controlled vacuum pump with a rotary pump can be used to keep the required vapor pressure for gaseous hydrocarbons in the CVD reactor (W. Z. Li et al., 2001).
- Precursor gas flow rate: Selecting the proper flow rate is crucial during optimization studies. Since hydrocarbon gas serves as the system's primary carbon source, it must be passed through the CVD reactor at the appropriate flow rate and during suitable decomposition periods. Otherwise, the catalyst particles will not be able to receive enough carbon atoms to produce tubular morphology. On the other hand, many tubular CNTs can be produced above a

certain flow rate, but it is possible to find impurities like amorphous carbon(Haidari et al., 2022).

- Carrier gas flow rate: In addition to the hydrocarbon gas precursor, a carrier gas is also used in the CVD process. The carrier gas is usually chosen from nitrogen and argon gases, which also provide an inert atmosphere. In CNT growth, the carrier gas fed to the CVD furnace from the first step of the process is also applied while the hydrocarbon gas is fed. Therefore, it has a say in the structural and morphological features of the final CNTs. For instance, higher nitrogen carrier gas flow rates indicate MWCNTs with a higher degree of graphitization and lead to more defects in the final MWCNTs. Moreover, nitrogen carrier gas flow rates greater than or equal to 200 sccm have been reported unsuitable for CNT formation (Khorrami and Lotfi 2016; Malgas et al., 2008).
- Agent gas and gas mixture ratios: The ratio of hydrocarbon gas precursor and carrier gases is crucial for effectively synthesizing CNTs. Numerous studies have optimized these ratios in the literature by mentioning and relating to the characteristics of the catalyst. Additionally, auxiliary gases, such as H_2, also known as agent gas, are added to the CVD system to strengthen the reducing environment (M. Jung et al., 2001; Simionescu et al., 2022).

2.4 Extraordinary Features of Carbon Nanotubes

Extensive research has been done on carbon nanotubes because of the extraordinary physical, chemical, and biological properties of the CNTs (Meyyappan 2004; Reich, Thomsen, and Maultzsch 2004), mentioned above caused by their structural characteristics. This section will thoroughly examine the most outstanding characteristics of CNTs, which stand out in various application fields, particularly considering their physical, chemical, and biological characteristics.

2.4.1 Carbon Nanotubes Physical Properties

Graphene and SWCNTs electronic band structures are nearly identical. The valence and conduction bands of metallic SWCNTs and graphene touch at locations in the two-

dimensional space. The valence band and conduction band of semiconducting SWCNTs are separated (Figure 2.15) (Avouris et al., 2003; Imry and Landauer 1999; McEuen and Park 2004). Ideal nanotubes are ballistic conductors for distances of a micron, according to theoretical studies. Ballistic conduction results from the confinement of electrons in a single dimension and the prerequisites for momentum and energy conservation(Kong et al., 2001; McEuen et al., 1999).

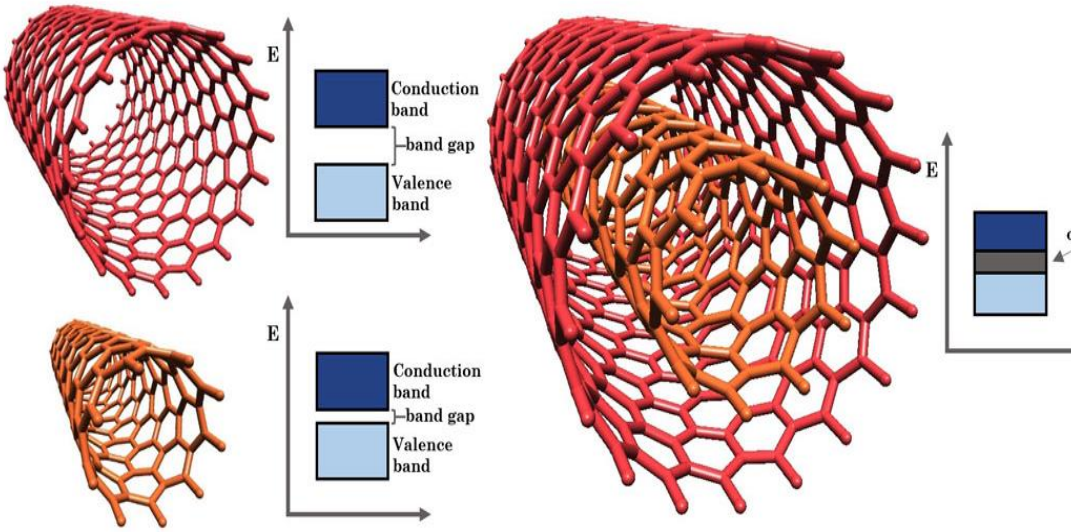


Figure 2.15 Schematic representation of band gaps of single- and double-walled CNTs; SWCNTs have band gaps and are semiconductors, whereas DWCNTs' overlapping band gaps make them semi-metal. However, as the number of walls increases, the conductivity features will change (Soto et al., 2015)

The electrical characteristics of SWCNTs have been the subject of extensive study, whereas similar efforts have not been made for MWCNTs (Awano et al., 2006; Kong et al., 1999; Soh et al., 1999; C. Zhou, Kong, and Dai 2000). Because investigating the electrical properties of multi-walled CNTs are extremely challenging due to the different electronic properties and chirality of each wall, the additional complexities arising from their structure, and the interactions between the walls themselves(P G Collins and Avouris 2002; Philip G Collins, Arnold, and Avouris 2001). However, band gap searches have shown that SWCNT and MWCNT have different electronic structures, as shown in Table 2.2 Although MWCNTs are considered non-semiconductive, it has been shown that outer-wall conduction controls electronic transport at low bias and temperatures, even though the MWCNTs are connected at

both ends by metallic contacts (P G Collins and Avouris 2002; Rau and Schock 1999). The resistance of MWCNTs with numerous walls can be significantly reduced by wall-to-wall interactions, according to theoretical models (Naeemi and Meindl 2006) and experimental findings(H. Li et al., 2005).

In summary, SWCNTs can behave metallically or semiconductors depending on their diameters and the chiral angle between their hexagons and the tube axis, whereas MWCNTs can bring up to 10^9 A cm^{-2} of current, are always metallic, and have no bandwidth. Furthermore, compared to graphite electrodes, the open end of MWCNTs has a fast electron transfer rate, whereas the open end of SWCNTs has a much slower electron transfer rate. The MWCNTs are like the metallic/semiconductor SWCNTs in structural complexity and current carrying capacity. In contrast to SWCNTs, MWCNTs also have different parameters for each wall. Furthermore, CNTs are particularly excellent candidates for electrical applications due to their superior electrical features, including electrical conductivity (104 S/cm), field effect mobility (79,000 cm^2/Vs), and electron mobility (100,000 cm^2/Vs) (Gergeroglu, Yildirim, and Ebeoglugil 2020).

Table 2. 2 Some physical characteristics of MWCNTs and SWCNTs (X.-D. Wang, Vinodgopal, and Dai 2019)

Features		SWCNTs	MWCNTs
Electrical	Bandgap	When n-m is divisible by 3 (0 eV, metallic) When n-m is not divisinle by 3 (0.4-2 eV, semiconducting)	0 eV (non-semiconducting)
	Typical resistivity	10^{-6} Ωm	
	Maximum current density	10^7-10^9 Acm^{-1}	–
	Typical quantized conductance	12.9 $k\Omega^{-1}$	
Mechanical	Young's Modulus	~1 TPa	~1- 1.2 TPa
	Tensile Strength	~60 GPa	~0.15 TPa
Thermal	Thermal conductivity	1750- 5800 Wmk^{-1}	>3000 Wmk^{-1}

Analyzing the electrical structure of capless nanotubes allows us to anticipate their optical properties, and some electronic features and geometrical structures can be determined by measuring the optical characteristics. However, the complexity of nanotube tips, and the geometric construction of nanotubes, pose a considerable problem in predicting optical features. Some nanotubes, for instance, have closed ends, while others have open ends; this extreme state has the potential to dominate the optical characteristics of nanotubes. As a result, the geometry of an open-ended nanotube becomes highly complicated. Long length does not affect the determination of optical characteristics of open-ended CNTs (Hartschuh et al., 2005; Shyu et al., 2003). At this point, the rotational symmetry of the nanotubes influences the electronic structure's features. Figure 2.16 shows that (6,4)200 and (6,3)198 tubes have C_2 and C_3 symmetry, respectively. The band gap of (6,3)198 is not zero, but the highest occupied and lowest unoccupied molecular orbitals degenerate for (6,4)200. If (6,3) and (6,4) nanotubes' lengths are increased, the tubes and their electronic structures will be identical to those found at (6,3)198 and (6,4)200, respectively. Furthermore, the bandgaps for open-ended (6,3) nanotubes are not zero, and the intervals between two nearby energy levels close to the Fermi surface are similar. The bandgap of the nanotubes is zero for open-ended (6,4), and the energy difference between the HOMO and the next highest filled level is substantially more than the gap between the other two nearby energy levels. Similarly, the energy difference between the LUMO and the next lowest empty level is significantly more significant than the difference between the other two nearby energy levels. Thus, tubes (6,4) and (6,3) are metal and semiconductor, respectively. In the case of infinite-length nanotubes, however, (6,4) and (6,3) tubes are semiconductor and metal, respectively. The periodic boundary condition along the infinite-length nanotube axis accounts for the variation in electrical structures between infinite and finite-length nanotubes (Wan, Dong, and Xing 1998). Therefore, while determining the optical characteristics of an SWCNTs or MWCNTs, a hypothesis based on their geometric structure can be advanced via their electronic states. The optical characteristics of SWCNTs and MWCNTs are commonly investigated independently for a single CNT. Because of their bigger size, MWCNT has more regular and uniform optics than SWCNTs (E. T. Abdullah, Hasan, and Naje 2013). As predicted for a one-dimensional (1-D) system, intrinsic SWCNTs photoluminescence

possesses a simple narrow Lorentzian line shape and polarization dependency. Although the immediate environment influences the optical transition wavelength and intensity, single nanotubes are remarkably photostable(Carlson and Krauss 2008).

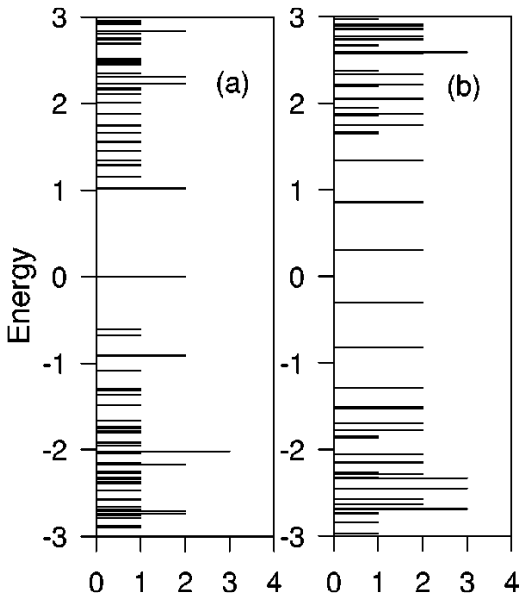


Figure 2.16 Energy-level structure based on nanotube HOMO and LUMO. The length of the line is related to the energy level's degeneracy. The undegenerated levels have the shortest line. (a) (6,4); (b) (6,3) (Wan, Dong, and Xing 1998)

The geometric structure, like all other features, dominates the magnetic characteristics. In one theoretical investigation, for example, it was shown that close-ended nanotubes exhibit an extraordinarily strong paramagnetism (L. Liu et al., 2002). However, the measured value of diamagnetic susceptibility for MWCNTs is generally identical to quasi-two dimensional (2-D) graphite (Figure 2.17) (Shunji Bandow 1996). In the case of single-walled, due to the inevitable presence of ferromagnetic particles of the catalyst, the magnetic properties of SWCNTs are controversial, and research that can be evaluated individually is limited. On the other hand, it has been confirmed that short SWCNT closed on one side are like fullerenes in magnetic characteristics (S Bandow et al., 2001). Moreover, If the magnetic field is aligned along the nanotube axis, it has been demonstrated that the magnetic characteristics of SWCNTs are primarily determined by spin polarization and ring currents around the nanotube (M.-F. Lin and Shung 1995).

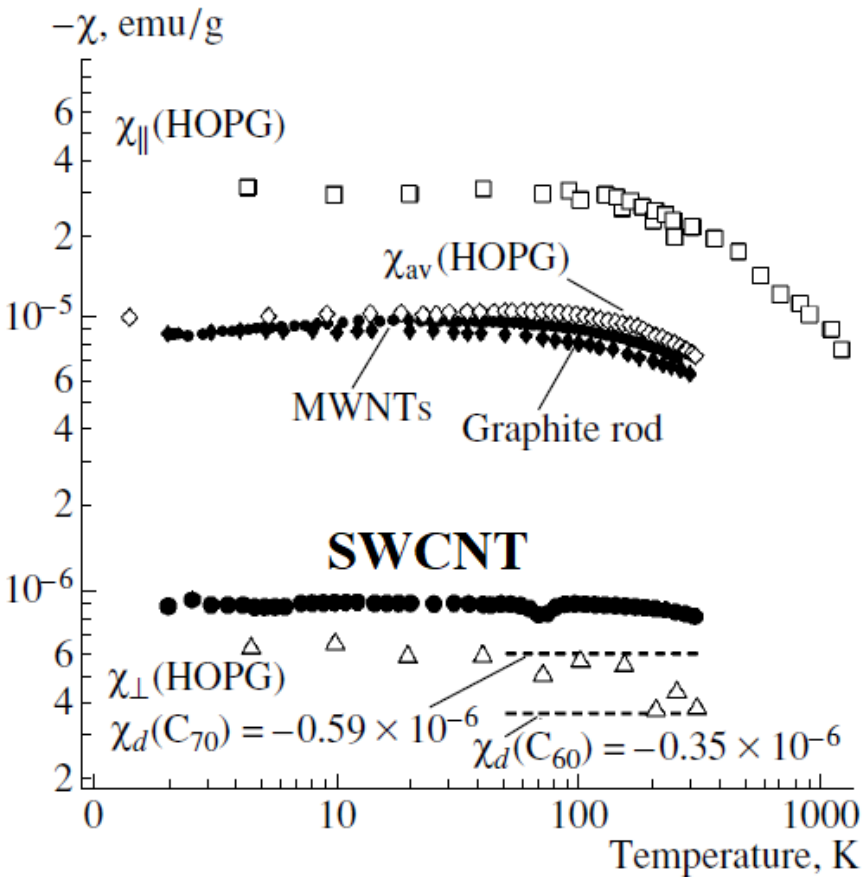


Figure 2.17 Magnetic susceptibility of different carbons measured experimentally. highly oriented pyrolytic graphite (HOPG) in the longitudinal (c||) and transverse (c^) directions, powdered HOPG (cav), a graphite rod, MWCNTs, SWCNTs, and fullerenes (Makarova 2004)

According to theoretical calculations (J. P. Lu 1997; B I Yakobson 1998) and experimental findings (Salvetat, Bonard, and Thomson 1999), CNTs have the highest tensile strength and Young's modulus of any material (Figure 2.18) making them harder than diamonds. Walls of CNT can be compared to coiled graphene sheets. Therefore, the graphene's modulus, approximately 1000 GPa, would be the first approximation for estimating the elastic modulus (five times that of steel) of CNTs (X.-D. Wang, Vinodgopal, and Dai 2019). Numerous scientific research has confirmed the theoretical hypotheses, supporting the comparison in Table 2.2.

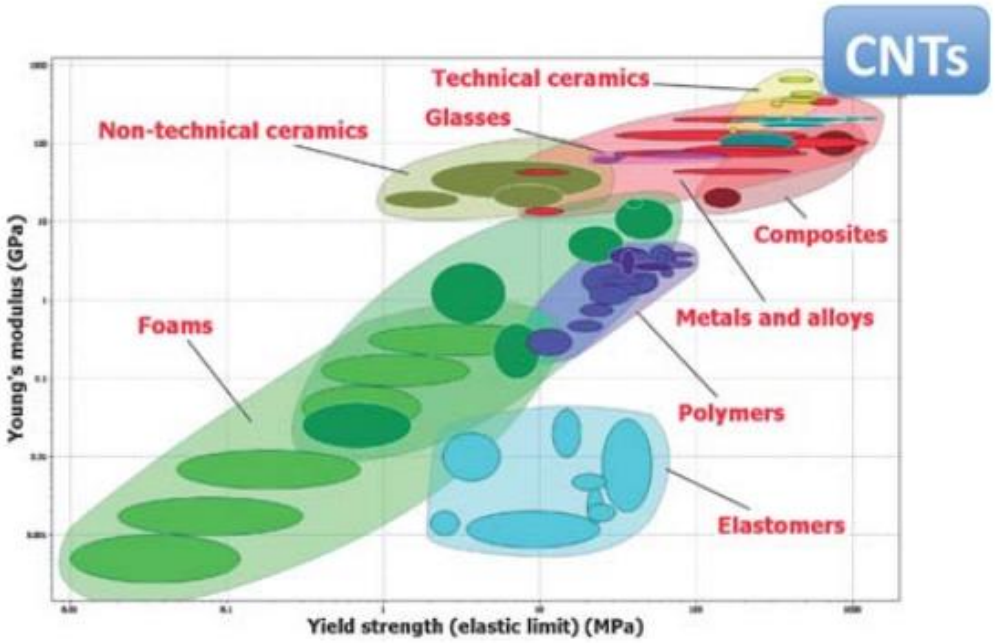


Figure 2.18 Young's modulus is plotted against tensile strength for many engineering materials in an Ashby plot. According to theoretical calculations and experimental measurements, CNTs have the highest tensile strength and Young's modulus (Nessim 2010)

Strength, and stiffness are some of the exceptional high material properties of SWCNT that are very close to their theoretical limits. SWCNT' exceptional mechanical characteristics can be related to their geometric formation and C-C bonds. One of the strongest bonds in nature is the C-C bond found in the fundamental plane of graphite. SWCNT of small sizes have high tensile strength and Young's modulus. The traditional way assumes that very hard SWCNT will be challenging to bend and deform. On the other hand, SWCNT can bend like a pipette without breaking. They can safely revert to their original structure once the load has been lifted. Most materials fracture when a load is applied and bend because of defects or dislocations. However, there are not many sidewall defects in SWCNT. Thus, they are very flexible and have excellent mechanical characteristics. Additionally, when comparing the mechanical features of MWCNT and SWCNT, the tensile strengths of the two materials are comparable (Table 2.2), but the flexural strength values differ significantly (28.5 GPa and 14.2-80, respectively) (Gergeroglu, Yildirim, and Ebeoglugil 2020).

SWCNTs are anticipated to display comparable values for thermal characteristics since graphite and diamond exhibit extremely low heat capacity and high thermal

conductivity. Also, it should approach graphene's values at high temperatures, where the effects of phonon quantization are irrelevant. Therefore, low-temperature specific heat is produced by the inner tube connection in SWCNT ropes and the outer wall connection in MWCNTs, comparable to three-dimensional (3-D) graphite (T. Y. Choi et al., 2005; Hone 2001; Hone et al., 1999). By creating a thermal conductivity model that considers temperature and nanotube diameter, the thermal characteristics of metallic SWCNT have been revealed. An SWCNT with dimensions of 1.7 nm in diameter and 2.6 mm in length has been reported to have a thermal conductivity of about 3500 W $m^{-1}K^{-1}$ at room temperature (Pop et al., 2006). However, as noted in Table 2.2, SWCNT may have thermal conductivity values that are much higher than these values (X.-D. Wang, Vinodgopal, and Dai 2019). Additionally, MWCNT has been found to have thermal conductivity values above 3000 W $m^{-1}K^{-1}$ (P. Kim et al., 2001). As thermal management and distribution become crucial for downsizing future microprocessors, these high thermal conductivity values represent another beneficial property for CNTs in electrical applications.

2.4.2 Carbon Nanotubes Chemical Properties

The ground-state electron configuration of a six-electron carbon atom in its lowest energy *state is* $1s^2 2s^2 2p \mathbf{2p_x^1\ 2p_y^1}$. The 1s and 2s orbitals have a huge energy difference, which has long been recognized, but the 2s and 2p orbitals have a relatively minor energy difference. The presence of two firmly bonded electrons in the $1s^2$ orbital and four electrons in the weakly bonded and $2s^2 2p^2$ valence orbitals explains why carbon may create an almost unlimited variety of compounds. Most medications, polymers, and food compounds have long chains of carbon atoms because carbon can make a wide range of bonds, and other atoms may readily be included in the bond chain. In this scenario, we come across carbon hybridization (Peschel 2011).

Consider valence electrons as efficient small instruments for forming covalent bonds in crystalline carbon. The difference in energy levels between the 2s and 2p orbitals is critical here. This distinction facilitates the mixing of carbon's electrical wave functions. As a result, a carbon atom hybridizes with nearby atoms to boost its bonding energy. Carbon's urge to make four equal energy bonds culminates in

hybridization, defined as the typical mix of 2s and 2p orbitals. Carbon lifts one of its 2s electrons to the unoccupied $2p_z$ orbital, producing an excited state and hybridizing it. The excited state is relatively stable since the 2s and 2p subshells are half-filled (Peschel 2011; Y. Wang et al., 2020).

Carbon is the only element that can form lengthy chains because of its low atomic number or atomic mass and its electronic structure, allowing it to enter numerous hybridization states easily. As a result, carbon may form single, double, and triple bonds, and hybridization can result in four single bonds (sp^3), two single and one double bond (sp^2), and one single and one triple bond (sp) (Figure 2.19) (Mathur, Singh, and Pande 2016).

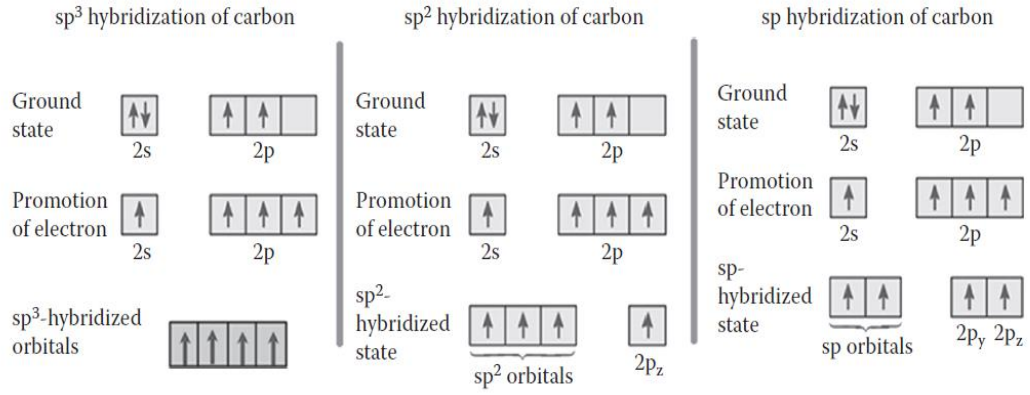


Figure 2.19 A carbon atom's hybridization types (Mathur, Singh, and Pande 2016)

In sp^3 hybridization, one electron from the s orbital transfers to the unoccupied p orbital, resulting in four hybridized orbitals with equal strength equivalent bonds (energy). In sp^2 hybridization, a p orbital does not merge with the other three hybridized orbitals, and one electron remains, resulting in the orbital resembling a lobe in a plane perpendicular to the other three hybridized orbitals. Combined with other hybridized orbitals, it produces a double bond known as a π-bond. In sp hybridization, a similar process occurs, but the two p orbitals link together to create a triple bond. The maximum electron density is found in sp^3, the lowest in sp. Every carbon atom's initial bond is a sigma (σ) bond, followed by a pi (π) bond. The hybridized orbitals always create the first σ-bond, whilst the remaining p orbital forms the π-bond. A single bond can spin, but a double bond does not. All bonds overlap between the nucleus, except for π-bonds at the top and bottom of the nucleus. A double bond is

stronger than a single bond, but it is not twice as strong(Y. Wang et al., 2020; Yan et al., 2018). Figure 2.20 depicts the depiction of carbon atoms with various hybridizations leading to distinct morphologies at the nano level. CNTs frequently have sp^2 hybridization and strong covalent bonding at this phase. However, they have been observed to include sp^3 hybridization in certain cases (Tingaev and Belenkov 2017).

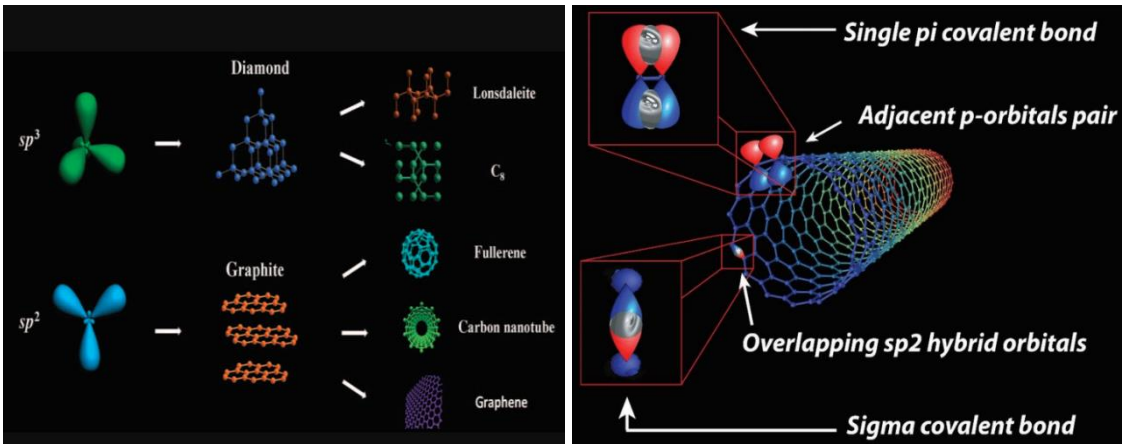


Figure 2.20 Hybridization of carbon structures and schematic representation of bond structure of CNT (Batmunkh, Biggs, and Shapter 2015; Radauscher 2016)

Due to the strong bond formed by the carbon atoms among themselves and the bonding features mentioned above, CNTs maintain their chemical stability even in harsh chemical environments. CNTs are insoluble in aqueous solutions and all organic solvents. Even though they can be dispersed in some solvents, they tend to precipitate as soon as the process stops(Niyogi et al., 2002). However, it has also been reported that CNTs can hardly interact with different classes of compounds (Tasis et al., 2003). Although all this information shows that the chemical stability of CNTs is high, it becomes necessary to encourage chemical reactions that can make them soluble to ensure their integration for some application areas (X. Lu and Chen 2005; Tasis et al., 2006).

Modifications of CNTs are almost inevitable to adapt CNTs to inorganic, biological and organic systems, and components. At this point, three basic approaches, covalent, noncovalent, and filling the gaps, are noteworthy. In the covalent approach, chemical groups are covalently bonded to the d-conjugated regions of the CNT backbone to be modified through strong reactions. In the noncovalent approach, the desired functional

molecules are adsorbed onto the CNT backbone, or it wraps around it via weak bonds. In the last approach, the internal spaces of the CNTs are endohedral-filled (Tasis et al., 2006). Ultimately, chemical stability is an advantage, while in some cases, additional processes are required to modify CNTs.

2.4.3 Carbon Nanotubes Biological Properties

CNTs are being created in massive quantities for various applications because of their unique physical and chemical characteristics; as noted above, the manufacturing volume continually expands without regard for the impact on biological systems, including people.

The use of CNTs, particularly in biomedical applications, should be conducted after a thorough evaluation and examination of CNT toxicity (Belyanskaya et al., 2007). Most publications on CNT toxicity concern theirs in vitro effects (Helland et al., 2007). CNTs may be hazardous to human health, according to a few in vivo investigations conducted on rats (Warheit et al., 2004) and mice(C.-W. Lam et al., 2004; Shvedova et al., 2005). On the other hand, several studies have shown that CNTs can produce an efficient biocidal surface that can be utilized in medical devices. Because of the physical interactions between the cell walls of bacteria, it has been found that CNTs, which have been claimed to have an antibacterial property, have this effect (S. B. Lee et al., 2004).

Furthermore, CNTs are thought to operate as "nano syringes," causing extremely localized destruction of bacterial cell walls (Lopez et al., 2004). They may pass through the lipid bilayer of microbial cells, releasing intracellular content through the artificial hole. However, because needle-like particles might cause foreign body neoplasia, nanotubes cannot be incorporated into the body separately. CNT-like nanostructures with large length-to-diameter ratios have been found in vivo to lead to lethal problems akin to asbestos-related mesothelioma (Black 2005). As a result, making CNTs biocompatible and non-toxic by chemical changes and modifications is still a topic of controversy, with few experiments being done (Khalid et al., 2016; J. Patel et al., 2021).

2.5 Applications of Carbon Nanotubes

Many research discoveries have indicated application areas where the exceptional features of CNTs might be most efficiently utilized since their discovery in 1991, with an expanding understanding of their chemical, physical, and biological capabilities. Because of their unusual properties, CNTs continue to be the topic of more research (Figure 2.21). These studies are examples of understanding the characteristics of CNTs and obtaining composite structures by combining them with varied materials depending on the application area. Other examples include manipulating CNTs in their characteristics and examining the structure-property-performance relationship depending on the application area.

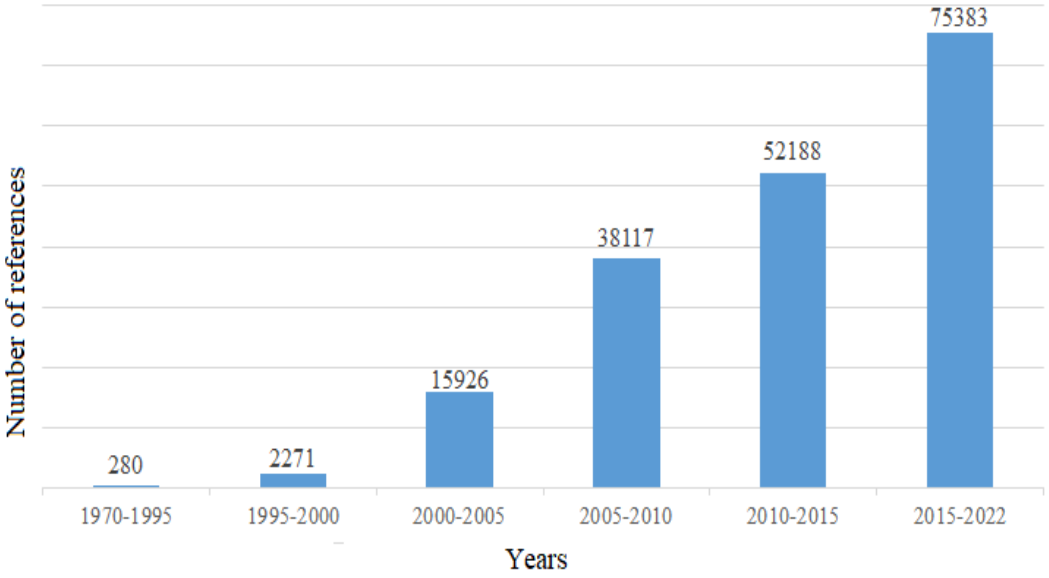


Figure 2.21 Change of carbon nanotube research developments by years in terms of published articles (Designed according to the information in the Scopus database as of August 3, 2022)

Based on the extraordinary material characteristics of nanotubes stated in the preceding sections, several applications range from the military sector to space technologies and biosensors to microelectronics. Figure 2.22 illustrates as a pie chart the areas where it has tremendous potential for broad usage in a wide range of applications, based on information acquired from the Scopus database during the previous 10 years. In the pie chart, the largest slice draws attention as energy application areas such as hydrogen storage, fuel cell and solar cell. The superior mechanical and electrical qualities of integrating carbon materials, particularly CNTs,

are beneficial as part of the electrode material. They support the underlayer mechanically while increasing its conductive and electrochemical characteristics. Because the carbon precursor material utilized to synthesize CNTs is inexpensive, product manufacture is scalable and commercially practical (Kierzek et al., 2004). CNT assemblies can have huge specific surface areas, which is critical in capacitor design. CNT electrode materials can be limited to a smaller region, increasing electrode-electrolyte contact and lowering device weight, enhancing total gravimetric performance (Izadi-Najafabadi et al., 2010; W. Ma et al., 2021; Z. Sun et al., 2021). CNTs are also chemically stable, which makes them more resistant to electrode surface deterioration (Gorduk et al., 2021). These unique properties have made CNTs indispensable materials for energy storage and conversion (Rajesh Kumar et al., 2022).

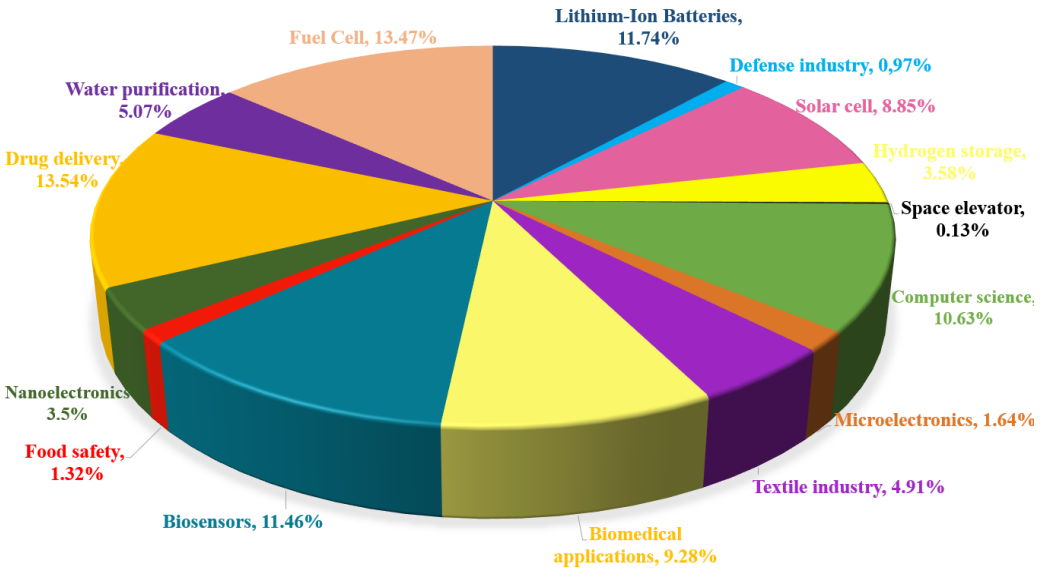


Figure 2.22 Pie chart showing the distribution of CNTs in different application areas. Between 2012-3 August 2022, ‘‘lithium-ion batteries’’, ‘‘defense industry’’, ‘‘solar cell’’, ‘‘hydrogen storage’’, ‘‘space elevator’’, ‘‘computer science’’, ‘‘microelectronics’’, ‘‘textile industry’’, ‘‘biomedical applications’’, ‘‘biosensors’’, ‘‘food safety’’, ‘‘nanoelectronics’’, ‘‘drug delivery’’, ‘‘water purification’’, ‘‘fuel cell’’ keywords were searched in the Scopus database, and a pie chart was created by classifying the studies on CNTs according to their application areas

As the semiconductor industry experiences more economical and technological constraints, new concepts must be examined and put into practice. Because of their exceptional characteristics, CNTs are a prospective nanomaterial for purposes in micro and nanoelectronics (Kharlamova and Kramberger 2021; Shoukat and Khan 2022).

The ballistic (without scattering) and spin-preserving transfer of electrons along tubes, the capacity to have metallic and semiconducting behavior, and the diameter-dependent bandgap state were discussed in detail in the physical properties section are the most interesting properties for applications in microelectronics. Another intriguing aspect of CNTs for microelectronics is the peculiar heat conductivity of the material, which is nearly double that of the diamond (An et al., 2022). Because of these exceptional qualities, CNTs are now regarded as one of the most effective tools for addressing the semiconductor industry's present and probable future problems (Raj Kumar, Bala, and Kumar 2021).

CNTs are used in lithium-ion batteries to create potentially valuable anodes. Nanotubes increase contact in this situation by increasing the surface area of the anode. In other words, by adding CNTs into the structure, it is feasible to boost the electrical contact conductivity of the electrodes (L. Li et al., 2021; S. Zhu and Ni 2022). The electrodes' great flexibility is obtained using a tube mat, a network of graphite particles produced on the anode, and nanotubes(Han, Shin, and Lee 2021). Furthermore, the anode's capacity does not diminish during cycling; CNTs absorbs and decreases the stress caused by lithium-ion intercalation. The uniform distribution of nanotubes improves the electrolyte around the anode's penetration ability, and the Li-ion battery's cyclic activity is improved. It has been discovered that adding nanotubes to the active anode material of the same electrode considerably improves the cyclic behavior of CNTs (Han, Shin, and Lee 2021). Furthermore, when CNTs are introduced to the anode, the resistance reduces. It has been observed that adding a small number of these nanotubes to the negative electrode increases its cyclic characteristics relative to the pure electrode; this is connected to the CNTs' binding ability and avoids material spilling from the electrodes or electrode disintegration (Shoukat and Khan 2022).

Even though their superior mechanical properties make them stand out in the textile industry (Bilisik and Syduzzaman 2021) and the defense industry for their armor design (Krishnan et al., 2021), researchers have focused their attention on promising CNTs for work in developing a space elevator because of those very same mechanical features (S. Luo et al., 2022; Saharudin, Sagar Iqbal, and Inam 2022). CNTs continue to be one of the most talked-about topics in the construction of biological devices (S. Zhang et al., 2022), drug delivery (Jampilek and Kralova 2021), biotechnological

application areas (N. Kumar and Chauhan 2021), and the biosensor industry (X. Yao et al., 2021) since they have superior electronic performance; this is the case, although there are concerns regarding the toxicity of CNTs to living organisms.

CHAPTER THREE

CARBON NANOTUBES BASED ELECTROCHEMICAL BIOSENSORS

3.1 Introduction

Detection of biomolecules is of paramount importance, ranging from health drugs, clinical medicine, food safety, environmental monitoring, and homeland security to detecting and diagnosing diseases and screening new drug molecules. Therefore, developing reliable and affordable instruments that enable direct, high sensitivity/selective, and quick analysis for biomolecule detection may alter humanity's ability to live a healthier and safer life (N. Yang et al., 2015). Sensors are a type of equipment that has lately gained popularity for this purpose, ranging from the detection of gas molecules to the real-time monitoring of chemical signals in living cells (Balasubramanian and Burghard 2006). Biosensors differ from conventional chemical sensors in two ways: the sensing element in the biosensor is made of biological material such as proteins (e.g., cell receptors, enzymes, antibodies), oligo or polynucleotides, microorganisms, or even whole biological tissues; and the biosensor is used to monitor biological processes or recognize biomolecules. Therefore, biosensor technology can considerably influence drug development, disease screening, biohazard monitoring, and fundamental research in general (Fatima, Younas, and Ali 2022).

3.2 Historical Background

With the introduction of electrochemical devices for analyte detection in the 1950s, the first biosensors arose as electrochemical oxygen. The biosensor, subsequently known as the Clark oxygen electrode, was described by Leland Clark in 1956 and comprised of a reduced silver/silver chloride reference electrode and a platinum cathode containing oxygen (Qlark Jr 1956). Clark then paired this electrode with glucose oxidase embedded in a dialysis membrane to monitor the glucose concentration in the solution, and the enzyme electrode was discovered (Clark and Lyons 1962; Qlark Jr 1956).

In 1967, the oxygen electrode for detecting glucose in fluid and tissues in vitro was disclosed using glucose oxidase immobilization. As a result, initiating an electrochemical process to detect glucose became a helpful tool (Clark and Lyons 1962). The first potentiometric enzyme electrode for urea detection was used in 1969 (Guilbault and Montalvo Jr 1969). Since then, a wide variety of biosensors for in vitro and in vivo applications have been created, ranging from enzymatic to antibody, aptamer, polypeptide, or nucleic acid based. Similarly, biosensor transduction mechanisms have evolved in tandem with contemporary demands and technology, from electrochemical and electronic biosensors to thermal biosensors that monitor temperature changes linked with the amount of heat produced by an enzyme-catalyzed reaction (A. Turner, Karube, and Wilson 1987; A. P. F. Turner 2013; Vestergaard and Tamiya 2015).

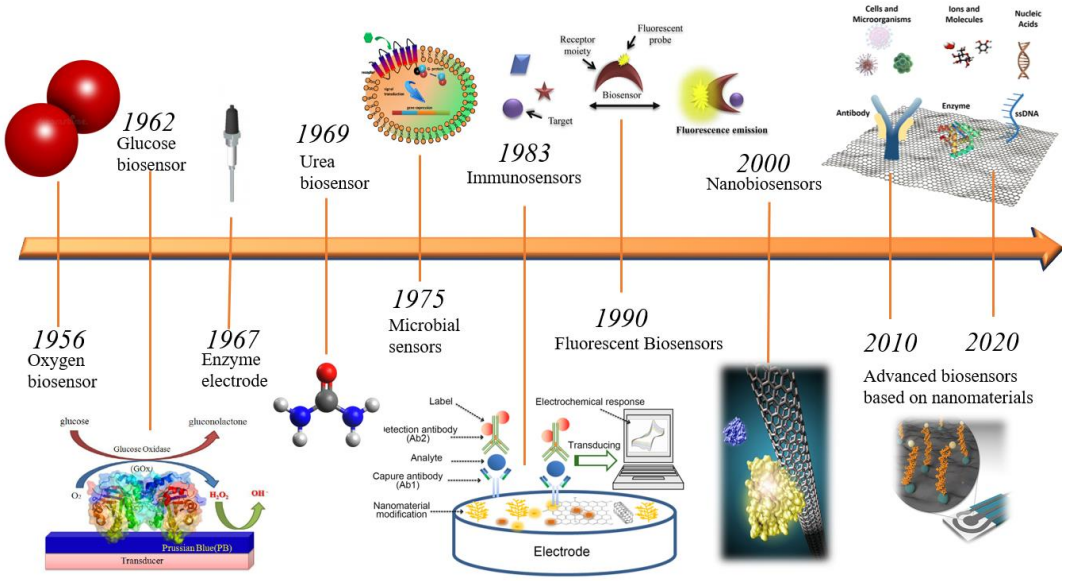


Figure 3.1 Biosensor development timeline, Redesigned based on (Tîlmaciu and Morris 2015)

Since the early 2000s (Figure 3.1), a new class of biosensors known as nano biosensors has been a prominent topic due to the development of nanotechnologies and the introduction of nanomaterials with unique physicochemical features (Vestergaard and Tamiya 2015). NPs and nanotubes have been created that combine the benefits of nanomaterials with the functionality of "macro"-biosensors, owing to their tiny size and high surface-to-volume ratio (Pandit et al., 2016; Pumera et al., 2007). CNTs have various benefits for sensing purposes among particular

nanomaterials, and due to their unique structural, mechanical, electrical, and optical characteristics, CNTs have become a significant study topic for creating next-generation probes (Gergeroglu, Yildirim, and Ebeoglugil 2020; Sireesha et al., 2018). According to past research, CNTs have earned their position in the scientific literature as essential components of an ideal biosensor design now and in the future (Aykaç et al., 2021; Gergeroglu, Yildirim, and Ebeoglugil 2020).

3.3 Desirable Properties in an Ideal Biosensor

A biosensor, in general, consists of an active sensing element and a signal converter that creates an electrical, optical, thermal, or magnetic output signal (Figure 3.2). While the sensing element detects the analyte selectively, the transducer turns a chemical event into a signal that may be utilized to measure the analyte concentration in a specific test sample. Although biosensors can be classified based on these elements, they share some similarities in desired features (Aykaç et al., 2021; Gergeroglu, Yildirim, and Ebeoglugil 2020). In various applications, such as clinical diagnostics, the biomedical industry, food production, and analysis, biosensors deliver more precise and consistent findings than traditional approaches (Clark JR et al., 1953; Updike and Hicks 1967). Their broad usage in these crucial application areas has revealed that an ideal biosensor term which has some of the desired biosensor characteristics, such as high selectivity, stability, high sensitivity, simplicity, long service life, low cost, repeatability, reproducibility, high signal-to-noise ratio, a wide measurement range, and a quick reaction time (Farka et al., 2017; Rogers, Taylor, and Church 2016).

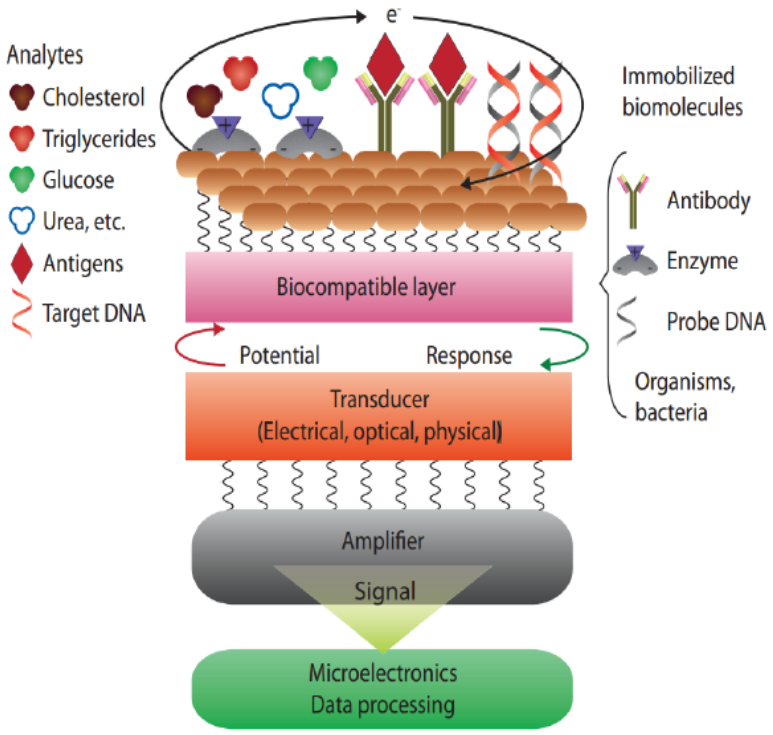


Figure 3.2 Schematic representation of biosensors (Gergeroglu, Yildirim, and Ebeoglugil 2020)

Additionally, these essential characteristics of biosensors in a clinical environment cannot be neglected and require extreme caution while being handled. The lowest concentration of an analyte that can be detected by a biosensor is referred to as its sensitivity (Koyun et al., 2012; Pohanka and Skládal 2008; Ramanathan and Danielsson 2001). This may be measured in anything from nanograms to femtograms per milliliter. In general, biosensors that are manufactured for use in medical or environmental monitoring might have the lowest possible sensitivity, such as nanograms per milliliter or even femtograms per milliliter (Bhattarai and Hameed 2020). The detection limit of the ideal biosensor should be lower than the concentration that was stated. The resolution of the electronic equipment that is used for the measurement ought to be the only aspect that plays a role in determining how low of a substrate concentration a biosensor can detect effectively. Because of this, we refer to the parameter that we are interested in as the determination limit. Parameters such as the breadth of the electrode surface, the affinity of the enzyme to the analyte, and the quantity of immobilized enzyme all play a role in determining it. For the biosensor to be helpful, it needs to be able to detect the expected range of analyte concentrations within a given application. The current-concentration curve of the biosensor is linear

across a large range, which is the upper limit of its detection capabilities. Alternately, linearity reflects the accuracy of the output acquired throughout a working range in which the concentration of the analyte in the sample is precisely proportional to the measured signal.; this is the case when linearity is said to exist. It is desirable that the performance of the biosensor that was developed be maintained for an extended period. At this juncture, one of the most important qualities that an ideal biosensor should possess is the electrode's capacity to maintain its stability. The stability factor of the biosensor that was created is found by computing the rate of change in the activity of the biomolecule against the number of measurements that are taken in succession(Bhattarai and Hameed 2020; Scott 1994).

It should be feasible to acquire the same findings in subsequent measurements of the biosensor when measuring it against the analyte that possesses the same attribute; this describes that the biosensor is repeatable. When it comes to reproducibility, several biosensors that have been created in the same manner and subjected to the same circumstances should provide the same results. A biosensor feature that is greatly sought to have in practical applications is one that is reproducible and repeatable. This is because these characteristics indicate that the biosensor may be employed with the maximum possible level of efficiency (Hall 1990; Scott 1994). The biological elements that are utilized in a biosensor are often the components of the system that are the least stable. The length of time that biosensors can maintain their sensitivity under regular working settings is a significant aspect of their design. There is a possibility that the overall number of measures taken will determine longevity. There is a possibility that the repeatability of the biosensor will be affected by the amount of time it may be stored between usages. To keep the biosensor's bioactive properties intact, it may be necessary to keep it in the fridge while it's being stored or to give the biological part a certain kind of chemical medium (Eggins 2013; Scott 1994). Thus, it can be protected their lifetime or prolonged their lifespan. The lengthy lifespan of biosensors makes them a more cost-effective strategy in the long term when compared to other approaches. Additionally, it is also preferable that the biosensors be easy to use for everyone (Bergveld 1996; Pohanka and Skládal 2008; Scheller and Schubert 1991).

Furthermore, one of the latest hot themes for an ideal biosensor has been the highest signal-to-noise ratio for high accuracy. Furthermore, when it comes to measures such as bedside measurements, transducers with high electron transfer rates have emerged as one of the most outstanding research areas for biosensors that can produce quick measurements. The current is intended to stay consistent once the analyte is supplied to the cell. When the current is constant, the analyte of choice is added, and the current value is monitored. The reaction time is the period after the addition and before the current stabilized. This duration should be as brief as feasible in an ideal biosensor (Hall 1990; Scott 1994).

3.4 Biosensor Types

Biosensors are categorized based on the type of biological receptor employed, as well as the signaling method and signal type used. This section delves into the biosensor types in detailed, shown in Figure 3.3 for the fundamental categorization of biosensors.

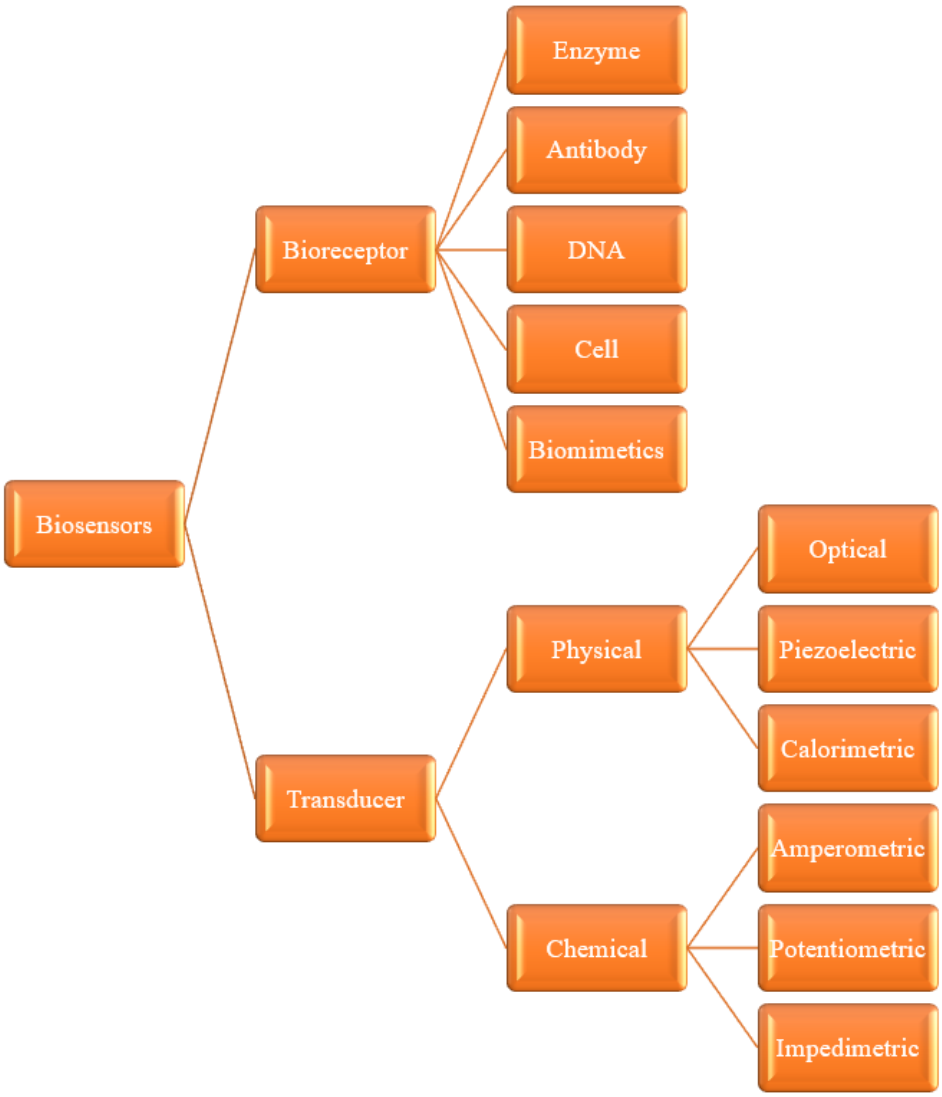


Figure 3.3 Biosensor Types, Redesigned based on (Perumal and Hashim 2014)

3.4.1 Biosensors by Bioreceptors

A biosensor's most distinctive characteristic is its bioreceptor, or biological recognition element. Because the bioreceptor defines a sensor's recognition system, it is directly vital for selectivity and sensitivity, which are the most significant qualities of an ideal biosensor. To avoid interference from other substances in the sample matrix, a bioreceptor must be selective and sensitive to the specific target analyte (Kulkarni, Ayachit, and Aminabhavi 2022). Biosensors are categorized based on the

sort of biological signaling mechanism they employ. The five primary biological signaling systems used by biosensors are shown in Figure 3.4.

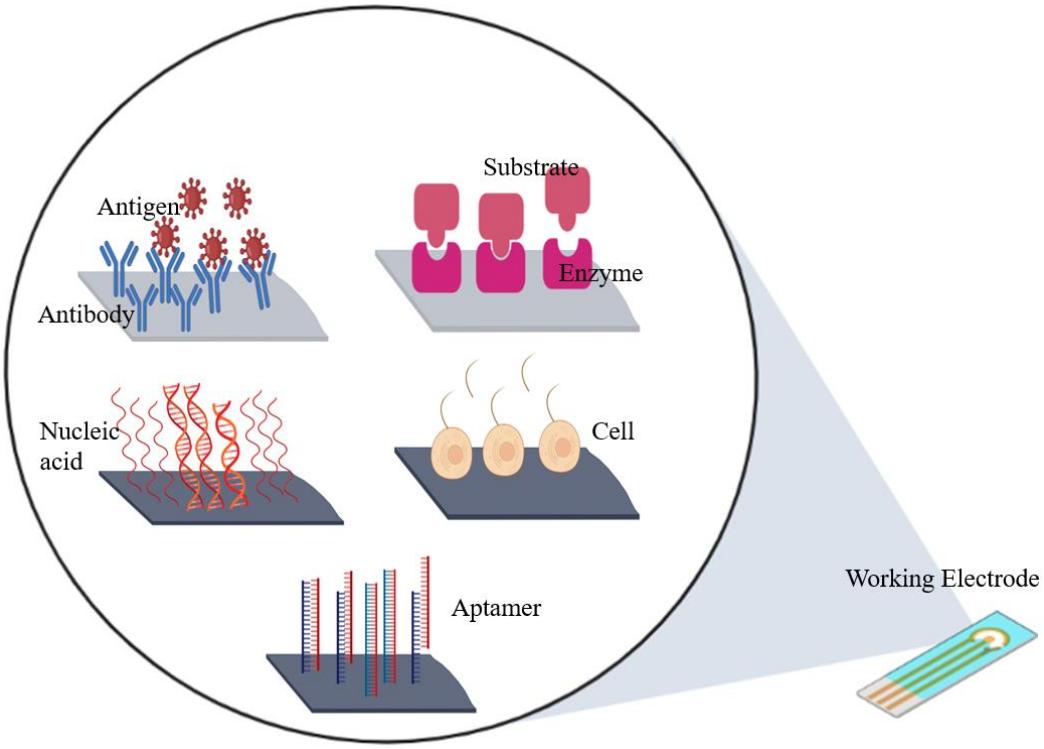


Figure 3.4 Techniques of biosensing use diverse biological signaling mechanisms: (a) antibody/antigen; (b) enzyme catalyze; (c) nucleic acid; (d) cell-based; (e) biomimetic (Kulkarni, Ayachit, and Aminabhavi 2022)

3.4.1.1 Enzyme-based Biosensors

Enzyme-based biosensors were the foremost sensors discovered by Clark and Lyons in 1962, and previously described in the section on Historical Background. Since the introduction of the initial biosensor, the usage of enzyme-based biosensors in several applications has exploded. Enzymes are highly effective biocatalysts that can identify and convert their substrates. These distinctive characteristics make enzymes potent instruments for developing analytical equipment (Leca-Bouvier and Blum 2010). Biosensors based on enzymes combine a transducer with a biocatalyst comprising a sensor. It operates based on its catalytic activity and binding capabilities for selective detection (Morrison et al., 2008).

The lock-and-key reasonable hypotheses may explain the mechanism of enzyme activity for this kind of biosensor. This unique enzyme catalytic reaction enables these

biosensors to detect significantly lower limitations than conventional binding approaches. This excellent specificity of enzyme-substrate interactions and the often-high turnover rates of biocatalysts are the basis for sensitive and selective enzyme-based biosensors (Leca-Bouvier and Blum 2010). Horseradish peroxidase and glucose oxidase is the most often reported enzyme-based biosensors(Alvarado-Ramírez et al., 2021; Sellami et al., 2022). Recent research, however, has shown that enzyme-based biosensors may be utilized to detect heavy metals (Hara and Singh 2021), pesticides (Karadurmus, Kaya, and Ozkan 2021), cholesterol (Yadav et al., 2021), environmental monitoring (Ahangari et al., 2021), and food safety (Ahangari et al., 2021).

3.4.1.2 Antibody-based Biosensors

The first *antibody-based biosensor* was used for identification in the 1950s, opening the way to immunodiagnostics (Donahue and Albitar, 2010). Since then, many attempts have been made to construct an immunosensor consisting of an antigen/antibody as a bioreceptor diagnostic tool for clinical use (Conroy et al., 2009; Maynard and Georgiou 2000). An antibody has two heavy chains and two light chains. Nevertheless, many human antibodies combine disulfide bonds and an additional protein known as coupling or J-chain to build a dimeric or pentameric structure (Maynard and Georgiou 2000; Wood 2006). Every chain has both fixed and flexible links. The variable region binds with a matching antigen that is very specific and selective (Conroy et al., 2009; Donahue and Albitar 2010). Therefore, an immunosensor consisting of an antigen as a bioreceptor exploits the antibody's particular, stable, and adaptable capacity to attach to the target antigen. The amino acids of an antibody determine its specificity towards the binding side of its antigen (Fowler et al., 2008).

This antigen-antibody interaction is believed to play a significant role in enhancing public health by enabling applications where quick detection, high sensitivity, and specificity of immunosensors are crucial, such as in environmental monitoring (Dong and Ueda 2021), food safety (Daliri et al., 2019), and clinical chemistry (Mollarasouli, Kurbanoglu, and Ozkan 2019). A recent study indicates that the immunological sensor's role in cancer/tumor detection is being intensively studied. Due to the lack of

sensitivity, specificity, and speed of the conventional diagnostic procedure, immunosensors have become potential instruments for identifying the early stages of cancer (Ahirwar 2021; Dutta et al., 2021). In addition, detection, and diagnostic approaches for Severe Acute Respiratory Syndrome Coronavirus-2 (SARS-CoV-2), a highly fatal virus that contributed to the pandemic, emphasized immunosensors due to their excellent selectivity. Researchers from across the globe have exerted considerable effort to use immunosensors as one of the efficient weapons against the virus (Aydın, Aydın, and Sezgintürk 2021; Layqah and Eissa 2019; Munoz and Pumera 2021).

3.4.1.3 DNA-based Biosensors

In *nucleic acid-based biosensors*, as a nucleic acid biological recognition element, the affinity binding between two single-stranded DNA (ssDNA) strands to generate double-stranded DNA (dsDNA) is used as an advantage. Since its inception in the early 1950s, the use of a nucleic acid sequence for a precise diagnosis has advanced steadily (Parkinson and Pejcic 2005).The nucleic-acid-based technique is far more sensitive than other costly, hazardous, and time-consuming techniques, such as electrophoretic separations and combining radio isotropic (Parkinson and Pejcic 2005). DNA-based biosensors generate a stable hydrogen connection between two nucleic acids by recognizing the complementary ssDNA strand; to accomplish this, an immobilized ssDNA probe with a base sequence corresponding to the target of interest is used in a bioreceptor. Exposure of the target to the probe, leading to the formation of dsDNA from the hybridization of complementary ssDNA, produces a biochemical response. However, DNA-based biosensors have the problem of requiring the use of binders for immobilization on the sensing surface.

Nevertheless, DNA-based biosensors allow for designing analytical instruments that can determine the presence of a single kind of molecule in a complicated combination with extraordinary sensitivity (Hua et al., 2022). The DNA-based biosensor has the potential to be used in clinical diagnostics for the detection of viruses and diseases and may satisfy requirements such as increased quick response, high

sensitivity, excellent selectivity, and experimental adaptability (Saha, Todi, and Malhotra 2021; Qiong Wang et al., 2022)

3.4.1.4 Cell-based Biosensors

Since the early 1970s, living cells have been utilized as bioreceptors in biosensors(Niharika Gupta et al., 2019). The live cell serves as the bio-specific sensing element in cell-based sensors. This class of biosensors is based on the capacity to detect a live cell's intracellular and extracellular environment and physiological parameters and may receive a response via the interaction between the stimulus and the cell (Chung and Dhar 2021). As biosensing elements, microorganisms such as bacteria and fungus may detect particular molecules; some specific proteins in cells may act as bioreceptors (Acha et al., 2010; Q. Liu et al., 2014).

In contrast to other biosensors, the detection limit of cell-based biosensors is dictated by the environment in which the cell can survive for an extended period. If natural ambient circumstances cannot accurately establish the required physical and chemical conditions, the detection limit and use of biosensors will be constrained. In addition, the biosensor's sterilization, biocompatibility, and shelf life depend entirely on the viability and stability of the live cell (Niharika Gupta et al., 2019; Hicks, Bachmann, and Wang 2020); cell-based biosensors lack the high-selectivity characteristics of other kinds of biosensors (Y. Cui, Lai, and Tang 2019). Additionally, due to complicated and costly expression/purification methods, the major drawbacks of this kind of biosensor are poor manufacturing effectiveness and increased price (N. Zhang et al., 2020).

3.4.1.5 Biomimetics

Biomimetic biosensors are described as sensors that comprise a synthetic biosensing element replicating a natural biosensor's function. Since the initial usage of aptamers in the early 1990s, biomimetic sensors, particularly aptasensors, have achieved considerable advancements (Kozitsina et al., 2018; Morrison et al., 2008). Initially characterized as nucleic acid ligands, aptamers may be synthesized as synthetic nucleic acid chains that can be engineered to identify amino acids,

oligosaccharides, peptides, and proteins. Thus, they are chemically linked to nucleic acid probes, but their ability to function as antibodies makes them flexible biosensing components (Brys et al., 2006; Schneider, Lim, and Strongin 2010).

Biomimetics has resulted in ineffective biosensors owing to structural pleomorphism and chemical simplicity while having benefits such as better affinity and less complexity compared to antibody-based biosensors (Hosseinzadeh and Mazloum-Ardakani 2020; Sharma et al., 2022). Nonetheless, as a consequence of several research, substantial attempts have been undertaken to resolve these issues (Hosseinzadeh and Mazloum-Ardakani 2020; Schneider, Lim, and Strongin 2010). Thus, it has been used effectively to maximize several biosensing formats, including compact size, renewability, high specificity, immobilization, and modification adaptability (L. S. Liu et al., 2020; Schneider, Lim, and Strongin 2010). Biosensors based on aptamers have lately been used extensively in clinical settings to detect viruses and infectious illnesses (L. S. Liu et al., 2020).

3.4.2 Biosensors by Transducers

CNTs that can be functionalized with bioreceptors such as proteins, enzymes, antibodies, cell receptors, microbes, and even all biological microorganisms, thus bio-sensitized, serve as transducer biosensor platforms. The primary goal of the transducer platform is to transform a range of physical, chemical, or biological processes occurring in a biosensor into a legible and processable output signal with little distortion to the measured magnitude and high sensitivity. According to the type of the transducer platform, the kind of output signal differs; thus, biosensors are also categorized according to the transduction method. Based on the interactions between analytes and bio-sensitive materials, CNT-based biosensors will be split into two types according to their transducer working mechanism like all other types, physical (optical, piezoelectric, and calorimetric) and chemical (amperometric, potentiometric, and impedimetric), and addressed in the following sections.

3.4.2.1 Physical Transducers

Optical biosensors include a transducer platform that changes specific optical characteristics such as reflectance, absorbance, and excitations in the presence of biological molecules through the material on the transducer platform's surface, resulting in a detectable output signal (Ramsden 1997). In biomedical applications, detecting biomolecules using near-infrared light between 0.9 and 1.3 eV with increased tissue penetration and lower auto-fluorescence background has led to searching for suitable materials (Manso et al., 2007). Due to the unique interband transition, SWCNTs display diameter/chirality dependent and surface-sensitive photoluminescence features in addition to the unique electrical properties described in *Chapter 2*. Moreover, certain optical features of SWCNTs, including an excellent wavelength conversion function (Crawford et al., 2007) and tunable near-infrared emission (Barone et al., 2005) that responds to changes in local dielectric function but is stable against permanent photobleaching and high light intensity (Saito et al., 2002), are desirable for an optical sensor. Most SWCNTs generate photostable NIR fluorescence between 800 and 1600 nm. Target molecules may selectively adjust a particular SWCNT's fluorescence wavelength and quantum yield by attaching to its surface. In contrast, the near-infrared (NIR) window in biological tissue is between 700 to 1300 nm, where the scattering and absorption of blood and tissues are almost insignificant (P. Liu et al., 2022). SWCNTs are thus seen as ideal prospects for biosensing as novel optical biosensors. However, a single sensor is inadequate to deal with the complexities of biological systems. Multiplexed sensing is required due to co-release of pathogen virulence factors (Kaper, Nataro, and Mobley 2004; Ramachandran 2014) or co-secretion of neurotransmitters (Tritsch, Granger, and Sabatini 2016). At this point, the utility of single chiral SWCNTs, which are challenging and costly compared to other nanotube types yet allow for data acquisition in a certain range for multiplexing, will be called into doubt (Figure 3.5a). SWCNTs with 10 distinct chirality, on the other hand, may produce complicated detections with typical emission peak widths of 100 nm (Figure 3.5b) (Nißler et al., 2022). All this evidence indicates that the use of CNTs in optical biosensors has been restricted due to difficulties in controlling chirality. To overcome this problem, there are many studies for hybridizing CNTs with other nanomaterials or nano carbons, and it has been

demonstrated that they improved photoluminescence qualities in many ways(Gillen and Boghossian 2019; A. Wang et al., 2018). As a result, the majority of research focuses on hybrid nanostructures created with SWCNT and seeks more cost-effective options for next-generation optical biosensors.

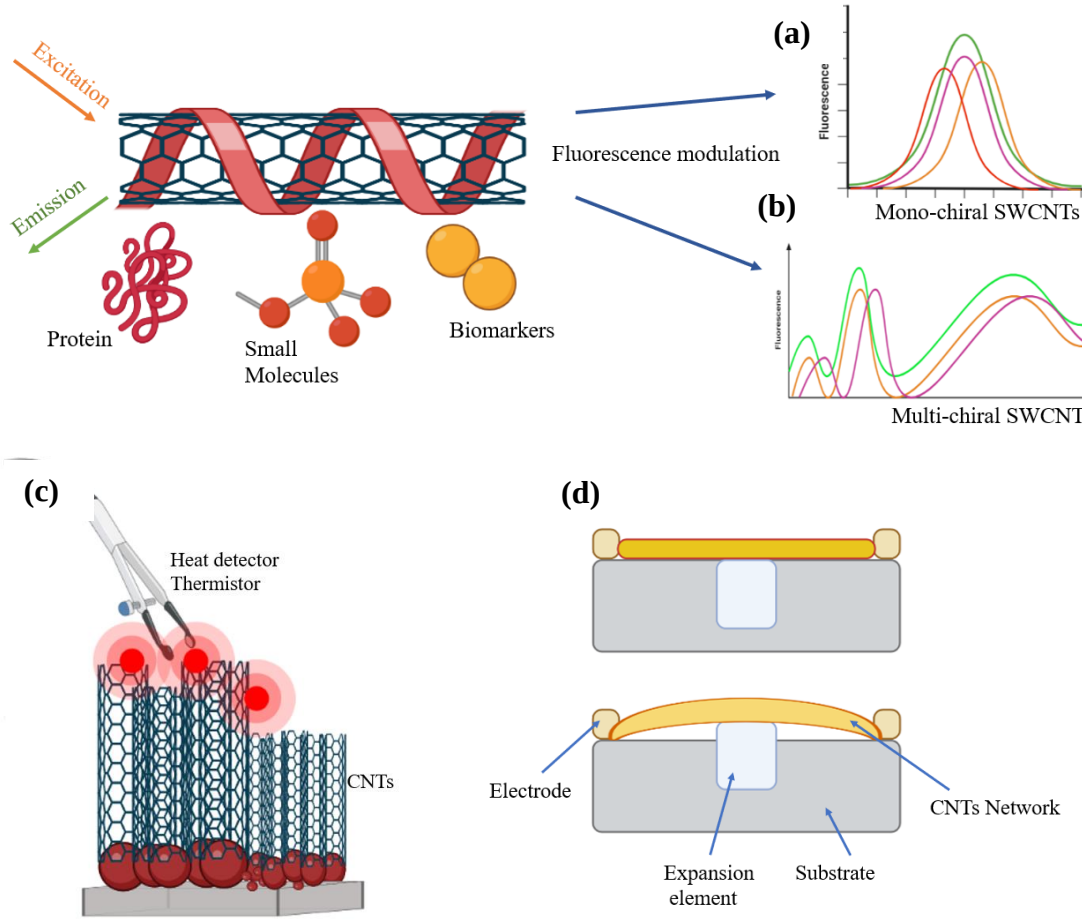


Figure 3.5 SWCNTs with different chirality for enhanced optical biosensing (a) Mono-chiral, (b) Multi-chiral, Redesigned based on (Nißler et al., 2022), (c) CNT-based converter detects the heat generated by the reaction between biological materials and corresponding objects, (d) Expansion element changes due to temperature change and cause deformation of CNTs, Redesigned based on (N. Yang et al., 2015))

Piezoelectric biosensors use piezoelectric materials whose electrical properties change under the influence of external force as transduction elements. The surface of the piezoelectric material coated with the bioreceptor, or sensing material oscillates with natural frequency under the action of an electric field. When the analyte reacts with the sensing element coated on the piezoelectric material, there is a change in the material's natural frequency. This change in natural frequency can be measured and

correlated with the mass of the analyte under investigation (Nagraik et al., 2021). As mentioned in *Chapter 2*, superior mechanical characteristics of CNTs, such as high strength, toughness, and unusual flexibility, have made them promising signal transducer platforms for flexible piezoelectric biosensors. Therefore, last decade, highly sensitive piezoelectric CNT-based biosensors for food safety (Maghsoudi and Hosainzadegan 2021),heavy metal ions (Eddaif, Shaban, and Telegdi 2019) , agriculture applications (Sellappan et al., 2022), clinical and non-clinical areas (Akgönüllü and Denizli 2021; Arunadevi 2022) have been developed. However, concerns with non-specific chemical immobilization are still regarded as the majority of the key disadvantage of CNT-based piezoelectric biosensors (Joshi, Mishra, and Narayan 2021; Nagraik et al., 2021).

Calorimetric biosensors, in principle, measure temperature variations in a reaction that correlate to analyte concentration (A. B. Das, Kumari, and Sahu 2022). Calorimetric biosensors with microfluidic channels have also been devised for application in cancer cell detection to monitor temperature changes in real-time (S.-C. Park et al., 2007; Yuyan Zhang and Tadigadapa 2004). It is widely known that calorimetric biosensors are utilized for environmental monitoring (Jha 2021), cancer diagnostics applications (Quazi 2022), and the food processing industry (Aggarwal, Sehgal, and Tandon 2021). The basic idea behind CNT-based thermometric measurement is to quantify the temperature change that results in a heating effect when interacting with the target analyte corresponding to the immobilized biological components on the CNTs' surface and body (Crawford et al., 2007; B. Zhao et al., 2021). Figure 3.5c illustrates the detecting method of thermal CNT-based biosensors. Temperature variations may modify the size and volumetric characteristics of CNTs in this case, unlike in traditional calorimetric biosensors. Stresses will result from these dimensional changes in the CNT. Therefore, in theory the mechanism of CNT-based calorimetric biosensors (See Figure 3.5d) is similar to that of CNT-based piezoelectric biosensors (Crawford et al., 2007).

3.4.2.2 Chemical Transducers

An electrochemical biosensor is a self-contained integrated device that may offer quantitative or semi-quantitative analytical data through an electrochemical transduction element coupled with a bioreceptor (Thevenot et al., 1999; Thévenot et al., 2001). The current generated by oxidation and reduction processes are measured by electrochemical biosensors. The generated current may be connected to the concentration of the electroactive species or the production/consumption ratio. The generated electrical signal is proportional to the analyte concentration and is connected to the recognition process by the target and the analyte. Significant benefits over other detection technologies, such as high responsiveness, cheap cost, high sensitivity, and relatively simple components, have prompted scientific research to focus on electrochemical biosensor types (Ensafi 2019; Kour et al., 2020; A. Singh et al., 2021). Electrochemical biosensors are classified into three types based on the nature of the electrochemical changes recorded during the biorecognition event: amperometric, potentiometric, and impedimetric (Bahadır and Sezgintürk 2015; Iqbal, Gupta, and Hussaini 2012).

Amperometric biosensors measure current as a function of time as a consequence of the oxidation and reduction of an electroactive species in a biochemical process dependent on the concentration of an analyte with a fixed voltage. The Amperometric system does this by using three kinds of electrodes: a working electrode, a fixed potential silver or silver chloride electrode that regulates the potential of the working electron, and an incorporated counter (auxiliary electrode) to assist in measuring current flow (Bollella and Gorton 2018; Schachinger et al., 2021). When specific molecules undergo oxidation or reduction processes, electrons are transported from the analyte to the working electrode or from the electrode to the analyte on the working electrode's surface, where these molecules are situated. This change may therefore be used to gain information about the analyte concentration (Bollella and Gorton 2018; Sahin and Kaya 2019). The flow direction of the electrons may be positive or negative depending on the analyte characteristics, which can be adjusted by the electric potential given to the working electrode, allowing the redox reaction to be handled(Parkinson and Pejcic 2005). Thus, amperometric CNT-based biosensors use

an enzyme-immobilized CNT electrode to catalyze the oxidation or reduction of the target analyte (Ferrier and Honeychurch 2021; Rernglit et al., 2019). CNTs' previously described structural features make them ideal for enzyme adsorption. Therefore, CNTs are always employed to build enzyme CNT electrodes or functionalize them with enzymes to change the surface of the electrodes in amperometric biosensors made using CNTs. CNT-based amperometric transduction may be combined with biological recognition elements such as antibodies, DNA, and enzymes for use in clinical applications (Manivel et al., 2019), environmental monitoring (Campuzano, Yáñez-Sedeño, and Pingarrón 2020), and food safety(Yuanyuan Zhang et al., 2020).

Potentiometric biosensors collect analytical information using ion-selective electrodes and ion-sensitive field-effect transistors. In such sensors, the biological recognition element translates the identification process into a potential signal to provide an analytical signal (Isildak and Özbek 2021; Özbek et al., 2022). Potentiometric sensors comprise two electrodes: an indicator electrode that generates a changing potential throughout the remembering process and a reference electrode (often Ag/AgCl) that is necessary to maintain a constant half-cell potential. Potentiometric transduction measures the potential difference between the indicator electrode and the reference electrode, which builds up throughout the recognition process in an electrochemical cell while zero or insignificant current flows through the electrode (Karimi-Maleh et al., 2021; Walker et al., 2021). Unfortunately, even though typical potentiometric carbon electrodes are extraordinarily selective and sensitive, their low detection limit restricts their applicability (Švancara et al., 2009). In order to overcome this problem, especially in the last five years, chemical modifications with CNT on the electrode surface have been widely applied to increase selectivity and sensitivity to target species (J. Ding and Qin 2020). It has been shown that potentiometric biosensors developed with CNTs, which have strong electrochemical capabilities due to their high conductivity, can perform measurements such as heavy metal ion (Hadi Khani et al., 2010), pro-drug (Khalil, Moaty, and Korany 2018), and an anionic surfactant (Jozanović et al., 2021) with high detection limits.

Impedimetric biosensors employ a transduction mechanism based on electrical impedance spectroscopy (EIS). Although it is not as prevalent as other approaches, it has become a vital and effective tool for biological recognition element transduction

in recent years (Bahadır and Sezgintürk 2016; Magar, Hassan, and Mulchandani 2021). It is similar to the other electrochemical detection devices mentioned above but differently; EIS offers great advantages over low concentration detection methods, such as being suitable for real-time monitoring as it can provide label-free or reagent-free detection (Assaifan et al., 2022; McGuinness and Verdonk 2009). The EIS system consists of three electrodes: a reference electrode for measuring voltage, a counter electrode for supplying current to the cell, and a working electrode for measuring current (Magar, Hassan, and Mulchandani 2021; Shangshang Wang et al., 2021). A controlled alternating voltage is given to the electrode once the sample has been inserted into the sensing device. Consequently, the electrical impedance is computed as the voltage-to-current ratio by observing the current flowing through the sample (Magar, Hassan, and Mulchandani 2021). At this stage, electrically conductive transduction components are required. Therefore, CNT-based impedimetric biosensors that offer real-time monitoring of the high electrical property of CNTs have gained popularity (Chawla, Rai, and Garain 2023; Prakash et al., 2021). It has been demonstrated that CNT-based impedimetric biosensors, which have recently been suggested for use in point of care (Brownlee, Claussen, and Iverson 2020; Xie et al., 2020) and clinical applications (Rodríguez, Ferreira, and Dutra 2022), provide rapid detection of nucleic acid hybridization (Prakash et al., 2022), amino acids (Roy et al., 2021), and pathogens (D. Patel, Zhou, and Ramasamy 2021).

3.5 Functionalization of CNTs with Bioreceptors

The chemical characteristics of CNTs, as discussed in *Chapter 2*, are highly stable. Although this stability trait makes CNTs useful in many possible applications, it results in insolubility, one of the most challenging issues in biosensor applications (Yogeswaran and Chen 2008). In most situations, including many inorganic strong solvents, CNTs remain chemically stable and insoluble. On the other hand, immobilization is a significant issue, particularly for biosensors. Therefore, many scientific investigations have indicated that CNTs must be functionalized with other nanomaterials such as DNA, enzymes, proteins, and polymers (Figure 3.6) to deal with the insolubility of CNTs for biosensors applications (Gergeroglu, Yildirim, and Ebeoglugil 2020).

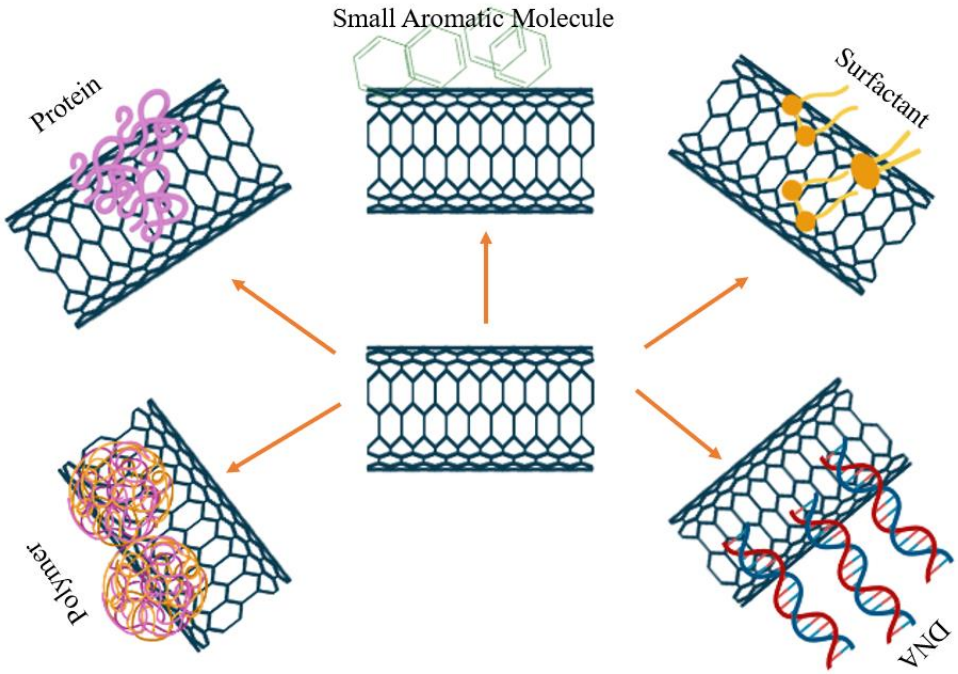


Figure 3.6 Illustrations of functionalized CNTs with different nanomaterials, Redesigned based on (N. Yang et al., 2015)

By functionalizing, CNTs' dispersibility may be improved, as can their compatibility with the target biological species(Pérez-López and Merkoçi 2012). The benefits of functionalized CNTs in many biosensor platforms include higher functional groups, high catalytic efficiency, high surface activity, and a broad edge plane (Nie et al., 2012). Additionally, biosensors built from functionalized CNTs have been shown to have better sensitivity, quicker reaction times, and a broader detection range than other sensors (Aykaç et al., 2021). This section will go over the techniques for functionalizing CNTs in-depth and the role of functionalized CNTs in the biosensor.

3.5.1 Methods for Functionalizing CNTs

CNTs may be functionalized using both physical and chemical methods. Physical methods containing mechanical techniques such as friction, crushing, grinding, and ultrasonic are used to activate the surfaces of CNTs in order to modify their physical and chemical structure (Ana Maria Díez-Pascual 2021; Fujigaya and Nakashima 2008). This approach may be helpful for CNTs' internal energy and surface activity, causing the tubes to react or connect with other materials to accomplish surface modification. For instance, CNTs currently can be dispersed in a specific solution by

high shear force or ultrasonic machining (Hasan, Crawford, and Ivanova 2013; Špitalský et al., 2009). Furthermore, high-energy modification (e.g., electron beam, plasma beam, and ultraviolet) methods are a practical surface modification approach for CNTs (Ana Maria Díez-Pascual 2021; Luais et al., 2010).

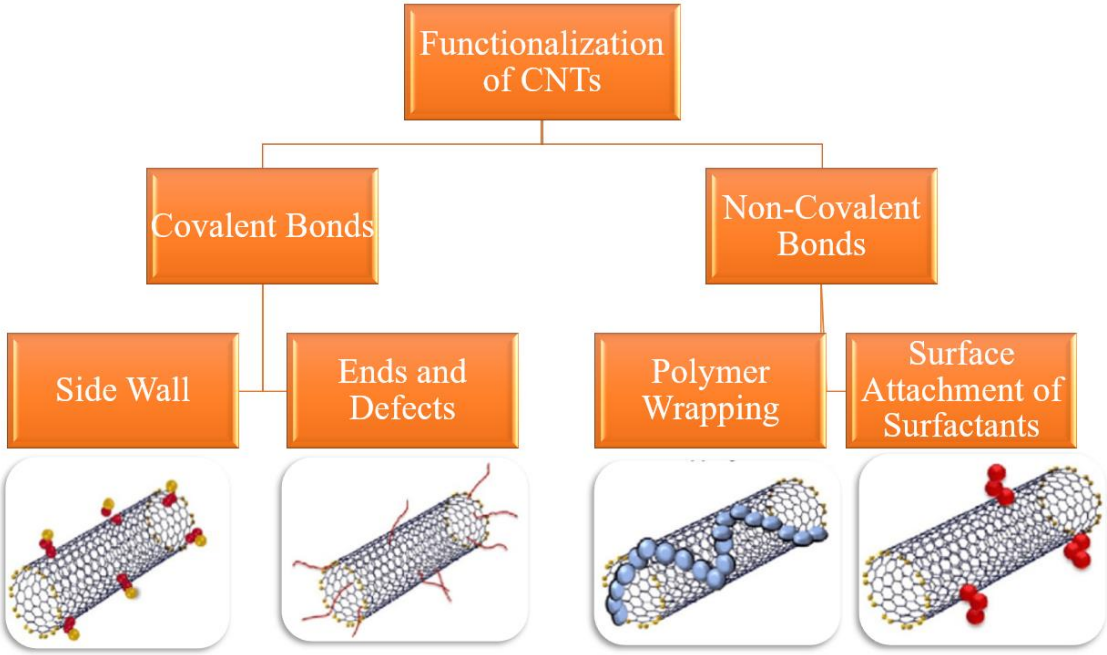


Figure 3.7 Chemical functionalization techniques for CNTs (Jun et al., 2018)

Chemical functionalization includes covalent and non-covalent modifications (Figure 3.7). When covalent modification occurs at the sidewalls or ends and defects of CNTs, carbon atoms undergo a covalent change from sp^2 to sp^3 hybridization. The end covalent modification mainly involves carboxylation followed by derivatization such as amidation and esterification reaction. In contrast, covalent modification on the sidewall usually includes fluorination, alkylation reaction, cycloaddition (N. Yang et al., 2015). In the first place, the covalent method starts with processing CNTs with various acids such as HNO_3, H_2SO_4, HCl and their combinations. As result of this acid treatment, the end caps of the CNTs are opened, and thus the CNTs can be oxidized (Basheer et al., 2020; Naqvi et al., 2020). Oxidation of CNTs can result in the formation of epoxy, carbonyl, hydroxyl, carboxyl, and ketone groups on the CNT surface, which improves the interactions of CNTs with other biological species (Ana Maria Díez-Pascual 2021). However, covalent functionalization can reduce the length-to-diameter ratio and alter the CNT's electrical structure, increasing sp^3 hybridization,

broadening the band gap, and decreasing conductivity (Bottini, Rosato, and Bottini 2011; Ana Maria Díez-Pascual 2021; Khurshed Ahmad Shah and Parvaiz 2022). The non-covalent modification that does not alter the original structure and characteristics of CNTs seems advantageous at this point (Yi Zhang, Bai, and Yan 2010; Y.-L. Zhao and Stoddart 2009).

In the non-covalent modification, the highly delocalized electron resulting from the sp2 hybridization of carbon atoms in CNTs may be coupled with other electron-containing components via the non-covalent bonding effect (R. J. Chen et al., 2003; Y. Zhou, Fang, and Ramasamy 2019). In this method, as seen in Figure 3.7, molecules are physically adsorbed onto the CNT surface and/or wrapped around the CNT body. Additionally, the walls of CNTs may interact with the bioreceptor through π-π stacking interactions and interactions involving heteroatoms with free electron pairs (Ana M Díez-Pascual et al., 2009). Non-covalent approach to CNTs functionalization does not compromise the structural integrity of CNTs. CNTs may retain their exceptional physical qualities even when their surfaces are covered with numerous functional groups. However, non-covalent interactions are much weaker than covalent ones (Tuncel 2011; Y. Zhou, Fang, and Ramasamy 2019). To functionalize CNTs, non-covalent modification often employs conjugated polycyclic aromatic hydrocarbons (Yue et al., 2022), bioactive molecules (Muthukumar 2021), and polymers (Gu et al., 2021; Matiyani et al., 2021).

3.5.2 The Roles of Functionalized CNTs

There are several reasons why functionalized CNTs are the most effective in biosensor mechanisms, which may explain why they have dominated the biosensor industry for the last decade (Chawla, Rai, and Garain 2023; B. Dai et al., 2022). Using functionalized CNTs as a transduction platform makes it simple to get the previously required qualities of an ideal biosensor. The most notable characteristic of CNTs in the biosensor mechanism is their ability to facilitate fast electron transfer between bio-receptors and transduction platforms due to their large surface area and activity (Wooten et al., 2014). When functionalized, CNTs may enable direct electronic

transmission. In other words, CNTs operate as wires that facilitate electron transmission to the redox center of bio-receptors (G. Yang et al., 2012).

Another advantage of CNT functionalization is reducing the redox reaction's over potential (W. Yang et al., 2010). The CNT surface is covered with many functional groups in functionalized CNT-based biosensors; this improves the redox reaction's bio-electrocatalytic activity (M. Musameh et al., 2002; Rahman, Umar, and Sawada 2009). Additionally, the unique hollow tube architectures of CNTs result in a greater specific surface area and a huge surface area to which enzymes may bind in large numbers (H. Dai 2002b). Due to the ease with which carboxyls on the surface of CNTs may form covalent bonds with amino acids, CNTs have been utilized to immobilize enzyme molecules and enhance the response signal of enzymatic biosensors (M. M. Musameh et al., 2012; I V Pavlidis et al., 2010). Moreover, the covalent functionalization of CNTs creates significant surface flaws to which several functional groups may be attached, resulting in a differential surface energy distribution of CNTs (Fan et al., 2012; Ioannis V Pavlidis et al., 2012). Therefore, it is simple to guarantee that CNTs have high catalytic activity against the target analyte in electrochemical biosensors.

Furthermore, the functionalization of CNTs is advantageous for enhancing the reversible redox reactions of biological molecules. Numerous studies have shown that adding functional groups to CNTs increases the number of active sites for most electrochemical processes (Hyun et al., 2015; Miodek et al., 2015). Thus, CNT functionalization considerably enhances the electron transfer process in biosensor applications and may be a crucial tool for achieving perfect biosensor features such as a rapid reaction time.

3.6 Electrochemistry Behind CNT-based Biosensors

Theoretically, it is conceivable to demonstrate that CNTs with a very tiny diameter have different electronic characteristics than graphite. However, a theoretical strategy has not yet been developed for MWCNTs with a diameter greater than 10 nm to explain the electrochemical behavior that would separate them from graphite, despite experimental evidence to the contrary(Unwin, Guell, and Zhang 2016). The faultless

and immaculate walls inside the body of MWCNTs function similarly to the basal graphite plane, where the limit of the heterogeneous electron transfer constant is zero. Figure 3.8a shows regular graphite crystals; this representation depicts a single MWCNT, with edge-plane-like areas at the tube's end and along its axis (in the whole body). Due to structural commonalities, the CNT-modified and graphite electrodes exhibit virtually comparable electrochemical responses. On the other hand, defects on the walls and ends of MWCNTs may allow rapid electron transit (Banks et al., 2005; Holloway, Wildgoose, et al., 2008). Moreover, these defects can be created in a controllable way (Figure 3.8b), and electrochemical activity can be increased by inducing these defects (Pumera and Miyahara 2009).

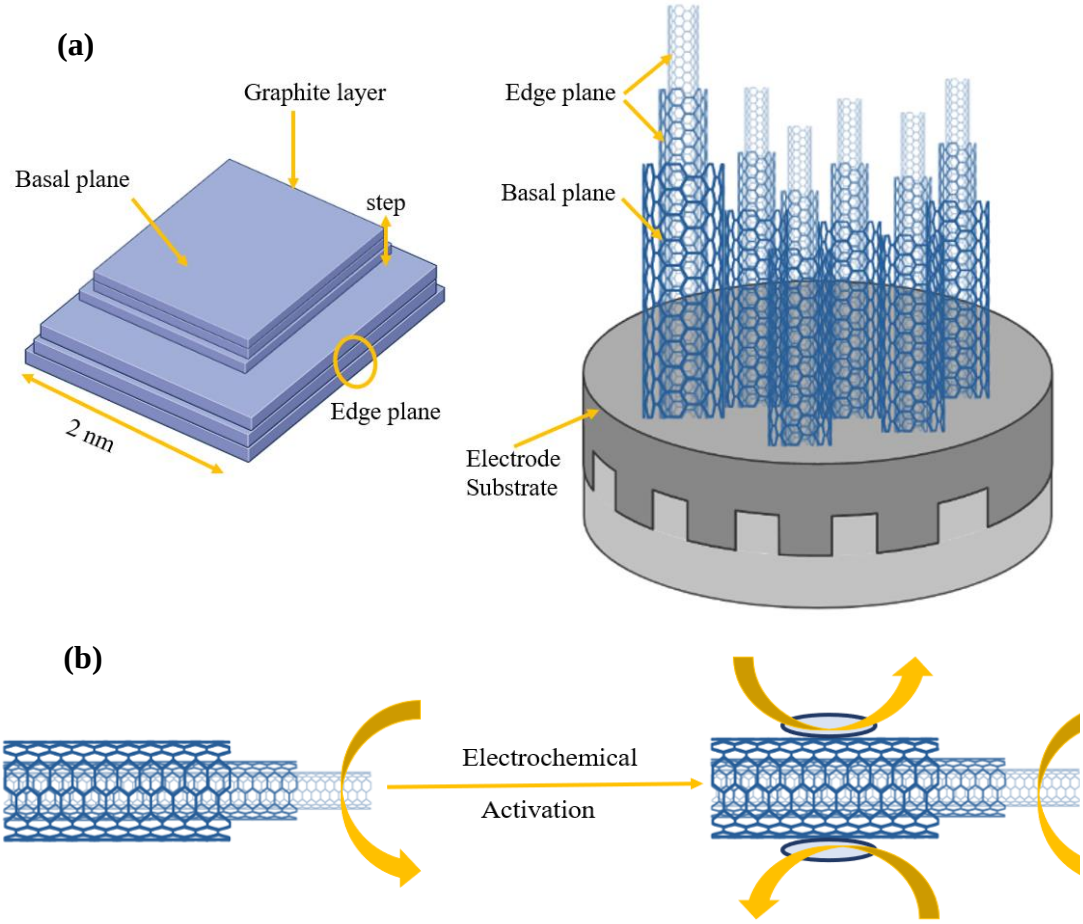


Figure 3.8 Electrochemistry of carbon nanotubes is similar to that of graphite, Redesigned based on (Pumera 2009)

The electrical structure of SWCNTs differs from that of MWCNTs, as described in detail in *Chapter 2*. Smaller SWCNT diameters decrease the overlap distance between

p orbitals on nearby carbon atoms in π-bonds. The gradually decreasing diameter increases the ultimate structure's curvature. Consequently, it is arguable that the electrochemical activity may increase (Holloway, Toghill, et al., 2008; Kruusma et al., 2007). In the case of SWCNTs, it is possible that not only the flaws on their ends and sides are electroactive, as with MWCNTs, but also the complete walls (M. Musameh, Lawrence, and Wang 2005; Pumera et al., 2007). However, scientific findings and particularly theoretical techniques have shown that the electrochemical behavior of CNTs is comparable to that of graphite. Any variance is a result of contaminants inside the carbon nanotubes' electrochemistry (Jingfang Wang et al., 2009). CNTs may someday have an electrocatalytic effect, although this has not yet been shown. CNTs are particularly beneficial systems in electrochemical sensing-based biosensor technology because of their large surface area and rigid structure, which permits the fabrication of fully superior electrode designs, although they lack electrocatalytic capabilities. Therefore, one may anticipate a prolonged and aggressive growth in this field and fascinating finding with practical applications.

CHAPTER FOUR

DESIGN AND METHODOLOGY

4.1 Introduction to Experimental Design and Studies

Production optimization studies of CNTs via the CVD method have been successfully carried out using different catalysts, substrate types, catalyst concentrations, growth times, and growth temperatures. Optimum process parameters were determined as a result of the performed characterizations, and the most suitable substrate type, catalyst type and concentration, processing temperature, and growth time parameters were determined for the most efficient CVD-based CNTs. This chapter describes in detail the experimental materials, equipment, experimental studies, and characterization process.

Section 4.2 describes the chemical and structural characteristics of the precursor materials utilized in CVD-based CNT synthesis. Section 4.3 outlines the characteristics of the devices and equipment employed for manufacturing CVD-based CNTs, whereas Section 4.4 explains how experiments are performed using precursors and equipment. Section 4.5 indicates the techniques used to explore the structural, morphological, physical, and chemical properties of CNTs.

4.2 Raw Materials and Chemicals Used in Experimental Studies

4.2.1 Substrates

Four different substrate materials were used to produce CNTs via CVD and evaluate the link between the production efficiency of CNTs and the underlayer (Figure 4.1). The substrates' features can be specified as follows: the copper sheet (12x15 cm) with a thickness of 80 µm, 99.99% purity, and Si wafer with 99.999% purity and n-type. Both Cu and Si substrates were achieved from Sigma Aldrich Company. The single-crystal Si substrate (n-type) is in the (100) direction and has a diameter of 15.9 mm, obtained from Good Fellow Company. Commercially available 1x1x1 cm in size quartz glass substrates was 99.95% purity.

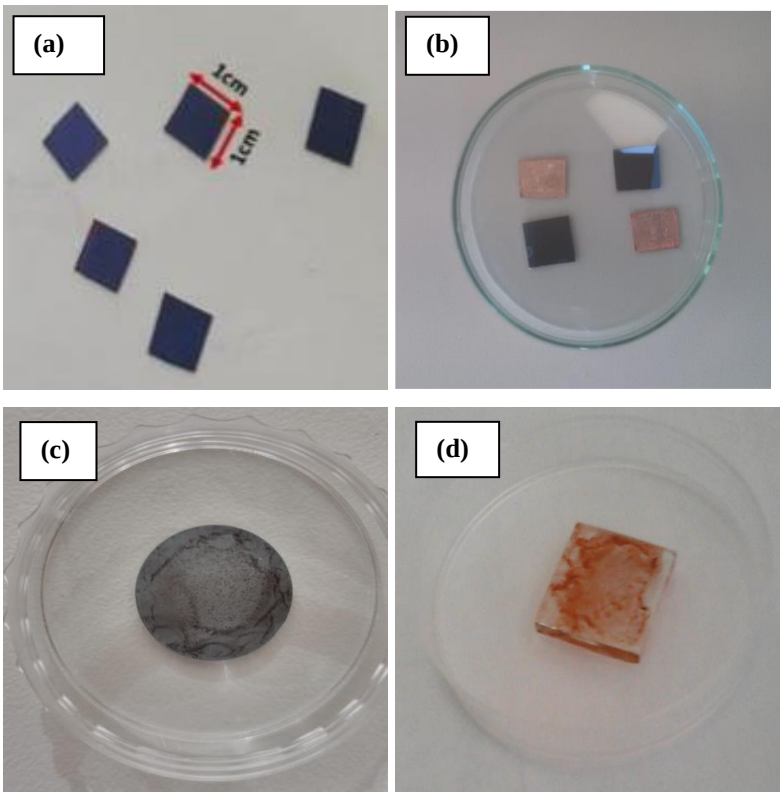


Figure 4.1 Images of the substrates; (a) 1x1 cut of Si wafer, (b) Side-by-side view of cutted Si wafer and Cu sheet substrates, (c) View of Si single crystal ingot, (d) Quartz substrate.

4.2.2 Catalysts

Fe_2O_3 (<50 nm), $FeO \cdot Fe_2O_3$ (50-100 nm), and Nb_2O_5 (99.99% trace metals basis) catalysts were achieved from Sigma Aldrich Company. Au (<30 nm) and Pt (<200 nm) NPs were obtained from the same company. TiO_2 (99.99%) with 17 nm average diameter nano powder was purchased from Sigma Aldrich.

4.2.3 Gas precursors

The hydrocarbon gas precursor required for applying the CVD method was the methane (CH_4) gas. The gas is of high purity (99.99%) and was obtained from Akbaşoğlu Kardeşler Gaz - Metal Kimya San. Tic. Ltd. Şti. Argon gas (purity 99.999%), which will provide an inert atmosphere in the CVD system, was also supplied from the same company.

4.3 Equipments Used in Experimental Studies

4.3.1 Precision Balance and Ultrasonic Bath

In order to generate a solution at specific concentrations from each catalyst and to clean substrates, the precision balance and ultrasonic bath were utilized, respectively. The catalyst powders were weighed in grams on a precision balance of the RADWAG brand AS 220/C/2 model to obtain the required concentration (Fig 4. 3a). Prior to each CVD process, these solutions were treated in an ultrasonic bath to improve the dispersion and reduce agglomeration. Additionally, ultrasonic bath was useful tool for cleaning substrates. Figure 4. 3b depicts the employed ultrasonic bath, a BLULAB 4LT brand unit.

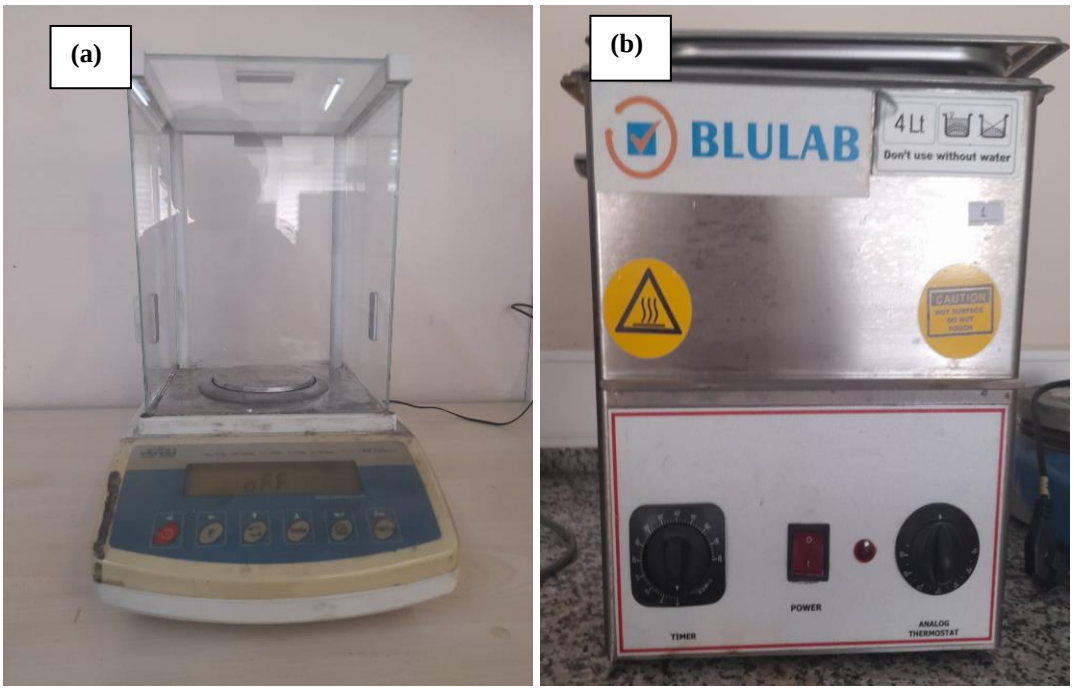


Figure 4.2 (a) Precision balance, (b) Ultrasonic bath

4.3.2 The Oven

To remove the solvent of the solutions treated in the ultrasonic bath, the catalysts dispersed in the solvent were applied to the substrate surface and then processed in the JEIOTECH ON-01E oven shown in Figure 4. 4.



Figure 4.3 Oven used in the preparation of catalyst supported substrates to be sent to the CVD system.

4.3.3 Chemical Vapor Deposition System

The exterior view of the CVD reactor used in the production of CNTs (Zhengzhou Protech technology Co. Ltd-PT 1200-CVD) is given in Figure 4.5a. The experimental temperature of the reactor can reach up to 1100C. Additionally, the system's active reaction site is shown in Figure 4.5b and marked with a blue circle.



Figure 4.4 The CVD System, Zhengzhou Protech technology Co. Ltd-PT 1200-CVD, (Smart Materials's Lab., IKCU); (a) External view of the system, (b) Active reaction zone.

4.4 Experimental Studies

4.4.1 Substrate Cleaning Route

Silicon wafer and Cu sheet were first to cut into 1x1 cm^2 substrates and then prepared for the cleaning steps. Single crystal ingot Si and quartz glass did not undergo any cutting process. The quartz substrates used are 1x1x1 cm in size.

The silicon wafer and single crystal ingot Si were immersed in hot acetone (55°C) for 10 minutes and then in methanol for 5 minutes. Immediately afterward, it was washed with distilled water and dried. Then, Si substrates were treated in an ultrasonic bath with deionized water: HCl (8:2) at 70^{o}C for 3 minutes to remove possible metal contamination on the surface. After each cleaning step, the silicone-based substrates were washed with continuous field deionized water for 3 minutes and then air dried. Additionally, the surface of the single-crystal Si substrate and Si wafer was thoroughly polished with ethanol before use. Cu sheets were etched with hydrochloric acid. Cu sheets and quartz glass were polished before matching by catalysts.

4.4.2 Preparation of Catalyst-Containing Solutions

In the synthesis of CNTs, the catalyst powders must first be combined with the substrates. Therefore, 0.0095 from each catalyst; 0.06 and 0.025 grams were taken and weighed on a precision balance. The catalyst powders were then added into 1.5 mL of ethanol. Thus, catalyst solutions with 6, 4 and 2 (wt.%) were prepared. The solutions were then treated in an ultrasonic bath for 12 hours. In addition, before each CVD process, it was treated in an ultrasonic bath at 25^{o}C for at least 1 hour to increase dispersion and minimize agglomeration. Thus, it was aimed to keep the particles in suspension. Figure 4.6 shows the solutions containing different weight percentages of the catalyst after an ultrasonic bath treatment.

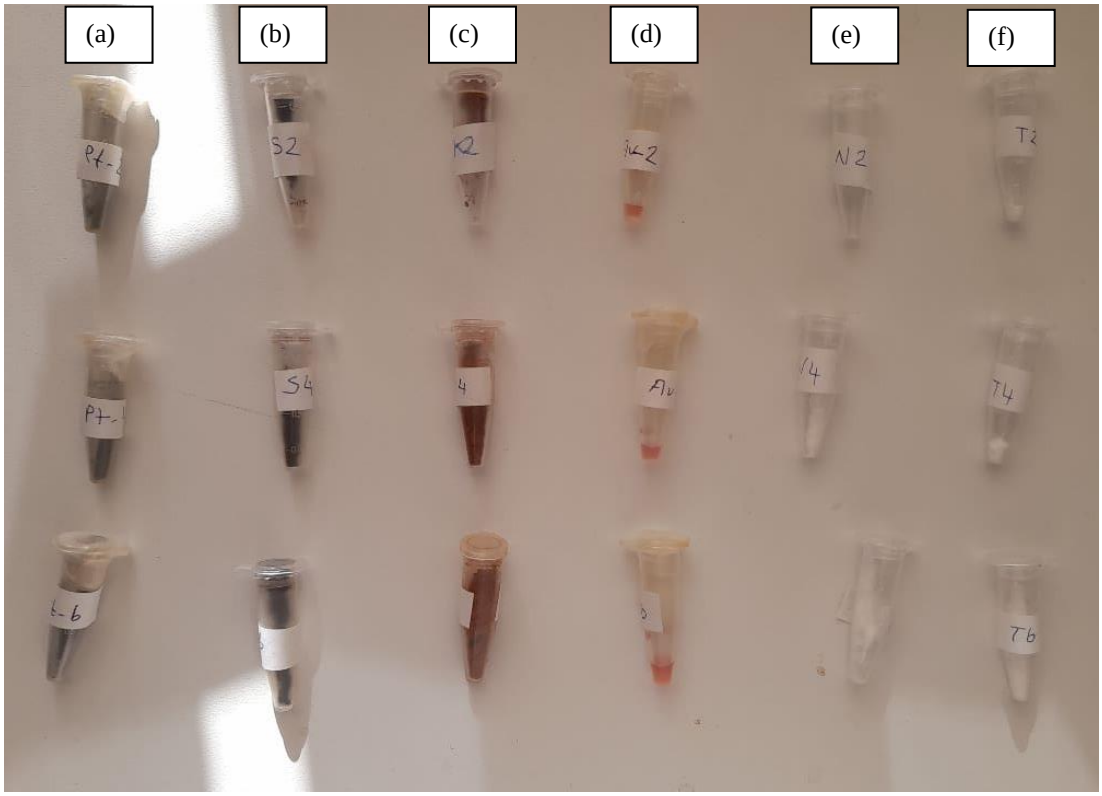


Figure 4.5 The solutions containing different percentages by weight of catalysts (a) Pt NPs, (b) Fe_3O_4, (c) Fe_2O_3, (d) Au NPs, (e) Nb_2O_5, (f) TiO_2.

4.4.3 Integration of Catalyst and Substrate

The solutions prepared in Fig 4.4.2 were dripped onto the substrates with the help of a Pasteur pipette. Then, to remove the ethanol, the substrates with catalyst particles, which were dried in an oven at 60^{o}C for about 30 minutes (Figure 4.7a), were placed on the quartz rod (Figure 4.7b) to be sent to the CVD furnace (Figure 4.7c). Ultimately, after the CVD process, the treated catalyst-supported substrates are shown in Figure 4.7d.

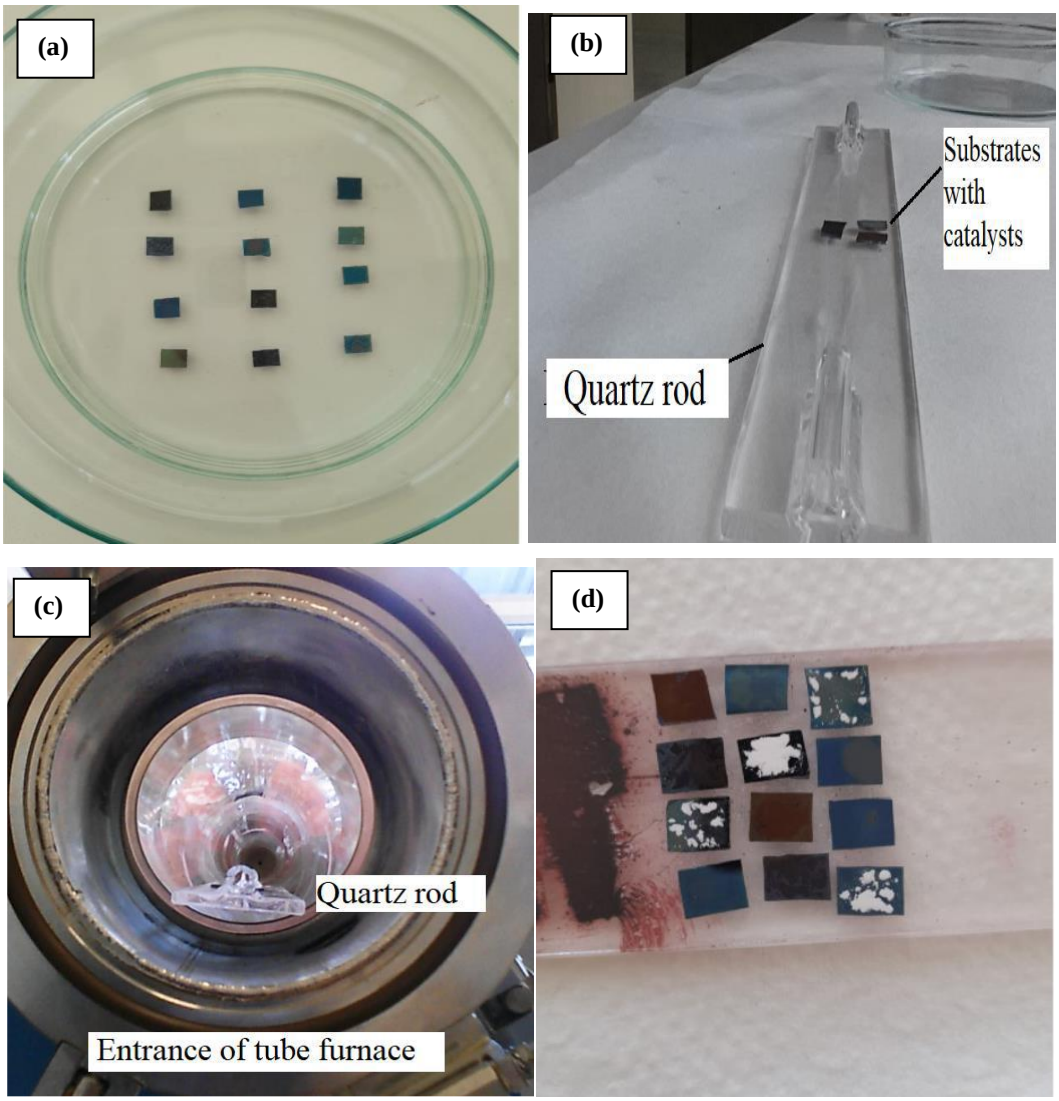


Figure 4.6 (a) Catalyst supported substrates, (b) Placing catalyst supported substrates on quartz rod, (c) insertion of the quartz rod into the CVD system, (d) appearance of substrates after CVD treatment

4.4.4 Chemical Vapor Deposition Process

The catalyst-supported substrates sent to the system on the quartz rod were first heated to 1000^{o}C at a temperature step of 20^{o} /min under an Argon atmosphere. After being heat-treated at this temperature for approximately 40 minutes, CH_4 gas was fed to the system for 3, 5, 7, and 20 minutes each. The methane gas was then turned off, and the furnace was cooled to room temperature in an argon atmosphere (Figure 4.8). The same procedure was followed for processing temperatures of 600 and 800^{o}C by setting to the corresponding process temperature.

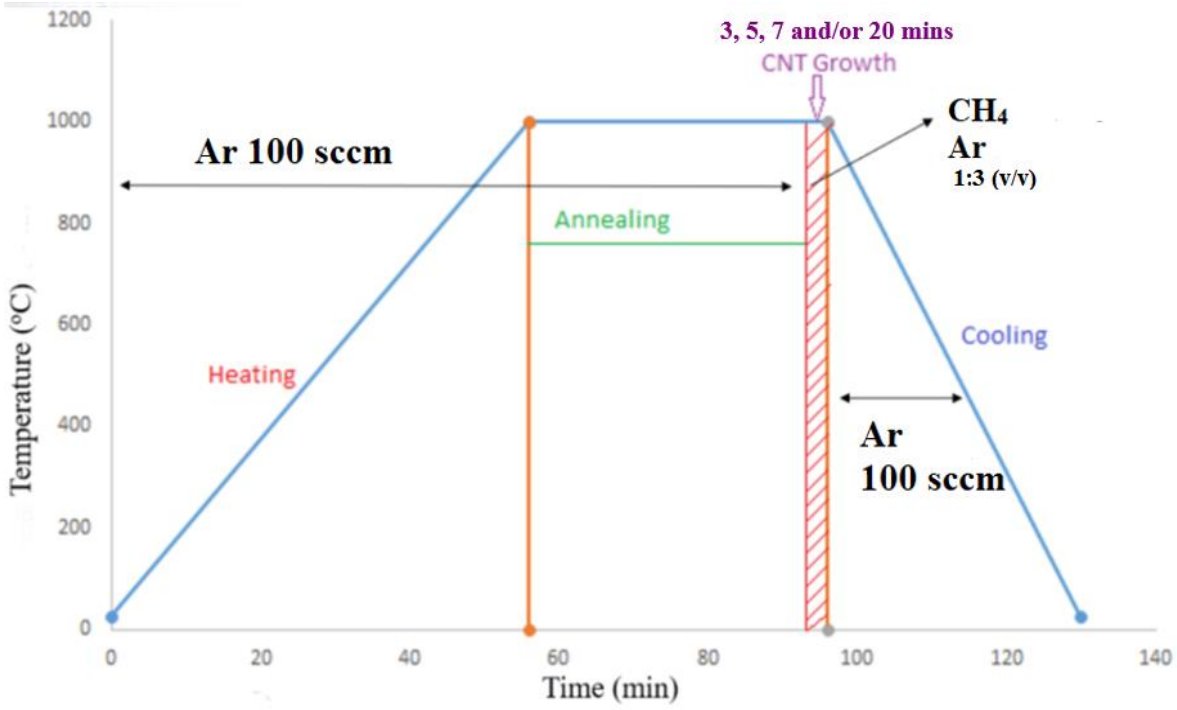


Figure 4.7 CVD process for CNT growth

4.4.5 Nomenclature of Samples

In this study, besides processing temperatures of 600, 800, and 1000°C, four different substrate types were initially optimized for CNT production. Then, the substrates found to be optimum CNT production were subjected to CVD treatment with different catalyst types and concentrations. Moreover, the growth time was also changed, and evaluations were made for production optimization. Additionally, the system was fed fixed to the flow rate at volume ratios of 1 and 3 for CH_4 and Ar, respectively. The nomenclature of all samples based on relevant variables is presented in Table 4.1 based on growth time, percentage of catalyst, and type of nanoparticle catalyst (NPs).

Due to a large number of samples, experimental sets were created and expressed as a group in Table 4.1. While grouping, material groups that were subjected to the CVD process at the same time were considered. Even if the process parameters were the same, the experimental sets were also carried out with the same process parameters to evaluate the repeatability of the process.

Table 4.1 Experimentally applied parameters for CNT production

Group No	Sample No	Substrate Type	Catalyts type	Catalyst conc. (wt. %)	Process Temperature (^oC)	Gas flow rates (sccm)		Growth time (min)
						Ar	CH_4	
1	1	Cu sheets	Fe_2O_3	6	1000	13.4	42.5	20
	2		$FeO{\cdot}Fe_2O_3$					5
	3		Fe_2O_3					
	4		$FeO{\cdot}Fe_2O_3$					
	5	Si wafer	Fe_2O_3					
	6		$FeO{\cdot}Fe_2O_3$					
2	7	Quartz	Fe_2O_3			15	60	
	8							
	9	Si wafer			800			
	10		$FeO{\cdot}Fe_2O_3$					
	11		Nb_2O_5					
	12	Si (single crystal)	$FeO{\cdot}Fe_2O_3$					
	13	Si wafer	Fe_2O_3		600			
	14		$FeO{\cdot}Fe_2O_3$					
	15		Nb_2O_5					
	16	Quartz	$FeO{\cdot}Fe_2O_3$					
	17	Quartz	Fe_2O_3		800	31.5	100	
	18		$FeO{\cdot}Fe_2O_3$					
	19		Nb_2O_5					
3	20	Si wafer	Fe_2O_3		1000			3
	21		$FeO{\cdot}Fe_2O_3$					
	22		Nb_2O_5					
	23		TiO_2					
	24		Au NPs					
	25		Pt NPs					
4	26		Fe_2O_3	4				
	27		$FeO{\cdot}Fe_2O_3$					
	28		Nb_2O_5					
	29		TiO_2					
	30		Au NPs					
	31		Pt NPs					
5	32		Fe_2O_3	2				
	33		$FeO{\cdot}Fe_2O_3$					
	34		Nb_2O_5					
	35		TiO_2					
	36		Au NPs					
	37		Pt NPs					
6	38		Fe_2O_3	6				5
	39		$FeO{\cdot}Fe_2O_3$					
	40		Nb_2O_5					
	41		TiO_2					
	42		Au NPs					
	43		Pt NPs					
7	44		Fe_2O_3	4				
	45		$FeO{\cdot}Fe_2O_3$					
	46		Nb_2O_5					
	47		TiO_2					
	48		Au NPs					

Table 4.2 Continues

	49		Pt NPs					
8	50		Fe_2O_3	2				
	51		$FeO{\cdot}Fe_2O_3$					
	52		Nb_2O_5					
	53		TiO_2					
	54		Au NPs					
	55		Pt NPs					
9	56		Fe_2O_3	6				7
	57		$FeO{\cdot}Fe_2O_3$					
	58		Nb_2O_5					
	59		TiO_2					
	60		Au NPs					
	61		Pt NPs					
10	62		Fe_2O_3	4				
	63		$FeO{\cdot}Fe_2O_3$					
	64		Nb_2O_5					
	65		TiO_2					
	66		Au NPs					
	67		Pt NPs					
11	68		Fe_2O_3	2				
	69		$FeO{\cdot}Fe_2O_3$					
	70		Nb_2O_5					
	71		TiO_2					
	72		Au NPs					
	73		Pt NPs					

4.5 Characterization Techniques

4.5.1 Scanning Electron Microscopy (SEM)

Scanning Electron Microscopy (SEM) is a robust characterization technique used to gain insight into CNTs' morphology and surface structure. Scanning a small high-energy electron beam across the sample surface creates an interaction between the sample and the electron beam, resulting in many radiations. Radiation is used to obtain images in SEM analysis. This radiation is obtained due to primary and secondary electrons. Backscattered primary electrons provide information about the topography and composition of the sample. The topographic information of the surface that produces the depth of field is obtained with the help of secondary electrons. Signal modulation of these two types of radiation provides an output as an image. This image allows the morphological evaluation of the sample through SEM analysis(Abd Mutalib et al., 2017; Mohammed and Abdullah 2018).

In this study, it was determined which samples required further analysis based on the SEM characterization findings. SEM analysis of samples numbered 1 and 2 was

carried out in İzmir Kâtip Çelebi University (IKCU) Central Research Laboratory with Carl Zeiss 300VP SEM Device (Figure 4. 9a). Samples 3, 4, 5, and 6 were analyzed at Dokuz Eylül University (DEU) Center for Fabrication and Application of Electronic Materials with COXEM EM-30 Plus SEM device (Figure 4. 9b). In the samples' SEM analysis, different magnifications as ×1K, ×5K, ×10K, and ×20K were applied.

The remaining SEM imageable samples were performed with the Carl Zeiss Sigma 500-FESEM Device in Dokuz Eylül University Izmir Biomedicine and Genome Center (IBG) (Figure 4. 9c). In the SEM analysis of the samples, ×523 magnification was applied to measure the overall image and density, ×5K for the calculation of the tube radii, and ×18.8K magnification for detailed examination.

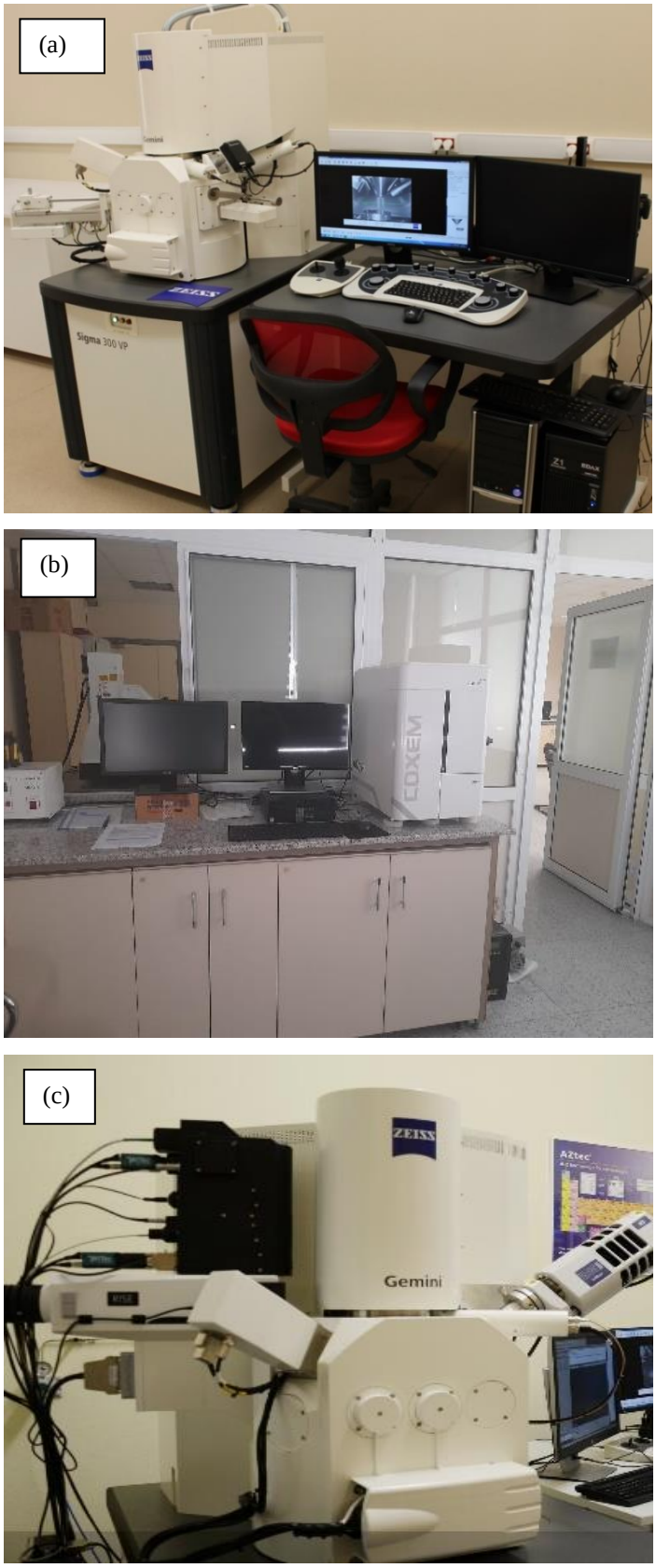


Figure 4. 8 Devices used in SEM characterization: (a) Carl Zeiss 300VP (SEM Lab., IKCU), (b) COXEM EM-30 Plus (Advanced Nanotechnology Lab., EMUM), (c) (Optical Imaging Lab., IBG).

Diameter and size distributions of nanotubes were achieved from SEM photographs obtained with x18K magnification, using Image J program, by measurements performed from 100 different locations for each sample. Density calculations were performed using the Image J program Plugins-Macro function of SEM photographs obtained with x523 K magnification.

The yield of carbon products was calculated according to the following formula 4.1 (Y. Luo et al., 2012):

$$Y\ (w\%) = \frac{M_1 - M_2}{M_2} \times 100\% \quad (4.1)$$

Y indicates the yield (%w) of carbon products; M_1 and M_2 represent the mass of synthetic products and the ash of the catalyst, respectively, obtained by the CVD method.

4.5.2 Energy Dispersive X-Ray Analysis (EDX)

Energy dispersive X-ray spectroscopy (EDX) coupled to the SEM instrument uses X-rays produced from the interaction between the electron beam and the sample to quantitatively determine and measure the sample's elemental composition. Therefore, the elemental composition can be detected simultaneously while detecting the sample's morphology (Abd Mutalib et al., 2017). In this study, the production of CNTs with catalysts on the substrate surface revealed the necessity of applying EDX characterization to evaluate element composition and efficiency. For this reason, EDX analysis, operating at an accelerating voltage of 17 kV, was applied to the samples determined to be tubular after SEM analysis by Carl Zeiss Sigma 500-FESEM Device (Figure 4. 10) in Dokuz Eylül University Izmir Biomedicine and Genome Center.



Figure 4.9 Device used in EDX characterization, Carl Zeiss Sigma 500-FESEM (Optical Imaging Lab., IBG)

4.5.3 Fourier Transform Infrared Spectroscopy (FTIR)

Fourier Transform Infrared Spectroscopy, also known as FTIR Analysis or FTIR Spectroscopy, is an analytical technique used to identify and evaluate different functional groups in the chemical structures of organic, polymeric, and, in some cases, inorganic materials. The FTIR analysis method uses infrared light to scan test samples and observe chemical characteristics. When infrared is applied to the sample, the molecules of the material absorb infrared light of different wavelengths, thus determining the molecular composition and structure of the material (Berthomieu and Hienerwadel 2009).

In this study, FTIR analysis was realized via the Thermo scientific NICOLET iS10 (Figure 4. 11) equipped with an ATR apparatus to determine the functional groups on the samples at Dokuz Eylül University Center for Fabrication and Application of Electronic Materials. The measurement wavelength range of FTIR studies was set to 550–4,000 cm^{-1}.

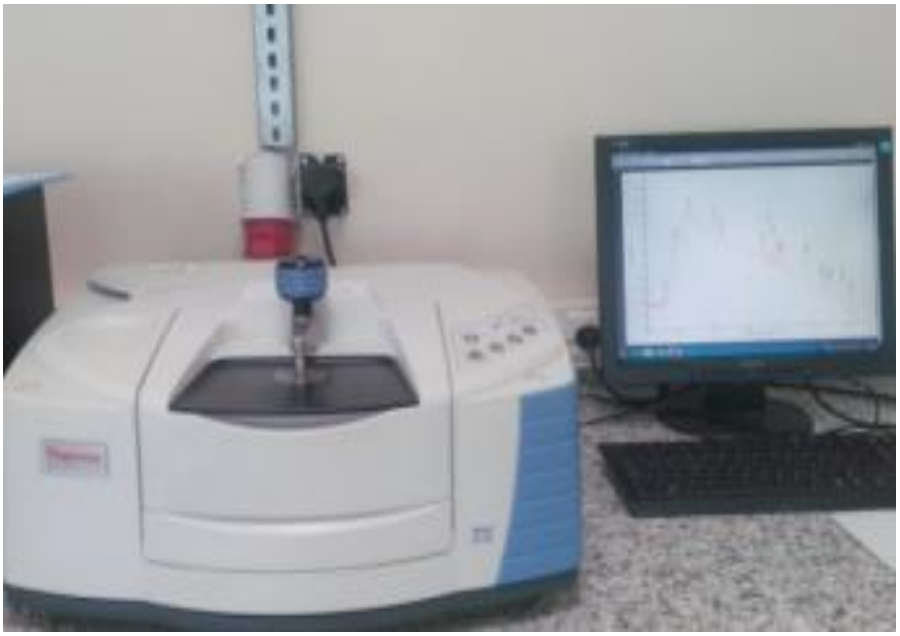


Figure 4.10 FTIR Spectrometer, Thermo scientific NICOLET iS10 (Advanced Nanotechnology Lab., DEU)

4.5.4 Raman Spectroscopy

Raman scattering, which provides essential information about the nature and quality of electron confinement of CNTs, is an important and valuable qualitative technique to distinguish CNTs from other nanocarbons. Basically, Raman scattering is based on the light interacting between the material and the phonon creating higher transition energy where the electron interacts with a phonon before returning to its ground state. Thus, –C–O–C–, –C≡C–, and –C=C– vibrations with very low effect in FTIR analysis can form strong Raman bands, which also shows sp^2 or sp^3 hybridizations of nanocarbons. Moreover, in the Raman analysis of CNTs, the most prominent peaks that distinguish CNTs from other nanocarbons are low frequency, radial breathing beams (RBM), and higher frequency of D, G, and G' modes (Arepalli et al., 2008; Reich, Thomsen, and Maultzsch 2004).



Figure 4.11 Raman spectrometer device, Renishaw/In via (Spectroscopy Lab., IKCU)

D, G, and G' modes can be observed in other nanocarbons and graphite. However, RBM is specific to SWCNTs and can give direct information about diameter distribution and chirality (Arepalli et al., 2008). Therefore, in this study, in addition to FTIR analysis, Raman spectra of samples, using an excitation source of 785 nm, were obtained with the Renishaw/In via device in İzmir Kâtip Çelebi University, Central Research Laboratories (Figure 4.12).

4.5.5 X-Ray Diffraction Analysis (XRD)

X-ray diffraction (XRD) is an efficacious technique for obtaining information about the crystal structure and properties of all kinds of materials, such as powders and crystals, structural phases, and phase changes. For example, the crystal size and interlayer spacing can be measured by detecting the carbon reflection of graphite from the XRD profiles of CNTs (Anjalin 2014). Due to the unique nature of CNT, it is known that the main properties of the X-ray diffraction pattern of CNTs are close to those of graphite(Hassan Khani and Moradi 2013).



Figure 4.12 X-Ray Diffractometer, Rigaku, D/Max-2200/PC (X-Ray Lab., DEU).

The phase composition of samples was investigated by X-ray diffraction (XRD) with a Rigaku (Figure 4. 13), D/Max-2200/PC with uses Cu-Kα radiation (0.15418 nm). XRD analyzes were performed at Dokuz Eylül University Metallurgical and Materials Engineering Department. XRD data of samples were recorded with a 2^{o} /min scanning speed in the range of $10 < 2\theta < 90^{o}$, and all samples were analyzed by means of XRD with a grazing angle attachment and an incident angle of 3°. Material Analysis Using Diffraction (MAUD) software, and High Score Plus X-ray diffraction software, based on Rietveld refinement, was used to get the relevant quantitative crystallographic information.

4.5.6 X-Ray Photoelectron Spectroscopy (XPS)

X-ray photoelectron spectroscopy (XPS), a surface analysis technique, was used to discover the fundamental composition of the elements on the surface of a catalyst-supported substrate, the chemical formula of the relevant molecules, and the bond structures and electronic states of the carbon atoms (Van der Heide 2011).

The surface chemical compositions of catalyst supported substrates were performed by XPS with K-Alpha equipment (Thermo Scientific, Figure 4.14) at Dokuz Eylül University Center for Fabrication and Application of Electronic Materials. The emission source of monochromatic radiation was aluminum K of 1486.68 eV, at a voltage of 12 KV and a current of 6 mA. The electron gun for charge compensation

was activated. The measurement spot size was 400 μm and the beam current 4.2 mA ion. The instrument was calibrated in accordance with gold; 4*f* 7/2. The pressure of the system was kept at below $5x10^{-10}$ mbar for the period of data acquisition. The XPS data of the survey scan was performed from -10 to 1350 eV with a scanning speed of 1 eV applying pass energy of 150 eV. Whole samples were scanned 20 times from a single point. XPS spectra showed up binding energies of Si2p, O1s, C1s, and Fe2p. Binding energies were measured referred to as the C1s peak at 285 eV and XPS spectra were background subtracted using the Shirley method.



Figure 4.13 X-Ray Photoelectron Spectroscopy, Thermo Scientific K-Alpha (Thin Film Lab., DEU).

Furthermore, the C1s elemental spectrum was obtained in the binding energy range of 281 to 296 eV. C1s peaks of CNTs obtained within the scope of the study were analyzed by e deconvoluting them with XPSPEAK41, the peak analysis program obtained from Washington State University Chemistry Department and Materials Science and Engineering Program. In the analysis process, the sum of the Gauss-Lorentzian function is deconvoluted to the Pseudo-Voigt function (Equation 4.2) (J.-M. Lee et al., 2009).

$$F(E) = H\left[(1-S)\exp\left(-\ln(2)\left(\frac{E-E_0}{FWHM}\right)^2\right) + \frac{S}{1+\left(\frac{E-E_0}{FWHM}\right)^2}\right] \quad (4.2)$$

where S is the shape function related to symmetry and Gaussian-Lorentzian mixing ratio, FWHM is the half-height full width, E_0 is the vertex center, H is the peak height, and F(E) is the density at energy E (J.-M. Lee et al., 2009; S.-M. Yun et al., 2007).

4.5.7 Current-Voltage Characterizations

The most used method for measuring resistance is the four-probe approach. This approach employs four collinear probes with identical spacing to create electrical contact with the substance. It is termed a four-point probe because the current is driven through the two outer probes while the two internal probes measure voltage. Consequently, the resistance of a thin film layer is measured in ohms per square (Smits 1958).



Figure 4.14 Current-Voltage Characterization Device, Keithley 4200 analyzer (Electric-Electronic Measurement Lab., DEU).

The electrical characterization of the samples was carried out by averaging 3 replicates of 60 surface data from a 1 µm surface thickness. using a Keithley 4200 semiconductor parameter analyzer (Figure 4.15) connected to a probe station at Dokuz Eylül University Center for Fabrication and Application of Electronic Materials. The

measured average resistance value was used to calculate electrical conductivity and resistivity by applying the following equations.

$$\rho = R \, x \frac{A}{l} = Rx \frac{t \, x \, r}{l} \quad (4.3)$$

$$\sigma = \frac{1}{\rho} \quad (4.4)$$

Where *l* is the distance between the probes touching the surface (Unit: cm, l : 0.0652 inch = 0.1656 cm), t is the thickness of the surface (Unit: cm, t=1 µm, 10^{-4} cm), r is the diameter/width of the probes touching the surface (Unit: cm, r : 0.0016 inch = 0.0041 cm), R : Measured resistance value (Unit: Ω), and ρ is Resistivity value (Unit: Ωcm), σ is electrical conductivity (Unit: 1/Ωcm).

CHAPTER FIVE

RESULT AND DISCUSSION

5.1 Introduction to shaping experimental outputs according to optimization

Since the production process depends on many variables such as diverse substrates, catalyst type, catalyst concentration, growth temperature, and growth time, many unsuccessful productions have been one of the difficulties encountered in the first place. For this reason, the optimum parameters of a tubular structure that can be included in future characterizations were revealed by SEM analysis. This section covers the detailed analysis of the EDS, FTIR, Raman, XRD, XPS, and current-voltage characterizations of the samples based on the parameters from which the tubular structures observed in the SEM analysis were obtained during the application of the experimental methodology. Moreover, he explains the reason for the failed productions by referring to the CVD-based process parameters.

5.2 Scanning Electron Microscopy (SEM)

5.2.1 Group 1

Figure 5.2.1 shows the SEM image of samples numbered 1 and 2, at different magnifications, exposed to methane gas for 20 min using Fe_2O_3 (Figures 5.1a and b) and Fe_3O_4 (Figures 5.1c and d) NPs catalysts on a copper substrate. The heterogeneous distribution of Fe_2O_3 NPs in Figs. 1 a and b are clearly seen. Additionally, in sample number 2, where Fe_3O_4 NPs were used, the particles' agglomeration was observed (Figure 5.1d). In Figures 5.1a and c, it is revealed that copper cannot be used as a useful substrate due to applying the process temperature at 1000^oC at a temperature close to 1074^oC, the melting temperature of Cu. The reason for this is that Cu substrate with very low carbon solubility is thought to exhibit melting behavior at this temperature. Therefore, the surfaces where hydrocarbon decomposition may occur during the CVD process (i.e., an area necessary and sufficient for the nucleation of CNTs) could not be provided. The most significant support of this idea is to obtain a similar observation in

samples 3 and 4, which were exposed to methane gas for 5 minutes. In SEM images of samples 3 and 4 (Figures 5.1e and g), as in the samples exposed to methane gas for 20 minutes, no CNTs structure was found here. The images obtained suggest that the copper substrate's processing temperature at 1000°C may have led to grain growth and / or recrystallization behavior. Additionally, the absence of the applied catalysts NPs on the surface led to the possibility that Fe_2O_3 (Figures 5.1e and f) and Fe_3O_4 (Figures 5.1g and h) could not adhere to the Cu substrate surface and could be swept by Ar gas during the CVD process.

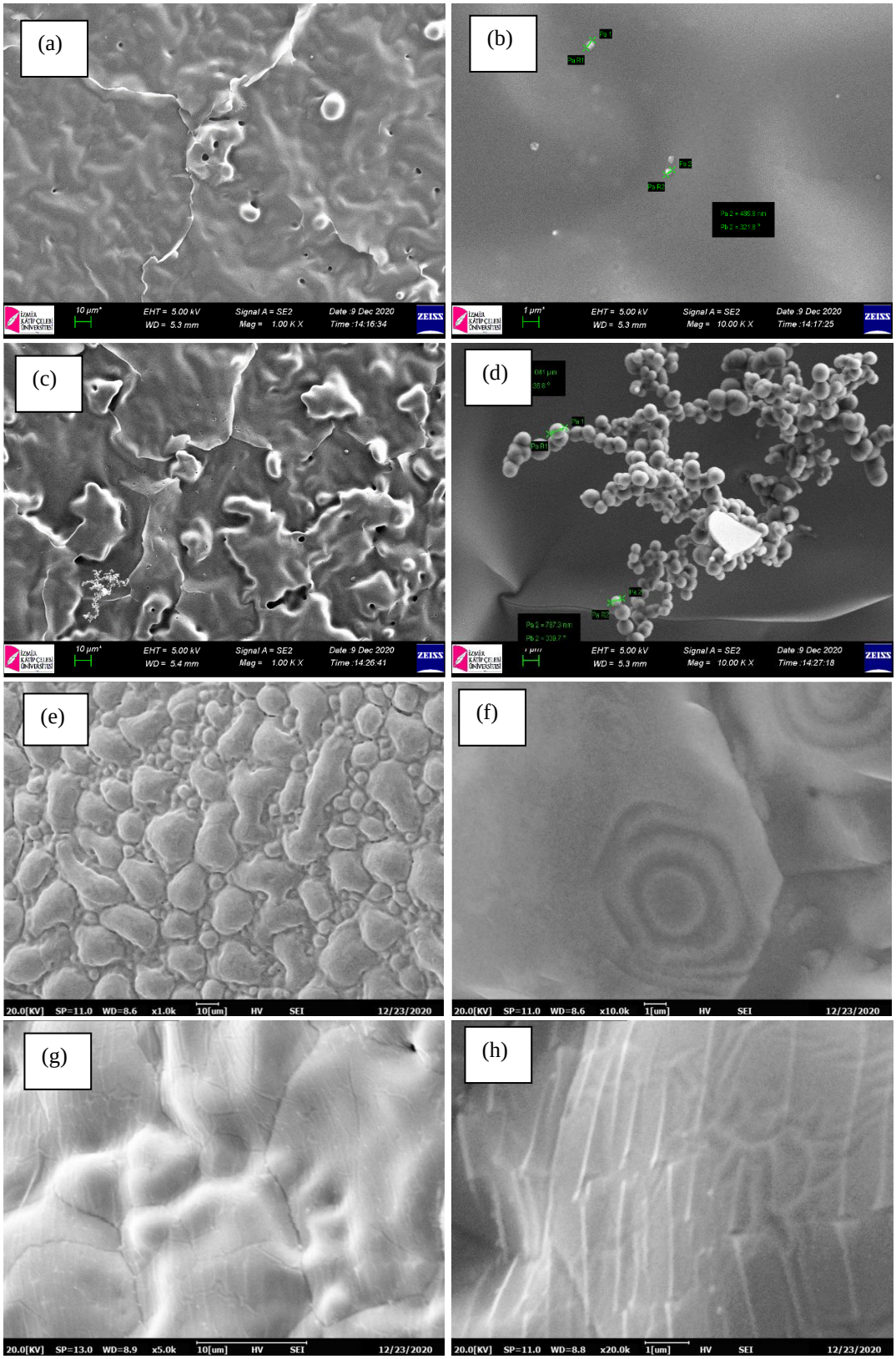


Figure 5.1 SEM Images of samples 1 and 2; Sample 1 (a) at ×1K, (b) at ×10K; Sample 2 (c) at ×1K, (d) at ×10K magnification; Sample 3 (e) at ×1K, (f) at ×10K; Sample 4 (g) at ×5K, (h) at ×20K magnification.

In Figures 5.2 several magnifications of the SEM image of sample number 5, which was exposed to methane gas for 5 minutes utilizing Fe_2O_3 NPs catalysts on a Si substrate, are shown. It is evident from Figures 5.2a, b, and c that Fe_2O_3 nanoparticles are not uniformly dispersed on the Si substrate surface. In Figures 5.2a, b, and c, however, it was also found that the CNTs structure was produced. In addition, it was established that the nanotube diameter range varied between 27 and 60 nm as a consequence of Image J measurements taken at fifty distinct places. Figure 5.2d depicts the catalyst, CNT, and substrate structures. At various magnifications, Figures 5.2e, f, g, and h show the SEM image of Sample 6, which was exposed to methane gas for 5 minutes utilizing Fe_3O_4 NPs catalysts on Si substrate. Figures 5.2e, f, g, and h indicate the agglomeration and non-homogeneous distribution of Fe_3O_4 NPs catalysts, comparable to sample 5 in which Fe_2O_3 is utilized as a catalyst. Alternatively, it is important to highlight that the nanotube structure is created. The nanotube diameter range varied between 50 and 66 nm, as established by measurements taken at 50 distinct places using the Image J software.

In the first group of the study, no tubular form was observed with the copper sheet substrates, and it was concluded that the catalysts could not adhere to the surface. However, the outputs from Group 1 shed some light on the focus of research for the Si wafer substrate. However, Group 2 will examine the success of quartz and Si crystal ingots in tubular form production and will be able to give results will allow evaluation in terms of processing temperature and shape the optimization of the research.

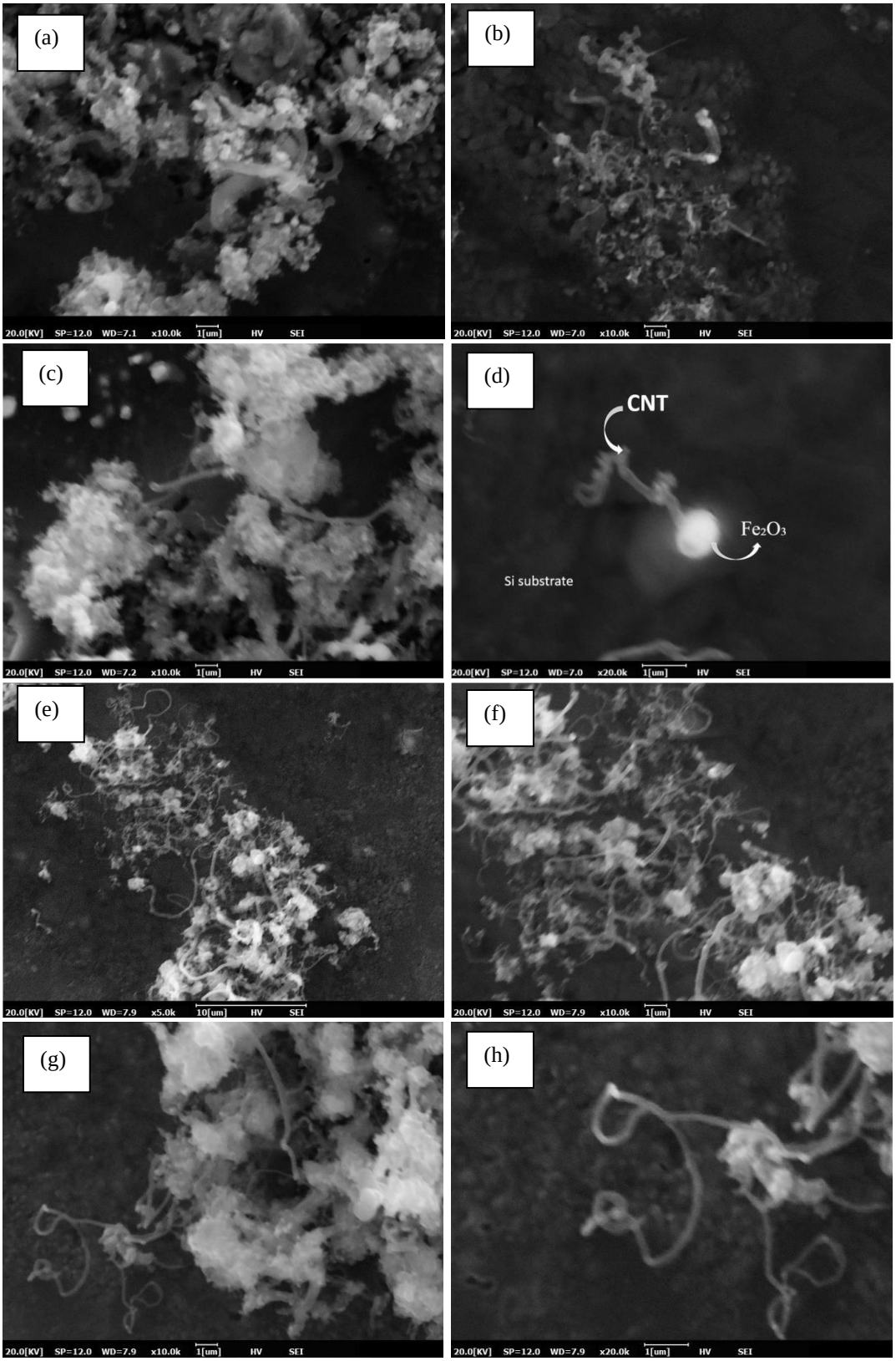


Figure 5.2 SEM Images of samples 5 and 6; Sample 5 (a,b and c) at ×10K, (d) at ×20K magnification; Sample 6; (e) at ×5K, (f, and g) at ×10K, (h) at ×20K magnification

5.2.2 Group 2

Since the processing temperature was 1000ºC for the CNT manufacture of samples 5 and 6 in Group 1, which was successfully completed, the CVD production of samples 7 and 8 on quartz glass substrates was initially studied using the same processing temperature. Nonetheless, as seen in Figure 5.3, a small melting behavior was noticed in the glasses owing to the transition temperature of the quartz glass after the treatment, and the catalyst-coated quartz glasses began to split as they cooled to ambient temperature. Therefore, SEM characterization with these materials were not possible.

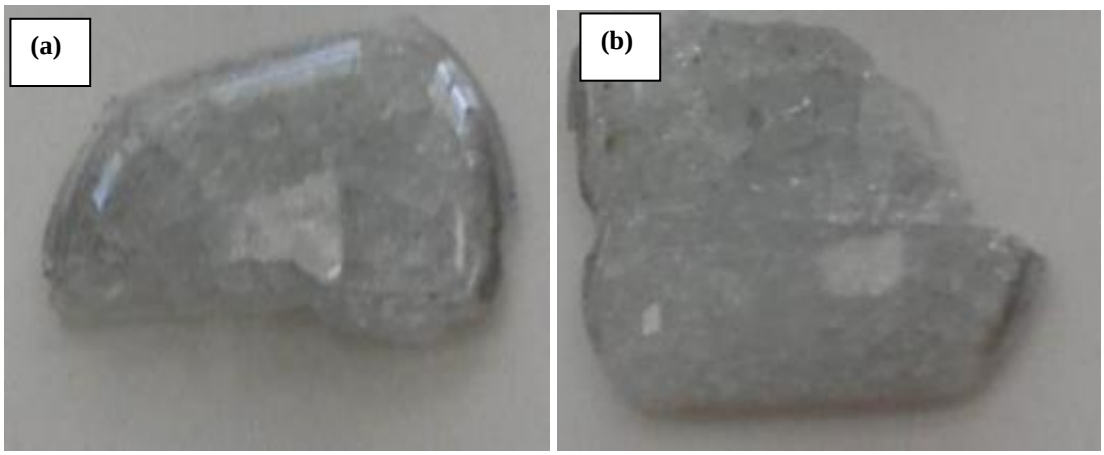


Figure 5.3 Images of samples 7 and 8 after CVD process at 1000ºC; (a) Sample 7, (b) Sample 8

Two different substrate strategies were applied for the synthesis of CNTs via the CVD process at 800oC. While Si wafer substrate was used in samples 9, 10, and 11, $FeO \cdot Fe_2O_3$ nanoparticle catalyst support was applied on Si (single crystal) substrate in sample 12. CVD method optimization studies were carried out for CNT production in catalyst support at lower temperatures. Figure 5.4 shows the SEM images of sample 9 at different magnifications, CVD-treated at 800ºC, in which Fe_2O_3 NPs were used as catalysts on Si wafer. As can be seen in Figure 5.4a, the NPs were homogeneously dispersed on the substrate surface.

However, it can be supposed that there are agglomerations in Figures 5.4b, c, and d. But, upon closer inspection, it can be concluded that CH_4 has a reducing property on Fe_2O_3 NPs, and an initiation resembling a short rod-like nanotube form is present. However, it cannot be claimed that the CNT form was observed as distinctly as the samples 5 and 6 synthesized in the Group 1 carried out at 1000ºC. The reason for this

can be shown as the increase in the C solubility of Fe at high temperatures. Considering the iron-carbon diagram, it can be said that the metals with few d-vacancies, such as Fe, have limited carbon solubility at specific temperature ranges. By reducing the temperature below 1000^{o}C, the carbon solubility was limited for sample 9.

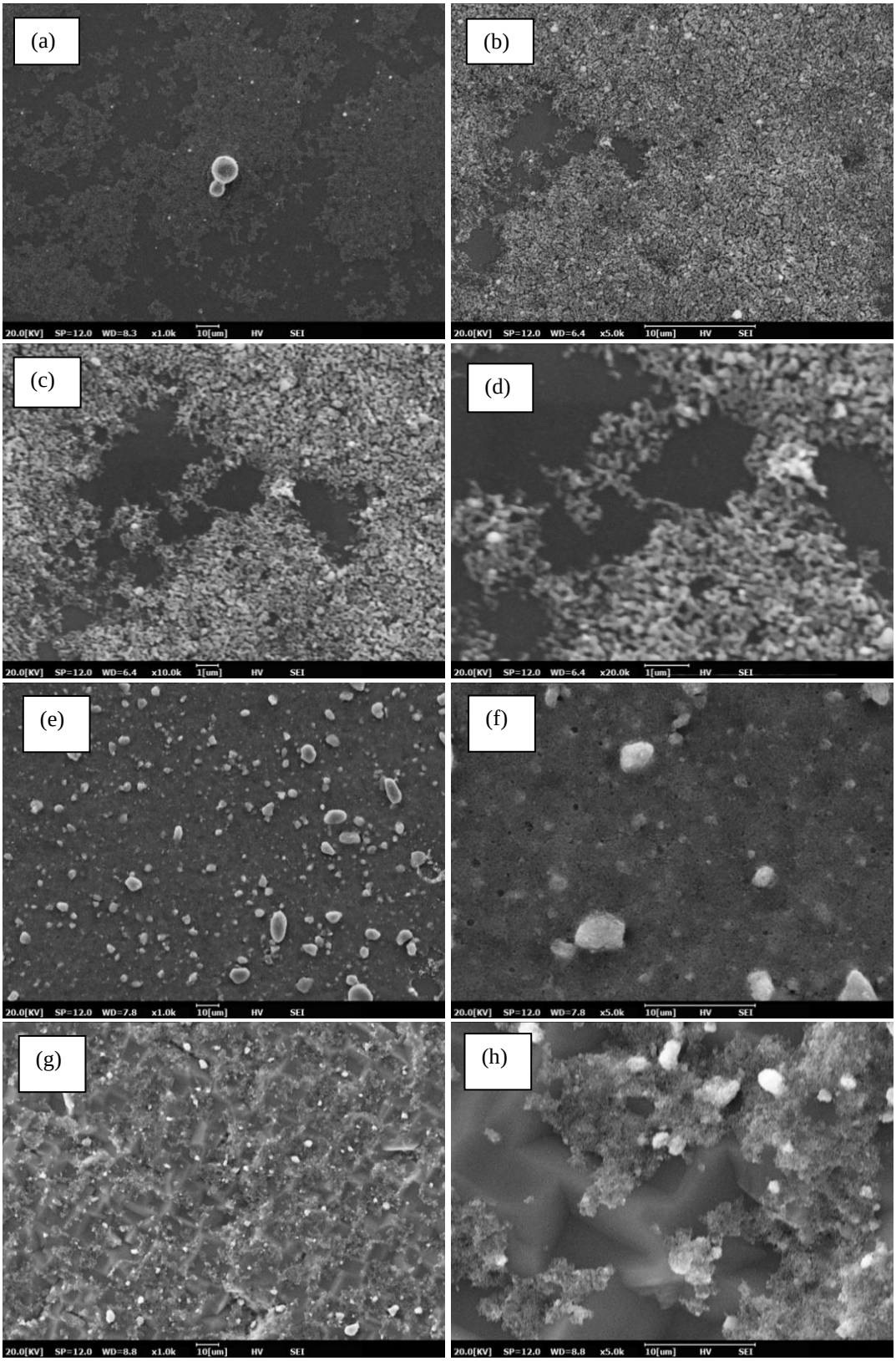


Figure 5.4 SEM Images of samples 9 and 10 at different magnifications and locations; Sample 9 (a) x1K, (b) x5K, (c) x10K, (d) x20K; Sample 10; (e) x1K, (f) x5K, (g) x1K, (h) x5K.

Fe_3O_4 was applied as a catalyst at 800°C in a CVD furnace in sample 10, whose SEM images are shown in Figure 5.4e, f, g and h. Although the homogeneous distribution of the NPs applied as the catalyst on the substrate surface, the process temperature was not sufficient for carbon solubility. This caused the CNT not to form, which is like Sample 9. On the other hand, it should be noted that in the previous study carried out at 1000°C, the CNT structure was successfully obtained, although all other process parameters were applied the same. CNTs that started to form on Fe_2O_3 in Fig. 6 may need more time to reduce CH_4 gas if Fe_3O_4 catalysts are used. Therefore, it was thought that an observation like sample 9 could not be obtained in sample 10. As a result, CNT formation at 800°C could not be realized when the Fe_3O_4 catalyst was used.

It was observed that limited carbon solubility with Fe-based catalyst with few d-vacancies did not lead to CNT formation in the final structure depending on temperature. On the other hand, strong chemical bonds can be formed with carbon to obtain stable carbides with the 3d metal Nb-based catalyst with many d-vacancies(Arthur and Cho 1973). For this purpose, SEM images of sample 11 obtained using a CVD-treated Nb_2O_5 catalyst supported Si wafer substrate at 800°C are shown in Figure 5.5a and b. Due to the reducing property of CH_4, it is thought that $Nb_2O_5 \rightarrow NbO \rightarrow Nb \rightarrow NbC \rightarrow NbC+C$ transformations may occur, and a possible chemical reaction (5.1) takes place. Moreover, the agglomeration of Nb_2O_5 particles and fine tube-shaped structures that form on the catalyst particles can be seen in Figures 5.5a and b. It is predicted that these structures can be obtained more efficiently at higher temperatures and/or longer CH_4 exposure times.

$$Nb_2O_5(k) + 8CH_4 \rightarrow 2NbC(k) + C(k) + 5CO + 16H_2 \qquad (5.1)$$

Similar observations were obtained in Fe_3O_4 catalysts on the Si single crystal surface (Figures 5.5c, d, e and f) to the results obtained from the previous Fe-based catalysts on the Si wafer surface (Figure 5.4). In sample 12 obtained by CVD treated Si single crystal substrates supported with Fe_3O_4 NPs catalysts at 800°C, it was concluded that the catalysts could be dispersed homogeneously (Figures 5.5c and d), but the CNT structure could be formed on the catalysts, albeit very rarely (Figures 5.5c and d).

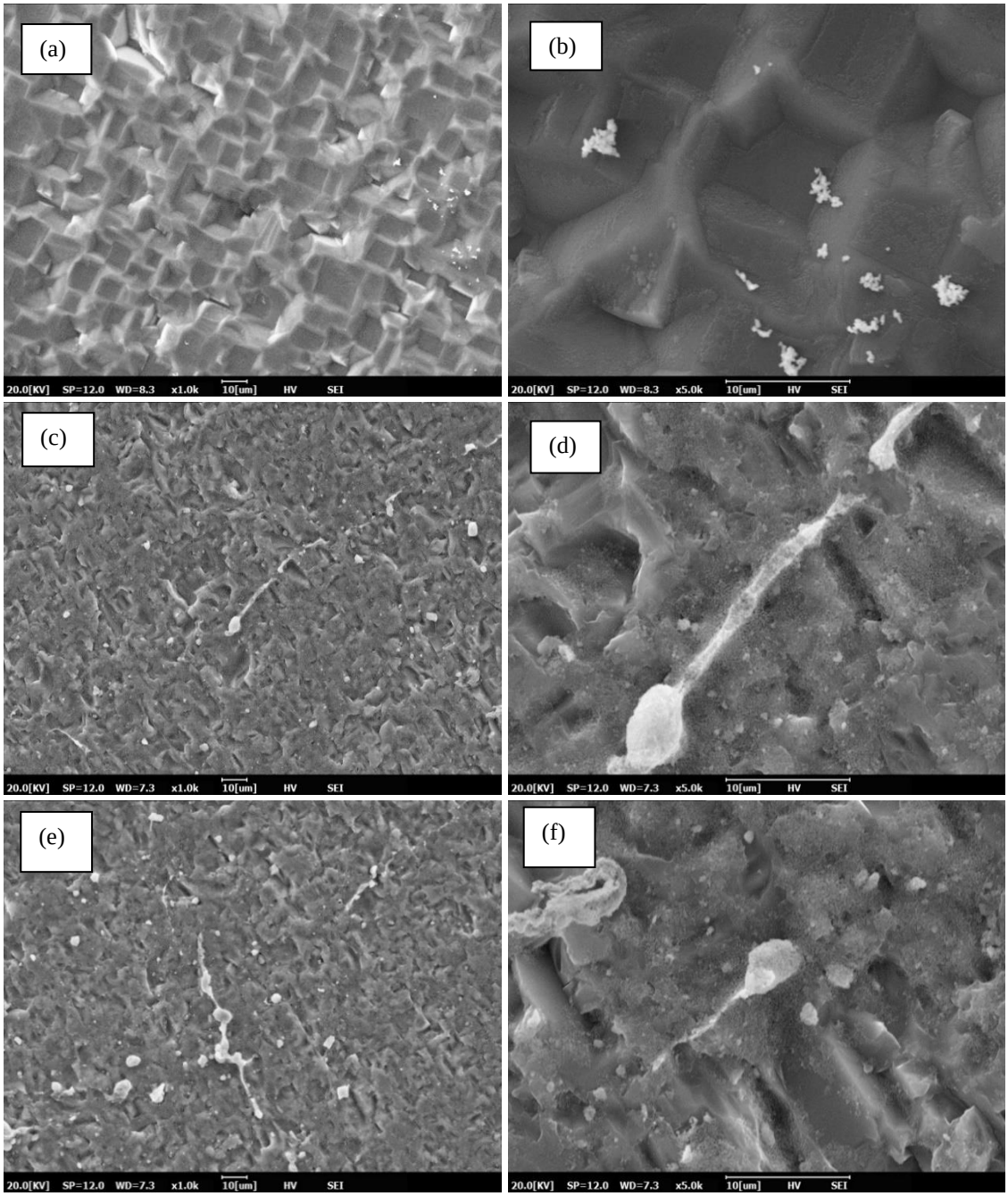


Figure 5.5 SEM Images of samples 11, and 12 at different magnifications and locations; Sample 11 (a) x1K, (b) x5K; Sample 12 (c) x1K, (d) x5K, (e) x1K, (f) x5K

Experimenting with lower process temperatures is primarily motivated by the need for less energy and the ability to create CNT in the presence of a catalyst. However, as observed in the SEM images of samples 13 and 14 (Figure 5.6) on which Fe-based catalysts were used, only Fe_2O_3 and Fe_3O_4 nanoparticles are uniformly dispersed over the Si wafer substrate surfaces. These surfaces do not form the CNT structure (Figures

5.6a and c). This data supports the notion that at 800°C, the solubility of carbon at low temperatures is limited in samples 9, 10, and 12 (Figures 5.4 and 5.5). Therefore, it is believed that investigations using Fe-based catalysts at 600 and 800°C should conclude at this point, and experiments should proceed at 1000°C afterwards.

The CVD procedure was conducted using Nb_2O_5 catalyst at 600°C (Sample 15), comparable to sample 11 which was produced using Nb_2O_5 catalyst at 800°C. Figures 5.6e and f show SEM images of the acquired sample 15. Similarly sample 11 (Figure 5.5b), Nb_2O_5 particles aggregate in Figures 5.6e and f. Furthermore, following the CVD procedure at 600°C in the presence of Nb_2O_5 catalyst, small tubular structures were detected on the catalyst of sample 15. (Figure 5.6f). However, it should be noted that more characterizations are required to substantiate this discovery since manufacturing is inefficient. Similar to the experimental tests conducted with other Fe-based catalysts on quartz substrate surfaces supported by Fe_3O_4 NPs catalysts, the SEM examination of sample 16 at an operating temperature of 600°C (Figures 5.6g and h) revealed that neither the agglomeration of the catalysts nor the CNT structure could be achieved. In contrast, it was not able to capture SEM pictures of samples 17, 18, and 19 at an operating temperature of 800°C because the quartz substrate melted and solidified after cooling.

In this part of the study, different substrates such as Si wafer, Cu sheet, quartz and Si single crystal ingot have been tried to be optimized so that other parameters are stable. The study focused on Si wafer substrate because the catalysts could not show sufficient adhesion to Cu layers, Cu layers melted at the processing temperature, Quartz glass melted at the processing temperature and solidified and cracked during cooling. On the other hand, a common understanding of the processes for CNT production with iron group catalysts by CVD is the catalytic decomposition of carbon-bearing precursors at the catalyst surface and the consequent incorporation of carbon atoms into the catalyst. When supersaturation occurs, carbon atoms precipitate from the catalyst, leading to nanotube growth. For this reason, CNT or tubular-like production was successfully performed in all iron-based catalysts treated at 1000°C, regardless of the catalyst concentration and growth time applied. Below this temperature (600 and 800°C), no CNT morphology could be observed with any substrate.

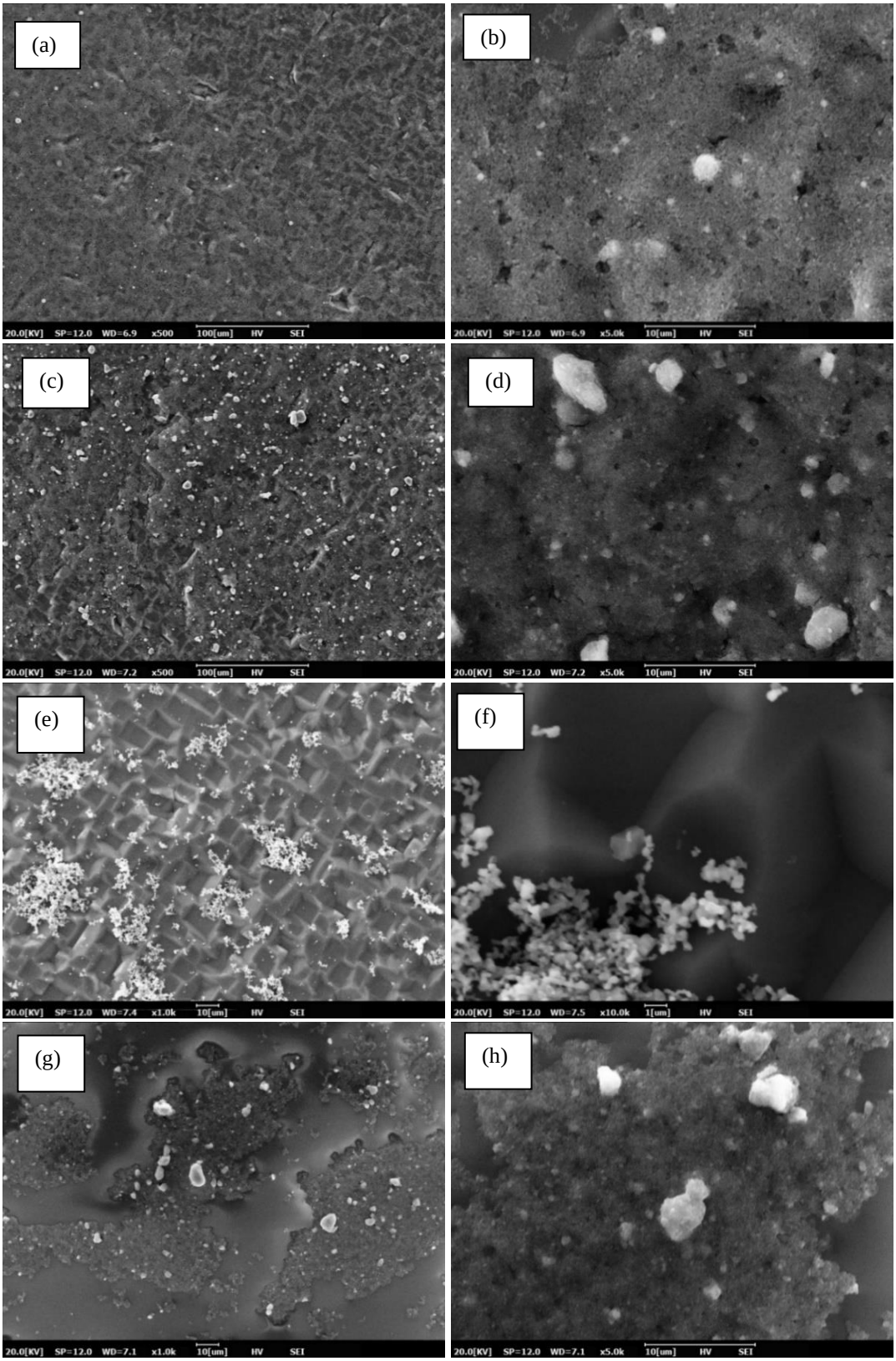


Figure 5.6 SEM Images of samples 13, 14,15 and 16 at different magnifications and locations; Sample 13 (a) x500K, (b) x5K; Sample 14 (c) x1K, (d) x5K; Sample 15 (e) x1K, (f) x10K; Sample 16 (a) x1K, (b) x5K.

5.2.3 Group 3

Si wafer substrates supported by 6% by weight Fe_2O_3, Fe_3O_4, Nb_2O_5, Au NPs and Pt NPs were named samples 20, 21, 22, 23, 24, and 25, respectively. The samples, exposed to methane gas for 3 minutes at 1000°C processing temperature, were then cooled to room temperature under the Ar atmosphere. As can be seen in Figure 5.9, an efficient CNT morphology could not be obtained for other catalyst types, except for samples 20 and 21 supplemented with Fe-based catalysts.

In all optimization studies performed at a lower temperature in the previous six-month period, no CNT formation was obtained in Fe-based catalysts. However, despite the 3-minute hydrocarbon gas precursor application in this section, CNT was obtained in all samples using a Fe-based catalyst with a processing temperature of 1000°C. The reason for this can be manifested as the increased C solubility of Fe at high temperatures. Considering the Fe-C diagram (Figure 5.7), it can be said that metals with few d vacancies, such as Fe, have limited carbon solubility in a specific temperature range. The carbon solubility of samples 20 and 21 was increased by increasing the operating temperature.

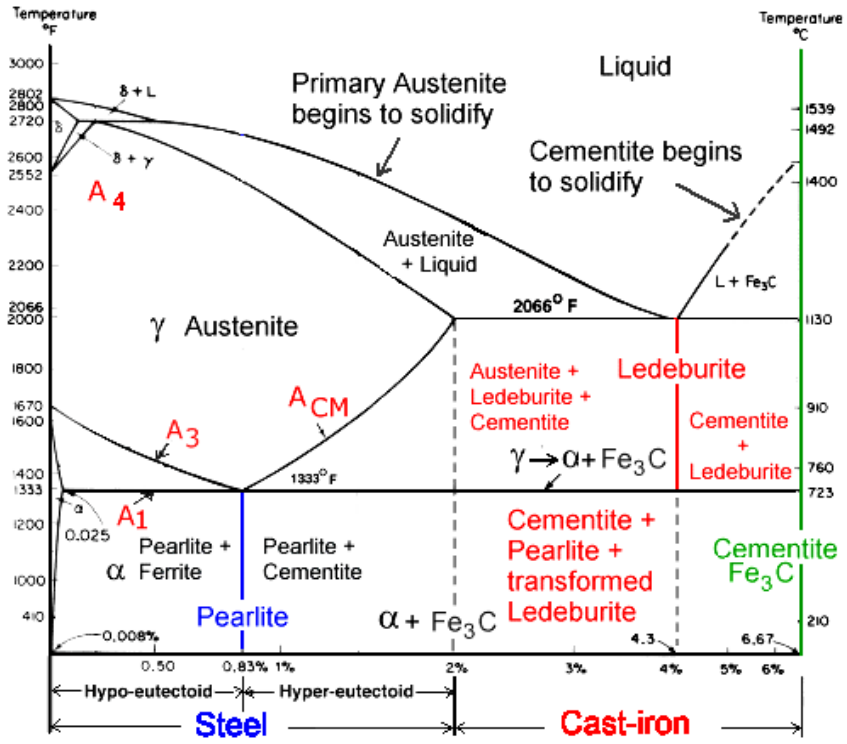


Figure 5.7 Iron-carbon equilibrium diagram(Ho Okamoto 1992)

Furthermore, it should be kept in mind that from previous studies, FeO→Fe→Fe_3C→Fe_3C+C transformation and possible chemical reactions (5.2) may occur in the presence of CH_4 in Fe_2O_3 NPs. Additionally, it has been demonstrated in the previous study that Fe_3O_4+FeO→FeO→Fe→Fe_3C→Fe_3C+C transformations and possible chemical reaction (5.3) can occur in Fe_3O_4 NPs with the presence of CH_4. Therefore, it is demonstrated that CNT formation does occur efficiently at 1000°C for Fe_2O_3 and Fe_3O_4 NPs. Thus, it can be concluded that the relationship between the process temperature and the catalyst type directly affects the production efficiency (Figure 5.8).

$$3Fe_2O_3(s) + 12\ CH_4 \rightarrow 2Fe_3C(s) + C(s) + 9CO + 24H_2 \quad (5.2)$$

$$Fe_3O_4(s) + 6\ CH_4 \rightarrow Fe_3C(s) + C(s) + 4CO + 12H_2 \quad (5.3)$$

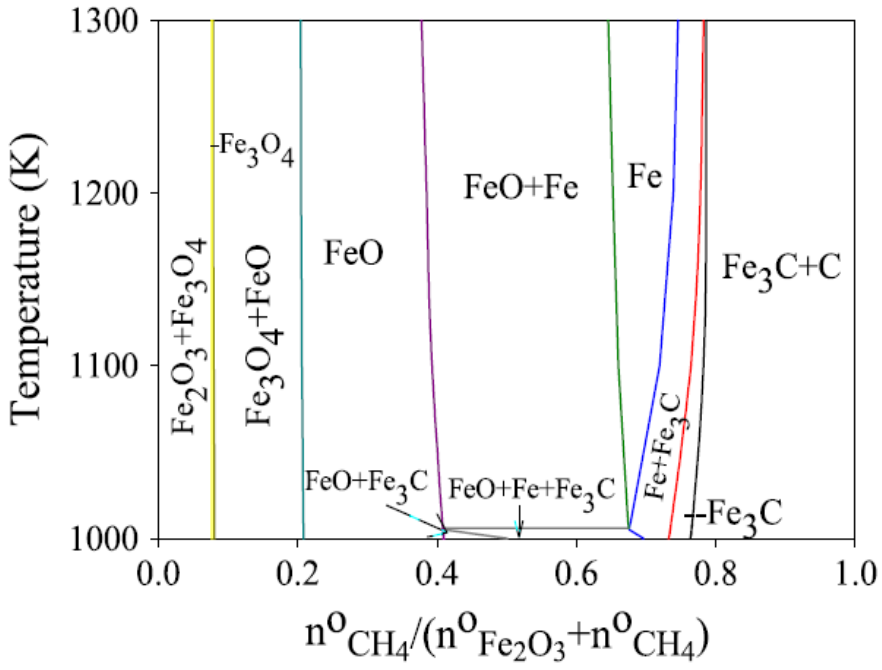


Figure 5.8 Diagram illustrating Fe_2O_3–CH_4 solid stability in equilibrium with the gas phase as a function of temperature and mole fraction of CH_4 (Altay and Eroglu 2013).

On the other hand, in the SEM image of Pt NPs supported Si wafer (Sample 25, Figure 5.9), the tubular structure was observed, as well as clustered and nested particles. However, the average diameter values could not be obtained using the Image J program since these structures are less amount and cannot be regularly obtained on the wafer surface. However, it is necessary to evaluate the role of transition metals in

the CVD method to explain why tubular observation is received in the Pt NPs structure. Typically, active catalysts for CNT growth contain transition metals such as Fe, Co, Ni, Cr, V, Mo, Pt, Y, Mg, Si or their alloys (Audier et al., 1981; Hernadi, Fonseca, Nagy, Bemaerts, et al., 1996; Oberlin, Endo, and Koyama 1976; Rodriguez 1993). These metals can decompose the carbon source or form the corresponding metal carbides such as CH_4, CO, H_2/CO, C_2H_2, C_2H_4 and C_6H_6 with the carbon source. The metal catalyst aggregates to form larger particles as the reaction temperature increases, decreasing hydrocarbon decomposing activity. It has known that to prevent thermal aggregation, a second transition metal such as La can be introduced into the catalyst to form an alloy structure with a higher melting point (Coon et al., 1976; Imamoto, Mita, and Yokoyama 1987; Reilly Jr and Wiswall Jr 1968; Rodriguez 1993; Soga, Imamura, and Ikeda 1976). Therefore, a tubular form was observed in a rare region where Pt NPs did not undergo thermal aggregation.

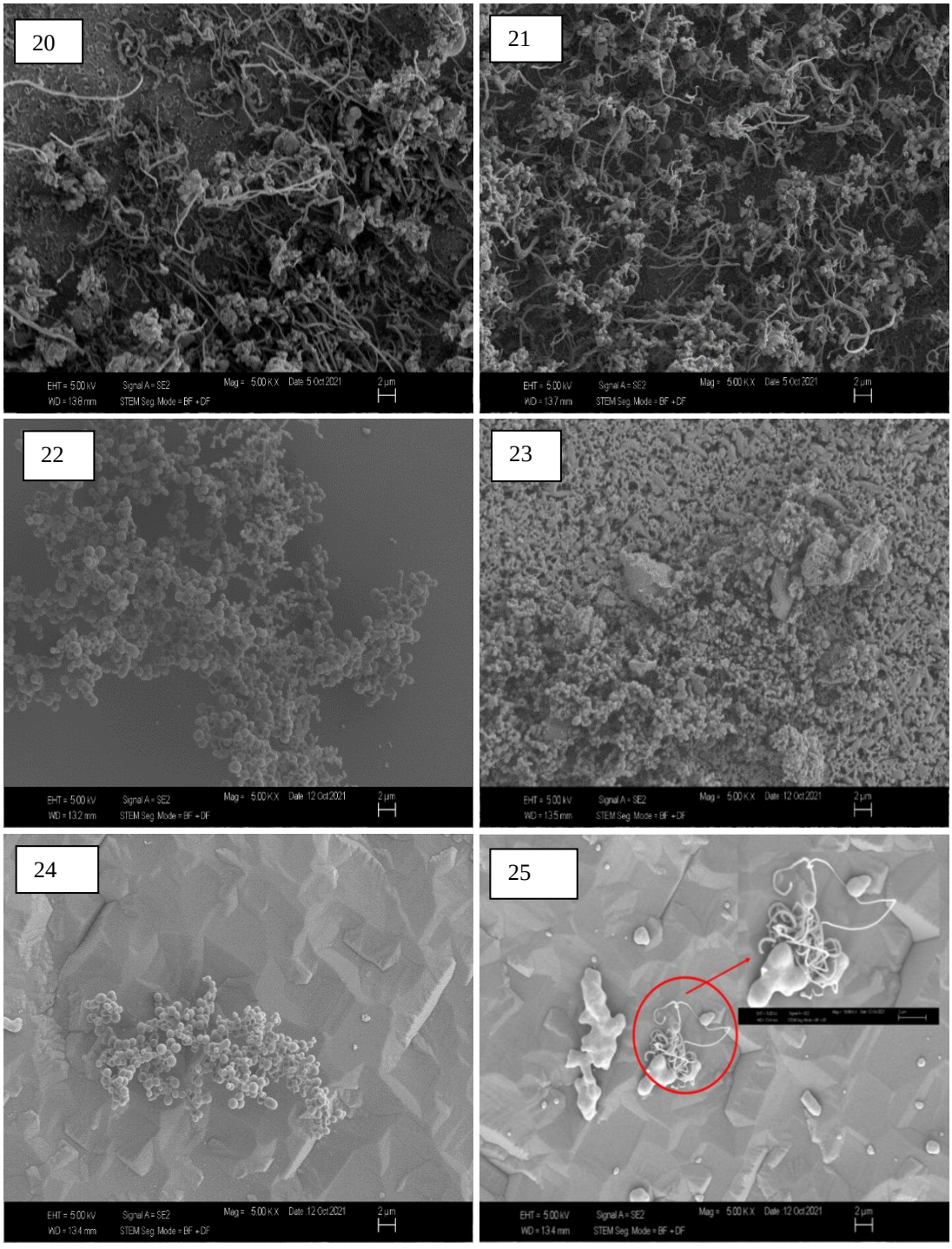


Figure 5.9 SEM images at x5K magnification of samples applied 6 wt.% catalysts and 3 min growth time.

5.2.4 Group 4

Si wafer substrates supported by 4% by weight Fe_2O_3, Fe_3O_4, Nb_2O_5, Au NPs and Pt NPs were named samples 26, 27, 28, 29, 30, and 31, respectively. The samples, exposed to methane gas for 3 minutes at 1000^oC processing temperature, were then cooled to room temperature under the Ar atmosphere. As in Group 3 (Figure 5.9), effective CNT morphology was only obtained when Fe-based catalysts were applied (Figure 5.10).

On the other hand, unlike Group 3, tubular-like structures were also observed in the Au NPs-supported sample 30, albeit a small amount. However, these structures were not in sufficient quantity and level to make measurements. Therefore, no diameter measurements were made. We need to remember the basic of the CVD method because this tubular structure is seen in sample 30 using Au NPs.

CNT formation in Fe-based catalysts is mainly based on the vapour-liquid-solid (VLS) mechanism, which explains the carbon uptake and supersaturation in the catalyst (Gavillet et al., 2001). The VLS growth mechanism is based on the carbon solubility of the catalysts applied in the CVD process. However, it has recently been reported that gold with extremely low carbon solubility can catalyse CNT (Bhaviripudi et al., 2007; Takagi et al., 2006). Unlike the Fe group elements, the carbon solubility of Au is extremely low in the bulk phase (H Okamoto and Massalski 1984).

However, studies have emphasized the importance of Au catalyst size for CNT synthesis. It has been demonstrated that Au NPs with a diameter of 5 nm or less should be applied for CNT production on Au supported Si wafer. It is known that the average radius of Au NPs used in this study is 30 nm and below. Although it is dispersed, it is thought that in most cases, a much higher average value than this radius is obtained due to agglomeration. Therefore, although a tubular form was observed in a small number of non-agglomerated Au clusters, CNT synthesis was not observed in clustered Au NPs on most of the Si wafer surface.

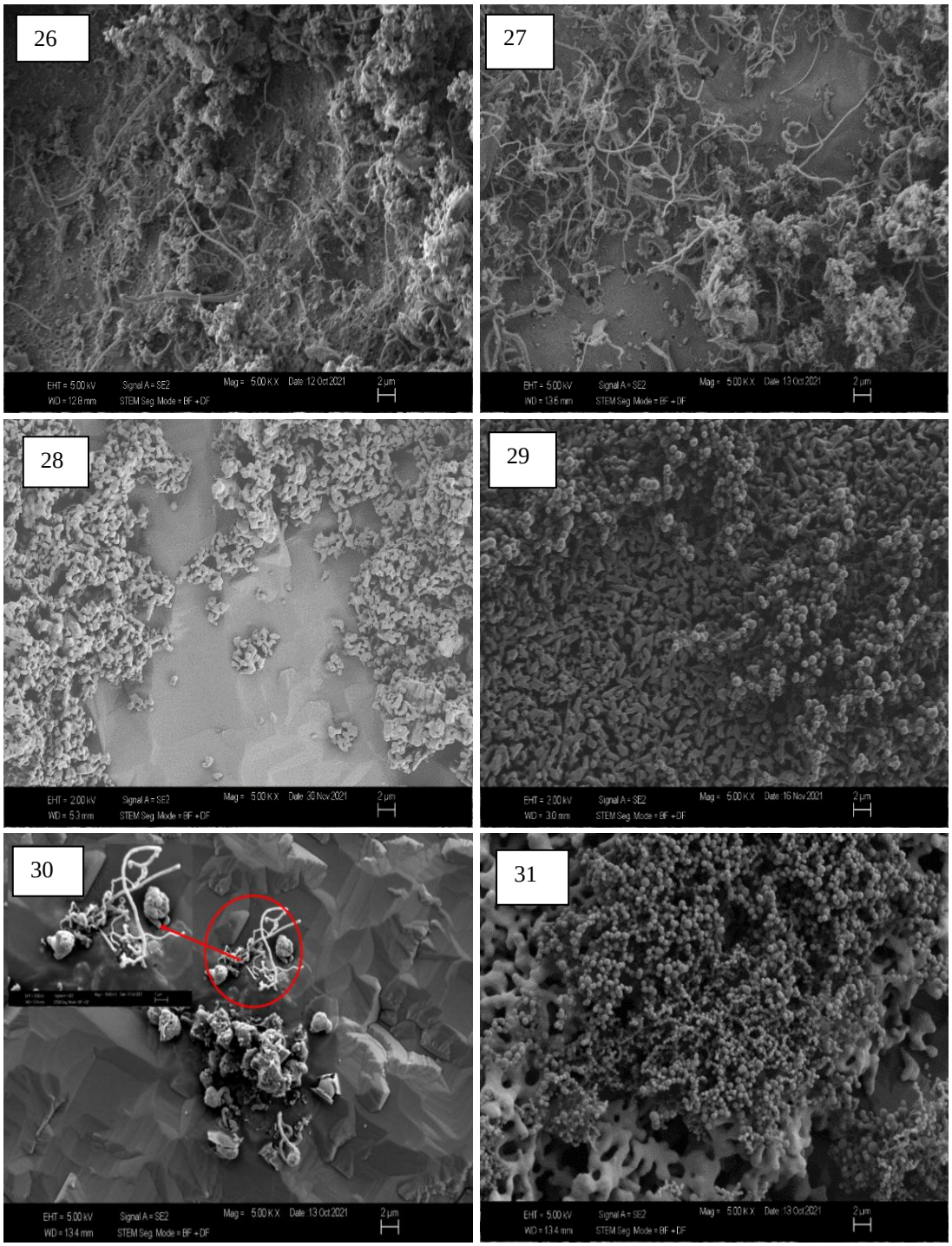


Figure 5.10 SEM images at x5K magnification of samples applied 4 wt.% catalysts and 3 min growth time.

5.2.5 Group 5

Si wafer substrates supported by 2% by weight Fe_2O_3, Fe_3O_4, Nb_2O_5, Au NPs and Pt NPs were named samples 32, 33, 34, 35, 36, and 37, respectively. The samples, exposed to methane gas for 3 minutes at 1000^oC processing temperature, were then cooled to room temperature under the Ar atmosphere.

Similar to Group 3 and Group 4, efficient CNT production was only observed in Si wafer samples (32 and 33) supplemented with Fe-based catalysts. A small amount of tube structure or tubular-like form was not obtained in any other sample (Figure 5.11). The reason is that can be the concentration is used at least amount in this group among 3 minutes growth time groups.

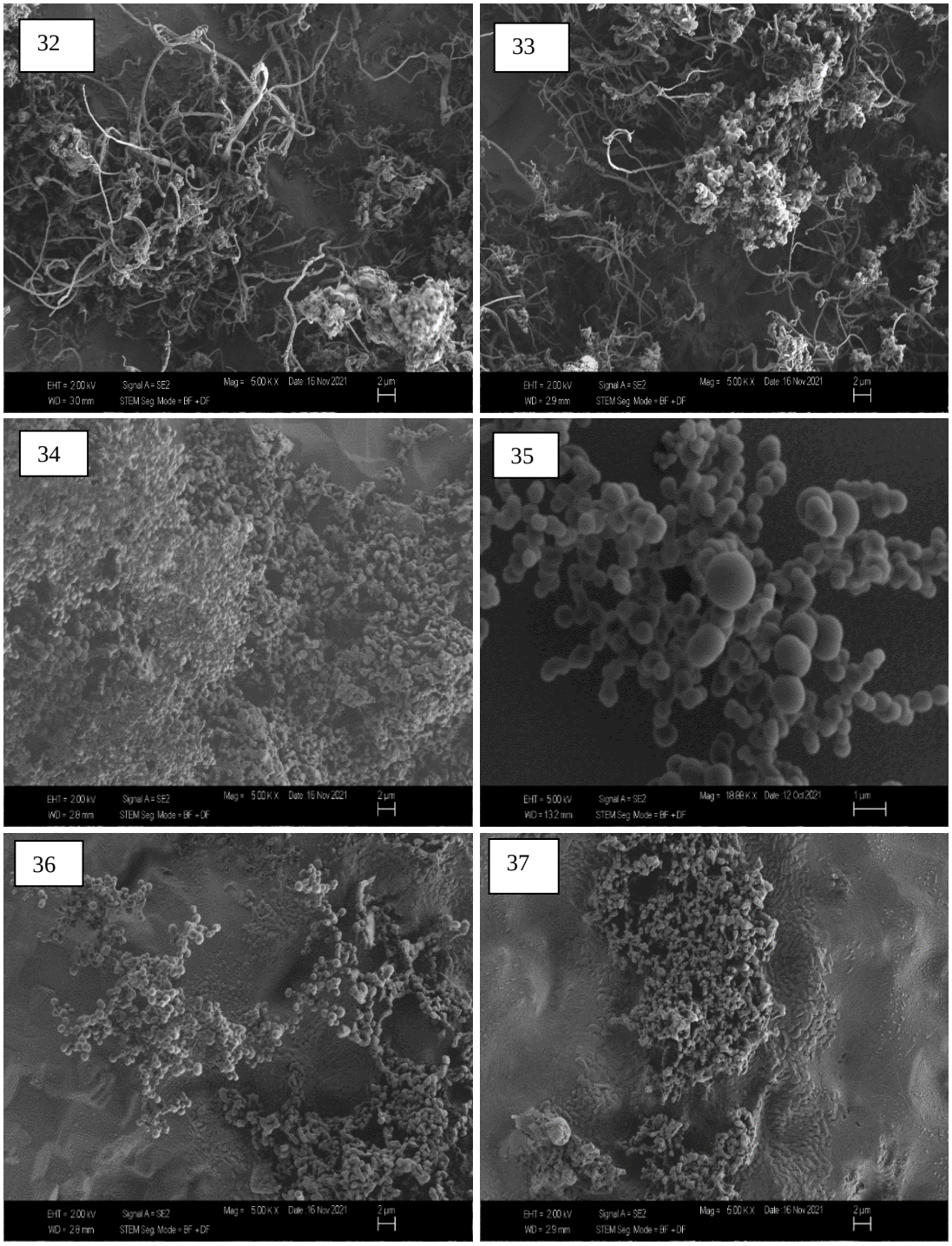


Figure 5.11 SEM images at x5K magnification of samples applied 2 wt.% catalysts and 3 min growth time.

5.2.6 Group 6

Si wafer substrates supported by 6% by weight Fe_2O_3, Fe_3O_4, Nb_2O_5, Au NPs and Pt NPs were named samples 38, 39, 40, 41, 42, and 43, respectively. The samples, exposed to methane gas for 5 minutes at 1000^oC processing temperature, were then cooled to room temperature under the Ar atmosphere. The tubular structure was observed in Fe-based catalyst supported samples 38 and 39, Nb_2O_5 supported sample 40 and Pt NPs based sample 43 (Figure 5.12). On the other hand, it was explained above why the tubular form is obtained in Pt NPs-based samples. However, no Nb_2O_5-based CNT structure has been observed in any of the previous samples. Group 4, unlike the others, is the group in which tubular form is observed in the Nb_2O_5-based catalyst.

The 3d metal Nb-based catalyst with several d-vacancies may establish strong chemical bonds with carbon to produce stable carbides Due to the reducing nature of CH_4, it is believed that $Nb_2O_5 \rightarrow NbO \rightarrow Nb \rightarrow NbC \rightarrow NbC+C$ transformations are feasible, as well as a probable chemical reaction (3). Figure 5.12 depicts the agglomeration of Nb_2O_5 particles and the formation of tiny tube-shaped structures on the catalyst particles (Sample 40). The studies mentioned above that contained lower concentration, temperatures, and CH_4 exposure times could not obtain CNT structure in any way. However, in this part of the study, we clearly see it for the first time because of higher temperatures and longer growth time.

5.2.7 Group 7

The samples 44, 45, 46, 47, 48, and 49 correspond to Si wafer substrates supported by 4% by weight of Fe_2O_3, Fe_3O_4, Nb_2O_5, Au NPs, and Pt NPs. After being exposed to methane gas for five minutes at a processing temperature of 1000^oC, the samples were cooled to ambient temperature in an Ar environment. Except for samples assisted by Fe-based catalysts, no CNTs or tubular-like structures were found in any of the samples (Figure 5.13, Sample 44 and 45). Although the drop in concentration did not significantly alter the diameter structure of the tube.

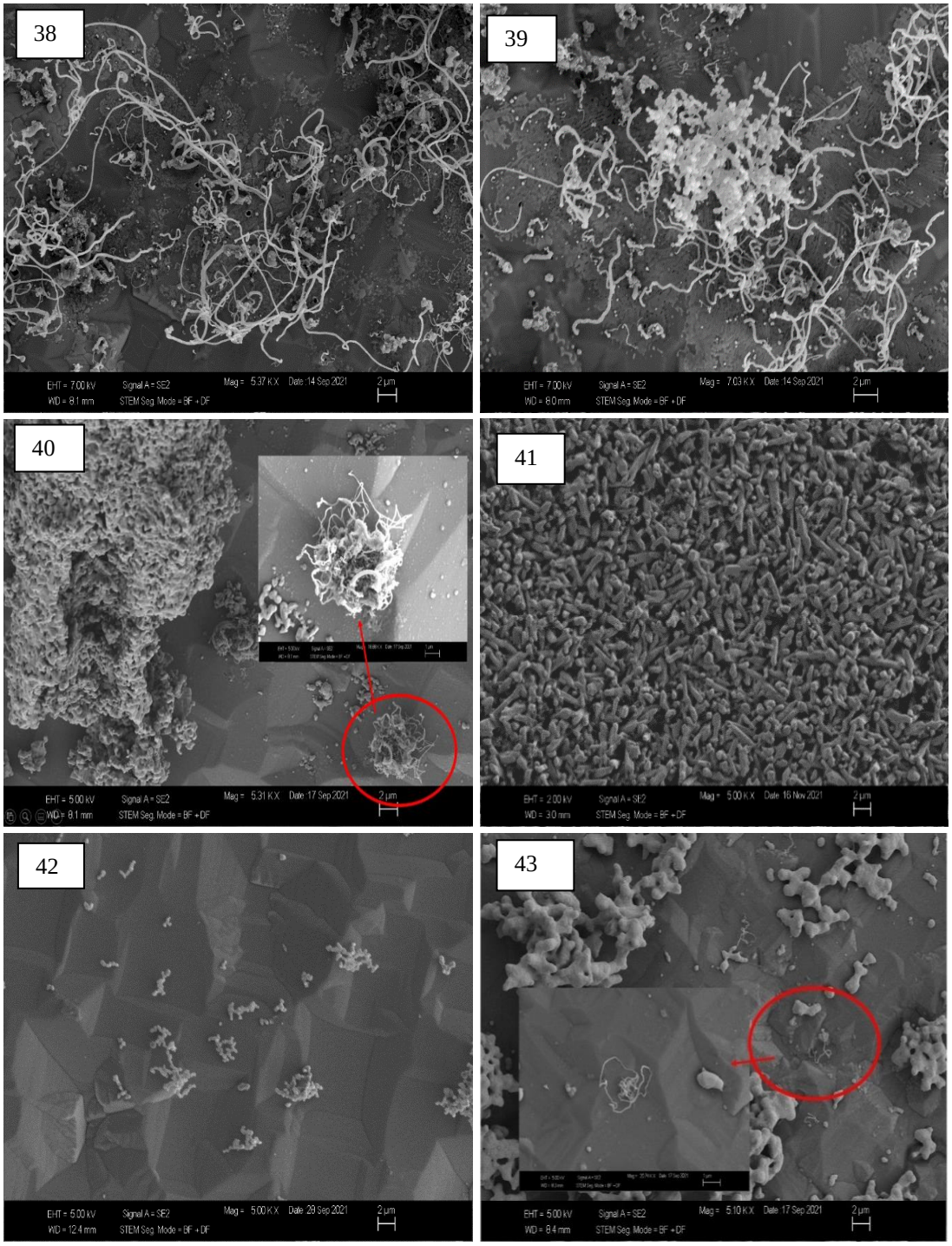


Figure 5.12 SEM images at x5K magnification of samples applied 6 wt.% catalysts and 5 min growth time.

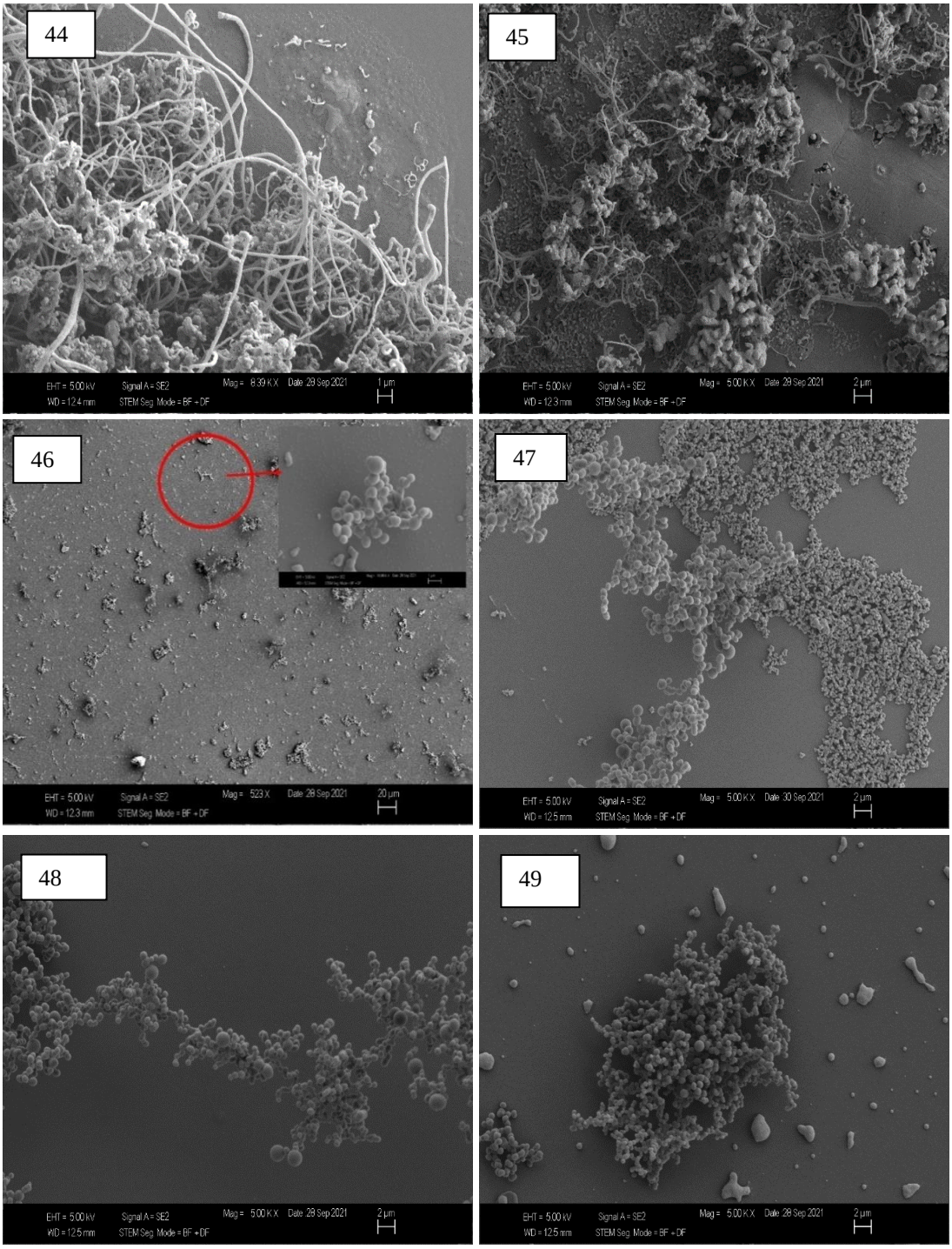


Figure 5.13 SEM images at x5K magnification of samples applied 4 wt.% catalysts and 5 min growth time.

5.2.8 Group 8

The samples 50, 51, 52, 53, 54, and 55 correspond to Si wafer substrates supported by 2% by weight of Fe_2O_3, Fe_3O_4, Nb_2O_5, Au NPs, and Pt NPs. After being exposed

to methane gas for five minutes at a processing temperature of one thousand degrees Celsius, the samples were cooled to ambient temperature in an Ar environment. Similar to Group 7, CNT observation was seen exclusively in samples supported by Fe-based catalysts (Figure 5.14). It is believed that low catalyst concentration results in the maximum yield and smallest mean radius among five-minute samples.

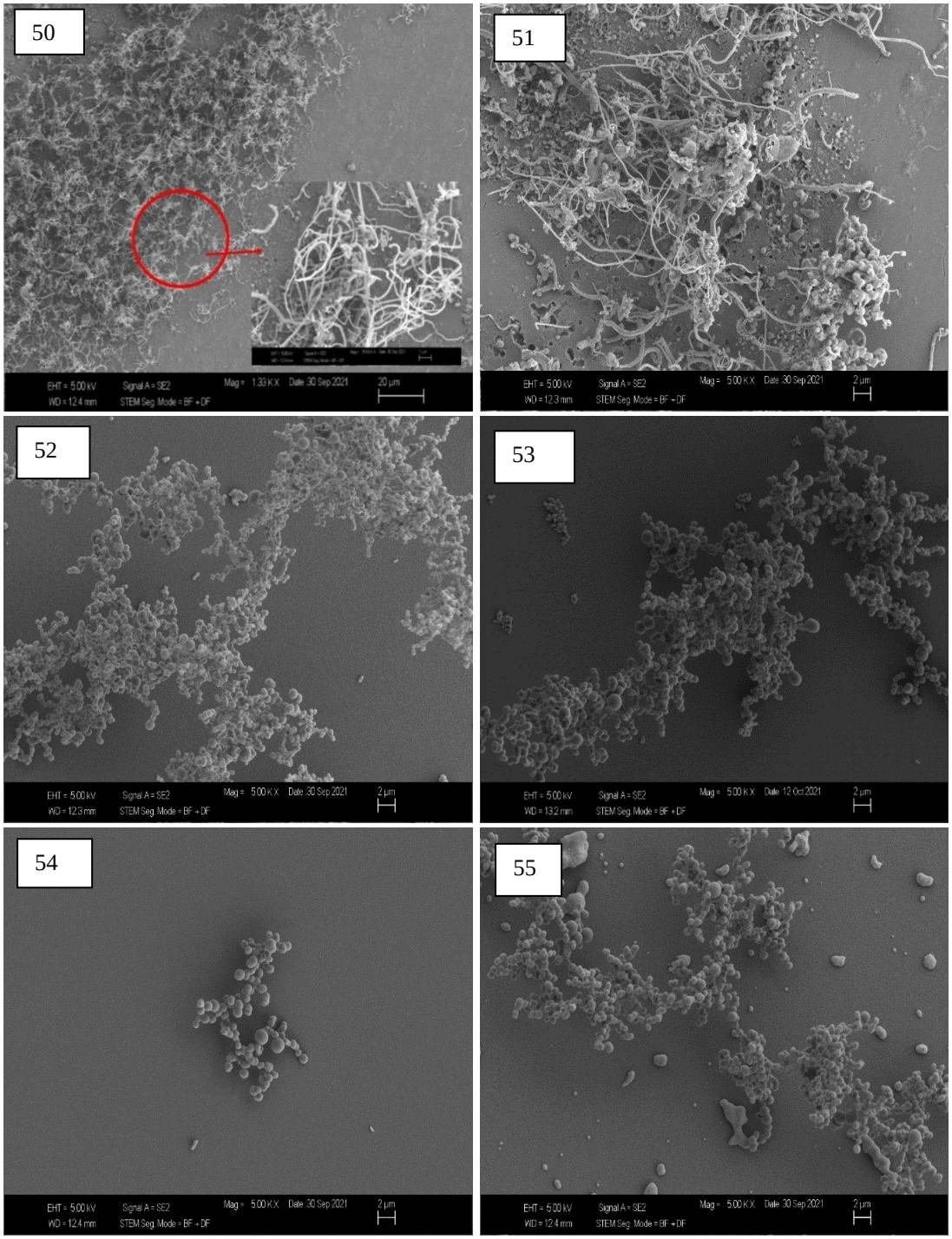


Figure 5.14 SEM images at x5K magnification of samples applied 2 wt.% catalysts and 5 min growth time.

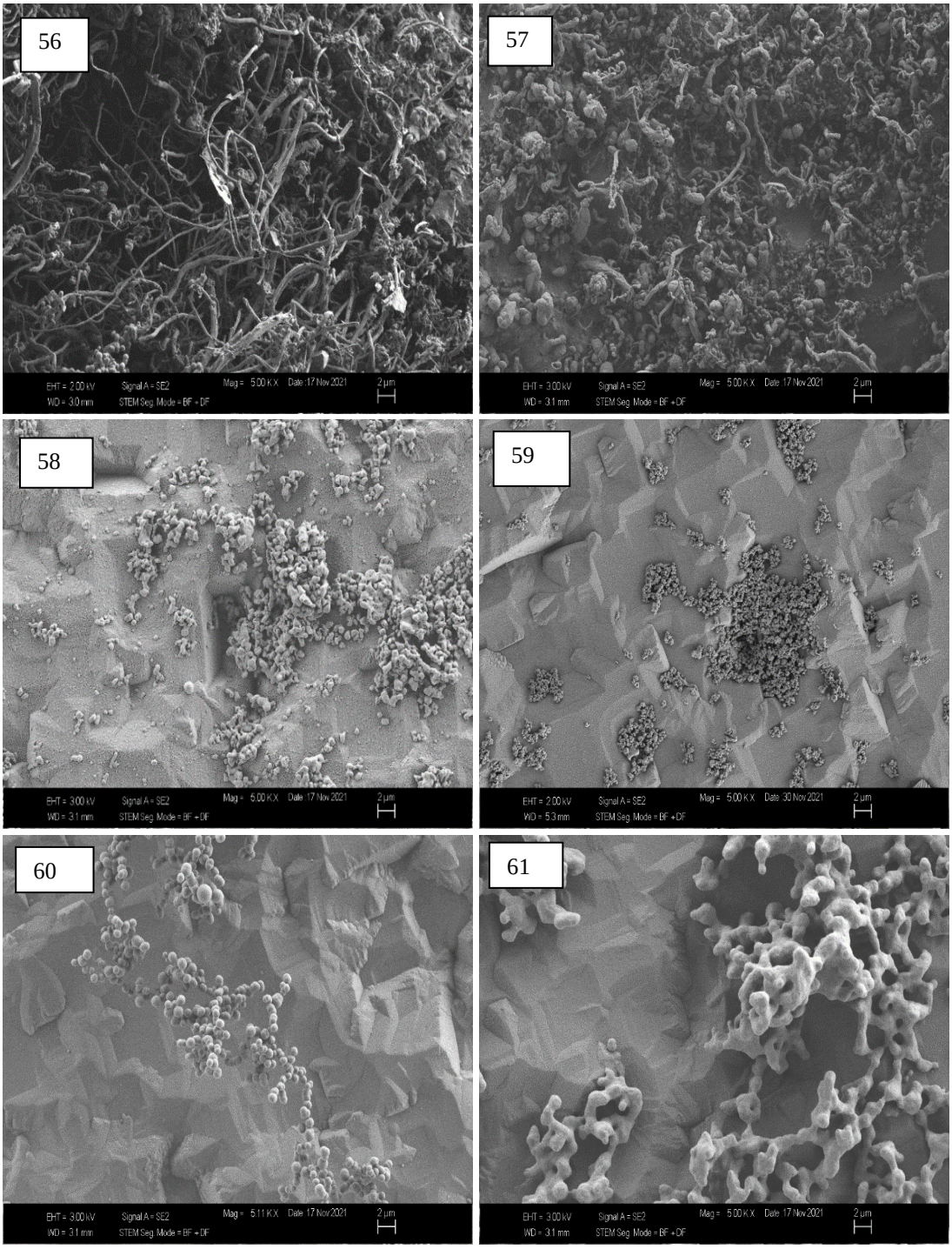


Figure 5.15 SEM images at x5K magnification of samples applied 6 wt.% catalysts and 7 min growth time.

5.2.9 Group 9

Si wafer substrates supported by 6% by weight Fe_2O_3, Fe_3O_4, Nb_2O_5, Au NPs and Pt NPs were named samples 56, 57, 58, 59, 60, and 61, respectively. The samples,

exposed to methane gas for 7 minutes at 1000^{o}C processing temperature, were then cooled to room temperature under the Ar atmosphere. As in all previous samples, the tubular form was obtained in Fe-based catalyst supported samples (No 56 and 57) in this group. However, a thick layer of carbon in the form of coating was observed in the other four samples exposed to the hydrocarbon gas precursor for more extended periods (Figure 5.15).

5.2.10 Group 10

Si wafer substrates supported by 4% by weight Fe_2O_3, Fe_3O_4, Nb_2O_5, Au NPs and Pt NPs were named samples 62, 63, 64, 65, 66, and 67, respectively. The samples, exposed to methane gas for 7 minutes at 1000^{o}C processing temperature, were then cooled to room temperature under the Ar atmosphere. Like Group 9, the tubular structure was obtained in Fe-based catalyst supported samples (62 and 63). Additionally, similar to Group 9, a carbon layer in the form of a coating was observed for samples 65, 66 and 67 depending on the 7 min growth time (Figure 5.16). Furthermore, as mentioned above, a tubular-like structure was obtained, possibly due to exposure to more hydrocarbon gas precursors than the Nb_2O_5 supported sample 64.

5.2.11 Group 11

Si wafer substrates supported by 2% by weight Fe_2O_3, Fe_3O_4, Nb_2O_5, Au NPs and Pt NPs were named samples 68, 69, 70, 71, 72, and 73, respectively. The samples, exposed to methane gas for 7 minutes at 1000^{o}C processing temperature, were then cooled to room temperature under the Ar atmosphere. Tubular structure was observed in samples 68 and 69 where only Fe-based catalysts were used (Figure 5.17).

As in the other seven-minute samples, samples 70, 71, 72 and 73 were obtained, in which the carbon looked like a layered film (Figure 5.17). In addition, the previously mentioned thermal aggregation was observed in samples 70, 71 and 73. In the Au NPs supported sample 72, it was thought that the gold was removed from the substrate (due to the scavenging gases in the furnace system); therefore, it was subjected to physical aggregation (Figure 5.17).

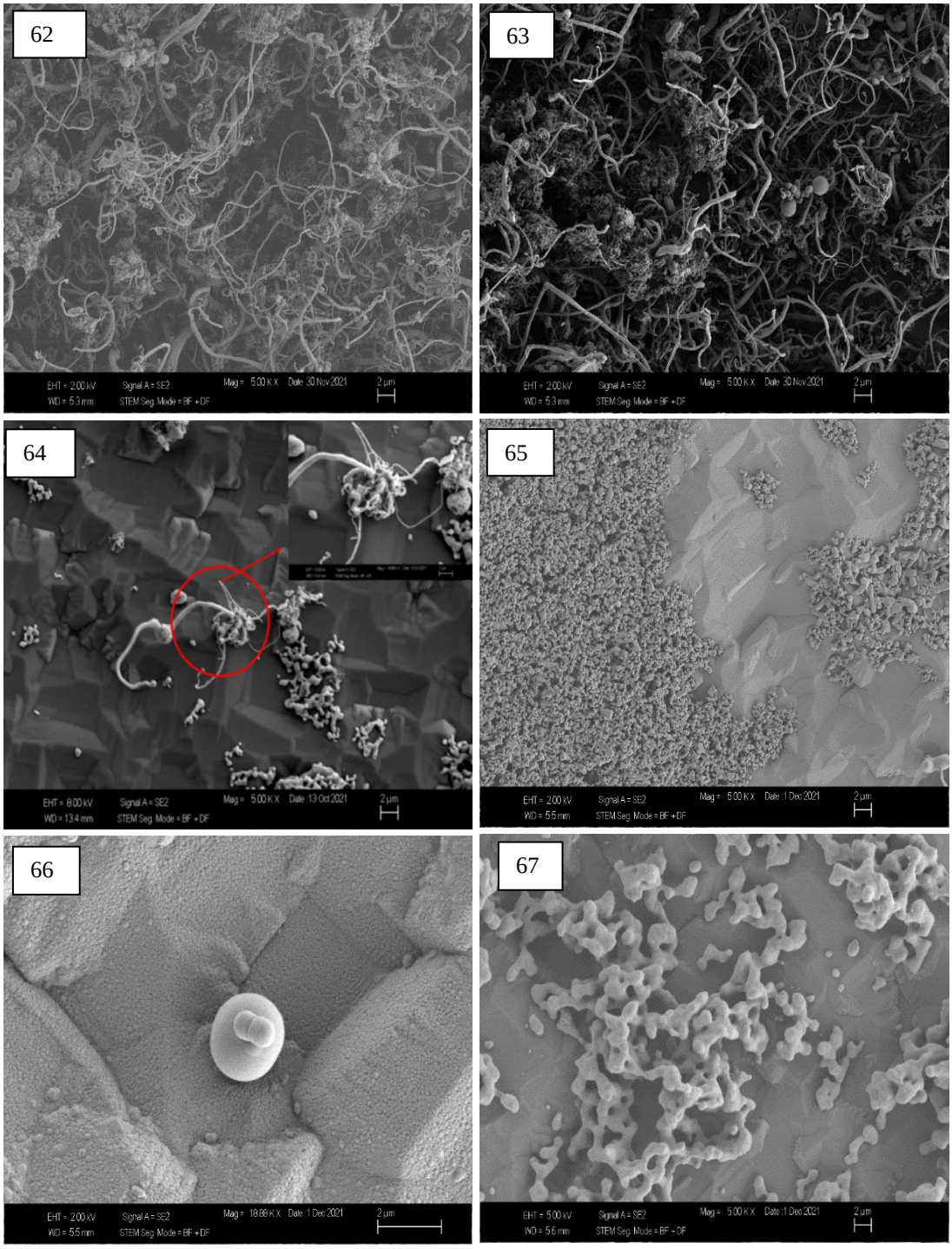


Figure 5.16 SEM images at x5K magnification of samples applied 4 wt.% catalysts and 7 min growth time.

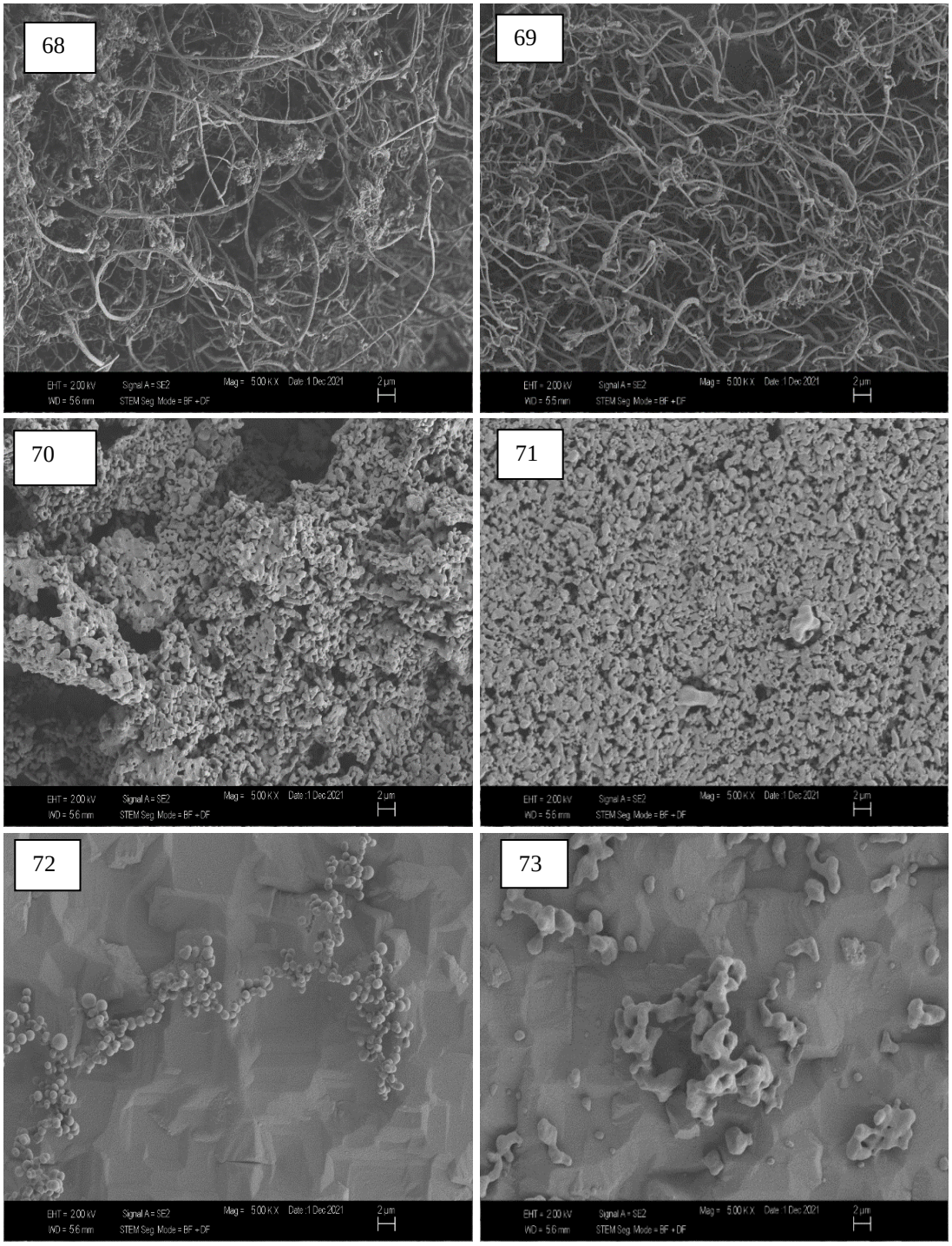


Figure 5.17 SEM images at x5K magnification of samples applied 2 wt.% catalysts and 7 min growth time.

5.3 CNT Formation by Catalysts Type

In the CVD method, many parameters affect the growth of CNTs. The catalyst type is one of the most critical parameters affecting CNT growth. Many articles in the

literature point out that catalysts are essential materials for the well-defined shapes and structures of CNTs. The catalyst material has been considered as one of the indispensable parameters influencing the growth and kinetics of CNT, as it is the substrate responsible for either single-walled CNT (SWCNT) or multi-walled CNT (MWCNT) structures or is responsible for end-growth or base-growth mechanisms. The tip growth or base growth mechanisms are essential mechanisms in determining the final morphology of CNTs. These growth mechanisms play an active role in controlling chirality and thus in determining the final physical, morphological and chemical features of CNTs. The most critical approach for both growth techniques is the interactions between the catalyst material and the substrate. For this reason, optimization studies were started to determine the substrate first. In the first part of the morphological characterization of the study, the outputs from the two groups provided a framework for the substrate and the processing temperature. Therefore, in the next study (Group 3-11 range), Si wafer was used as a substrate for all samples, and the processing temperature was used as 1000^{o}C.

In Group 3-11 range, Fe_2O_3, Fe_3O_4, Nb_2O_5, TiO_2, Au NPs, and Pt NPs were applied as 6, 4% and 2% by weight on Si wafer at 1000^{o}C operating temperature due to the interactions between the catalyst and the substrate and the temperature factor. Additionally, 3, 5 and 7 minutes of hydrocarbon gas precursor CH_4 were used because of the critical role of growth time on tubular structure and final morphology. However, it has been claimed that the tubular form was efficiently observed only in Fe-based samples. The reason for this is the vapor-liquid-solid (VLS) growth mechanism attributed to temperature dependent carbon solubility. Nevertheless, the mechanism of limited carbon solubility with Fe-based catalyst with few d-vacancies is not applicable for 3d metal Nb-based catalyst with many d-vacancies. Strong chemical bonds can be formed with carbon to obtain Nb-based catalyst stable carbides.

In the Group 6 and 10, the tubular structure was observed albeit slightly, except agglomeration and thermal aggregations, in two samples (samples 40 and 64) containing 6 and 4 wt.% Nb_2O_5 catalyst with a growth time of 5 and 7 min, respectively. However, this observation was considered inefficient because the tubular structure could not be obtained in the amount that could be measured, and it was found in very small amounts in the samples in the SEM analysis.

The interaction of catalysts on the substrate surface and the effect of processing temperature on the carbon solubility of catalysts are mentioned above. The main purpose of this thesis is to provide CNTs synthesis by obtaining solid carbon solutions at high temperatures for transition metals such as Fe, which is known to have low carbon solubility. Therefore, Fe can dissolve carbon only in specific temperature ranges, as they have few d-voids. However, for Ti and Nb, which have many d-voids, this cannot be attributed to temperature alone. This is because Nb and Ti tend to form high carbide ratios with many d-voids. However, no tubular structure was obtained in any TiO_2-based sample in all groups. It has been believed that the main reason for this is thermal aggregation. SEM images of nearly all TiO_2-based samples show clusters of interlocking, seemingly adherent particles.

The VLS (vapor-liquid-solid) growth mechanism is based on the carbon solubility of the catalysts applied in the CVD process. Gold's very poor solubility in carbon has recently been studied to see whether it might serve as a catalyst for CNT. In contrast to the elements of the Fe group, the bulk phase carbon solubility of gold is very low. On an Au-supported Si wafer, it has been established that Au particles with a diameter of 5 nm or less should be used for CNT manufacturing. Due to their propensity to aggregate in some places, it is believed that the Au NPs used in this work cannot properly create CNT. Nonetheless, a negligible quantity of CNT was seen in sample 30 subjected to 3 min of growing period containing 4% Au concentration.

Typically, essential catalysts for CNT growth are transition metals such as Fe, Co, Ni, Cr, V, Mo, Pt, Y, Mg, Si or their alloys. These metals can degrade the carbon source or often form metal carbides. The metal catalyst aggregates to form larger particles as the reaction temperature increases, reducing the hydrocarbon separation activity. Due to this thermal aggregation, interlocking coarse grains were clearly observed in the SEM images in the vast majority of Pt NPs catalyst supported samples. However, in the rare cases that could escape aggregation, a small amount of tubular structure was also obtained. For instance, both intertwined coarse catalyst grains and CNT structure were observed in samples 25 and 43 containing 6 wt.% Pt catalyst and exposed to growth times of 3 minutes and 5 minutes, respectively.

All subsequent investigations will examine the characteristics of CNTs grown at 1000^{o}C for three different growth times and three different catalyst concentrations on Si wafer surfaces supported by Fe2O3 and Fe2O4- catalysts, where the tubular shape is effectively attained.

5.4 CNT Morphology by Catalysts Concentration and Growth Time

Table 5.1 displays the mean radii of the samples from Group 3-11, which 3, 5 and 7 minutes of hydrocarbon gas precursor CH_4 were used because of the critical role of growth time on tubular structure and final morphology. In generally, while there was a systematic decrease in mean tube diameter due to a decrease in catalyst concentration in samples treated for 3 and 7 minutes, there was no significant difference in tube diameter in samples treated for 5 minutes. However, as the catalyst concentration was reduced, the yield and density of CNTs synthesized on the substrate surface increased; this could be due to the distribution of the catalyst on the substrate surface when a small amount is used, which creates more space for the CNTs to grow. Additionally, longer growth times and higher catalyst concentrations resulted in a broader size distribution. The smallest size range is obtained in 4 wt percent at a growth time of 5 minutes with the concentration, which can be considered the average value among all samples. Except for a 3-minute growth time, all Fe_3O_4-based samples had a larger mean diameter than Fe_2O_3 (see Table 5.1). This can be attributed to the difference in reduction reactions in the presence of methane. The effect of catalyst particle size, on the other hand, was observed in all samples exposed to the other 5- and 7-min growth times. While the particle size for Fe_2O_3 is 50 nm or less, the particle size for Fe_3O_4 is 50 to 100 nm. As a result, it was assumed that all Fe_3O_4 samples except the 3 min samples had a higher mean radius.

Furthermore, it is worth noting that a significant increase in diameter thickness is also obtained depending on the increase in growth time. So much so that most of the 7-minute samples were measured in thickness, reaching diameters of about 400 nm. The concentration increase did not significantly differ in the size distribution for all growth times. Also, the CNT yield decreased with increasing concentration for all growth times. The best results among Fe-based catalysts were obtained in sample 50, which contains 2 wt.% Fe_2O_3 catalyst and is exposed to 5 min. growth time, with the

highest efficiency of 84.8% and the lowest mean radius of 88 ± 31 nm, size distribution 37-164 nm.

Table 5.1 Morphological features of CNTs

Sample No	Mean radius (nm)	Size distribution (nm)	CNT density (%)	CNT yield (w %)
20	152 ± 32	55 - 246	61.3	51.1
21	127 ± 40	50 - 232	70.1	49.8
26	154 ± 40	69 - 249	79.5	61.0
27	138 ± 40	46 - 226	87.5	57.6
32	133 ± 33	57 - 203	74.7	78.4
33	126 ± 39	57 - 230	70.0	79.8
38	103 ± 52	38 - 177	73.1	52.4
39	122 ± 38	26 - 195	71.9	66.3
44	107 ± 37	35 - 174	86.2	70.6
45	125 ± 42	48 - 217	91.2	73.2
50	88 ± 31	37 - 164	91.0	84.8
51	121 ± 36	61 - 218	94.8	82.4
56	211 ± 97	52 - 479	77.9	53.8
57	249 ±107	80 - 588	86.2	55.5
62	137 ± 58	41-393	69.7	59.2
63	172 ± 75	70 - 381	78.9	63.6
68	134 ± 63	38 - 285	74.5	77.2
69	157 ± 50	66 - 307	82.3	84.0

5.5 Energy Dispersive X-Ray Analysis (EDX)

As a result of SEM examination, EDX investigation was conducted on samples acquired with a growth duration of 5 minutes, which were believed to have the most efficient tubular shape. After CVD treatment, EDX analysis demonstrated the presence of oxygen, iron, carbon, and silicon in Fe-based catalysts on the surface of Si wafers (Table 5.2). SiO_2 is responsible for the O concentration in all five-minute samples. The high carbon content is attributed to the formation of carbon deposits such as amorphous carbon, SiC or CNTs. Moreover, the Fe content in all 5-min samples is due to the presence of Fe_2O_3 and Fe_3O_4 catalysts.

Table 5.2 Chemical composition of the investigated samples

Sample No	Mass (%)			
	C	Si	Fe	O
38	55.10	6.38	30.44	8.09
39	42.62	15.48	29.97	11.93
44	77.88	7.44	9.69	4.99
45	60.26	9.22	20.92	9.61
50	80.49	8.10	8.69	2.73
51	87.49	2.36	5.00	5.14

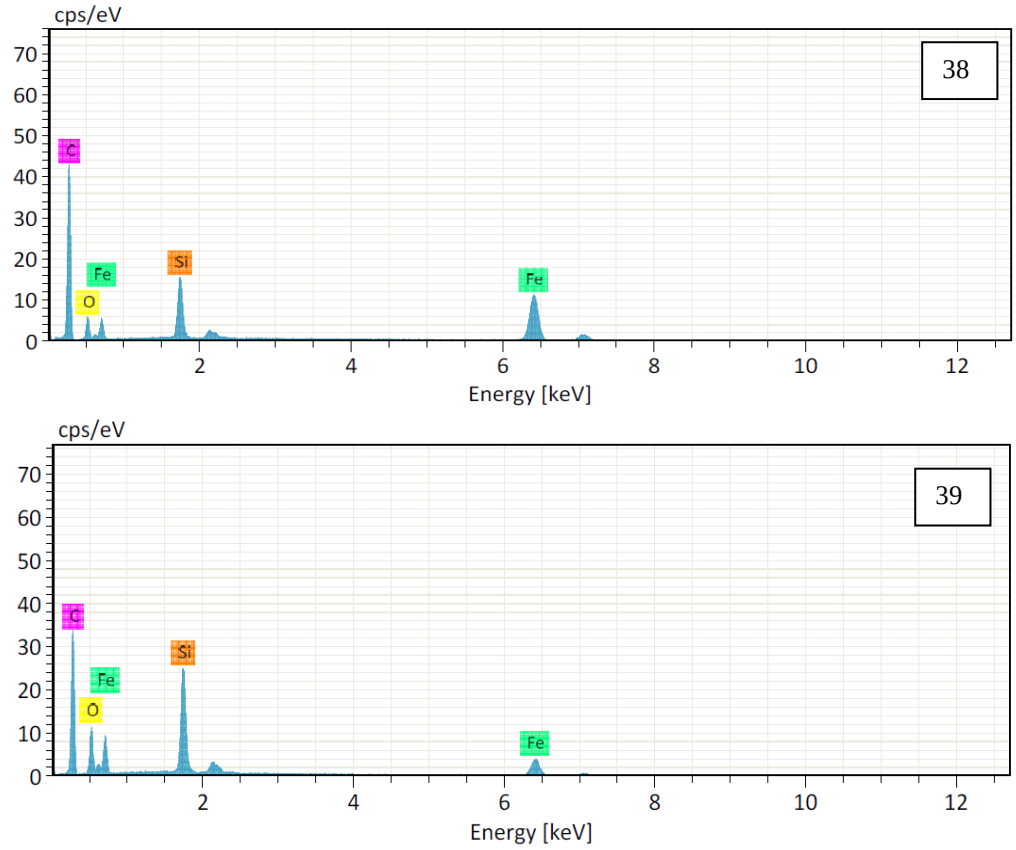


Figure 5.18 EDX spectrum of Samples 38 and 39

Figure 5.18 displays EDX results that was taken of samples that had a catalyst concentration that was equal to 6wt.%. There was not a significant variation in the percentages of Fe and O amongst the samples, despite the fact that different catalysts were used for each one. Nevertheless, compared to the other samples, the proportion of carbon is the lowest. In the case of samples 38 and 39, where the concentration of the catalyst was the greatest, this did not come as a surprise. Because there is a correlation between the proportion of catalysts present and their propensity to create agglomeration. Because of this, as can be seen in the SEM samples (see Figure 5.12), there is a growing propensity to construct forests with carbon nanotubes. Additionally, these samples have the greatest Fe % overall (Table 5.2). According to the findings of the EDX study, the hypothesis that a high catalyst concentration might lower carbon nanotube efficiency is correct.

Furthermore, the decrease in catalyst concentration was shown to be the cause of the increase in carbon percentage seen in samples (44 and 45) that included a catalyst concentration of 4%. When compared to the samples containing 6 wt.% Fe-based catalyst, the lower iron level in the samples containing 4 wt.% Fe-based catalyst probably produced greater room on the surface of the silicon wafer for the creation of CNTs (Figure 5.19). The regular drop in the concentration of catalyst was corroborated by the systematic decrease in the amount of iron present, as well as the systematic rise in the amount of carbon present (Table 5.2). A further discovery made by EDX that confirmed this approach was seen in samples 50 and 51 that included a catalyst concentration of 2% (Figure 5.20).

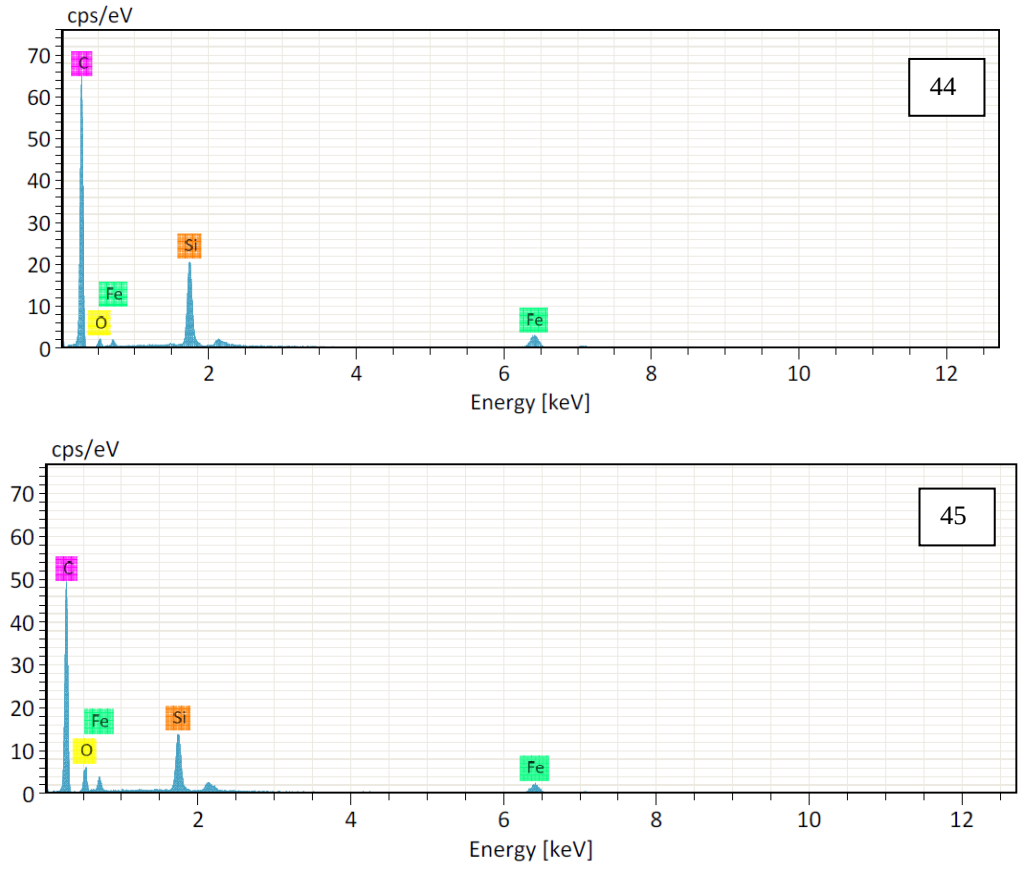


Figure 5.19 EDX spectrum of Samples 44 and 45

According to the data that were obtained from the SEM characterization (Table 5.1), the samples that included the highest efficiency CNTs% were the ones that had both the highest percentage of carbon and the lowest concentration of catalyst, which was 2%. The findings of the EDX analysis (Figure 5.20) revealed that Sample 50,

with the smallest nanotube diameter with 88 ± 31 nm, had the highest carbon concentration at 80.49% (Table 5.2).

As a consequence of EDX investigation, a conclusion was drawn to the effect that a drop in the concentration of the catalyst results in an increase in the percentage and content of carbon.

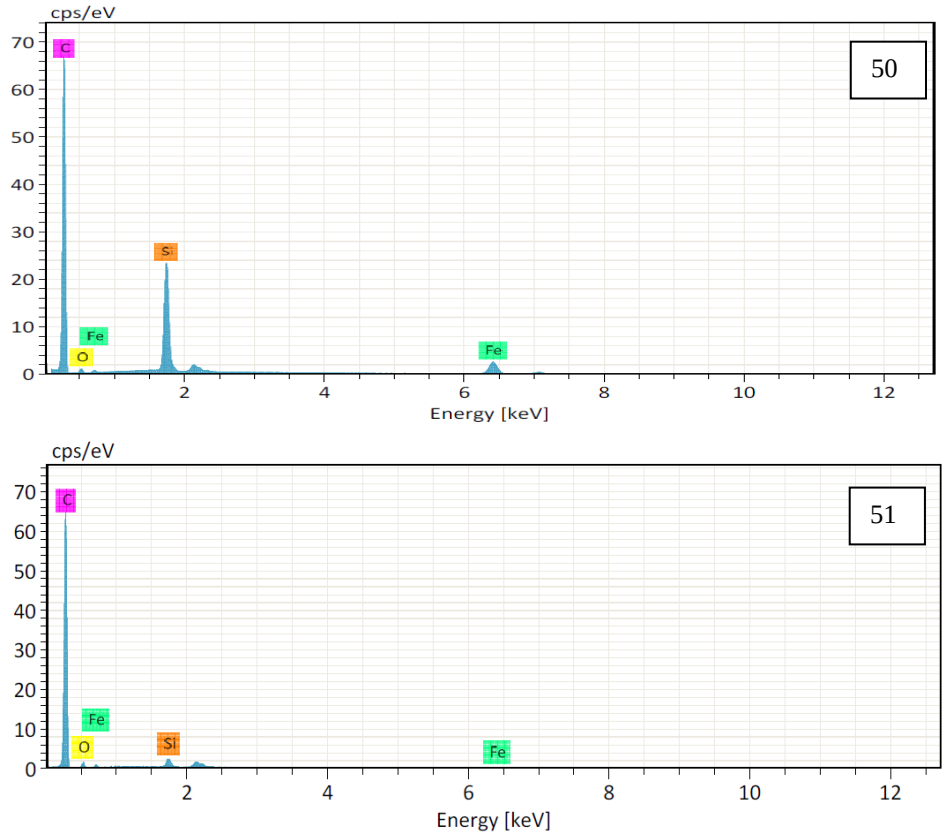


Figure 5.20 EDX spectrum of Samples 50 and 51

5.6 Fourier Transform Infrared Spectroscopy (FTIR)

The Fourier Transform Infrared Spectrophotometer, FTIR, spectra of all Fe_2O_3 and Fe_3O_4 based samples are shown in Figures 5.21, 5.22, and 5.23. There are four major peaks in all FT-IR spectrum, located around at 2470, 1720, 1560, 1150 and 870 cm^{-1}.

At 1000°C processing temperature, Si wafer substrates supported by 6, 4, and 2 wt.% Fe_2O_3 and Fe_3O_4 NPs were exposed to methane gas for 3 minutes, as shown in Figure 5.21. For Fe_2O_3-based samples 20, 26, 32, the peak at 2470 cm^{-1} can be

associated with the -OH stretch from strongly hydrogen-bonded -COOH (Moosa, Ridha, and Abdullha 2015). When a Fe_3O_4 catalyst was used, however, this peak shifted to 2483 cm^{-1}. Furthermore, -OH groups were observed in samples 20, 26, and 32 in the range of 3500-4000 cm^{-1}, most likely due to impurities, but were ignored because they focused on major peaks. The peak in 1720 cm^{-1} can be seen to be associated with -C=O stretching of the carboxyl group. In samples 20, 26, and 32, the peak at 1560 cm^{-1} is related to the carboxylate anion stretch model (Davis et al., 1999). Whereas in samples 21, 27, and 33, these peaks shifted to 1682 cm^{-1} and 1579 cm^{-1}, respectively. The dominant band at 1153 cm^{-1} is caused by the asymmetric stretching vibration of the Si-O-Si bond from substrate (Obaidullah et al., 2019).

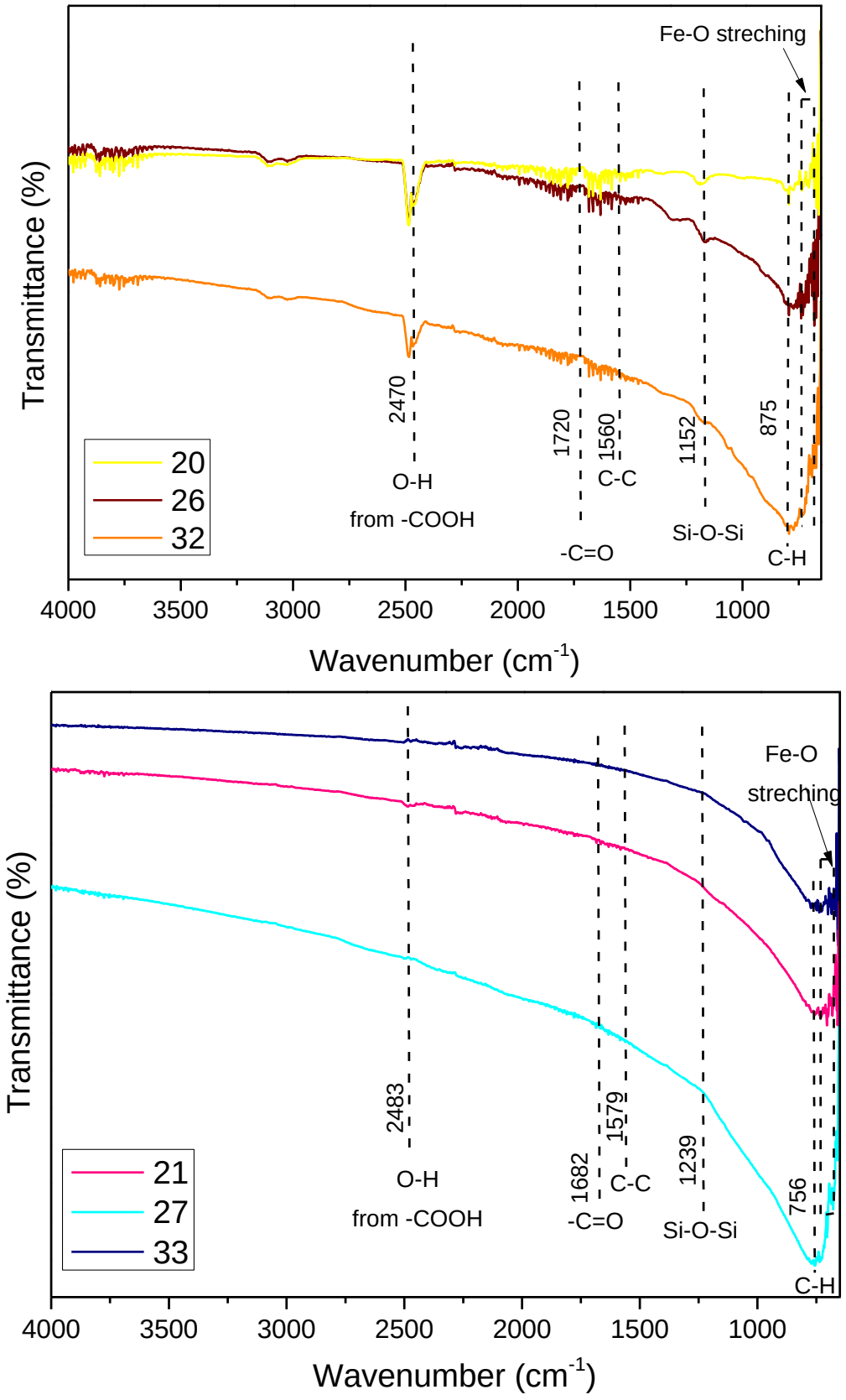


Figure 5.21 FT-IR spectra of the 3-minute samples

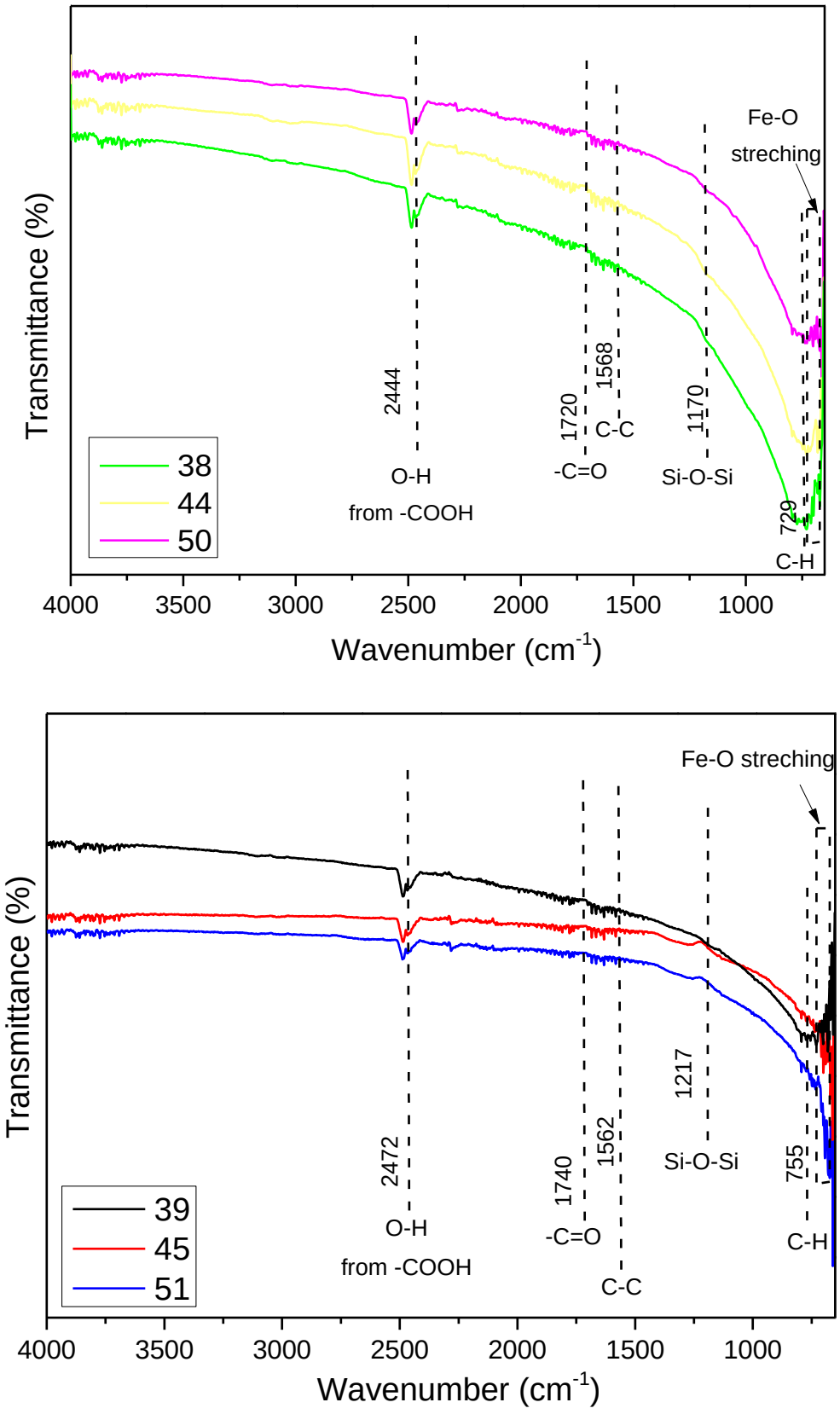


Figure 5.22 FT-IR spectra of the 5-minute samples

Figures 5.22 and 5.23 show the FT-IR spectra of the 5- and 7-minute samples. Like 3-minute samples, major peaks are indicated on the graphs. The peak at 729-800 cm^{-1} is caused by C-H stretching vibration, while the strong band below 700 cm^{-1} is caused by Fe-O stretching vibration. At 555 cm^{-1}, the sample's characteristic absorption bands are assigned to iron(II) oxide stretching and can be assigned to the bending vibration mode of Fe_2O_3-based samples (Sobhanardakani et al., 2018). The observed band at 1150-1250 cm^{-1} for the synthesized samples In Figures. 5.22 and 5.23 is related to Si-O-Si antisymmetric stretching vibrations, indicating the presence of silicon dioxide substrate in the sample. Additionally, in Figures 5.22 and 5.23, the stretching vibration of Fe-O at around 579 cm^{-1} is observed in FT-IR spectra of Fe_3O_4-based samples (Z. Chen et al., 2019).

Pristine CNTs only have a limited number of IR active modes, the exact number of which is determined on the symmetry shape and kind of CNT. The diameter of the nanotubes has an effect on the wavenumbers that are produced by the FTIR spectra of CNTs (Barrios et al., 2012; Mitróová et al., 2010). Van der Waals attraction is responsible for the considerable agglomeration that CNTs create. As was discussed in the preceding sections, CNTs are materials that are chemically inert and hydrophobic. These drawbacks restrict their uses, and in order to circumvent this issue, functionalization is performed in the bodies of CNTs, with certain alterations made at the open ends of the CNTs. At this point, FT-IR analysis is a useful technique for examining functionalization results.

However, Figures 5.21, 5.22, and 5.23 show peaks that correspond to the wafer, the catalyst, and the CNTs; this is because the Fe-based catalyst-bound CNTs structures were generated on the surface of the Si wafer. In contrast to functionalized CNTs, however, unmodified CNTs will not exhibit any discernible infrared (IR) signals. This is an important point to keep in mind. All of the samples had peaks at around 1580–1530 cm^{-1}, which indicated that the hexagonal structure in the entire CNT skeletons was verified. It should be noted that these peaks were caused by the sp^2-hybridization of carbon. In addition to this, it is claimed that CVD-based CNTs exhibit also sp^3 hybridization. It is well knowledge that irregular sp^3 carbon hybridization may be seen in an IR spectrum between 1200 and 1100 cm^{-1} (Ţucureanu, Matei, and Avram 2016). On the other hand, it is believed that this peak overlaps with the peak of the Si wafer.

Nonetheless, this approach needs to be validated by doing further Raman and XPS analyses.

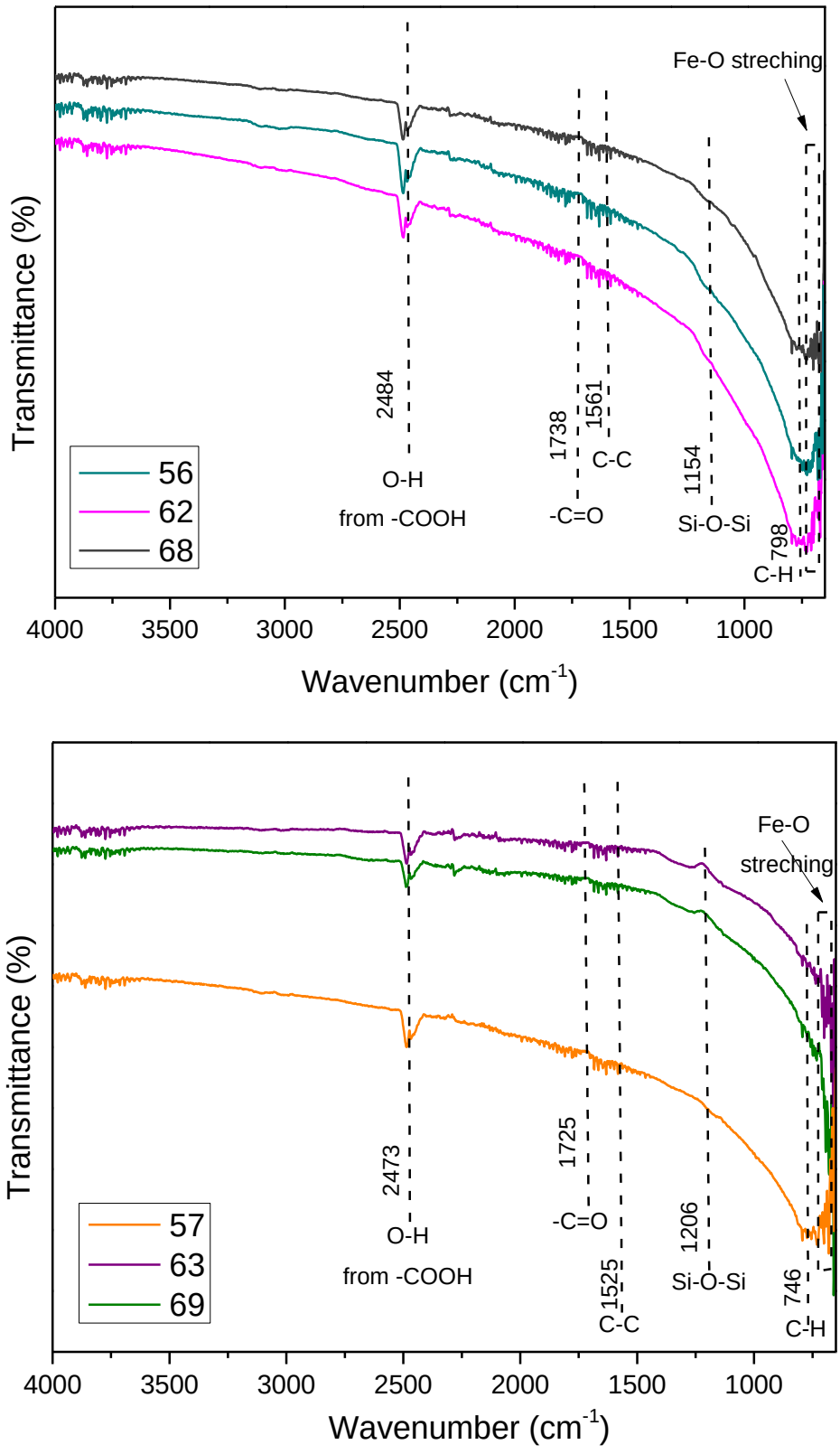


Figure 5.23 FT-IR spectra of the 7-minute samples

5.7 Raman Spectroscopy

Raman spectroscopy reveals three peaks: the D peak, the G peak, and the 2D peak. The D peak represents the sp^3 hybridization of the carbon atoms formed in the structure and is a peak that increases as the defect concentration increases. The G peak, on the other hand, indicates sp^2 hybridization of carbon atoms, and a high peak indicates high crystallinity values. However, in the Raman spectrum of carbon nanotubes, sp^3 hybridization and a higher D band are expected (Szybowicz, Nowicka, and Dychalska 2018). Therefore, Raman spectroscopy is an effective method for distinguishing between carbon nanostructures.

SWCNT resonates and has a distinct Raman fingerprint. Diameter can be calculated using a very sharp G band, an extremely low D band, and Breath mode (100-300 cm^{-1}). The G' band is also an important consideration (2600 cm^{-1}). Because of the perfectly isolated electronic structure, this is a 2^{nd} order transition developed in SWCNT. The very low D, sharp G, strong G', and RBM indicate that the structure we have is a SWCNTs (M S Dresselhaus et al., 2002; Heller et al., 2004).

Raman spectra of Fe_2O_3-based and Fe_3O_4- based samples were acquired (Figure 5.24, 5.25 and 5.26) for the purpose of additional verification. First of all, although a low density RBM was observed in all figures, this band indicates that the structure is MWCNT rather than SWCNT. In previous studies(Nikita Gupta, Gupta, and Sharma 2019; Kang et al., 2020), three well-defined groups helped to discover the structural characteristics of MWCNTs. These groups were as follows: the G band at 1582 cm^{-1}, which varies in characteristic Raman line shape depending on whether the nanotube is semiconductor or metallic; the D band caused by defects in the range of 1250-1450 cm^{-1}; and the G' band in the 2500-2900 cm^{-1} range, which is secondarily related to structural defects. Depending on the type of nanotube, the characteristic Raman line shape differ. All relevant groups were observed at the ranges indicated for all samples and are summarized in Table 5.3.

It should be considered that comparing the ratios of the intensities of the G band ($\boldsymbol{I_G}$), which specifies the crystal structure of graphite (sp^2), and the D band ($\boldsymbol{I_D}$), which is close to 1380 cm^{-1} (sp^3) and represents defects, is how crystallinity is determined by Raman analysis (S. Kim et al., 2021). The findings of the Raman examination of

samples based on Fe_2O_3 indicated that the I_D/I_G value ranged anywhere from 0.5 to 1.5 (Table 5.3). However, the I_D/I_G ratio improved as the growth periods increased, but a change in the catalyst concentration did not result in a discernible improvement in the ratio. Because of the intensity ratios, it is possible to deduce that the longer growth period has resulted in more flaws being generated in the samples that are based on Fe_2O_3.

Furthermore, when looking at samples based on Fe_2O_3 and Fe_3O_4 (Figures 5.24, 5.25, and 5.26), one might claim that the variation in the kind of catalyst does not cause significant changes in the distinctive peaks of CNTs. On the other hand, the findings of the Raman analysis conducted on samples based on Fe_3O_4 revealed that the I_D/I_G ratio was between 1.2 and 1.5 (Table 5.3). Because of the reduction in catalyst concentration, the I_D/I_G ratio rose when each of the samples taken after three minutes was analyzed on its own. The growth time was extended from 3 minutes to 5 minutes, however the I_D/I_G ratio of sample 63, which had a growth duration of 7 minutes, was the highest of all of the samples. Similar to Fe_2O_3-based samples, structural flaws in Fe_3O_4-assisted CVD-based CNTs have risen as the length of the development period has increased.

Table 5.3 Raman shifts of the peaks of the samples and intensity ratios of D-band to G-band.

Sample	λ_D (cm^{-1})	λ_G (cm^{-1})	$\lambda_{G'}$ (cm^{-1})	I_D	I_G	I_D/I_G ratio	I_G/I_D ratio
20	1307	1578	2613	8117.2	7944.4	1.02	0.98
21	1309	1582	2617	5752.7	5028.4	1.14	0.87
26	1312	1581	2604	4169.4	3311.9	1.25	0.79
27	1308	1578	2620	3609.5	3007.7	1.2	0.83
32	1318	1580	2629	944.2	1637.9	0.57	1.73
33	1306	1576	2599	2920.5	2299.8	1.26	0.79
44	1316	1576	2620	5302.6	4725.1	1.12	0.89
45	1305	1581	2642	3747.5	2931.2	1.27	0.78
50	1313	1590	2614	1765.4	1304.9	1.35	0.74
51	1308	1584	2648	1602.2	1458.7	1.09	0.91
56	1306	1589	2610	9496.6	6875.5	1.38	0.72
62	1312	1594	2602	3359.1	2286.3	1.46	0.68
63	1311	1580	2618	3754.5	2586.5	1.45	0.69
68	1317	1590	2613	5357.5	3633.2	1.47	0.68
69	1313	1588	2612	6821.5	5150.6	1.32	0.76

On the other hand, peaks connected to the Si wafer substrate were seen at 301 and 520 cm^{-1} for Fe_2O_3 based samples numbered 20, 26,32,38,44,50,56,62 and 68 whereas, peaks of Si wafer were at 305 and 519 cm^{-1} for Fe_3O_4 based samples numbered 21,27,33,39,45,51,63, and 69 (Figure 5.24, 5.25 and 5.26). The results of the FT-IR investigation were therefore validated from another perspective.

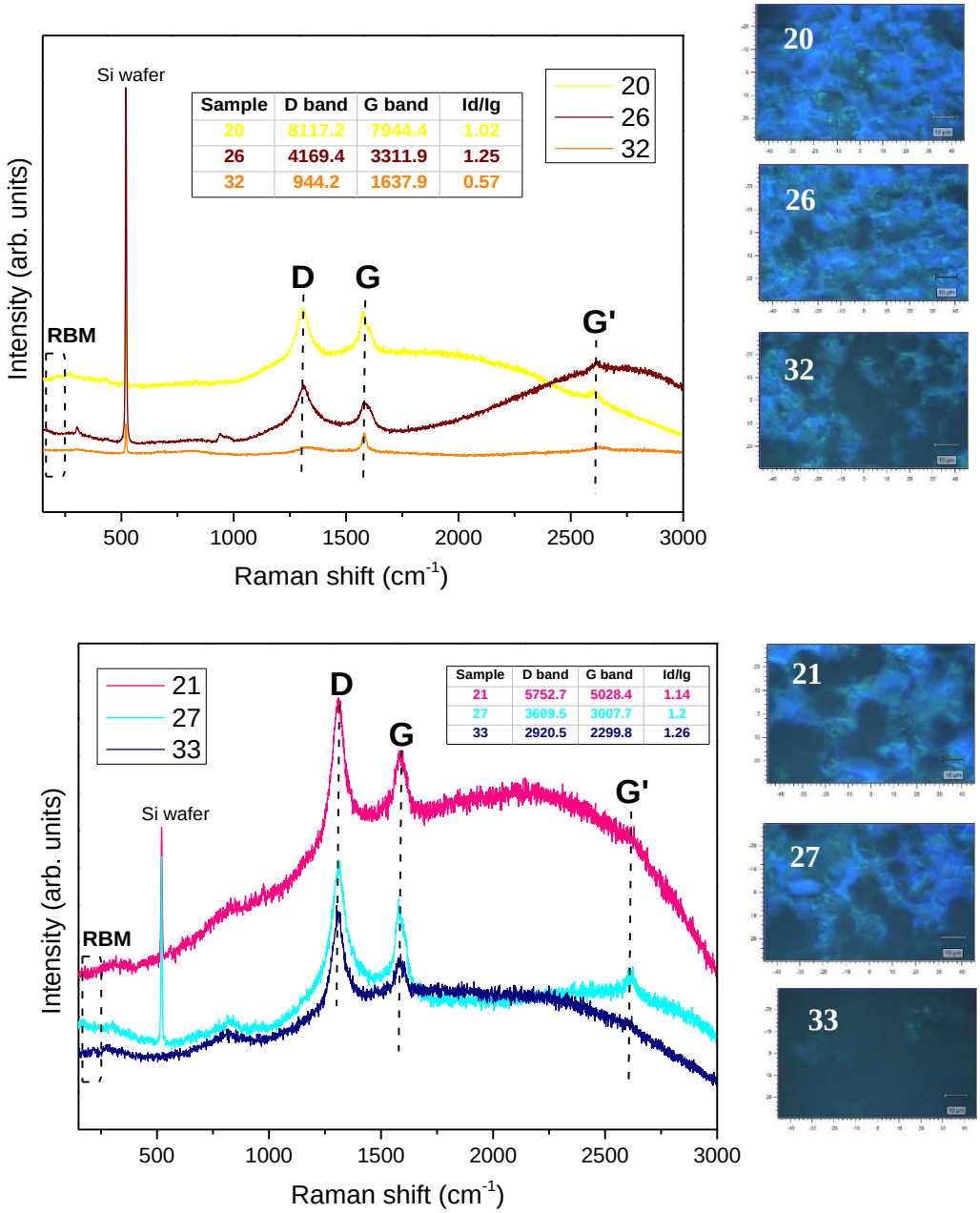


Figure 5.24 Raman spectrum of the 3-minute samples.

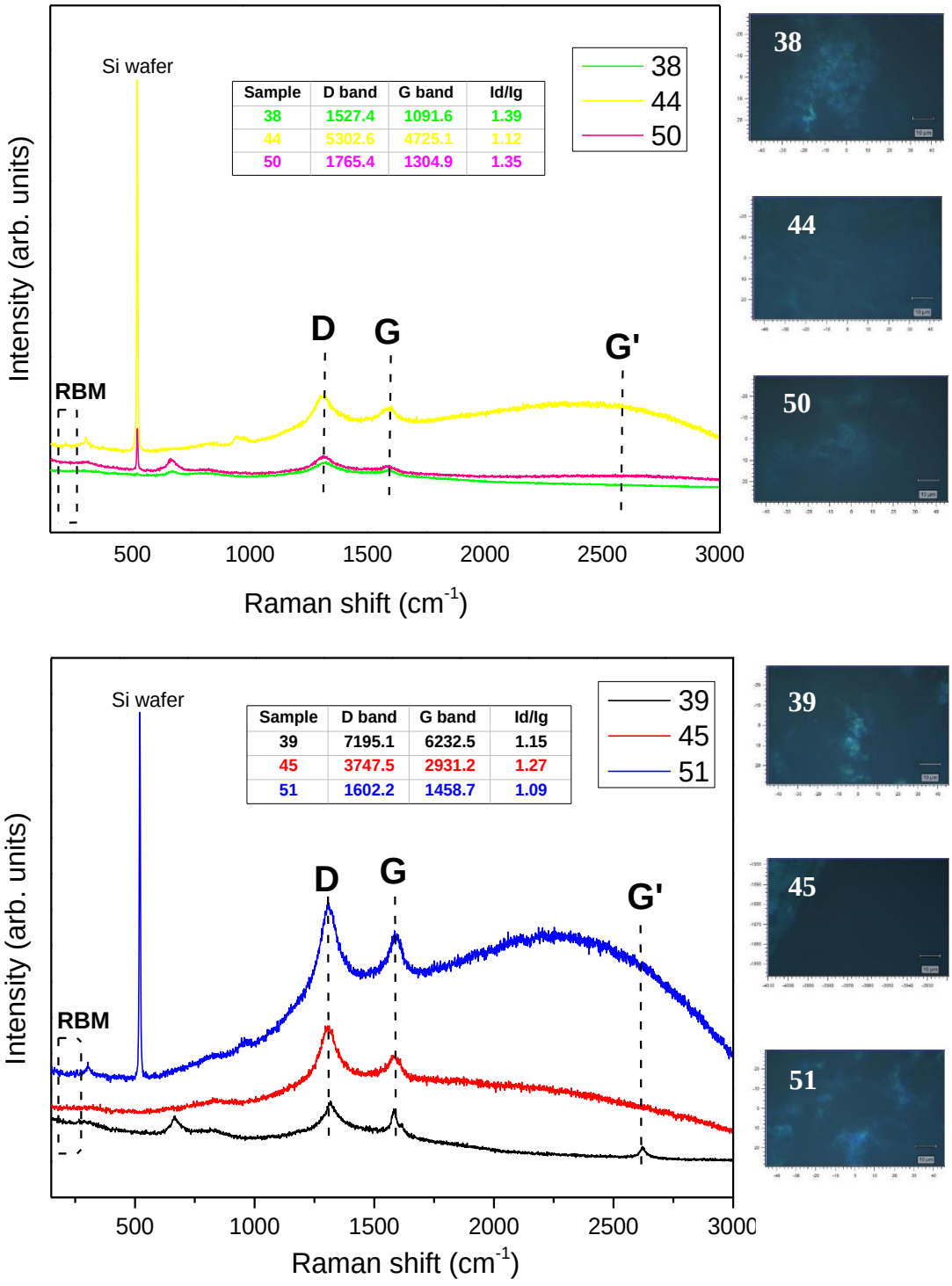


Figure 5.25 Raman spectrum of the 5-minute samples.

Raman graphs of CVD-based CNTs synthesized with Fe_3O_4, like Fe_2O_3-based samples, indicated that D bands were in the range of 1305-1315 cm^{-1}, G bands were in the range of 1575-1590 cm^{-1}, and G' bands were in the range of 2620 cm^{-1}. These results are similar to those found in Fe_2O_3-based samples. It is important to note that in samples based on Fe_3O_4, variations in growth time did not result in a substantial difference in the Raman shift for particular bands of CNTs, despite the fact that the concentration of the catalyst was altered. However, significant differences in intensity were detected in the 3-minute Raman spectrum of both Fe_2O_3-based and Fe_3O_4-based samples in Figure 5.24. Similarly, differences were observed in 5-minute samples (Figure 5.25). For instance, in Figure 5.24, a significant decrease was observed in the intensity of the D band due to the decrease in catalyst concentration in Fe_2O_3 based samples 20, 26 and 32. Additionally, the lowest D band intensity was obtained as 944 arb. units in sample 32 containing 2 wt.% Fe_2O_3. Nevertheless, a similar observation could not be obtained for the 5-minute Fe_2O_3-based samples (Samples 38, 44 and 50) (Figure 5.25).

In Fe_3O_4-based 3-minute samples, the lowest D intensity was obtained in sample 33 as 2920 arb. units. This can be interpreted as the use of less catalyst concentration in 3-minute samples may result in fewer defects in the final structure when evaluating catalyst concentrations in themselves. This approach is also confirmed by the intensity value of the D band of the sample 51 with 2 wt.% concentration obtained in the Raman spectrums of the 5-minute samples.

In biosensor applications, high-defect regions can be created by external interventions so that superficial modifications of CNTs can be easily applied. However, highly defective structures were also observed in the 7-minute samples obtained within the scope of this study (Figure 5.26). On the other hand, Raman spectroscopy cannot be evaluated only by looking at the intensities of the D and G bands. For this reason, $\boldsymbol{I_G/I_D}$ ratios are also checked to confirm whether it is of high quality and crystalline structure. These density ratios indicate that the obtained CNTs are defective, for biosensor applications, imperfect structures to which chemical or biological molecules can easily bind, but it can be said that they are of relatively low quality and crystallinity.

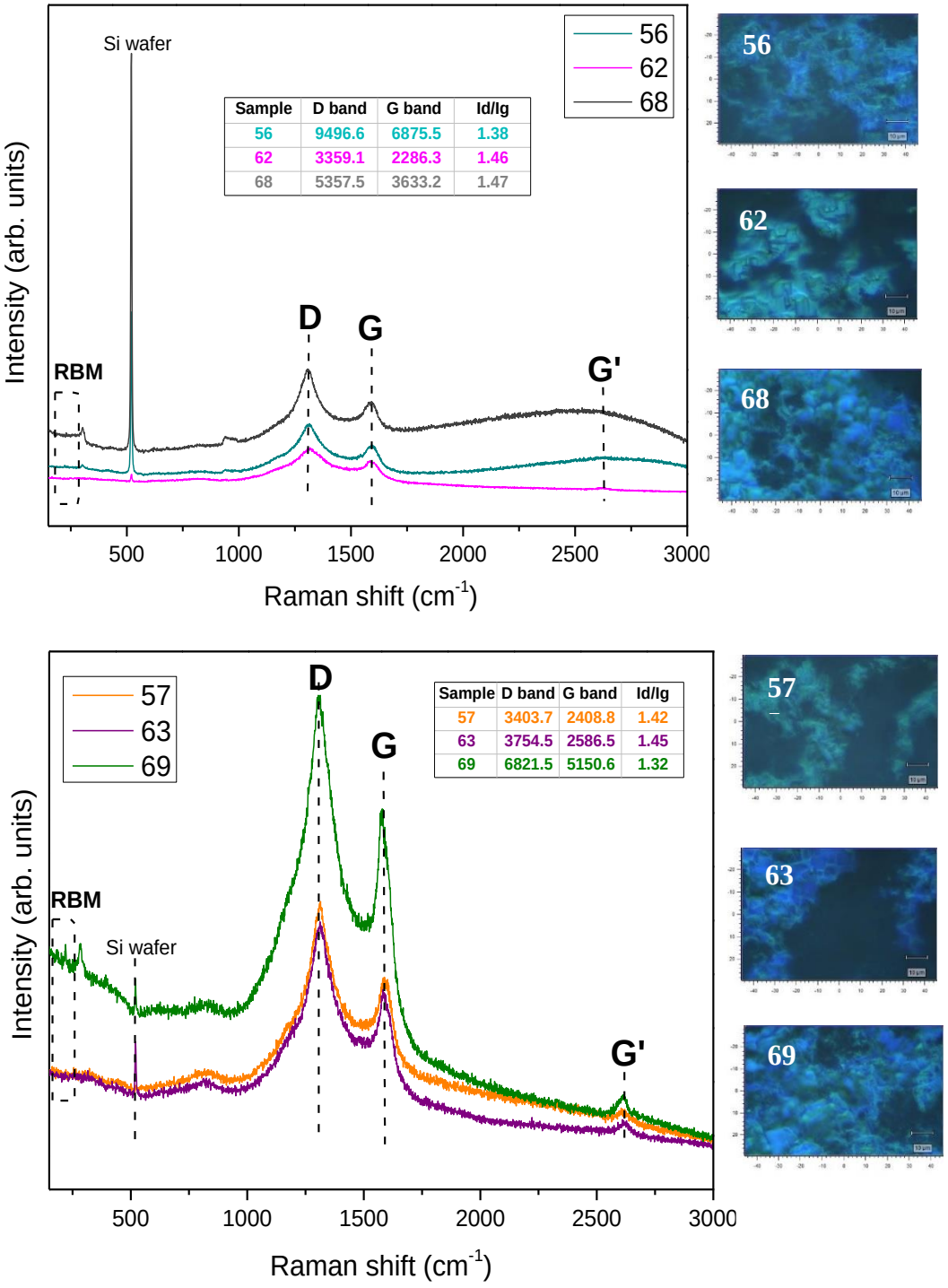


Figure 5. 26 Raman spectrum of the 7-minute samples.

Consequently, the highest quality and crystallinity was obtained with an I_G/I_D ratio of 0.79 in Sample 33 containing 2 wt.% of Fe_3O_4 catalyst concentration, in which a 3-minute growth time was applied, and the highest defective structure was obtained in the 5-minute sample containing 2 wt.% Fe_2O_3 with the highest I_D/I_G ratio of 1.35.

5.8 X-Ray Diffraction Analysis (XRD)

The XRD spectra of all samples using 3.5- and 7-min amplification times are shown in Figures 5.27, 5.28, and 5.29. Peaks referring to the (111) and (311) planes of the Si wafer, indicated by the "□" symbol, substrate appeared at 2θ= 28.2 and 56.3° in all XRD patterns, which is consistent with previous studies (Katharria et al., 2006; Y. C. Lam et al., 2009).

In Figures 5.27, 5.28, and 5.29 the different color lines shows the XRD pattern of samples 20, 26, 32, 38, 44, 50, 56, 62, and 68 using Fe_2O_3 NPs as a catalyst. The characteristic peaks of Fe_2O_3 are 2θ = 21.5, 31.75, 35.2, 36.74, 45.32, 53.0, 56.08 and 61.48°, corresponding to (220), (311), (222), (400), (422), (511) and (440) planes, respectively. It is also worth noting that the catalyst used is remarkably similar to the JCPDS file 019-0629. Furthermore, the "∇" symbol represents the strong and sharp peaks of the Fe_2O_3 NPs, which are consistent with previous studies (Suryawanshi et al., 2018).

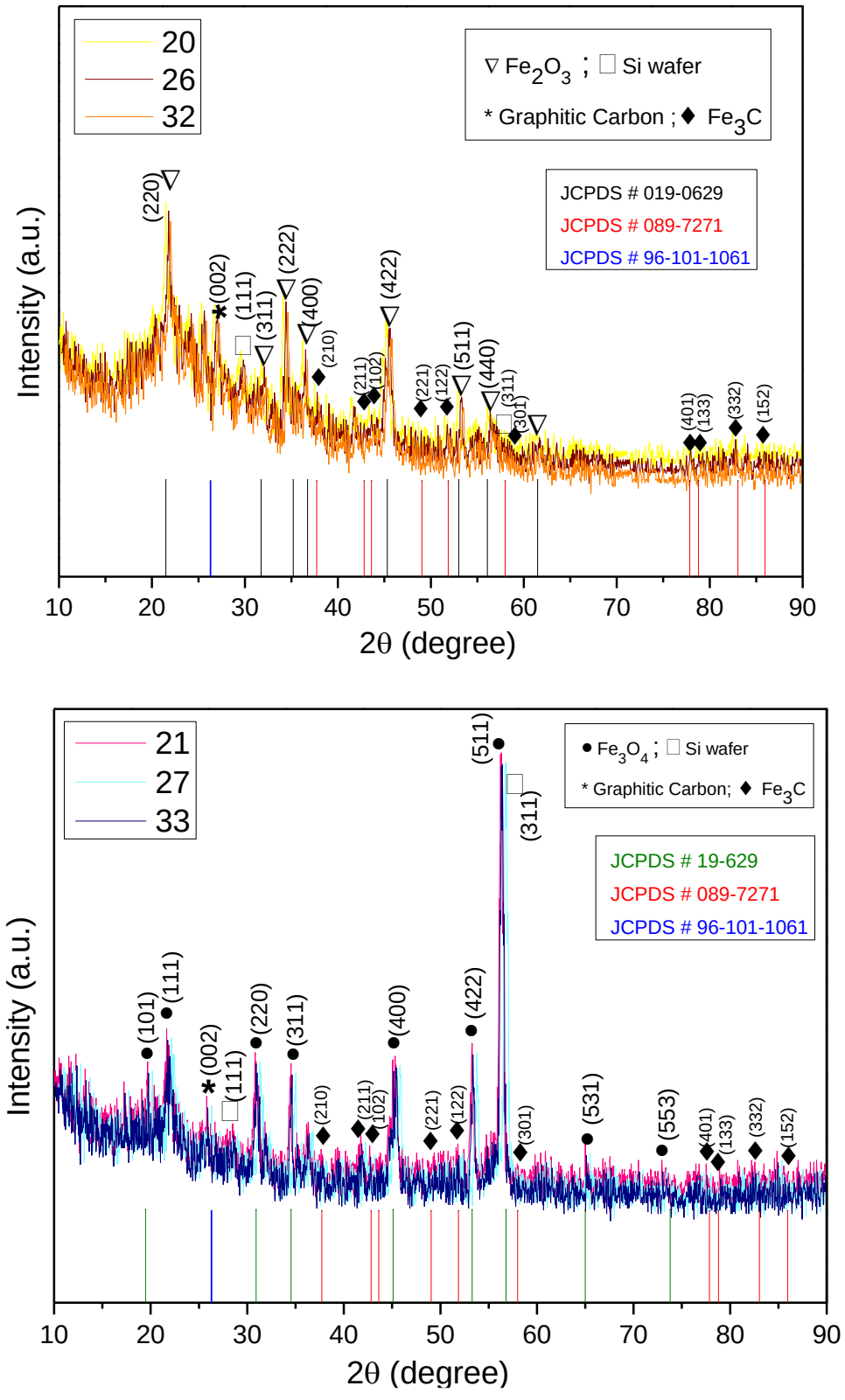


Figure 5.27 X-ray diffraction (XRD) graph of the 3-minute samples

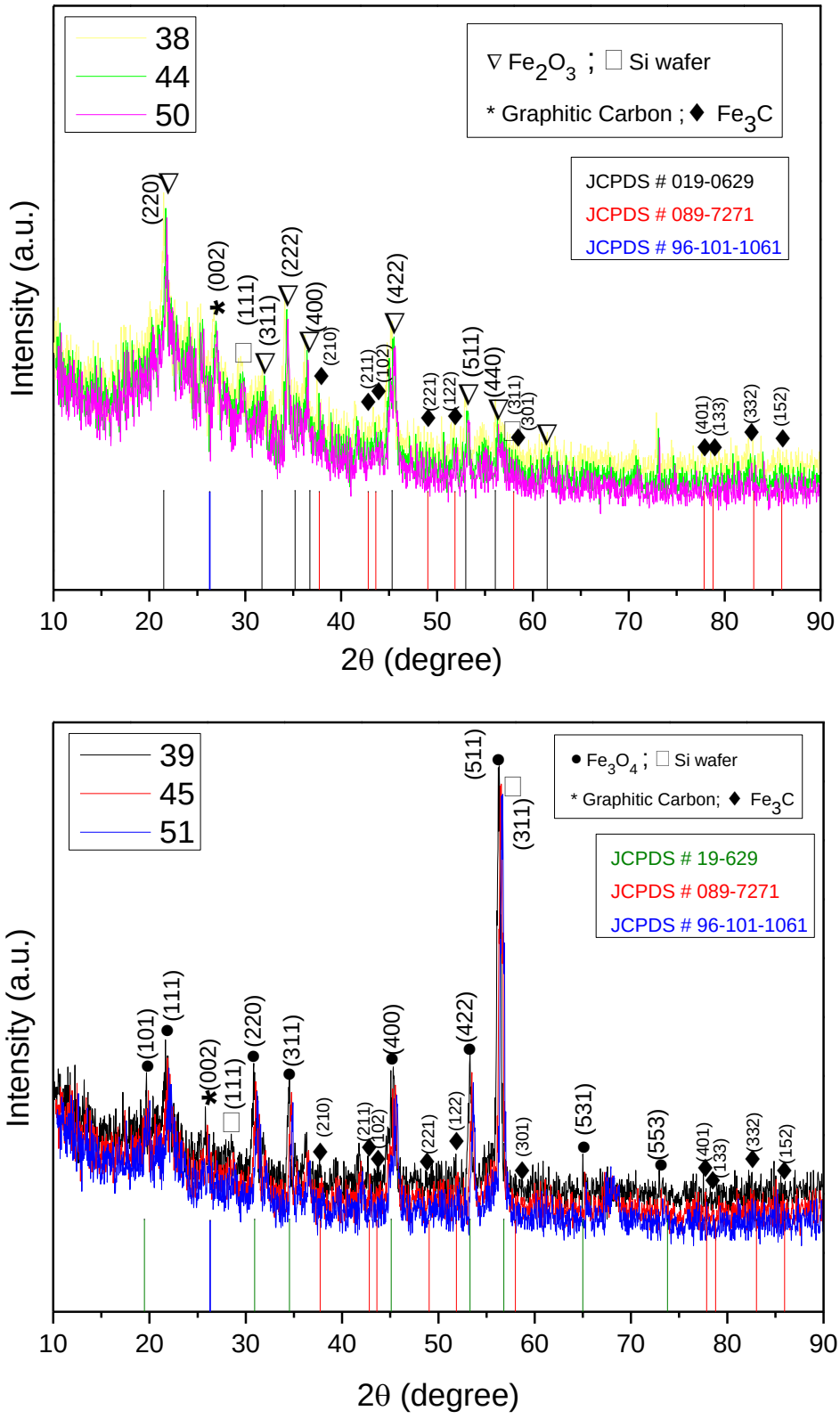


Figure 5.28 X-ray diffraction (XRD) graph of the 5-minute samples

The XRD patterns of the 21,27,33,39,45,51,57,63, and 69 samples using Fe_3O_4 NPs as a catalyst are shown in Figures 5.27, 5.28, and 5.29 with different color lines. The "•" symbol denotes specific Fe_3O_4 NP peaks in all samples. The reflection peaks observed at 2θ = 19.48, 30.92, 34.54, 44.1, 53.28, 56.8, 65.0, and 73.8^o correspond to the planes (111), (220), (311), (400), (422), (511), (531), and (553), respectively. Furthermore, the results are consistent with previous studies(Bao et al., 2017; Compeán-Jasso et al., 2008) and match well with the magnetite database in JCPDS Card: 19-629.

Fe_3C structure was also observed in the XRD graphs of all samples, confirming the previously recommended Fe-C reaction. Relevant peaks are in high agreement with the literature (Krishnia et al., 2016) and are indicated by the symbol "♦" in the patterns. Additionally, the diffraction peaks at 2θ = 37.72, 42.82, 43.61, 49.04, 51.87, 58.00, 77.86, 78.79, 83.04, and 85.96 ^{o} identified and found corresponding to the planes (210), (211), (102), (221), (122), (301), (401), (133), (332), and (152) respectively, are associated with the orthorhombic structure of Fe_3C (JCPDS Card: 089-7271).

The CNTs structure, with the symbol "*" in Fe_2O_3 and Fe_3O_4 based samples, was observed at 2θ = 26.6^o in all patterns in Figures 5.27, 5.28, and 5.29. The (002) plane is responsible for the graphitic structure of MWCNTs. This result, which agrees with the literature for CNT structures obtained with both catalysts (Alijani and Shariatinia 2017; C. Hou et al., 2013; Y. Sun et al., 2013), is one of the key indicators that CNTs are successfully synthesized.

When the Fe_3O_4-based samples are evaluated separately, the increase in growth time does not appear to cause a significant change in peak positions. XRD diffraction peaks in Fe_2O_3-based samples were observed in the same way as those in Fe_3O_4-based samples. The C peak received special attention, and only a significant difference was found between Fe_2O_3 and Fe_3O_4 catalysts. The difference between the reduction reactions, which has been mentioned above, is most likely the cause of this. Fe_3O_4 takes longer than Fe_2O_3 to catalyze carbon nanotubes. As a result, the peak intensity reflects this difference.

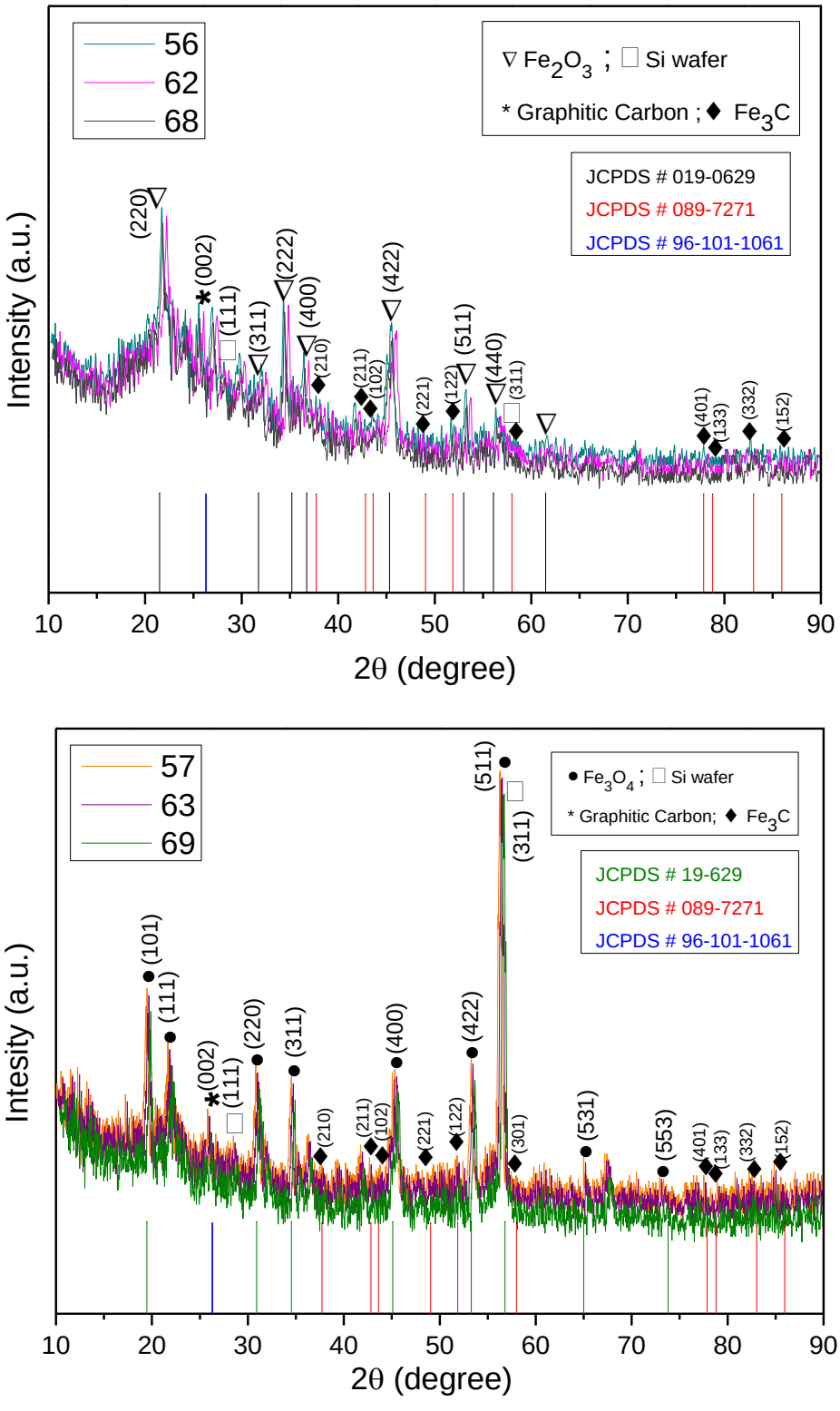


Figure 5.29 X-ray diffraction (XRD) graph of the 7-minute samples

5.9 X-Ray Photoelectron Spectroscopy (XPS)

XPS survey spectrum of all samples shown in Figures 5.30, 5.31, and 5.32. The Si wafer substrate produced a peak at 104.08 and 155.06 eV as Si 2p, while with the help of Fe_2O_3 and Fe_3O_4 catalysts, a peak in the 711.08-731.02 eV range was observed. Because of iron oxide and silicon, the peak of O 1s was 533.09 eV. Consistent XPS survey spectra across all samples confirm previous FT-IR characterization and XRD analysis results. Although the C 1s peak peaked at different densities in each sample due to density differences, the carbon nanotubes showed carbon bonds at around 286 eV. For this reason, a thorough investigation of this peak was conducted.

The deconvoluted high-resolution C 1s XPS spectra of all samples with different catalysts, concentrations, and growth times are shown in Figures 5.30, 5.31, and 5.32. The calibration of the C 1s peak of all reference samples was performed at 284.6 eV in reference to the sp^2 carbon phase. The absence of the π - π * shake-up feature did not complicate the deconvolution of the C 1s peak of the mentioned samples (Enevoldsen and Juhler 2010). The C 1s peaks were thus fitted with two main peaks: sp^2 (284.6 eV) and sp^3 (285.2 eV) (Minghua Li et al., 2008; H. Wang et al., 2007). The C 1s peak in all samples was calibrated at around 285.1 eV, corresponding to the sp^3 carbon phase. The samples' C 1s peaks were deconvolved into two distinct peaks: sp^2 (284.2 eV) and sp^3 (285.1 eV) (Artemenko et al., 2015).

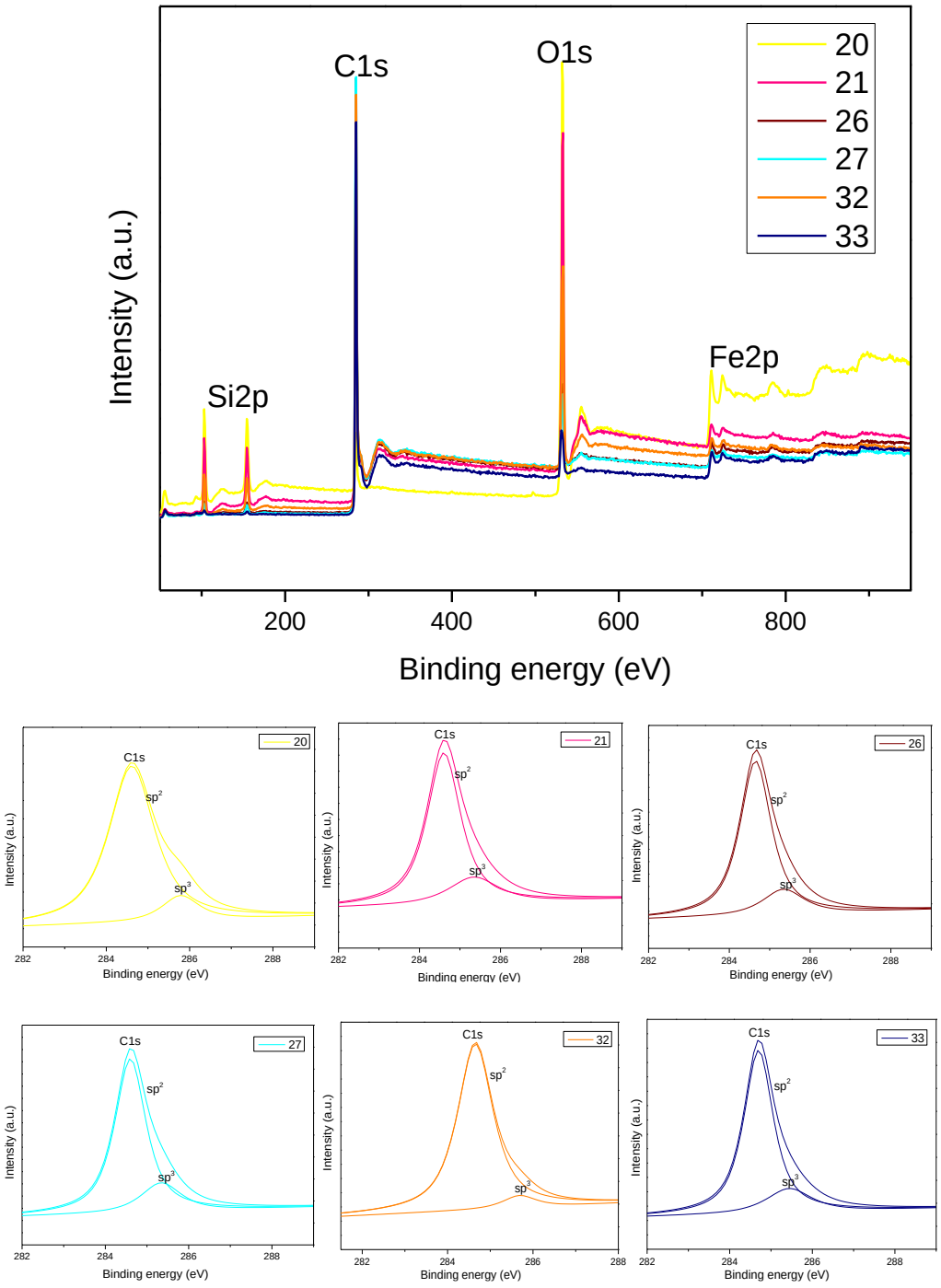


Figure 5.30 XPS Survey spectra and the deconvoluted C 1s spectra of the 3-minute samples.

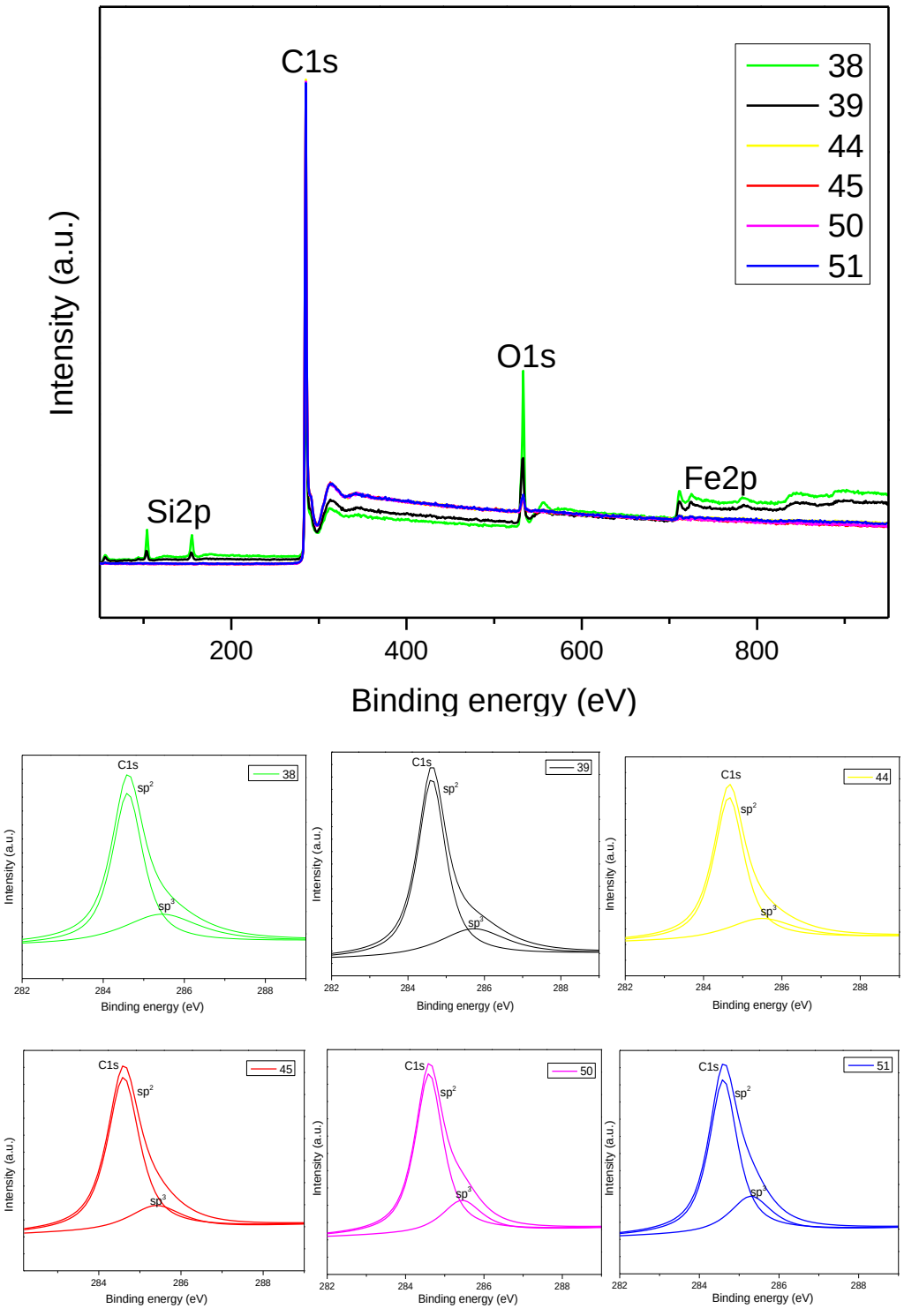


Figure 5.31 XPS Survey spectra and the deconvoluted C 1s spectra of the 5-minute samples.

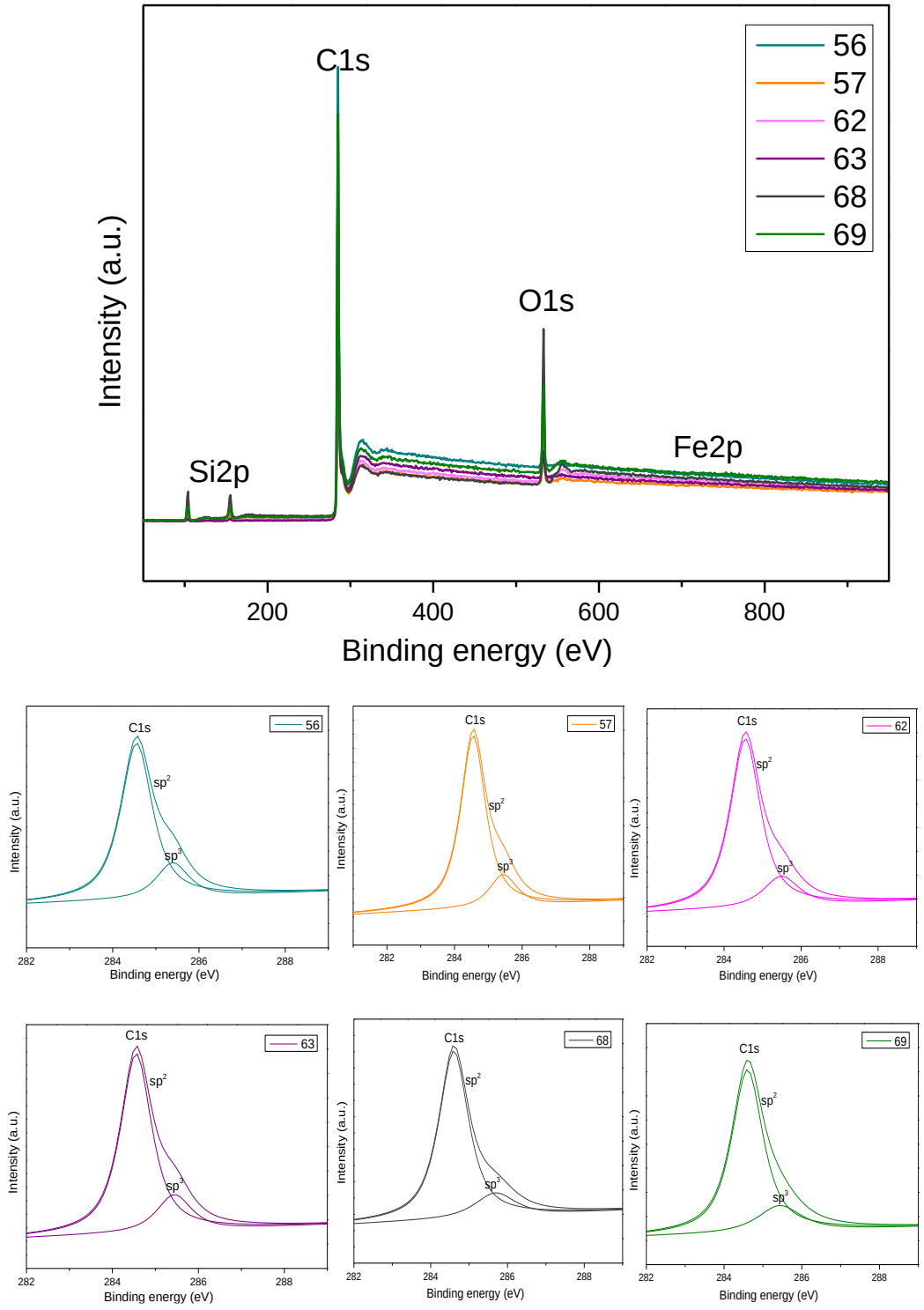


Figure 5.32 XPS Survey spectra and the deconvoluted C 1s spectra of the 7-minute samples.

Detailed C 1s spectra of all the films were recorded in the binding energy range 275–300 eV and fitted using a XPS peak 4.1. software. Gaussian to Lorentzian ratio (G/L ratio) of 30: 70 (obtained from the fitted peak of pyrolytic graphite), has been consistently used in our curve fitting. Figures 5.30, 5.31, and 5.32 shows the fitted spectra for carbon 1s of the samples, and C1s spectrum is fitted with three peaks corresponding to sp^3 carbon (diamond), and sp^2 carbon (graphite). The fitted spectra match very well with the experimental data. Low observed value of the residuals shows the validity of our fitting. The peak positions, their full width at half maxima (FWHM) and the sp^3/sp^2 ratio obtained from the area fraction of sp^3 peak and sp^2 peak in C 1s spectrum are given in Table 5.5. As can be seen from Table 5, the sp^3 /sp^2 ratio of the films estimated from the peak fitting of C 1s spectrum is found to increase with increase in the concentration whereas there is no critical difference by increasing growth time.

Table 5. 4 Chemical composition, FWHM and sp^3/sp^2 ratio on the samples surface calculated from XPS spectra

Sample No	Chemical Composition (wt.%)		Chemical Composition (at.%)		FWHM (eV)		sp^3 /sp^2
	C1s	O1s	C1s	O1s	sp^2	sp^3	ratio
20	42.49	9.26	53.19	17.38	1.63	1.41	0.20
21	44.7	27.2	60.73	25.47	1.27	1.48	0.27
26	75.56	12.14	89.89	7.02	1.17	1.27	0.25
27	78.67	10.37	91.03	6.22	1.18	1.18	0.27
32	61.82	11.51	76.81	15.53	1.15	1.38	0.24
33	79.26	8.88	93.72	4.68	1.08	1.25	0.25
38	59.56	20.59	75.32	16.56	1.27	2.07	0.34
39	77.81	11.22	90.84	6.37	1.12	1.12	0.30
44	97.68	2.32	98.7	1.3	1.18	1.59	0.26
45	95.34	3.23	98.54	1.35	1.16	1.34	0.26
50	96.91	3.09	98.65	1.35	1.17	1.21	0.29
51	97.05	2.95	98.54	1.46	1.18	1.23	0.31
56	92.12	5.97	95.34	3.88	1.23	1.06	0.29
57	86.87	8.09	92.26	38.76	1.19	1.12	0.26
62	77.03	12.44	86.16	9.68	1.23	1.21	0.26
63	93.57	4.7	96.55	2.86	1.20	1.09	0.24
68	67.07	18.42	76.8	16.02	1.16	1.36	0.28
69	81.73	11.07	88.98	8.01	1.23	1.36	0.25

5.10 Current-Voltage Characterizations

Electrical conductivities of multi-wall carbon nano tubes have been measured using a micro manipulator by two probe method. The nano tubes are 30 - 450 nm in diameter and longer than 2 μm in length. The resistance of tubes is several kΩ per μm, which gives the average conductivity as 117,2 - 142857.1 1/Ωcm. The current-voltage characteristics at high field are also studied until the dielectric breakdown takes place. The preliminary result that the tube with low resistance shows metallic behavior and that of high resistance exhibits semiconductive behavior indicates the various helicities for the MWCNTs too.

Table 5.6 displays the IV characteristics of all available MWCNT samples. All measurements are near and consistent, except for sample 45. It is worth noting that the error in these measurements from the mean resistivity is less than 1% across all runs. However, compared to hot-pressed sintered CNTs (2–3 10^{-4} Ωcm) (Ma et.al, 1999), the resistance of MWCNTs measured with a four-point probe is quite close; these values are attributed to the production procedure resulting in strong connections between the tubes and the exceptional purity and crystallinity that resulted.

Table 5.5 Electrical features of samples

Sample No	Resistance(Ω)	Specific Resistance (ρ) (Ωcm)	Conductivity (σ) (1/(Ωcm)
20	0.029	$0.9x10^{-5}$	$11x10^{4}$
21	5.51	$0.2x10^{-2}$	$3.97x10^{2}$
26	0.024	$0.7x10^{-5}$	$14.2x10^{4}$
27	5.17	$0.2x10^{-2}$	$3.97x10^{2}$
32	0.026	$0.7x10^{-5}$	$14.2x10^{4}$
33	4.29	$1.3x10^{-3}$	$7.3x10^{2}$
38	0.026	$0.8x10^{-5}$	$12.5x10^{4}$
39	6.07	$0.2x10^{-2}$	$3.97x10^{2}$
44	0.026	$0.9x10^{-5}$	$11x10^{4}$
45	6.98	$0.8x10^{-2}$	11.7x10
50	0.027	$1x10^{-5}$	10^{5}
51	2.62	$1.1x10^{-3}$	$8.5x10^{2}$
56	0.026	$0.7x10^{-5}$	$14.2x10^{4}$
57	0.023	$0.7x10^{-5}$	$14.2x10^{4}$
62	0.027	$0.7x10^{-5}$	$14.2x10^{4}$
63	0.027	$0.7x10^{-5}$	$14.2x10^{4}$
68	0.027	$0.8x10^{-5}$	$12.5x10^{4}$
69	0.026	$0.7x10^{-5}$	$14.2x10^{4}$

When Fe_2O_3-based samples were evaluated in themselves, the change in growth time and catalyst concentration did not cause a significant change in resistivity and

conductivity values. Similar results were observed when the Fe_3O_4 catalyst was applied. As a result, conductivity values used in biosensor applications were obtained in CNT samples, whose resistivity values were obtained in the range of $0.2x10^{-2}$ – $1.4x10^{-5}$ Ωcm.

In previous studies, Li et al. reported that the resistivity values were in the range of $(4.4–12.6) \times 10^{-4}$ Ωcm with the Four-point method of CNT ribbons (Li et al., 2002), while Qin et al. have shown that these values were $(1.2–1.6) \times 10^{-4}$ Ωcm for the Four-point method of sintered CNTs compact (Qin et al., 2006). The resistance of bulk CNTs may depend on the measurement condition. Still, our measurement method is a relatively simple tool for measuring the resistance of bulk CNTs, and the results are consistent with the literature.

CHAPTER SIX

CONCLUSION AND RECOMMENDATIONS

6.1 Conclusion

The production and shape of CVD-based carbon nanotubes are both affected by a wide variety of factors, including gas flow rate, type of catalyst, length of growth period, substrate, interaction between substrate and catalyst, and presence of reducing environment. The selection of the kind of catalyst and how it interacts with the substrate is the one of these characteristics that is considered to be the most essential. According to the findings of a number of important research, the CVD approach is capable of producing CNTs from a wide variety of materials, both with and without iron groups. At this juncture, the kind of catalyst is the most important component that decides whether or not CNT synthesis will take place via a VLS mechanism that is typical for CVD. The results of this research show that a nanotube or tubular shape may be generated using any sort of catalyst that is based on iron, independent of the concentration or the amount of time spent growing. On the other hand, it was not possible to get considerable tubular formation with any of the other catalysts, including Nb, Ti, Au, or Pt-based catalysts. As a result, the emphasis of the study has been on samples derived from catalysts based on iron.

Based on the results of the SEM, it was determined that a systematic rise in catalyst concentration led to a systematic increase in diameter in Fe_2O_3-based catalysts. This was the conclusion reached as a consequence of the findings. A thicker carbon layer also led to an increase in the pipe's diameter as time passed throughout the growth process. However, the sample number 50 produced the lowest radius, which was 88 ± 31 nm.

The EDX investigation was applied only to specimens treated with a 5 min growth time and yielding the most efficient tubular structure. EDX revealed that a decrease in catalyst concentration causes an increase in carbon percentage and content. The highest carbon percentage was determined as 80.49 and 87.49, respectively, in samples 50 and 51 containing the lowest catalyst concentration of 2% by weight. This situation

was associated with the fact that carbon structures such as tubular form and amorphous carbon found more space on the surface as the catalyst concentration decreased.

In the FT-IR analysis, all four major peaks located around 2470, 1720, 1560, 1150 and 870 cm^{-1} were noted for all catalyst concentrations and growth times. However, the fact that the reflections from nonfunctionalized CNTs did not have significant peaks in the FT-IR analysis caused the analysis to reveal more details about the substrate surface and the catalyst used. However, the specific peak of sp^2 hybridization of probable carbon of pristine CNT was observed in all samples in the range of 1580–1530 cm^{-1}.

In the Raman spectrum of CVD-based CNTs synthesized with Fe_3O_4 and Fe_2O_3 catalysts, the expected D, G and G' bands from the CNT spectra were observed in line with the literature. Growth time to Raman spectra increased the $\boldsymbol{I_D/I_G}$ ratio for both types of catalyst supported samples, but a change in catalyst concentration did not result in a noticeable improvement in the ratio. As a result, an increase in the amount of defects in the CNT structures was revealed when longer growth times were applied.

XRD graphs reveal that the catalysts and Si wafer substrate dominates all graphs. However, the graphitic carbon peak expected for an ideal CNT was obtained for all samples at $2\theta=26.63^{o}$ indicated the 002 plane.

In XPS spectra, the C 1s peak in all samples was calibrated around 285.1 eV, corresponding to the sp^3 carbon phase. The C1s peaks of the samples were disaggregated into two distinct peaks: sp^2 (284.2 eV) and sp^3 (285.1 eV). It was found that the sp^3/sp^2 ratio thus obtained increased with increasing concentration, while there was no critical difference with increasing growth time.

The electrical properties of all CVD based CNT samples were revealed by current-voltage characterizations. Except for sample 45, all measurements were close and consistent. The highest conductivity value was observed in sample 56, which can be claimed as high catalyst concentration and high growth time.

The results of this study revealed that the catalyst type is much more dominant than other parameters such as catalyst concentration, substrate type, growth time, production temperature when it comes to CVD-based CNT production. However, the

imperfection of the obtained structure and the high conductivity values make them a potential candidate for biosensor applications.

6.2 Future Works and Recommendations

Further studies may focus on improving the morphological characteristics of the CNTs obtained from this study. Thinner diameter MWCNTs or SWCNT structure can be obtained. Reducing agents, agent gases can be used during CVD optimization using the same catalysts. Moreover, the ratios of these gases relative to each other can be examined. Also, the biggest challenge in the study is the agglomeration tendencies of catalysts dispersed on the substrate surface. It is well known that in the synthesis of CVD-based carbon nanostructures, the size of the catalyst is directly related to the size of the final structure. Therefore, CNTs can be obtained in smaller diameters by applying advanced coating techniques to prevent agglomeration.

The high-defect structure of CNTs for biosensor applications has made them a unique immobilization base for chemical and biological molecules. Therefore, the evaluation of the CNTs obtained as a result of this study in terms of immobilization may be the subject of another research.

Future work may also detect through analytical devices that can directly measure the function of CNTs as a transducer in enzyme, cell, DNA, aptamer-based electrochemical biosensor design.

REFERENCES

Abd Mutalib, M., Rahman, M. A., Othman, M. H. D., Ismail, A. F., & Jaafar, J. (2017). Scanning electron microscopy (SEM) and energy-dispersive X-ray (EDX) spectroscopy. In *Membrane Characterization*. Elsevier, 161–179.

Abdi, Y., Mohajerzadeh, S., Koohshorkhi, J., Robertson, M. D., & Andrei, C. M. (2008). A plasma enhanced chemical vapor deposition process to achieve branched carbon nanotubes. *Carbon*, *46*(12), 1611–1614.

Abdullah, E. T., Hasan, S. M., & Naje, A. N. (2013). Optical properties of PVC-MWCNT nano composites. *Indian Journal Pure&Applied Physics*, 51, 77-80.

Abdullah, H. B., Ramli, I., Ismail, I., & Yusof, N. A. (2017). Hydrocarbon aources for the carbon nanotubes production by chemical vapour deposition: A Review. *Pertanika Journal of Science & Technology*, *25*(2).

Acha, V., Andrews, T., Huang, Q., Sardar, D. K., & Hornsby, P. J. (2010). Tissue-based biosensors. In *Recognition Receptors in Biosensors*. Springer, 365–381.

Adewumi, H. K., Adewumi, A. S., Fajinmi, G. R., & Sanusi, Y. K. (2021). Optimization of microstrip patch antenna's bandwidth using fabricated multiwall carbon nanotubes-Al_2O_3-ceramic composite substrate. *Journal of Physics: Conference Series* (Vol. 2034). IOP Publishing, 12020.

Aggarwal, S., Sehgal, S., & Tandon, W. (2021). Biosensors-types and application in food processing industry. *J. Postharvest. Technol*, *9*, 1–19.

Ago, H., Nakamura, K., Imamura, S., & Tsuji, M. (2004). Growth of double-wall carbon nanotubes with diameter-controlled iron oxide nanoparticles supported on MgO. *Chemical Physics Letters*, *391*(4–6), 308–313.

Ahangari, H., Kurbanoglu, S., Ehsani, A., & Uslu, B. (2021). Latest trends for biogenic amines detection in foods: Enzymatic biosensors and nanozymes applications. *Trends in Food Science & Technology*, *112*, 75–87.

Ahirwar, R. (2021). Recent advances in nanomaterials-based electrochemical immunosensors and aptasensors for HER2 assessment in breast cancer.

Microchimica Acta, *188*(10), 1–18.

Ahmad, M., & Silva, S. R. P. (2020). Low temperature growth of carbon nanotubes–A review. *Carbon*, *158*, 24–44.

Ahmad, S., Liao, Y., Hussain, A., Zhang, Q., Ding, E.-X., Jiang, H., & Kauppinen, E. I. (2019). Systematic investigation of the catalyst composition effects on single-walled carbon nanotubes synthesis in floating-catalyst CVD. *Carbon*, *149*, 318–327.

Ahmed, S., Aitani, A., Rahman, F., Al-Dawood, A., & Al-Muhaish, F. (2009). Decomposition of hydrocarbons to hydrogen and carbon. *Applied Catalysis A: General*, *359*(1–2), 1–24.

Akgönüllü, S., & Denizli, A. (2021). Piezoelectric biosensors for virus detection. *Biosensors for Virus Detection*, 1–4.

Alexandrescu, R., Crunteanu, A., Morjan, R.-E., Morjan, I., Rohmund, F., Falk, L. K. L., Ledoux, G., & Huisken, F. (2003). Synthesis of carbon nanotubes by CO_2-laser-assisted chemical vapour deposition. *Infrared Physics & Technology*, *44*(1), 43–50.

Alijani, H., & Shariatinia, Z. (2017). Effective aqueous arsenic removal using zero valent iron doped MWCNT synthesized by in situ CVD method using natural α-Fe_2O_3 as a precursor. *Chemosphere*, *171*, 502–511.

Altay, M. C., & Eroglu, S. (2012). Synthesis of multi-walled C nanotubes by Fe–Ni (70 wt.%) catalyzed chemical vapor deposition from pre-heated CH_4. *Materials Letters*, *67*(1), 124–127.

Altay, M. C., & Eroglu, S. (2013). Thermodynamic analysis and chemical vapor deposition of multi-walled carbon nanotubes from pre-heated CH4 using Fe_2O_3 particles as catalyst precursor. *Journal of Crystal Growth*, *364*, 40–45.

Alvarado-Ramírez, L., Rostro-Alanis, M., Rodríguez-Rodríguez, J., Sosa-Hernández, J. E., Melchor-Martínez, E. M., Iqbal, H. M. N., & Parra-Saldívar, R. (2021). Enzyme (single and multiple) and nanozyme biosensors: Recent developments and their novel applications in the water-food-health nexus. *Biosensors*, *11*(11), 410.

An, L., Zhang, N., Zeng, X., Zhong, B., & Yu, Y. (2022). Quasi-isotropically thermoconductive, antiwear and insulating hierarchically assembled hexagonal boron nitride nanosheet/epoxy composites for efficient microelectronic cooling. *Journal of Colloid and Interface Science, 608,* 1907–1918.

Ando, Y., & Zhao, X. (2006). Synthesis of carbon nanotubes by arc-discharge method. *New Diamond and Frontier Carbon Technology*, *16*(3), 123–138.

Ando, Y., Zhao, X., Sugai, T., & Kumar, M. (2004). Growing carbon nanotubes. *Materials today*, *7*(10), 22–29.

Andrews, R., Jacques, D., Rao, A. M., Derbyshire, F., Qian, D., Fan, X., Dickey, E. C., & Chen, J. (1999). Continuous production of aligned carbon nanotubes: a step closer to commercial realization. *Chemical Physics Letters*, *303*(5–6), 467–474.

Anjalin, F. M. (2014). Synthesis and characterization of MWCNTs/PVDF nanocomposite and its electrical studies. *Der Pharma Chemica*, *6*(1), 354–359.

Aodkeng, S., Sinthupinyo, S., Chamnankid, B., Hanpongpun, W., & Chaipanich, A. (2022). Effect of carbon nanotubes/clay hybrid composite on mechanical properties, hydration heat and thermal analysis of cement-based materials. *Construction and Building Materials, 320,* 126212.

Arepalli, S., Freiman, S. W., Hooker, S. A., & Migler, K. D. (2008). Measurement issues in single-wall carbon nanotubes. *National Institute of Standards and Technology*, 960-19, 36-77.

Arora, N., & Sharma, N. N. (2014). Arc discharge synthesis of carbon nanotubes: Comprehensive review. *Diamond and Related Materials*, *50,* 135–150.

Artemenko, A., Kozak, H., Biederman, H., Choukourov, A., & Kromka, A. (2015). Amination of NCD films for possible application in biosensing. *Plasma Processes and Polymers*, *12*(4), 336–346.

Arthur, J. R., & Cho, A. Y. (1973). Adsorption and desorption kinetics of Cu and Au on (0001) graphite. *Surface Science*, *36*(2), 641–660.

Arunadevi, N. (2022). Metal nanocomposites for advanced futuristic biosensing

applications. *Materials Letters, 309*, 131320.

Assaifan, A. K., Alqahtani, F. A., Alnamlah, S., Almutairi, R., & Alkhammash, H. I. (2022). Detection and real-time monitoring of LDL-cholesterol by redox-free impedimetric biosensors. *BioChip Journal*, 1–10.

Attaf, B. (2015). An Eco-approach to boost the sustainability of carbon nanotube-based composite products. *Carbon Nanotube-Based Composites*.

Audier, M., Oberlin, A., Oberlin, M., Coulon, M., & Bonnetain, L. (1981). Morphology and crystalline order in catalytic carbons. *Carbon, 19*(3), 217–224.

Austen, W. C. R. (1899). The extraction of nickel from its ores by the mond process. (Includıng Plate at Back of Volume). *Minutes of the Proceedings of the Institution of Civil Engineers* (Vol. 135). Thomas Telford-ICE Virtual Library, 29–44.

Avouris, P., Appenzeller, J., Martel, R., & Wind, S. J. (2003). Carbon nanotube electronics. *Proceedings of the IEEE*, *91*(11), 1772–1784.

Awano, Y., Sato, S., Kondo, D., Ohfuti, M., Kawabata, A., Nihei, M., & Yokoyama, N. (2006). Carbon nanotube via interconnect technologies: size-classified catalyst nanoparticles and low-resistance ohmic contact formation. *Physica Status Solidi (A), 203*(14), 3611–3616.

Aydın, E. B., Aydın, M., & Sezgintürk, M. K. (2021). Highly selective and sensitive sandwich immunosensor platform modified with MUA-capped GNPs for detection of spike Receptor Binding Domain protein: A precious marker of COVID 19 infection. *Sensors and Actuators B: Chemical, 345*, 130355.

Aykaç, A., Gergeroglu, H., Beşli, B., Akkaş, E. Ö., Yavaş, A., Güler, S., Güneş, F., & Erol, M. (2021). An Overview on recent progress of metal oxide/graphene/CNTs-based nanobiosensors. *Nanoscale Research Letters*, *16*(1), 1–19.

Bahadır, E. B., & Sezgintürk, M. K. (2015). Electrochemical biosensors for hormone analyses. *Biosensors and Bioelectronics*, *68*, 62–71.

Bahadır, E. B., & Sezgintürk, M. K. (2016). A review on impedimetric biosensors. *Artificial cells, Nanomedicine, and Biotechnology, 44*(1), 248–262.

Bajwa, N., Li, X., Ajayan, P. M., & Vajtai, R. (2008). Mechanisms for catalytic CVD growth of multiwalled carbon nanotubes. *Journal of Nanoscience and Nanotechnology*, *8*(11), 6054–6064.

Baker, R. T. K., Barber, M. A., Harris, P. S., Feates, F. S., & Waite, R. J. (1972). Nucleation and growth of carbon deposits from the nickel catalyzed decomposition of acetylene. *Journal of Catalysis*, *26*(1), 51–62.

Baker, R. T. K., Harris, P. S., Thomas, R. B., & Waite, R. J. (1973). Formation of filamentous carbon from iron, cobalt and chromium catalyzed decomposition of acetylene. *Journal of Catalysis*, *30*(1), 86–95.

Baker, R. T. K., & Waite, R. J. (1975). Formation of carbonaceous deposits from the platinum-iron catalyzed decomposition of acetylene. *Journal of Catalysis*, *37*(1), 101–105.

Balasubramanian, K., & Burghard, M. (2006). Biosensors based on carbon nanotubes. *Analytical and Bioanalytical Chemistry*, 385(3), 452-468.

Bandow, S, Kokai, F., Takahashi, K., Yudasaka, M., & Iijima, S. (2001). Unique magnetism observed in single-wall carbon nanohorns. *Applied Physics A*, *73*(3), 281–285.

Bandow, Shunji. (1996). Magnetic properties of nested carbon nanostructures studied by electron spin resonance and magnetic susceptibility measurements. *Journal of Applied Physics*, *80*(2), 1020–1027.

Banks, C. E., Davies, T. J., Wildgoose, G. G., & Compton, R. G. (2005). Electrocatalysis at graphite and carbon nanotube modified electrodes: edge-plane sites and tube ends are the reactive sites. *Chemical Communications*, (7), 829–841.

Bao, S., Li, K., Ning, P., Peng, J., Jin, X., & Tang, L. (2017). Highly effective removal of mercury and lead ions from wastewater by mercaptoamine-functionalised silica-coated magnetic nano-adsorbents: behaviours and mechanisms. *Applied Surface Science*, *393*, 457–466.

Barone, P. W., Baik, S., Heller, D. A., & Strano, M. S. (2005). Near-infrared optical sensors based on single-walled carbon nanotubes. *Nature Materials*, *4*(1), 86–92.

Barrios, V. A. E., Méndez, J. R. R., Aguilar, N. V. P., Espinosa, G. A., & Rodríguez, J. L. D. (2012). FTIR–an essential characterization technique for polymeric materials, *InTech*, (Vol. 4).

Basheer, B. V, George, J. J., Siengchin, S., & Parameswaranpillai, J. (2020). Polymer grafted carbon nanotubes—Synthesis, properties, and applications: A review. *Nano-Structures & Nano-Objects*, *22*, 100429.

Batmunkh, M., Biggs, M. J., & Shapter, J. G. (2015). Carbon nanotubes for dye-sensitized solar cells. *Small*, *11*(25), 2963–2989.

Belyanskaya, L., Manser, P., Spohn, P., Bruinink, A., & Wick, P. (2007). The reliability and limits of the MTT reduction assay for carbon nanotubes–cell interaction. *Carbon*, *45*(13), 2643–2648.

Bergveld, P. (1996). The future of biosensors. *Sensors and Actuators A: Physical*, *56*(1–2), 65–73.

Berthomieu, C., & Hienerwadel, R. (2009). Fourier transform infrared (FTIR) spectroscopy. *Photosynthesis Research*, *101*(2), 157–170.

Bhattarai, P., & Hameed, S. (2020). Basics of biosensors and nanobiosensors. *Nanobiosensors: From Design to Applications*, 1–22.

Bhaviripudi, S., Mile, E., Steiner, S. A., Zare, A. T., Dresselhaus, M. S., Belcher, A. M., & Kong, J. (2007). CVD synthesis of single-walled carbon nanotubes from gold nanoparticle catalysts. *Journal of the American Chemical Society*, *129*(6), 1516–1517.

Bilisik, K., & Syduzzaman, M. (2021). Carbon nanotubes in carbon/epoxy multiscale textile preform composites: A review. *Polymer Composites*, *42*(4), 1670–1697.

Bistamam, M. S. A., & Azam, M. A. (2014). Tip-growth of aligned carbon nanotubes on cobalt catalyst supported by alumina using alcohol catalytic chemical vapor deposition. *Results in Physics*, *4*, 105–106.

Black, J. (2005). Biological performance of materials: fundamentals of biocompatibility. *Crc Press.*

Bogdanov, A. A., Deininger, D., & Dyuzhev, G. A. (2000). Development prospects of the commercial production of fullerenes. *Technical Physics*, *45*(5), 521–527.

Bollella, P., & Gorton, L. (2018). Enzyme based amperometric biosensors. *Current Opinion in Electrochemistry*, *10*, 157–173.

Bollmann, W., & Spreadborough, J. (1960). Action of graphite as a lubricant. *Nature*, *186*(4718), 29.

Bondi, S. N., Lackey, W. J., Johnson, R. W., Wang, X., & Wang, Z. L. (2006). Laser assisted chemical vapor deposition synthesis of carbon nanotubes and their characterization. *Carbon*, *44*(8), 1393–1403.

Bottini, M., Rosato, N., & Bottini, N. (2011). PEG-modified carbon nanotubes in biomedicine: current status and challenges ahead. *Biomacromolecules*, *12*(10), 3381–3393.

Bronikowski, M. J. (2022). Growth of carbon nanotubes from ethylene using catalyst particles that incorporate diffusion inhibitor metals. *MRS Advances*, *7*(9), 180–184.

Brownlee, B. J., Claussen, J. C., & Iverson, B. D. (2020). 3D Interdigitated vertically aligned carbon nanotube electrodes for electrochemical impedimetric biosensing. *ACS Applied Nano Materials*, *3*(10), 10166–10175.

Brys, E., Tombelli, S., Minunni, M., Mascini, M., & Turner, A. P. F. (2006). Approaches to allergy detection using aptasensors. In *Smart Biosensor Technology*. CRC Press, 561–588.

Byon, H.-R., Lim, H.-S., Song, H.-J., & Choi, H.-C. (2007). A synthesis of high purity single-walled carbon nanotubes from small diameters of cobalt nanoparticles by using oxygen-assisted chemical vapor deposition process. *Bulletin of the Korean Chemical Society*, *28*(11), 2056–2060.

Cameron, M. A., & George, S. M. (1999). ZrO2 film growth by chemical vapor deposition using zirconium tetra-tert-butoxide. *Thin Solid Films*, *348*(1–2), 90–98.

Campuzano, S., Yáñez-Sedeño, P., & Pingarrón, J. M. (2020). Electrochemical affinity biosensors based on selected nanostructures for food and environmental

monitoring. *Sensors*, *20*(18), 5125.

Carlson, L. J., & Krauss, T. D. (2008). Photophysics of individual single-walled carbon nanotubes. *Accounts of Chemical Research*, *41*(2), 235–243.

Chaisitsak, S., Yamada, A., & Konagai, M. (2004). Hot filament enhanced CVD synthesis of carbon nanotubes by using a carbon filament. *Diamond and Related Materials*, *13*(3), 438–444.

Chakrabarti, S., Nagasaka, T., Yoshikawa, Y., Pan, L., & Nakayama, Y. (2006). Growth of super long aligned brush-like carbon nanotubes. *Japanese Journal of Applied Physics*, *45*(7L), L720.

Chawla, S., Rai, P., & Garain, T. (2023). Carbon Nanotubes-Based Biosensors. *Recent Advances in Metrology*, 29–40.

Chen, R. J., Bangsaruntip, S., Drouvalakis, K. A., Wong Shi Kam, N., Shim, M., Li, Y., Kim, W., Utz, P. J., & Dai, H. (2003). Noncovalent functionalization of carbon nanotubes for highly specific electronic biosensors. *Proceedings of the National Academy of Sciences*, *100*(9), 4984–4989.

Chen, W. Q., Cheong, Y. H., Fu, X., Ge, L. Y., Veksha, A., & Lisak, G. (2021). Fe-assisted catalytic chemical vapor deposition of graphene-like carbon nanosheets over SrO. *Carbon*, *171*, 444–454.

Chen, W., Zhao, J., Zhang, J., Gu, L., Yang, Z., Li, X., Yu, H., Zhu, X., Yang, R., & Shi, D. (2015). Oxygen-assisted chemical vapor deposition growth of large single-crystal and high-quality monolayer MoS2. *Journal of the American Chemical Society*, *137*(50), 15632–15635.

Chen, Z., Chen, B., He, M., Wang, H., & Hu, B. (2019). A porous organic polymer with magnetic nanoparticles on a chip array for preconcentration of platinum (IV), gold (III) and bismuth (III) prior to their on-line quantitation by ICP-MS. *Microchimica Acta*, *186*(2), 1–8.

Chhowalla, M., Teo, K. B. K., Ducati, C., Rupesinghe, N. L., Amaratunga, G. A. J., Ferrari, A. C., Roy, D., Robertson, J., & Milne, a W. I. (2001). Growth process conditions of vertically aligned carbon nanotubes using plasma enhanced chemical

vapor deposition. *Journal of Applied Physics*, *90*(10), 5308–5317.

Cho, W., Schulz, M., & Shanov, V. (2014). Growth and characterization of vertically aligned centimeter long CNT arrays. *Carbon*, *72*, 264–273.

Choi, G. S., Cho, Y. S., Son, K. H., & Kim, D. J. (2003). Mass production of carbon nanotubes using spin-coating of nanoparticles. *Microelectronic Engineering*, *66*(1–4), 77–82.

Choi, T. Y., Poulikakos, D., Tharian, J., & Sennhauser, U. (2005). Measurement of thermal conductivity of individual multiwalled carbon nanotubes by the 3-ω method. *Applied Physics Letters*, *87*(1), 13108.

Chow, L., Wang, H., Kleckley, S., Daly, T. K., & Buseck, P. R. (1995). Fullerene formation during production of chemical vapor deposited diamond. *Applied Physics Letters*, *66*(4), 430–432.

Chung, T. H., & Dhar, B. R. (2021). based platforms for microbial electrochemical cell-based biosensors: A review. *Biosensors and Bioelectronics*, *192*, 113485.

Clark, I. J., & Lyons, C. (1962). Blood glucose determination. *Acad. Sci* (Vol. 102), 27.

Clark JR, L. C., Wolf, R., Granger, D., & Taylor, Z. (1953). Continuous recording of blood oxygen tensions by polarography. *Journal of Applied Physiology*, *6*(3), 189–193.

Cole, M. T., & Milne, W. I. (2013). Plasma Enhanced chemical vapour deposition of horizontally aligned carbon nanotubes. *Materials*, *6*(6), 2262–2273.

Collins, P G, & Avouris, P. (2002). Multishell conduction in multiwalled carbon nanotubes. *Applied Physics A*, *74*(3), 329–332.

Collins, Philip G, Arnold, M. S., & Avouris, P. (2001). Engineering carbon nanotubes and nanotube circuits using electrical breakdown. *Science*, *292*(5517), 706–709.

Colomer, J.-F., Stephan, C., Lefrant, S., Van Tendeloo, G., Willems, I., Konya, Z., Fonseca, A., Laurent, C., & Nagy, J. B. (2000). Large-scale synthesis of single-wall carbon nanotubes by catalytic chemical vapor deposition (CCVD) method.

Chemical Physics Letters, *317*(1–2), 83–89.

Compeán-Jasso, M. E., Ruiz, F., Martínez, J. R., & Herrera-Gómez, A. (2008). Magnetic properties of magnetite nanoparticles synthesized by forced hydrolysis. *Materials Letters*, *62*(27), 4248–4250.

Conroy, P. J., Hearty, S., Leonard, P., & O'Kennedy, R. J. (2009). Antibody production, design and use for biosensor-based applications. *Seminars in Cell & Developmental Biology* (Vol. 20). Elsevier, 10–26.

Coon, V. T., Takeshita, T., Wallace, W. E., & Craig, R. S. (1976). Rare earth intermetallics as catalysts for the production of hydrocarbons from carbon monoxide and hydrogen. *The Journal of Physical Chemistry*, *80*(17), 1878–1879.

Coquay, P., Peigney, A., De Grave, E., Flahaut, E., Vandenberghe, R. E., & Laurent, C. (2005). Fe/Co alloys for the catalytic chemical vapor deposition synthesis of single-and double-walled carbon nanotubes (CNTs). 1. The CNT− Fe/Co− MgO system. *The Journal of Physical Chemistry B*, *109*(38), 17813–17824.

Couteau, E., Hernadi, K., Seo, J. W., Thien-Nga, L., Mikó, C., Gaal, R., & Forro, L. (2003). CVD synthesis of high-purity multiwalled carbon nanotubes using CaCO3 catalyst support for large-scale production. *Chemical Physics Letters*, *378*(1–2), 9–17.

Crawford, B., Esposito, D., Jain, V., & Pelletier, D. (2007). Flexible carbon nanotube based temperature sensor for ultra-small-site applications. Department of Mechanical and Industrial Engineering College of Engineering, Northeastern University, 7–11.

Croslyn, A. E., Smith, B. W., & Winefordner, J. D. (1997). A review of microwave plasma sources in atomic emission spectrometry: literature from 1985 to the present. *Critical Reviews in Analytical Chemistry*, *27*(3), 199–255.

Cui, R., Zhang, Y., Wang, J., Zhou, W., & Li, Y. (2010). Comparison between copper and iron as catalyst for chemical vapor deposition of horizontally aligned ultralong single-walled carbon nanotubes on silicon substrates. *The Journal of Physical Chemistry C*, *114*(37), 15547–15552.

Cui, Y., Lai, B., & Tang, X. (2019). Microbial fuel cell-based biosensors. *Biosensors*, *9*(3), 92.

Dai, B., Zhou, R., Ping, J., Ying, Y., & Xie, L. (2022). Recent advances in carbon nanotube-based biosensors for biomolecular detection. *TrAC Trends in Analytical Chemistry*, 116658.

Dai, H. (2002a). Carbon nanotubes: opportunities and challenges. *Surface Science*, *500*(1–3), 218–241.

Dai, H. (2002b). Carbon nanotubes: synthesis, integration, and properties. *Accounts of Chemical Research*, *35*(12), 1035–1044.

Daliri, F., Aboagye, A. A., Kyei-Baffour, V., Elahi, F., Chelliah, R., & Daliri, E. B.-M. (2019). Immunosensors for food safety: current trends and future perspectives. *Journal of Food Hygiene and Safety*, *34*(6), 509–518.

Danafar, F., Fakhru'l-Razi, A., Salleh, M. A. M., & Biak, D. R. A. (2009). Fluidized bed catalytic chemical vapor deposition synthesis of carbon nanotubes—A review. *Chemical Engineering Journal*, *155*(1–2), 37–48.

Das, A. B., Kumari, T., & Sahu, P. P. (2022). Calorimetric Biosensors: Core Principles, Techniques, Fabrication and Application. In *Biosensors in Food Safety and Quality*. CRC Press, 11–21.

Das, R., Shahnavaz, Z., Ali, M., Islam, M. M., & Abd Hamid, S. B. (2016). Can we optimize arc discharge and laser ablation for well-controlled carbon nanotube synthesis? *Nanoscale Research Letters*, *11*(1), 1–23.

Davis, W. M., Erickson, C. L., Johnston, C. T., Delfino, J. J., & Porter, J. E. (1999). Quantitative Fourier Transform Infrared spectroscopic investigation humic substance functional group composition. *Chemosphere*, *38*(12), 2913–2928.

De Heer, W. A., Chatelain, A., & Ugarte, D. (1995). A carbon nanotube field-emission electron source. *Science*, *270*(5239), 1179–1180.

de los Arcos, T., Vonau, F., Garnier, M. G., Thommen, V., Boyen, H.-G., Oelhafen, P., Düggelin, M., Mathis, D., & Guggenheim, R. (2002). Influence of iron–silicon

interaction on the growth of carbon nanotubes produced by chemical vapor deposition. *Applied Physics Letters*, *80*(13), 2383–2385.

Delzeit, L., Nguyen, C. V, Chen, B., Stevens, R., Cassell, A., Han, J., & Meyyappan, M. (2002). Multiwalled carbon nanotubes by chemical vapor deposition using multilayered metal catalysts. *The Journal of Physical Chemistry B*, *106*(22), 5629–5635.

Di Gianfrancesco, A. (2017). Technologies for chemical analyses, microstructural and inspection investigations. In *Materials for Ultra-Supercritical and Advanced Ultra-Supercritical Power Plants*. Elsevier, 197–245.

Diao, G., Li, H., Liang, H., Ivanenko, I., Dontsova, T., & Astrelin, I. (2018). CVD synthesis of multi-walled carbon nanotubes onto different catalysts at low temperature. *Nano*, *13*(04), 1850036.

Díez-Pascual, Ana M, Naffakh, M., Gómez, M. A., Marco, C., Ellis, G., González-Domínguez, J. M., Ansón, A., Martínez, M. T., Martínez-Rubi, Y., & Simard, B. (2009). The influence of a compatibilizer on the thermal and dynamic mechanical properties of PEEK/carbon nanotube composites. *Nanotechnology*, *20*(31), 315707.

Díez-Pascual, Ana Maria. (2021). Chemical functionalization of carbon nanotubes with polymers: a brief overview. *Macromol*, *1*(2), 64–83.

Dinadayalane, T. C., & Leszczynski, J. (2007). Toward nanomaterials: structural, energetic and reactivity aspects of single-walled carbon nanotubes. In *Theoretical and Computational Chemistry* (Vol. 18). Elsevier, 167–199.

Ding, D., Wang, J., Cao, Z., & Dai, J. (2003). Synthesis of carbon nanostructures on nanocrystalline Ni-Ni 3 P catalyst supported by SiC whiskers. *Carbon*, *3*(41), 579–582.

Ding, F., Larsson, P., Larsson, J. A., Ahuja, R., Duan, H., Rosén, A., & Bolton, K. (2008). The importance of strong carbon− metal adhesion for catalytic nucleation of single-walled carbon nanotubes. *Nano letters*, *8*(2), 463–468.

Ding, J., & Qin, W. (2020). Recent advances in potentiometric biosensors. *TrAC Trends in Analytical Chemistry*, *124*, 115803.

Donahue, A. C., & Albitar, M. (2010). Antibodies in biosensing. In *Recognition Receptors in Biosensors*. Springer, 221–248.

Dong, J., & Ueda, H. (2021). Recent advances in quenchbody, a fluorescent immunosensor. *Sensors*, *21*(4), 1223.

Dresselhaus, G., & Riichiro, S. (1998). *Physical properties of carbon nanotubes*. World Scientific, 52–122.

Dresselhaus, M S, Dresselhaus, G., Jorio, A., Souza Filho, A. G., & Saito, R. (2002). Raman spectroscopy on isolated single wall carbon nanotubes. *Carbon*, *40*(12), 2043–2061.

Dresselhaus, Mildred S, Dresselhaus, G., & Eklund, P. C. (1996). Science of fullerenes and carbon nanotubes: their properties and applications. Elsevier.

Ducati, C., Alexandrou, I., Chhowalla, M., Amaratunga, G. A. J., & Robertson, J. (2002). Temperature selective growth of carbon nanotubes by chemical vapor deposition. *Journal of Applied Physics*, *92*(6), 3299–3303.

Duchamp, M., Lee, K., Dwir, B., Seo, J. W., Kapon, E., Forró, L., & Magrez, A. (2010). Controlled positioning of carbon nanotubes by dielectrophoresis: insights into the solvent and substrate role. *ACS Nano*, *4*(1), 279–284.

Dupuis, A.-C. (2005). The catalyst in the CCVD of carbon nanotubes—a review. *Progress in Materials Science*, *50*(8), 929–961.

Dutta, K., De, S., Das, B., Bera, S., Guria, B., Ali, M. S., & Chattopadhyay, D. (2021). Development of an Efficient Immunosensing Platform by Exploring Single-Walled Carbon Nanohorns (SWCNHs) and Nitrogen Doped Graphene Quantum Dot (N-GQD) Nanocomposite for Early Detection of Cancer Biomarker. *ACS Biomaterials Science & Engineering*, *7*(12), 5541–5554.

Duty, C., Jean, D., & Lackey, W. J. (2001). Laser chemical vapour deposition: materials, modelling, and process control. *International Materials Reviews*, *46*(6), 271–287.

Eddaif, L., Shaban, A., & Telegdi, J. (2019). Sensitive detection of heavy metals ions

based on the calixarene derivatives-modified piezoelectric resonators: A review. *International Journal of Environmental Analytical Chemistry*, *99*(9), 824–853.

Eggins, B. R. (2013). *Biosensors: an introduction*. Springer-Verlag, 51–86.

Enevoldsen, R., & Juhler, R. K. (2010). Perfluorinated compounds (PFCs) in groundwater and aqueous soil extracts: using inline SPE-LC-MS/MS for screening and sorption characterisation of perfluorooctane sulphonate and related compounds. *Analytical and Bioanalytical Chemistry*, *398*(3), 1161–1172.

Ensafi, A. A. (2019). An introduction to sensors and biosensors. In *Electrochemical Biosensors*. Elsevier, 1–10.

Esteves, L. M., Oliveira, H. A., & Passos, F. B. (2018). Carbon nanotubes as catalyst support in chemical vapor deposition reaction: A review. *Journal of Industrial and Engineering Chemistry*, *65*, 1–12.

Esteves, L. M., Oliveira, H. A., Xing, Y., & Passos, F. B. (2021). Cobalt supported on carbon nanotubes for methane chemical vapor deposition for the production of new carbon nanotubes. *New Journal of Chemistry*, *45*(31), 14218–14226.

Fan, H., Li, H., Wang, Q., He, P., & Fang, Y. (2012). A host–guest-recognition-based electrochemical aptasensor for thrombin detection. *Biosensors and Bioelectronics*, *35*(1), 33–36.

Farhat, S., & Scott, C. D. (2006). Review of the arc process modeling for fullerene and nanotube production. *Journal of Nanoscience and Nanotechnology*, *6*(5), 1189–1210.

Farka, Z., Juřík, T., Kovář, D., Trnková, L., & Skládal, P. (2017). Nanoparticle-based immunochemical biosensors and assays: recent advances and challenges. *Chemical Reviews*, *117*(15), 9973–10042.

Fatima, A., Younas, I., & Ali, M. W. (2022). An Overview on recent advances in biosensor technology and its future application. *Archives of Pharmacy Practice*, *13*(1).

Ferrier, D. C., & Honeychurch, K. C. (2021). Carbon nanotube (CNT)-based

biosensors. *Biosensors*, *11*(12), 486.

Fix, R., Gordon, R. G., & Hoffman, D. M. (1991). Chemical vapor deposition of titanium, zirconium, and hafnium nitride thin films. *Chemistry of Materials*, *3*(6), 1138–1148.

Fix, R., Gordon, R. G., & Hoffman, D. M. (1993). Chemical vapor deposition of vanadium, niobium, and tantalum nitride thin films. *Chemistry of Materials*, *5*(5), 614–619.

Fowler, J. M., Wong, D. K. Y., Halsall, H. B., & Heineman, W. R. (2008). Recent developments in electrochemical immunoassays and immunosensors. *Electrochemical Sensors, Biosensors and Their Biomedical Applications*, 115–143.

Fujigaya, T., & Nakashima, N. (2008). Methodology for homogeneous dispersion of single-walled carbon nanotubes by physical modification. *Polymer Journal*, *40*(7), 577–589.

Futaba, D. N., Hata, K., Namai, T., Yamada, T., Mizuno, K., Hayamizu, Y., Yumura, M., & Iijima, S. (2006). 84% catalyst activity of water-assisted growth of single walled carbon nanotube forest characterization by a statistical and macroscopic approach. *The Journal of Physical Chemistry B*, *110*(15), 8035–8038.

Futaba, D. N., Hata, K., Yamada, T., Mizuno, K., Yumura, M., & Iijima, S. (2005). Kinetics of water-assisted single-walled carbon nanotube synthesis revealed by a time-evolution analysis. *Physical Review Letters*, *95*(5), 56104.

Ganesh, E. N. (2013). Single walled and multi walled carbon nanotube structure, synthesis and applications. *International Journal of Innovative Technology and Exploring Engineering*, *2*(4), 311–320.

Garg, A., Chalak, H. D., Belarbi, M. O., Zenkour, A. M., & Sahoo, R. (2021). Estimation of carbon nanotubes and their applications as reinforcing composite materials–an engineering review. *Composite Structures*, *272*, 114234.

Gavillet, J., Loiseau, A., Journet, C., Willaime, F., Ducastelle, F., & Charlier, J.-C. (2001). Root-growth mechanism for single-wall carbon nanotubes. *Physical Review Letters*, *87*(27), 275504.

Gergeroglu, H., Yildirim, S., & Ebeoglugil, M. F. (2020). Nano-carbons in biosensor applications: an overview of carbon nanotubes (CNTs) and fullerenes (C 60). *SN Applied Sciences*, *2*(4), 1–22.

Ghaemi, F., Ali, M., Yunus, R., & Othman, R. N. (2019). Synthesis of carbon nanomaterials using catalytic chemical vapor deposition technique. In *Synthesis, Technology and Applications of Carbon Nanomaterials*. Elsevier, 1–27.

Ghai, V., Chatterjee, K., & Agnihotri, P. K. (2021). Vertically aligned carbon nanotubes-coated aluminium foil as flexible supercapacitor electrode for high power applications. *Carbon Letters*, *31*(3), 473–481.

Ghorannevis, Z., Kato, T., Kaneko, T., & Hatakeyama, R. (2010). Growth of single-walled carbon nanotubes from nonmagnetic catalysts by plasma chemical vapor deposition. *Japanese Journal of Applied Physics*, *49*(2S), 02BA01.

Ghoranneviss, M., & Elahi, A. S. (2016). Review of carbon nanotubes production by thermal chemical vapor deposition technique. *Molecular Crystals and Liquid Crystals*, *629*(1), 158–164.

Gillen, A. J., & Boghossian, A. A. (2019). Non-covalent methods of engineering optical sensors based on single-walled carbon nanotubes. *Frontiers in Chemistry*, *7*, 612.

Girun, N., Ahmadun, F., Rashid, S. A., & Ali Atieh, M. (2007). Multi-wall carbon nanotubes/styrene butadiene rubber (SBR) nanocomposite. *Fullerenes, Nanotubes, and Carbon Nanostructures*, *15*(3), 207–214.

Glerup, M., Kanzow, H., Almairac, R., Castignolles, M., & Bernier, P. (2003). Synthesis of multi-walled carbon nanotubes and nano-fibres using the aerosol method with metal-ions as the catalyst precursors. *Chemical Physics Letters*, *377*(3–4), 293–298.

Gorduk, O., Gencten, M., Gorduk, S., Sahin, M., & Sahin, Y. (2021). Electrochemical fabrication and supercapacitor performances of metallo phthalocyanine/functionalized-multiwalled carbon nanotube/polyaniline modified hybrid electrode materials. *Journal of Energy Storage*, *33*, 102049.

Gu, M., Zhao, Z., Liu, J., Liu, G., Zhang, B., El-Khouly, M. E., & Chen, Y. (2021). Conjugated polymer covalently modified multi-walled carbon nanotubes for flexible nonvolatile RRAM devices. *European Polymer Journal*, *142*, 110153.

Gubernat, M., & Zambrzycki, M. (2021). Catalytic activity of K10 montmorillonite in the chemical vapor deposition of multi-wall carbon nanotubes from methane. *Applied Clay Science*, *211*, 106178.

Guellati, O., Bégin, D., Antoni, F., Moldovan, S., Guerioune, M., Pham-Huu, C., & Janowska, I. (2018). CNTs' array growth using the floating catalyst-CVD method over different substrates and varying hydrogen supply. *Materials Science and Engineering: B*, *231*, 11–17.

Guéret, C., Daroux, M., & Billaud, F. (1997). Methane pyrolysis: thermodynamics. *Chemical Engineering Science*, *52*(5), 815–827.

Guilbault, G. G., & Montalvo Jr, J. G. (1969). Urea-specific enzyme electrode. *Journal of the American Chemical Society*, *91*(8), 2164–2165.

Guo, T., Nikolaev, P., & Rinzler, A. G. (1995). D. Toma nek, DT Colbert, RE Smalley. Self-assembly of tubular fullerenes. *J. Phys. Chem*, *99*, 10694.

Gupta, Niharika, Renugopalakrishnan, V., Liepmann, D., Paulmurugan, R., & Malhotra, B. D. (2019). Cell-based biosensors: Recent trends, challenges and future perspectives. *Biosensors and Bioelectronics*, *141*, 111435.

Gupta, Nikita, Gupta, S. M., & Sharma, S. K. (2019). Carbon nanotubes: Synthesis, properties and engineering applications. *Carbon Letters*, *29*(5), 419–447.

Haidari, J., Khabbaz, M. B., Radman, H., Maghrebi, M., & Baniadam, M. (2022). Effect of carbon precursor flowrate on the quality and quantity of carbon nanotubes. *Diamond and Related Materials*, *125*, 108984.

Hall, E. A. H. (1990). Biosensors, Ch. 1: Biosensors in context. *Open University Press*, *2*.

Hamada, N., Sawada, S., & Oshiyama, A. (1992). New one-dimensional conductors: Graphitic microtubules. *Physical Review Letters*, *68*(10), 1579.

Han, J. H., Shin, K. H., & Lee, Y. J. (2021). Scalable binder-free freestanding electrodes based on a cellulose acetate-assisted carbon nanotube fibrous network for practical flexible li-ion batteries. *ACS Applied Materials & Interfaces*, *13*(5), 6375–6384.

Hara, T. O., & Singh, B. (2021). Electrochemical biosensors for detection of pesticides and heavy metal toxicants in water: recent trends and progress. *ACS ES&T Water*, *1*(3), 462–478.

Hart, A. J., & Slocum, A. H. (2006). Rapid growth and flow-mediated nucleation of millimeter-scale aligned carbon nanotube structures from a thin-film catalyst. *The Journal of Physical Chemistry B*, *110*(16), 8250–8257.

Hartschuh, A., Pedrosa, H. N., Peterson, J., Huang, L., Anger, P., Qian, H., Meixner, A. J., Steiner, M., Novotny, L., & Krauss, T. D. (2005). Single carbon nanotube optical spectroscopy. *ChemPhysChem*, *6*(4), 577–582.

Hasan, J., Crawford, R. J., & Ivanova, E. P. (2013). Antibacterial surfaces: the quest for a new generation of biomaterials. *Trends in Biotechnology*, *31*(5), 295–304.

Hasanzadeh, I., & Eskandari, M. J. (2020). Direct growth of multiwall carbon nanotube on metal catalyst by chemical vapor deposition: In situ nucleation. *Surface and Coatings Technology*, *381*, 125109.

Hata, K., Futaba, D. N., Mizuno, K., Namai, T., Yumura, M., & Iijima, S. (2004). Water-assisted highly efficient synthesis of impurity-free single-walled carbon nanotubes. *Science*, *306*(5700), 1362–1364.

He, C. N., Zhao, N. Q., Du, X. W., Shi, C. S., Li, J. J., & He, F. (2008). Characterization of bamboo-shaped CNTs prepared using deposition-precipitation catalyst. *Materials Science and Engineering: A*, *479*(1–2), 248–252.

He, C., Zhao, N., Du, X., Shi, C., Ding, J., Li, J., & Li, Y. (2006). Low-temperature synthesis of carbon onions by chemical vapor deposition using a nickel catalyst supported on aluminum. *Scripta Materialia*, *54*(4), 689–693.

He, M., Fedotov, P. V, Chernov, A., Obraztsova, E. D., Jiang, H., Wei, N., Cui, H., Sainio, J., Zhang, W., & Jin, H. (2016). Chiral-selective growth of single-walled

carbon nanotubes on Fe-based catalysts using CO as carbon source. *Carbon*, *108*, 521–528.

Helland, A., Wick, P., Koehler, A., Schmid, K., & Som, C. (2007). Reviewing the environmental and human health knowledge base of carbon nanotubes. *Environmental Health Perspectives*, *115*(8), 1125–1131.

Heller, D. A., Barone, P. W., Swanson, J. P., Mayrhofer, R. M., & Strano, M. S. (2004). Using Raman spectroscopy to elucidate the aggregation state of single-walled carbon nanotubes. *The Journal of Physical Chemistry B*, *108*(22), 6905–6909.

Hernadi, K., Fonseca, A., Nagy, J. B., Bemaerts, D., Fudala, A., & Lucas, A. A. (1996). Catalytic synthesis of carbon nanotubes using zeolite support. *Zeolites*, *5*(17), 416–423.

Hernadi, K., Fonseca, A., Nagy, J. B., Bernaerts, D., & Lucas, A. A. (1996). Fe-catalyzed carbon nanotube formation. *Carbon*, *34*(10), 1249–1257.

Hicks, M., Bachmann, T. T., & Wang, B. (2020). Synthetic biology enables programmable cell-based biosensors. *ChemPhysChem*, *21*(2), 132–144.

Hillert, M., & Lange, N. (1959). The structure of graphite filaments. *Zeitschrift für Kristallographie-Crystalline Materials*, *111*(1–6), 24–34.

Ho, G. W., Wee, A. T. S., Lin, J., & Tjiu, W. C. (2001). Synthesis of well-aligned multiwalled carbon nanotubes on Ni catalyst using radio frequency plasma-enhanced chemical vapor deposition. *Thin Solid Films*, *388*(1–2), 73–77.

Hoecker, C., Smail, F., Bajada, M., Pick, M., & Boies, A. (2016). Catalyst nanoparticle growth dynamics and their influence on product morphology in a CVD process for continuous carbon nanotube synthesis. *Carbon*, *96*, 116–124.

Hoecker, C., Smail, F., Pick, M., & Boies, A. (2017). The influence of carbon source and catalyst nanoparticles on CVD synthesis of CNT aerogel. *Chemical Engineering Journal*, *314*, 388–395.

Hofmann, S., Kleinsorge, B., Ducati, C., Ferrari, A. C., & Robertson, J. (2004). Low-temperature plasma enhanced chemical vapour deposition of carbon nanotubes.

Diamond and Related Materials, *13*(4–8), 1171–1176.

Holloway, A. F., Toghill, K., Wildgoose, G. G., Compton, R. G., Ward, M. A. H., Tobias, G., Llewellyn, S. A., Ballesteros, B., Green, M. L. H., & Crossley, A. (2008). Electrochemical opening of single-walled carbon nanotubes filled with metal halides and with closed ends. *The Journal of Physical Chemistry C*, *112*(28), 10389–10397.

Holloway, A. F., Wildgoose, G. G., Compton, R. G., Shao, L., & Green, M. L. H. (2008). The influence of edge-plane defects and oxygen-containing surface groups on the voltammetry of acid-treated, annealed and "super-annealed" multiwalled carbon nanotubes. *Journal of Solid State Electrochemistry*, *12*(10), 1337–1348.

Homma, Y. (2014). Gold nanoparticles as the catalyst of single-walled carbon nanotube synthesis. *Catalysts*, *4*(1), 38–48.

Hone, J. (2001). Phonons and thermal properties of carbon nanotubes. In *Carbon Nanotubes*. Springer, 273–286.

Hone, J., Whitney, M., Piskoti, C., & Zettl, A. (1999). Thermal conductivity of single-walled carbon nanotubes. *Physical Review B*, *59*(4), R2514.

Hongo, H., Yudasaka, M., Ichihashi, T., Nihey, F., & Iijima, S. (2002). Chemical vapor deposition of single-wall carbon nanotubes on iron-film-coated sapphire substrates. *Chemical physics letters*, *361*(3–4), 349–354.

Hosseinzadeh, L., & Mazloum-Ardakani, M. (2020). Advances in aptasensor technology. *Advances in Clinical Chemistry*, *99*, 237–279.

Hou, B., Xiang, R., Inoue, T., Einarsson, E., Chiashi, S., Shiomi, J., Miyoshi, A., & Maruyama, S. (2011). Decomposition of ethanol and dimethyl ether during chemical vapor deposition synthesis of single-walled carbon nanotubes. *Japanese Journal of Applied Physics*, *50*(6R), 65101.

Hou, C., Li, T., Zhao, T., Liu, H., Liu, L., & Zhang, W. (2013). Electromagnetic wave absorbing properties of multi-wall carbon nanotube/Fe_3O_4 hybrid materials. *New Carbon Materials*, *28*(3), 184–190.

Hou, X., & Choy, K. (2006). Processing and applications of aerosol-assisted chemical vapor deposition. *Chemical Vapor Deposition*, *12*(10), 583–596.

Hu, A., Long, J., Shu, C., Liang, R., & Li, J. (2018). Three-dimensional interconnected network architecture with homogeneously dispersed carbon nanotubes and layered MoS2 as a highly efficient cathode catalyst for lithium–oxygen battery. *ACS Applied Materials & Interfaces*, *10*(40), 34077–34086.

Hua, Y., Ma, J., Li, D., & Wang, R. (2022). DNA-Based biosensors for the biochemical analysis: A Review. *Biosensors*, *12*(3), 183.

Huang, S., Cai, Q., Chen, J., Qian, Y., & Zhang, L. (2009). Metal-catalyst-free growth of single-walled carbon nanotubes on substrates. *Journal of the American Chemical Society*, *131*(6), 2094–2095.

Huseynov, A., Mammadova, S., Zeynalov, E., Israfilov, A., & Abdullayeva, S. (2022). Synthesis of MWCNTs from xylenes for fabrication of highly electrically conductive and gas-sensitive polymer composites. *Fullerenes, Nanotubes and Carbon Nanostructures*, 1–12.

Hyun, K., Han, S. W., Koh, W.-G., & Kwon, Y. (2015). Direct electrochemistry of glucose oxidase immobilized on carbon nanotube for improving glucose sensing. *International Journal of Hydrogen Energy*, *40*(5), 2199–2206.

Ichihashi, T. (1993). Erratum: Single-shell carbon nanotubes of 1-nm diameter. *Nature*, *364*(6439), 737.

Iijima, S. (1991). Helical microtubules of graphitic carbon. *Nature*, *354*, 56–58.

Imamoto, T., Mita, T., & Yokoyama, M. (1987). Reduction of organic compounds with rare-earth intermetallics containing absorbed hydrogen. *The Journal of Organic Chemistry*, *52*(26), 5695–5699.

Imry, Y., & Landauer, R. (1999). Conductance viewed as transmission. *Reviews of Modern Physics*, *71*(2), S306.

Iqbal, M. A., Gupta, S. G., & Hussaini, S. S. (2012). A Review on electrochemical biosensors: Principles and applications. *Advances in Bioresearch*, *3*(4).

Isildak, Ö., & Özbek, O. (2021). Application of potentiometric sensors in real samples. *Critical Reviews in Analytical Chemistry*, *51*(3), 218–231.

Ivanov, V., Nagy, J. B., Lambin, P., Lucas, A., Zhang, X. B., Zhang, X. F., Bernaerts, D., Van Tendeloo, G., Amelinckx, S., & Van Landuyt, J. (1994). The study of carbon nanotubules produced by catalytic method. *Chemical Physics Letters*, *223*(4), 329–335.

Izadi-Najafabadi, A., Yasuda, S., Kobashi, K., Yamada, T., Futaba, D. N., Hatori, H., Yumura, M., Iijima, S., & Hata, K. (2010). Extracting the full potential of single-walled carbon nanotubes as durable supercapacitor electrodes operable at 4 V with high power and energy density. *Advanced Materials*, *22*(35), E235–E241.

Jampilek, J., & Kralova, K. (2021). Advances in drug delivery nanosystems using graphene-based materials and carbon nanotubes. *Materials*, *14*(5), 1059.

Jauberteau, J. L., Thomas, L., Aubreton, J., Jauberteau, I., & Catherinot, A. (1998). High reactivity of CH2 radical in an Ar–CH4 post-discharge. *Plasma Chemistry and Plasma Processing*, *18*(1), 137–151.

Jha, A. (2021). Biosensors for environmental monitoring. In *Basic Concepts in Environmental Biotechnology*. CRC Press, 103–118.

Jia, X., & Wei, F. (2019). Advances in production and applications of carbon nanotubes. *Single-Walled Carbon Nanotubes*, 299–333.

Joshi, P., Mishra, R., & Narayan, R. J. (2021). Biosensing applications of carbon-based materials. *Current Opinion in Biomedical Engineering*, *18*, 100274.

Jourdain, V., & Bichara, C. (2013). Current understanding of the growth of carbon nanotubes in catalytic chemical vapour deposition. *Carbon*, *58*, 2–39.

Jozanović, M., Sakač, N., Karnaš, M., & Medvidović-Kosanović, M. (2021). Potentiometric sensors for the determination of anionic surfactants–a review. *Critical Reviews in Analytical Chemistry*, *51*(2), 115–137.

Jun, L. Y., Mubarak, N. M., Yee, M. J., Yon, L. S., Bing, C. H., Khalid, M., & Abdullah, E. C. (2018). An overview of functionalised carbon nanomaterial for

organic pollutant removal. *Journal of Industrial and Engineering Chemistry*, *67*, 175–186.

Jung, M., Eun, K. Y., Lee, J.-K., Baik, Y.-J., Lee, K.-R., & Park, J. W. (2001). Growth of carbon nanotubes by chemical vapor deposition. *Diamond and Related Materials*, *10*(3–7), 1235–1240.

Jung, Y., Song, J., Huh, W., Cho, D., & Jeong, Y. (2013). Controlling the crystalline quality of carbon nanotubes with processing parameters from chemical vapor deposition synthesis. *Chemical Engineering Journal*, *228*, 1050–1056.

Kanada, R., Pan, L., Akita, S., Okazaki, N., Hirahara, K., & Nakayama, Y. (2008). Synthesis of multiwalled carbon nanocoils using codeposited thin film of Fe–Sn as catalyst. *Japanese Journal of Applied Physics*, *47*(4R), 1949.

Kang, C.-S., Ko, Y.-I., Fujisawa, K., Yokokawa, T., Kim, J. H., Han, J. H., Wee, J.-H., Kim, Y. A., Muramatsu, H., & Hayashi, T. (2020). Hybridized double-walled carbon nanotubes and activated carbon as free-standing electrode for flexible supercapacitor applications. *Carbon Letters*, *30*(5), 527–534.

Kaper, J. B., Nataro, J. P., & Mobley, H. L. T. (2004). Pathogenic escherichia coli. *Nature Reviews Microbiology*, *2*(2), 123–140.

Karadurmus, L., Kaya, S., & Ozkan, S. A. (2021). Recent advances of enzyme biosensors for pesticide detection in foods. *Journal of Food Measurement and Characterization*, *15*(5), 4582–4595.

Karimi-Maleh, H., Orooji, Y., Karimi, F., Alizadeh, M., Baghayeri, M., Rouhi, J., Tajik, S., Beitollahi, H., Agarwal, S., & Gupta, V. K. (2021). A critical review on the use of potentiometric based biosensors for biomarkers detection. *Biosensors and Bioelectronics*, *184*, 113252.

Karousis, N., Tagmatarchis, N., & Tasis, D. (2010). Current progress on the chemical modification of carbon nanotubes. *Chemical Reviews*, *110*(9), 5366–5397.

Kataura, H., Kumazawa, Y., Maniwa, Y., Umezu, I., Suzuki, S., Ohtsuka, Y., & Achiba, Y. (1999). Optical properties of single-wall carbon nanotubes. *Synthetic Metals*, *103*(1–3), 2555–2558.

Katharria, Y. S., Kumar, S., Singh, F., Pivin, J. C., & Kanjilal, D. (2006). Synthesis of buried SiC using an energetic ion beam. *Journal of Physics D: Applied Physics*, *39*(18), 3969.

Kato, T., & Hatakeyama, R. (2010). Direct growth of short single-walled carbon nanotubes with narrow-chirality distribution by time-programmed plasma chemical vapor deposition. *ACS Nano*, *4*(12), 7395–7400.

Khalid, P., Hussain, M. A., Suman, V. B., & Arun, A. B. (2016). Toxicology of carbon nanotubes-a review. *International Journal of Applied Engineering Research*, *11*(1), 148–157.

Khalil, M. M., Moaty, S. A. A., & Korany, M. A. (2018). Carbon nanotubes based potentiometric sensor for determination of bambuterol hydrochloride: Electrochemical and morphology study. *Sensors and Actuators B: Chemical*, *273*, 429–438.

Khani, Hadi, Rofouei, M. K., Arab, P., Gupta, V. K., & Vafaei, Z. (2010). Multi-walled carbon nanotubes-ionic liquid-carbon paste electrode as a super selectivity sensor: application to potentiometric monitoring of mercury ion (II). *Journal of Hazardous Materials*, *183*(1–3), 402–409.

Khani, Hassan, & Moradi, O. (2013). Influence of surface oxidation on the morphological and crystallographic structure of multi-walled carbon nanotubes via different oxidants. *Journal of Nanostructure in Chemistry*, *3*(1), 1–8.

Kharlamova, M. V, & Kramberger, C. (2021). Applications of filled single-walled carbon nanotubes: Progress, challenges, and perspectives. *Nanomaterials*, *11*(11), 2863.

Khorrami, S. A., & Lotfi, R. (2016). Influence of carrier gas flow rate on carbon nanotubes growth by TCVD with Cu catalyst. *Journal of Saudi Chemical Society*, *20*(4), 432–436.

Kidambi, P. R., Ducati, C., Dlubak, B., Gardiner, D., Weatherup, R. S., Martin, M.-B., Seneor, P., Coles, H., & Hofmann, S. (2012). The parameter space of graphene chemical vapor deposition on polycrystalline Cu. *The Journal of Physical*

Chemistry C, *116*(42), 22492–22501.

Kierzek, K., Frackowiak, E., Lota, G., Gryglewicz, G., & Machnikowski, J. (2004). Electrochemical capacitors based on highly porous carbons prepared by KOH activation. *Electrochimica Acta*, *49*(4), 515–523.

Kim, M., Osone, S., Kim, T., Higashi, H., & Seto, T. (2017). Synthesis of nanoparticles by laser ablation: A Review. *KONA Powder and Particle Journal*, 2017009.

Kim, P., Shi, L., Majumdar, A., & McEuen, P. L. (2001). Thermal transport measurements of individual multiwalled nanotubes. *Physical Review Letters*, *87*(21), 215502.

Kim, S., Gang, I. J., Park, Y. S., & Han, J. H. (2021). Facile tuning of carbon nanotube morphologies via residual carbon control during catalyst preparation stage. *Carbon Letters*, *31*(4), 809–819.

Kitiyanan, B., Alvarez, W. E., Harwell, J. H., & Resasco, D. E. (2000). Controlled production of single-wall carbon nanotubes by catalytic decomposition of CO on bimetallic Co–Mo catalysts. *Chemical Physics Letters*, *317*(3–5), 497–503.

Klinbumrung, A., Phuruangrat, A., Thongtem, T., & Thongtem, S. (2018). Synthesis, characterization and optical properties of $BaMoO_4$ synthesized by microwave induced plasma method. *Russian Journal of Inorganic Chemistry*, *63*(6), 725–731.

Kong, J., Cassell, A. M., & Dai, H. (1998). Chemical vapor deposition of methane for single-walled carbon nanotubes. *Chemical Physics Letters*, *292*(4–6), 567–574.

Kong, J., Yenilmez, E., Tombler, T. W., Kim, W., Dai, H., Laughlin, R. B., Liu, L., Jayanthi, C. S., & Wu, S. Y. (2001). Quantum interference and ballistic transmission in nanotube electron waveguides. *Physical Review Letters*, *87*(10), 106801.

Kong, J., Zhou, C., Morpurgo, A., Soh, H. T., Quate, C. F., Marcus, C., & Dai, H. (1999). Synthesis, integration, and electrical properties of individual single-walled carbon nanotubes. *Applied Physics A*, *69*(3), 305–308.

Kour, R., Arya, S., Young, S.-J., Gupta, V., Bandhoria, P., & Khosla, A. (2020).

Recent advances in carbon nanomaterials as electrochemical biosensors. *Journal of the Electrochemical Society*, *167*(3), 37555.

Koyun, A., Ahlatcolu, E., Koca, Y., & Kara, S. (2012). Biosensors and their principles. *A Roadmap of Biomedical Engineers and Milestones*, 117–142.

Kozitsina, A. N., Svalova, T. S., Malysheva, N. N., Okhokhonin, A. V, Vidrevich, M. B., & Brainina, K. Z. (2018). Sensors based on bio and biomimetic receptors in medical diagnostic, environment, and food analysis. *Biosensors*, *8*(2), 35.

Krishnan, S. V., Ambalam, M. M., Venkatesan, R., Mayandi, J., & Venkatachalapathy, V. (2021). Technical review: Improvement of mechanical properties and suitability towards armor applications–Alumina composites. *Ceramics International*, *47*(17), 23693–23701.

Krishnia, L., Kumari, R., Kumar, V., Singh, A., Garg, P., S Yadav, B., & K Tyagi, P. (2016). Comparative study of thermal stability of filled and un-filled multiwalled carbon nanotubes. *Advanced Materials Letters*, *7*(3), 230-234.

Kruusma, J., Mould, N., Jurkschat, K., Crossley, A., & Banks, C. E. (2007). Single walled carbon nanotubes contain residual iron oxide impurities which can dominate their electrochemical activity. *Electrochemistry Communications*, *9*(9), 2330–2333.

Kukovecz, Á., Kozma, G., & Kónya, Z. (2013). Multi-walled carbon nanotubes. In *Springer handbook of nanomaterials*. Springer, 147–188.

Kukovitsky, E. F., L'vov, S. G., Sainov, N. A., Shustov, V. A., & Chernozatonskii, L. A. (2002). Correlation between metal catalyst particle size and carbon nanotube growth. *Chemical Physics Letters*, *355*(5–6), 497–503.

Kulkarni, M. B., Ayachit, N. H., & Aminabhavi, T. M. (2022). Biosensors and Microfluidic Biosensors: From Fabrication to Application. *Biosensors*, *12*(7), 543.

Kumar, M., & Ando, Y. (2003). A simple method of producing aligned carbon nanotubes from an unconventional precursor–Camphor. *Chemical Physics Letters*, *374*(5–6), 521–526.

Kumar, M., & Ando, Y. (2005). Controlling the diameter distribution of carbon

nanotubes grown from camphor on a zeolite support. *Carbon*, *43*(3), 533–540.

Kumar, M., & Ando, Y. (2008). Gigas Growth of Carbon Nanotubes. *Defence Science Journal*, *58*(4).

Kumar, M., & Ando, Y. (2010). Chemical vapor deposition of carbon nanotubes: a review on growth mechanism and mass production. *Journal of Nanoscience and Nanotechnology*, *10*(6), 3739–3758.

Kumar, M., Kakamu, K., Okazaki, T., & Ando, Y. (2004). Field emission from camphor–pyrolyzed carbon nanotubes. *Chemical Physics Letters*, *385*(3–4), 161–165.

Kumar, N., & Chauhan, N. S. (2021). Nano-biocatalysts: potential biotechnological applications. *Indian Journal of Microbiology*, *61*(4), 441–448.

Kumar, Raj, Bala, S., & Kumar, A. (2021). Comparative performance analysis of Carbon Nanotube and Si-Nanotube based Field effect Transistors. *IOP Conference Series: Materials Science and Engineering* (Vol. 1033). IOP Publishing, 12028.

Kumar, Rajesh, del Pino, A. P., Sahoo, S., Singh, R. K., Tan, W. K., Kar, K. K., Matsuda, A., & Joanni, E. (2022). Laser processing of graphene and related materials for energy storage: State of the art and future prospects. *Progress in Energy and Combustion Science*, 100981.

Kurtz, S. R., & Gordon, R. G. (1986). Chemical vapor deposition of titanium nitride at low temperatures. *Thin Solid Films*, *140*(2), 277–290.

Lam, C.-W., James, J. T., McCluskey, R., & Hunter, R. L. (2004). Pulmonary toxicity of single-wall carbon nanotubes in mice 7 and 90 days after intratracheal instillation. *Toxicological Sciences*, *77*(1), 126–134.

Lam, Y. C., Zheng, H. Y., Tjeung, R. T., & Chen, X. (2009). Seeing the invisible laser markings. *Journal of Physics D: Applied Physics*, *42*(4), 42004.

Laurent, C., Flahaut, E., Peigney, A., & Rousset, A. (1998). Metal nanoparticles for the catalytic synthesis of carbon nanotubes. *New Journal of Chemistry*, *22*(11), 1229–1237.

Lawal, A. T. (2016). Synthesis and utilization of carbon nanotubes for fabrication of electrochemical biosensors. *Materials Research Bulletin*, *73*, 308–350.

Layqah, L. A., & Eissa, S. (2019). An electrochemical immunosensor for the corona virus associated with the Middle East respiratory syndrome using an array of gold nanoparticle-modified carbon electrodes. *Microchimica Acta*, *186*(4), 1–10.

Leca-Bouvier, B. D., & Blum, L. J. (2010). Enzyme for biosensing applications. In *Recognition Receptors in Biosensors*. Springer, 177–220.

Lee, C. J., Lyu, S. C., Kim, H.-W., Park, J. W., Jung, H. M., & Park, J. (2002). Carbon nanotubes produced by tungsten-based catalyst using vapor phase deposition method. *Chemical Physics Letters*, *361*(5–6), 469–472.

Lee, C. J., Park, J., Huh, Y., & Lee, J. Y. (2001). Temperature effect on the growth of carbon nanotubes using thermal chemical vapor deposition. *Chemical Physics Letters*, *343*(1–2), 33–38.

Lee, C. J., Park, J., Kim, J. M., Huh, Y., Lee, J. Y., & No, K. S. (2000). Low-temperature growth of carbon nanotubes by thermal chemical vapor deposition using Pd, Cr, and Pt as co-catalyst. *Chemical Physics Letters*, *327*(5–6), 277–283.

Lee, J.-M., Kim, S. J., Kim, J. W., Kang, P. H., Nho, Y. C., & Lee, Y.-S. (2009). A high resolution XPS study of sidewall functionalized MWCNTs by fluorination. *Journal of Industrial and Engineering Chemistry*, *15*(1), 66–71.

Lee, S.-H., Park, J., Park, J. H., Lee, D.-M., Lee, A., Moon, S. Y., Lee, S. Y., Jeong, H. S., & Kim, S. M. (2021). Deep-injection floating-catalyst chemical vapor deposition to continuously synthesize carbon nanotubes with high aspect ratio and high crystallinity. *Carbon*, *173*, 901–909.

Lee, S. B., Koepsel, R., Stolz, D. B., Warriner, H. E., & Russell, A. J. (2004). Self-assembly of biocidal nanotubes from a single-chain diacetylene amine salt. *Journal of the American Chemical Society*, *126*(41), 13400–13405.

Li, H., Lu, W. G., Li, J. J., Bai, X. D., & Gu, C. Z. (2005). Multichannel ballistic transport in multiwall carbon nanotubes. *Physical Review Letters*, *95*(8), 86601.

Li, L., Zhang, D., Deng, J., Gou, Y., Fang, J., Cui, H., Zhao, Y., & Cao, M. (2021). Carbon-based materials for fast charging lithium-ion batteries. *Carbon*, *183*, 721–734.

Li, Minghua, Boggs, M., Beebe, T. P., & Huang, C. P. (2008). Oxidation of single-walled carbon nanotubes in dilute aqueous solutions by ozone as affected by ultrasound. *Carbon*, *46*(3), 466–475.

Li, Mochen, Hachiya, S., Chen, Z., Osawa, T., Sugime, H., & Noda, S. (2021). Fluidized-bed production of 0.3 mm-long single-wall carbon nanotubes at 28% carbon yield with 0.1 mass% catalyst impurities using ethylene and carbon dioxide. *Carbon*, *182*, 23–31.

Li, P., & Zhang, J. (2016). CVD growth of carbon nanotube forest with selective wall-number from Fe–Cu catalyst. *The Journal of Physical Chemistry C*, *120*(20), 11163–11169.

Li, Q., Yan, H., Zhang, J., & Liu, Z. (2004). Effect of hydrocarbons precursors on the formation of carbon nanotubes in chemical vapor deposition. *Carbon*, *42*(4), 829–835.

Li, W. Z., Wen, J. G., Tu, Y., & Ren, Z. F. (2001). Effect of gas pressure on the growth and structure of carbon nanotubes by chemical vapor deposition. *Applied Physics A*, *73*(2), 259–264.

Li, X., Gray, E. R., Islam, A. E., Sargent, G. A., Maruyama, B., & Amama, P. B. (2020). Magnesia and magnesium aluminate catalyst substrates for carbon nanotube carpet growth. *ACS Applied Nano Materials*, *3*(2), 1830–1840.

Li, Y. H., Wei, J., Zhang, X., Xu, C., Wu, D., Lu, L., & Wei, B. (2002). Mechanical and electrical properties of carbon nanotube ribbons. *Chemical Physics Letters*, *365*(1-2), 95–100.

Li, Y., Xu, G., Zhang, H., Li, T., Yao, Y., Li, Q., & Dai, Z. (2015). Alcohol-assisted rapid growth of vertically aligned carbon nanotube arrays. *Carbon*, *91*, 45–55.

Liang, T., Luan, C., Chen, H., & Xu, M. (2017). Exploring oxygen in graphene chemical vapor deposition synthesis. *Nanoscale*, *9*(11), 3719–3735.

Lieberman, M. A., & Lichtenberg, A. J. (2005). *Principles of plasma discharges and materials processing*. John Wiley & Sons.

Lin, J., Yang, Y., Zhang, H., Lin, Q., & Zhu, B. (2018). Synthesis and characterization of in-situ CNTs reinforced TiB_2-based composite by CVD using Ni catalysts. *Ceramics International*, *44*(2), 2042–2047.

Lin, M.-F., & Shung, K. W.-K. (1995). Magnetization of graphene tubules. *Physical Review B*, *52*(11), 8423.

Lipert, K., Ritschel, M., Leonhardt, A., Krupskaya, Y., Büchner, B., & Klingeler, R. (2010). Magnetic properties of carbon nanotubes with and without catalyst. *Journal of Physics: Conference Series* (Vol. 200). IOP Publishing, 72061.

Liu, B., Ren, W., Gao, L., Li, S., Liu, Q., Jiang, C., & Cheng, H.-M. (2008). Manganese-catalyzed surface growth of single-walled carbon nanotubes with high efficiency. *The Journal of Physical Chemistry C*, *112*(49), 19231–19235.

Liu, H., Zhang, Y., Arato, D., Li, R., Mérel, P., & Sun, X. (2008). Aligned multi-walled carbon nanotubes on different substrates by floating catalyst chemical vapor deposition: critical effects of buffer layer. *Surface and Coatings Technology*, *202*(17), 4114–4120.

Liu, L., Guo, G. Y., Jayanthi, C. S., & Wu, S. Y. (2002). Colossal paramagnetic moments in metallic carbon nanotori. *Physical Review Letters*, *88*(21), 217206.

Liu, L. S., Wang, F., Ge, Y., & Lo, P. K. (2020). Recent developments in aptasensors for diagnostic applications. *ACS Applied Materials & Interfaces*, *13*(8), 9329–9358.

Liu, P., Jiao, Y., Chai, X., Ma, Y., Liu, S., Fang, X., Fan, F., Xue, L., Han, J., & Liu, Q. (2022). High-performance electric and optical biosensors based on single-walled carbon nanotubes. *Journal of Luminescence*, 119084.

Liu, Q., Wu, C., Cai, H., Hu, N., Zhou, J., & Wang, P. (2014). Cell-based biosensors and their application in biomedicine. *Chemical Reviews*, *114*(12), 6423–6461.

Liu, Y., He, J., Zhang, N., Zhang, W., Zhou, Y., & Huang, K. (2021). Advances of microwave plasma-enhanced chemical vapor deposition in fabrication of carbon

nanotubes: a review. *Journal of Materials Science*, *56*(22), 12559–12583.

Lobiak, E. V, Shlyakhova, E. V, Bulusheva, L. G., Plyusnin, P. E., Shubin, Y. V, & Okotrub, A. V. (2015). Ni–Mo and Co–Mo alloy nanoparticles for catalytic chemical vapor deposition synthesis of carbon nanotubes. *Journal of Alloys and Compounds*, *621*, 351–356.

Loonam, A. C. (1959). Principles and applications of the iodide process. *Journal of The Electrochemical Society*, *106*(3), 238.

Lopez, C. F., Nielsen, S. O., Moore, P. B., & Klein, M. L. (2004). Understanding nature's design for a nanosyringe. *Proceedings of the National Academy of Sciences*, *101*(13), 4431–4434.

Lu, J. P. (1997). Elastic properties of single and multilayered nanotubes. *Journal of Physics and Chemistry of Solids*, *58*(11), 1649–1652.

Lu, X., & Chen, Z. (2005). Curved pi-conjugation, aromaticity, and the related chemistry of small fullerenes (< C_{60}) and single-walled carbon nanotubes. *Chemical Reviews*, *105*(10), 3643–3696.

Luais, E., Thobie-Gautier, C., Tailleur, A., Djouadi, M.-A., Granier, A., Tessier, P.-Y., Debarnot, D., Poncin-Epaillard, F., & Boujtita, M. (2010). Preparation and modification of carbon nanotubes electrodes by cold plasmas processes toward the preparation of amperometric biosensors. *Electrochimica Acta*, *55*(27), 7916–7922.

Luo, S., Cui, N., Wang, X., Fan, Y., & Gu, H. (2022). The stability analysis of a tether for a segmented space elevator. *Aerospace*, *9*(7), 376.

Luo, Y., Wang, X., He, M., Li, X., & Chen, H. (2012). Synthesis of high-quality carbon nanotube arrays without the assistance of water. *Journal of Nanomaterials*, *2012*.

Ma, R.Z., Xu, C.L., Wei, B.Q., Liang, J., Wu, D.H., Li & D.J., (1999) Electrical conductivity and field emission characteristics of hot-pressed sintered carbon nanotubes. *Materials Research Bulletin*, *34*(5), 741-747.

Ma, W., Li, W., Li, M., Mao, Q., Pan, Z., Hu, J., Li, X., Zhu, M., & Zhang, Y. (2021). Unzipped carbon nanotube/graphene hybrid fiber with less "dead volume" for

ultrahigh volumetric energy density supercapacitors. *Advanced Functional Materials*, *31*(19), 2100195.

Ma, Z., Wang, Y., Qin, J., Yao, Z., Cui, X., Cui, B., Yue, Y., Wang, Y., & Wang, C. (2021). Growth of carbon nanotubes on the surface of carbon fiber using Fe–Ni bimetallic catalyst at low temperature. *Ceramics International*, *47*(2), 1625–1631.

Magar, H. S., Hassan, R. Y. A., & Mulchandani, A. (2021). Electrochemical impedance spectroscopy (EIS): Principles, construction, and biosensing applications. *Sensors*, *21*(19), 6578.

Maghsoudi, Z., & Hosainzadegan, H. (2021). *Nonobiosensor for Food Safety: Microbial Detection. Impor-tance & Applications of Nanotechnology*. MedDocs Publishers.

Magrez, A., Seo, J. W., Smajda, R., Mionić, M., & Forró, L. (2010). Catalytic CVD synthesis of carbon nanotubes: towards high yield and low temperature growth. *Materials*, *3*(11), 4871–4891.

Makarova, T. L. (2004). Magnetic properties of carbon structures. *Semiconductors*, *38*(6), 615–638.

Malgas, G. F., Arendse, C. J., Cele, N. P., & Cummings, F. R. (2008). Effect of mixture ratios and nitrogen carrier gas flow rates on the morphology of carbon nanotube structures grown by CVD. *Journal of Materials Science*, *43*(3), 1020–1025.

Mallakpour, S., & Khadem, E. (2016). Carbon nanotube–metal oxide nanocomposites: Fabrication, properties and applications. *Chemical Engineering Journal*, *302*, 344–367.

Mamalis, A. G., Vogtländer, L. O. G., & Markopoulos, A. (2004). Nanotechnology and nanostructured materials: trends in carbon nanotubes. *Precision Engineering*, *28*(1), 16–30.

Man, Y., Chen, Z., Zhang, Y., & Guo, P. (2015). Patterned growth of vertically aligned carbon nanotube arrays using colloidal lithography and plasma enhanced chemical vapor deposition. *Journal of Alloys and Compounds*, *650*, 86–91.

Manawi, Y., Samara, A., Al-Ansari, T., & Atieh, M. (2018). A review of carbon nanomaterials' synthesis via the chemical vapor deposition (CVD) method. *Materials*, *11*(5), 822.

Manivel, P., Thamilselvan, A., Rajagopal, V., Nesakumar, N., & Suryanarayanan, V. (2019). Enhanced electrocatalytic activity of Ni-CNT nanocomposites for simultaneous determination of epinephrine and dopamine. *Electroanalysis*, *31*(12), 2387–2396.

Manso, J., Mena, M. L., Yanez-Sedeno, P., & Pingarron, J. (2007). Electrochemical biosensors based on colloidal gold–carbon nanotubes composite electrodes. *Journal of Electroanalytical Chemistry*, *603*(1), 1–7.

Maruyama, T., Okada, T., Sharma, K. P., Suzuki, T., Saida, T., Naritsuka, S., Iizumi, Y., Okazaki, T., & Iijima, S. (2020). Vertically aligned growth of small-diameter single-walled carbon nanotubes by alcohol catalytic chemical vapor deposition with Ir catalyst. *Applied Surface Science*, *509*, 145340.

Mathur, R. B., Singh, B. P., & Pande, S. (2016). *Carbon nanomaterials: synthesis, structure, properties and applications*. Taylor & Francis.

Matiyani, M., Pathak, M., Bohra, B. S., & Sahoo, N. G. (2021). Noncovalent functionalization of carbon nanotubes. In *Handbook of Carbon Nanotubes*. Springer, 1–28.

Matsumoto, S., Sato, Y., Kamo, M., & Setaka, N. (1982). Vapor deposition of diamond particles from methane. *Japanese Journal of applied physics*, *21*(4A), L183.

Mattevi, C., Wirth, C. T., Hofmann, S., Blume, R., Cantoro, M., Ducati, C., Cepek, C., Knop-Gericke, A., Milne, S., & Castellarin-Cudia, C. (2008). In-situ X-ray photoelectron spectroscopy study of catalyst− support interactions and growth of carbon nanotube forests. *The Journal of Physical Chemistry C*, *112*(32), 12207–12213.

Maynard, J., & Georgiou, G. (2000). Antibody engineering. *Annual Review of Biomedical Engineering*, *2*(1), 339–376.

Mayne, M., Grobert, N., Terrones, M., Kamalakaran, R., Rühle, M., Kroto, H. W., &

Walton, D. R. M. (2001). Pyrolytic production of aligned carbon nanotubes from homogeneously dispersed benzene-based aerosols. *Chemical Physics Letters*, *338*(2–3), 101–107.

McEuen, P. L., Bockrath, M., Cobden, D. H., Yoon, Y.-G., & Louie, S. G. (1999). Disorder, pseudospins, and backscattering in carbon nanotubes. *Physical Review Letters*, *83*(24), 5098.

McEuen, P. L., & Park, J.-Y. (2004). Electron transport in single-walled carbon nanotubes. *Mrs Bulletin*, *29*(4), 272–275.

McGuinness, R. P., & Verdonk, E. (2009). Electrical impedance technology applied to cell-based assays. *Label-free Biosensors: Techniques and Applications*, 251.

McLean, B., Mitchell, I., & Ding, F. (2022). Mechanism of alcohol chemical vapor deposition growth of carbon nanotubes: Catalyst oxidation. *Carbon*, *191*, 1–9.

Melechko, A. V., Merkulov, V. I., McKnight, T. E., Guillorn, M. A., Klein, K. L., Lowndes, D. H., & Simpson, M. L. (2005). Vertically aligned carbon nanofibers and related structures: Controlled synthesis and directed assembly. *Journal of Applied Physics*, *97*(4), 3.

Merkulov, V. I., Melechko, A. V, Guillorn, M. A., Lowndes, D. H., & Simpson, M. L. (2001). Alignment mechanism of carbon nanofibers produced by plasma-enhanced chemical-vapor deposition. *Applied Physics Letters*, *79*(18), 2970–2972.

Meyyappan, M. (2004). *Carbon nanotubes: science and applications*. CRC press.

Min, Y.-S., Bae, E. J., Oh, B. S., Kang, D., & Park, W. (2005). Low-temperature growth of single-walled carbon nanotubes by water plasma chemical vapor deposition. *Journal of the American Chemical Society*, *127*(36), 12498–12499.

Mintmire, J. W., Dunlap, B. I., & White, C. T. (1992). Are fullerene tubules metallic? *Physical Review Letters*, *68*(5), 631.

Miodek, A., Regan, E. M., Bhalla, N., Hopkins, N. A. E., Goodchild, S. A., & Estrela, P. (2015). Optimisation and characterisation of anti-fouling ternary SAM layers for impedance-based aptasensors. *Sensors*, *15*(10), 25015–25032.

Mirabootalebi, S. O., & Akbari, G. H. (2017). Methods for synthesis of carbon nanotubes-Review. *Int J Bio-Inorg Hybr Nanomater*, *6*(2), 49–57.

Mitra, R., Mandal, S., Trivedi, V., & Valand, J. (2022). Significant role of molybdenum promoted TiO2 catalysts for carbon nanotubes production and their polymer nanocomposites. *Materials Today: Proceedings*, *50*, 26–33.

Mitróová, Z., Tomašovičová, N., Lancz, G., Kováč, J., Vávra, I., & Kopčanský, P. (2010). Preparation and characterization of carbon nanotubes functionalized by magnetite nanoparticles. *Olomouc, Czech Republic, EU*, *10*, 12–14.

Mohammed, A., & Abdullah, A. (2018). Scanning electron microscopy (SEM): A review. *Proceedings of the 2018 International Conference on Hydraulics and Pneumatics—HERVEX, Băile Govora, Romania*, 7–9.

Mollarasouli, F., Kurbanoglu, S., & Ozkan, S. A. (2019). The role of electrochemical immunosensors in clinical analysis. *Biosensors*, *9*(3), 86.

Moosa, A. A., Ridha, A. M., & Abdullha, I. N. (2015). Chromium ions removal from wastewater using carbon nanotubes. *International Journal for Innovative Research in Science & Technology*, *4*(2), 275–282.

Morales, M. A., & Halpern, J. M. (2018). Guide to selecting a biorecognition element for biosensors. *Bioconjugate Chemistry*, *29*(10), 3231–3239.

Morrison, D. W. G., Dokmeci, M. R., Demirci, U., & Khademhosseini, A. (2008). Clinical applications of micro-and nanoscale biosensors. *Biomedical Nanostructures*, *1*, 433–458.

Moshkalev, S. A., & Verissimo, C. (2007). Nucleation and growth of carbon nanotubes in catalytic chemical vapor deposition. *Journal of Applied Physics*, *102*(4), 44303.

Munoz, J., & Pumera, M. (2021). 3D-Printed COVID-19 immunosensors with electronic readout. *Chemical Engineering Journal*, *425*, 131433.

Murakami, T., Sako, T., Harima, H., Kisoda, K., Mitikami, K., & Isshiki, T. (2004). Raman study of SWNTs grown by CCVD method on SiC. *Thin Solid Films*, *464*, 319–322.

Musameh, M., Lawrence, N. S., & Wang, J. (2005). Electrochemical activation of carbon nanotubes. *Electrochemistry Communications*, *7*(1), 14–18.

Musameh, M. M., Gao, Y., Hickey, M., & Kyratzis, I. L. (2012). Application of carbon nanotubes in the extraction and electrochemical detection of organophosphate pesticides: a review. *Analytical Letters*, *45*(8), 783–803.

Musameh, M., Wang, J., Merkoci, A., & Lin, Y. (2002). Low-potential stable NADH detection at carbon-nanotube-modified glassy carbon electrodes. *Electrochemistry Communications*, *4*(10), 743–746.

Muthukumar, S. (2021). Chapter-7: Carbon nanotubes. *Recent Research in Pharmaceutical*, 103.

Naeemi, A., & Meindl, J. D. (2006). Compact physical models for multiwall carbon-nanotube interconnects. *IEEE Electron Device Letters*, *27*(5), 338–340.

Nageswaran, G., Jothi, L., & Jagannathan, S. (2019). Plasma assisted polymer modifications. In *Non-thermal Plasma Technology for Polymeric Materials*. Elsevier, 95–127.

Nagraik, R., Sharma, A., Kumar, D., Mukherjee, S., Sen, F., & Kumar, A. P. (2021). Amalgamation of biosensors and nanotechnology in disease diagnosis: mini-review. *Sensors International*, *2*, 100089.

Naqvi, S. T. R., Rasheed, T., Hussain, D., ul Haq, M. N., Majeed, S., Ahmed, N., & Nawaz, R. (2020). Modification strategies for improving the solubility/dispersion of carbon nanotubes. *Journal of Molecular Liquids*, *297*, 111919.

Nessim, G. D. (2010). Properties, synthesis, and growth mechanisms of carbon nanotubes with special focus on thermal chemical vapor deposition. *Nanoscale*, *2*(8), 1306–1323.

Nessim, G. D., Seita, M., O'brien, K. P., Hart, A. J., Bonaparte, R. K., Mitchell, R. R., & Thompson, C. V. (2009). Low temperature synthesis of vertically aligned carbon nanotubes with electrical contact to metallic substrates enabled by thermal decomposition of the carbon feedstock. *Nano letters*, *9*(10), 3398–3405.

Neto, A. H. C., Guinea, F., Peres, N. M. R., Novoselov, K. S., & Geim, A. K. (2009). The electronic properties of graphene. *Reviews of Modern Physics*, *81*(1), 109.

Nie, C., Pan, L., Li, H., Chen, T., Lu, T., & Sun, Z. (2012). Electrophoretic deposition of carbon nanotubes film electrodes for capacitive deionization. *Journal of Electroanalytical Chemistry*, *666*, 85–88.

Nihei, M., Horibe, M., Kawabata, A., & Awano, Y. (2004). Simultaneous formation of multiwall carbon nanotubes and their end-bonded ohmic contacts to Ti electrodes for future ULSI interconnects. *Japanese Journal of Applied Physics*, *43*(4S), 1856.

Nißler, R., Ackermann, J., Ma, C., & Kruss, S. (2022). Prospects of fluorescent single-chirality carbon nanotube-based biosensors. *Analytical Chemistry*, *94*(28), 9941–9951.

Niyogi, S., Hamon, M. A., Hu, H., Zhao, B., Bhowmik, P., Sen, R., Itkis, M. E., & Haddon, R. C. (2002). Chemistry of single-walled carbon nanotubes. *Accounts of Chemical Research*, *35*(12), 1105–1113.

Obaidullah, M., Bahadur, N. M., Furusawa, T., Sato, M., Sakuma, H., & Suzuki, N. (2019). Microwave assisted rapid synthesis of Fe_2O_3@SiO_2 core-shell nanocomposite for the persistence of magnetic property at high temperature. *Colloids and Surfaces A: Physicochemical and Engineering Aspects*, *572*, 138–146.

Oberlin, A., Endo, M., & Koyama, T. (1976). Filamentous growth of carbon through benzene decomposition. *Journal of Crystal Growth*, *32*(3), 335–349.

Odom, T. W., Huang, J.-L., Kim, P., & Lieber, C. M. (2000). *Structure and electronic properties of carbon nanotubes*. ACS Publications.

Okamoto, H, & Massalski, T. B. (1984). The Au-C (gold-carbon) system. *Bulletin of Alloy Phase Diagrams*, *5*(4), 378–379.

Okamoto, Ho. (1992). The C-Fe (carbon-iron) system. *Journal of Phase Equilibria*, *13*(5), 543–565.

Öncel, Ç., & Yürüm, Y. (2006). Carbon nanotube synthesis via the catalytic CVD method: a review on the effect of reaction parameters. *Fullerenes, Nanotubes, and*

Carbon Nonstructures, *14*(1), 17–37.

Özbek, O., Berkel, C., Isildak, Ö., & Isildak, I. (2022). Potentiometric urea biosensors. *Clinica Chimica Acta*, *524*, 154–163.

Palgrave, R. G., & Parkin, I. P. (2006). Aerosol assisted chemical vapor deposition using nanoparticle precursors: a route to nanocomposite thin films. *Journal of the American Chemical Society*, *128*(5), 1587–1597.

Pandit, S., Dasgupta, D., Dewan, N., & Prince, A. (2016). Nanotechnology based biosensors and its application. *The Pharma Innovation*, *5*(6, Part A), 18.

Pant, M., Singh, R., Negi, P., Tiwari, K., & Singh, Y. (2021). A comprehensive review on carbon nano-tube synthesis using chemical vapor deposition. *Materials Today: Proceedings*.

Park, J.-B., Choi, G.-S., Cho, Y.-S., Hong, S.-Y., Kim, D., Choi, S.-Y., Lee, J.-H., & Cho, K.-I. (2002). Characterization of Fe-catalyzed carbon nanotubes grown by thermal chemical vapor deposition. *Journal of Crystal Growth*, *244*(2), 211–217.

Park, J.-H., & Sudarshan, T. S. (2001). *Chemical vapor deposition* (Vol. 2). ASM international.

Park, J., Henins, I., Herrmann, H. W., Selwyn, G. S., & Hicks, R. F. (2001). Discharge phenomena of an atmospheric pressure radio-frequency capacitive plasma source. *Journal of Applied Physics*, *89*(1), 20–28.

Park, S.-C., Cho, E.-J., Moon, S.-Y., Yoon, S.-I., Kim, Y.-J., Kim, D.-H., & Suh, J.-S. (2007). A calorimetric biosensor and its application for detecting a cancer cell with optical imaging. *World Congress on Medical Physics and Biomedical Engineering 2006*. Springer, 637–640.

Parkinson, G., & Pejcic, B. (2005). Using biosensors to detect emerging infectious diseases. *Prepared for The Australian Biosecurity Cooperative Research Centre*, 1–80.

Pasha, M. A., Shafiekhani, A., & Vesaghi, M. A. (2009). Hot filament CVD of Fe–Cr catalyst for thermal CVD carbon nanotube growth from liquid petroleum gas.

Applied Surface Science, *256*(5), 1365–1371.

Patel, D., Zhou, Y., & Ramasamy, R. P. (2021). A bacteriophage-based electrochemical biosensor for detection of methicillin-resistant staphylococcus aureus. *Journal of The Electrochemical Society*, *168*(5), 57523.

Patel, J., Parikh, S., Patel, S., Patel, R., & Patel, P. (2021). Carbon Nanotube (CNTs): Structure, Synthesis, Purification, Functionalisation, Pharmacology, Toxicology, Biodegradation and Application as Nanomedicine and Biosensor: Carbon Nanotube (CNTs). *The Journal of Pharmaceutical Sciences and Medicinal Research*, *1*(02), 17–44.

Patole, S. P., Alegaonkar, P. S., Lee, H.-C., & Yoo, J.-B. (2008). Optimization of water assisted chemical vapor deposition parameters for super growth of carbon nanotubes. *Carbon*, *46*(14), 1987–1993.

Pavlidis, I V, Tsoufis, T., Enotiadis, A., Gournis, D., & Stamatis, H. (2010). Functionalized multi-wall carbon nanotubes for lipase immobilization. *Advanced Engineering Materials*, *12*(5), B179–B183.

Pavlidis, Ioannis V, Vorhaben, T., Gournis, D., Papadopoulos, G. K., Bornscheuer, U. T., & Stamatis, H. (2012). Regulation of catalytic behaviour of hydrolases through interactions with functionalized carbon-based nanomaterials. *Journal of Nanoparticle Research*, *14*(5), 1–10.

Pérez-López, B., & Merkoçi, A. (2012). Carbon nanotubes and graphene in analytical sciences. *Microchimica Acta*, *179*(1), 1–16.

Perumal, V., & Hashim, U. (2014). Advances in biosensors: Principle, architecture and applications. *Journal of Applied Biomedicine*, *12*(1), 1–15.

Peschel, G. (2011). Carbon-carbon bonds: hybridization. *Obtained online from: http://www. physik. fu-berlin. de/einrichtungen/ag/ag-reich/lehre/Archiv/ss2011/docs/Gina_Peschel-Handout. pdf, published on*, *5*(5).

Pierson, H O, & Lieberman, M. L. (1975). The chemical vapor deposition of carbon on carbon fibers. *Carbon*, *13*(3), 159–166.

Pierson, Hugh O. (1999). *Handbook of chemical vapor deposition: principles, technology and applications*. William Andrew.

Pohanka, M., & Skládal, P. (2008). Electrochemical biosensors--principles and applications. *Journal of Applied Biomedicine*, *6*(2).

Pop, E., Mann, D., Wang, Q., Goodson, K., & Dai, H. (2006). Thermal conductance of an individual single-wall carbon nanotube above room temperature. *Nano Letters*, *6*(1), 96–100.

Powell, C. F., Oxley, J. H., Blocher, J. M., & Klerer, J. (1966). Vapor deposition. *Journal of The Electrochemical Society*, *113*(10), 266C.

Powell, Q. H., Kodas, T. T., & Anderson, B. M. (1996). Coating of TiO_2 particles by chemical vapor deposition of SiO_2. *Chemical Vapor Deposition*, *2*(5), 179–181.

Prakash, J., Dey, A., Uppal, S., Alexander, R., Kaushal, A., Misra, H. S., & Dasgupta, K. (2021). Label-free rapid electrochemical detection of DNA hybridization using ultrasensitive standalone CNT aerogel biosensor. *Biosensors and Bioelectronics*, *191*, 113480.

Prakash, J., Uppal, S., Kaushal, A., & Dasgupta, K. (2022). Effect of O/N doping in CNT aerogel film on their nucleic acid hybridization detection ability as electrochemical impedance biosensor. *Materials Today Communications*, *32*, 103965.

Prasek, J., Drbohlavova, J., Chomoucka, J., Hubalek, J., Jasek, O., Adam, V., & Kizek, R. (2011). Methods for carbon nanotubes synthesis. *Journal of Materials Chemistry*, *21*(40), 15872–15884.

Pumera, M. (2009). The electrochemistry of carbon nanotubes: fundamentals and applications. *Chemistry–A European Journal*, *15*(20), 4970–4978.

Pumera, M., & Miyahara, Y. (2009). What amount of metallic impurities in carbon nanotubes is small enough not to dominate their redox properties? *Nanoscale*, *1*(2), 260–265.

Pumera, M., Sanchez, S., Ichinose, I., & Tang, J. (2007). Electrochemical

nanobiosensors. *Sensors and Actuators B: Chemical*, *123*(2), 1195–1205.

Qian, Y., Lu, S., & Gao, F. (2011). Cadmium-catalyzed surface growth of single-walled carbon nanotubes with high efficiency. *Materials Research Bulletin*, *46*(6), 823–829.

Qin, C., Shi, X., Bai, S. Q., Chen, L. D., & Wang, L. J. (2006). High temperature electrical and thermal properties of the bulk carbon nanotube prepared by SPS. *Materials Science and Engineering: A*, *420*(1-2), 208-211.

Qlark Jr, L. C. (1956). Monitor and control of blood and tissue oxygen tensions. *Asaio Journal*, *2*(1), 41–48.

Quazi, S. (2022). Application of biosensors in cancers, an overview. *Preprints 2022***,** 2022010474.

Radauscher, E. J. (2016). *Design, Fabrication, and Characterization of Carbon Nanotube Field Emission Devices for Advanced Applications*. Duke University.

Radushkevich, L. V, & Lukyanovich, V. M. (1952). About the structure of carbon formed by thermal decomposition of carbon monoxide on iron substrate. *J. Phys. Chem.(Moscow)*, *26*, 88–95.

Rafique, M. M. A., & Iqbal, J. (2011). Production of carbon nanotubes by different routes-a review. *Journal of Encapsulation and Adsorption Sciences*, *1*(02), 29.

Rahman, M. M., Umar, A., & Sawada, K. (2009). Development of amperometric glucose biosensor based on glucose oxidase co-immobilized with multi-walled carbon nanotubes at low potential. *Sensors and Actuators B: Chemical*, *137*(1), 327–333.

Ramachandran, G. (2014). Gram-positive and gram-negative bacterial toxins in sepsis: a brief review. *Virulence*, *5*(1), 213–218.

Ramanathan, K., & Danielsson, B. (2001). Principles and applications of thermal biosensors. *Biosensors and Bioelectronics*, *16*(6), 417–423.

Ramsden, J. J. (1997). Optical biosensors. *Journal of Molecular Recognition*, *10*(3), 109–120.

Rana, M. M., Ibrahim, D. S., Mohd Asyraf, M. R., Jarin, S., & Tomal, A. (2017). A review on recent advances of CNTs as gas sensors. *Sensor Review*, *37*(2), 127–136.

Rashid, H. U., Yu, K., Umar, M. N., Anjum, M. N., Khan, K., Ahmad, N., & Jan, M. T. (2015). Catalyst role in chemical vapor deposition (CVD) process: A review. *Rev. Adv. Mater. Sci*, *40*(3), 235–248.

Rau, U., & Schock, H. W. (1999). Electronic properties of $Cu(In,Ga)Se_2$ heterojunction solar cells–recent achievements, current understanding, and future challenges. *Appl Phys A*, *69*, 131–147.

Redina, A. G., Avramenko, M. V, & Lyanguzov, N. V. (2021). Characteristics of carbon nanotubes synthesized from methane and acetylene in the presence of a $FeCl_3$ catalyst. *Technical Physics*, *66*(3), 445–452.

Reich, S., Thomsen, C., & Maultzsch, J. (2004). *Carbon nanotubes: basic concepts and physical properties*. John Wiley & Sons.

Reilly Jr, J. J., & Wiswall Jr, R. H. (1968). Reaction of hydrogen with alloys of magnesium and nickel and the formation of Mg_2NiH_4. *Inorganic Chemistry*, *7*(11), 2254–2256.

Rernglit, W., Teanphonkrang, S., Suginta, W., & Schulte, A. (2019). Amperometric enzymatic sensing of glucose using porous carbon nanotube films soaked with glucose oxidase. *Microchimica Acta*, *186*(9), 616.

Rodríguez, B. A. G., Ferreira, P. A. B., & Dutra, R. F. (2022). Impedimetric immunosensors for clinical practices: Focus on point-of-care diagnostics. In *Tools and Trends in Bioanalytical Chemistry*. Springer, 283–304.

Rodriguez, N. M. (1993). A review of catalytically grown carbon nanofibers. *Journal of Materials Research*, *8*(12), 3233–3250.

Rogers, J. K., Taylor, N. D., & Church, G. M. (2016). Biosensor-based engineering of biosynthetic pathways. *Current Opinion in Biotechnology*, *42*, 84–91.

Rohmund, F., Morjan, R.-E., Ledoux, G., Huisken, F., & Alexandrescu, R. (2002). Carbon nanotube films grown by laser-assisted chemical vapor deposition. *Journal*

of Vacuum Science & Technology B: Microelectronics and Nanometer Structures Processing, Measurement, and Phenomena, *20*(3), 802–811.

Roy, S., Sain, S., Wadhwa, S., Mathur, A., Dubey, S., & Roy, S. S. (2021). Electrochemical impedimetric analysis of different dimensional (0D–2D) carbon nanomaterials for effective biosensing of L-tyrosine. *Measurement Science and Technology*, *33*(1), 14002.

Ruan, C., Li, Z., Zhang, D., Yuan, X., Liang, C., Chang, Y., Huang, H., Xu, L., & Chen, M. (2020). A scalable chemical vapor deposition synthesis of high purity hollow carbon onions. *Carbon*, *161*, 622–628.

Saha, U., Todi, K., & Malhotra, B. D. (2021). Emerging DNA-based multifunctional nano-biomaterials towards electrochemical sensing applications. *Nanoscale*, *13*(23), 10305–10319.

Saharudin, M. S., Sagar Iqbal, S., & Inam, F. (2022). Carbon nanotubes after 30 years of research, development and commercialisation. *Nanomedicine and Nanotechnology Journal*, *5*(1).

Sahin, B., & Kaya, T. (2019). Electrochemical amperometric biosensor applications of nanostructured metal oxides: A review. *Materials Research Express*, *6*(4), 42003.

Saito, Y., Hata, K., Takakura, A., Yotani, J., & Uemura, S. (2002). Field emission of carbon nanotubes and its application as electron sources of ultra-high luminance light-source devices. *Physica B: Condensed Matter*, *323*(1–4), 30–37.

Saleh, H. E.-D., & El-Sheikh, S. M. M. (2019). *Perspective of Carbon Nanotubes*. BoD–Books on Demand.

Salvetat, J. P., Bonard, J. M., Thomson, N. H., Kulik, A.J., Forró, L., Benoit, W., & Zuppiroli, L. (1999). Mechanical properties of carbon nanotubes. *Appl. Phys. A Mater. Sci. Process*, *69*, 255–260.

Sawant, S. V, Dasgupta, K., Joshi, J. B., & Patwardhan, A. W. (2022). Synthesis of boron-doped carbon nanotubes by thermocatalytic decomposition of ethanol using a floating catalyst chemical vapor deposition method: kinetic study. *Reaction*

Chemistry & Engineering, *7*, 2163-2174.

Schachinger, F., Chang, H., Scheiblbrandner, S., & Ludwig, R. (2021). Amperometric biosensors based on direct electron transfer enzymes. *Molecules*, *26*(15), 4525.

Scheller, F., & Schubert, F. (1991). *Biosensors*. Elsevier.

Schneider, H.-J., Lim, S., & Strongin, R. M. (2010). Biomimetic synthetic receptors as molecular recognition elements. In *Recognition Receptors in Biosensors*. Springer, 777–816.

Schulz, U., Munzert, P., & Kaiser, N. (2001). Surface modification of PMMA by DC glow discharge and microwave plasma treatment for the improvement of coating adhesion. *Surface and Coatings Technology*, *142*, 507–511.

Scott, A. O. (1994). *Biosensors: Theory and applications: by Donald G. Buerk, Technomic, 1993. Sw. Fr. 187.00 (x+ 221 pages) ISBN 0 87762 975 7*. Elsevier.

Sellami, K., Couvert, A., Nasrallah, N., Maachi, R., Abouseoud, M., & Amrane, A. (2022). Peroxidase enzymes as green catalysts for bioremediation and biotechnological applications: A review. *Science of the Total Environment*, *806*.

Sellappan, L., Manoharan, S., Sanmugam, A., & Anh, N. T. (2022). Role of nanobiosensors and biosensors for plant virus detection. In *Nanosensors for Smart Agriculture*. Elsevier, 493–506.

Sen, R., Govindaraj, A., & Rao, C. N. R. (1997). Carbon nanotubes by the metallocene route. *Chemical Physics Letters*, *267*(3–4), 276–280.

Shah, Khurshed A, & Tali, B. A. (2016). Synthesis of carbon nanotubes by catalytic chemical vapour deposition: A review on carbon sources, catalysts and substrates. *Materials Science in Semiconductor Processing*, *41*, 67–82.

Shah, Khurshed Ahmad, & Parvaiz, M. S. (2022). Chemical functionalization of carbon nanotubes and applications to sensors. *Spectroscopy and Characterization of Nanomaterials and Novel Materials: Experiments, Modeling, Simulations, and Applications*, 261–286.

Shaikjee, A., & Coville, N. J. (2012). The role of the hydrocarbon source on the growth

of carbon materials. *Carbon*, *50*(10), 3376–3398.

Sharma, A., Dulta, K., Nagraik, R., Dua, K., Singh, S. K., Chellappan, D. K., Kumar, D., & Shin, D.-S. (2022). Potentialities of aptasensors in cancer diagnosis. *Materials Letters*, *308*, 131240.

Shi, J., Lu, Y. F., Yi, K. J., Lin, Y. S., Liou, S., Hou, J. B., & Wang, X. W. (2006). Direct synthesis of single-walled carbon nanotubes bridging metal electrodes by laser-assisted chemical vapor deposition. *Applied Physics Letters*, *89*(8), 83105.

Shoukat, R., & Khan, M. I. (2021). Carbon nanotubes: A review on properties, synthesis methods and applications in micro and nanotechnology. *Microsystem Technologies*, *27*(12), 4183–4192.

Shoukat, R., & Khan, M. I. (2022). Carbon nanotubes/nanofibers (CNTs/CNFs): a review on state of the art synthesis methods. *Microsystem Technologies*, 1–17.

Shudin, N. H., Aziz, M., Othman, M. H. D., Tanemura, M., & Yusop, M. Z. M. (2021). The role of solid, liquid and gaseous hydrocarbon precursors on chemical vapor deposition grown carbon nanomaterials' growth temperature. *Synthetic Metals*, *274*, 116735.

Shukrullah, S., Mohamed, N. M., Shaharun, M. S., & Naz, M. Y. (2014). Mass production of carbon nanotubes using fluidized bed reactor: A short review. *Trends in Applied Sciences Research*, *9*(3), 121.

Shvedova, A. A., Kisin, E. R., Mercer, R., Murray, A. R., Johnson, V. J., Potapovich, A. I., Tyurina, Y. Y., Gorelik, O., Arepalli, S., & Schwegler-Berry, D. (2005). Unusual inflammatory and fibrogenic pulmonary responses to single-walled carbon nanotubes in mice. *American Journal of Physiology-Lung Cellular and Molecular Physiology*, *289*(5), L698–L708.

Shyu, F.-L., Chang, C.-P., Chen, R.-B., Chiu, C.-W., & Lin, M.-F. (2003). Magnetoelectronic and optical properties of carbon nanotubes. *Physical Review B*, *67*(4), 45405.

Siefering, K. L., & Griffin, G. L. (1990). Kinetics of low-pressure chemical vapor deposition of TiO_2 from titanium tetraisopropoxide. *Journal of the Electrochemical*

Society, *137*(3), 814.

Simionescu, O.-G., Brîncoveanu, O., Romaniţan, C., Vulpe, S., & Avram, A. (2022). Step-by-step development of vertically aligned carbon nanotubes by plasma-enhanced chemical vapor deposition. *Coatings*, *12*(7), 943.

Singh, A., Sharma, A., Ahmed, A., Sundramoorthy, A. K., Furukawa, H., Arya, S., & Khosla, A. (2021). Recent advances in electrochemical biosensors: Applications, challenges, and future scope. *Biosensors*, *11*(9), 336.

Singh, R. P. (2011). Prospects of nanobiomaterials for biosensing. *International Journal of Electrochemistry*, 125487.

Sireesha, M., Jagadeesh Babu, V., Kranthi Kiran, A. S., & Ramakrishna, S. (2018). A review on carbon nanotubes in biosensor devices and their applications in medicine. *Nanocomposites*, *4*(2), 36–57.

Smits, F. M. (1958). Measurement of sheet resistivities with the four-point probe. *Bell System Technical Journal*, *37*(3), 711–718.

Snow, E. S., Novak, J. P., Campbell, P. M., & Park, D. (2003). Random networks of carbon nanotubes as an electronic material. *Applied Physics Letters*, *82*(13), 2145–2147.

Sobhanardakani, S., Jafari, A., Zandipak, R., & Meidanchi, A. (2018). Removal of heavy metal (Hg (II) and Cr (VI)) ions from aqueous solutions using Fe_2O_3@ SiO_2 thin films as a novel adsorbent. *Process Safety and Environmental Protection*, *120*, 348–357.

Soga, K., Imamura, H., & Ikeda, S. (1976). Hydrogenatıon of ethylene over $LaNi_5H_3$. *Chemistry Letters*, *5*(12), 1387–1388.

Soh, H. T., Quate, C. F., Morpurgo, A. F., Marcus, C. M., Kong, J., & Dai, H. (1999). Integrated nanotube circuits: Controlled growth and ohmic contacting of single-walled carbon nanotubes. *Applied Physics Letters*, *75*(5), 627–629.

Sohn, J. I., Lee, S., Song, Y.-H., Choi, S.-Y., Cho, K.-I., & Nam, K.-S. (2001). Patterned selective growth of carbon nanotubes and large field emission from

vertically well-aligned carbon nanotube field emitter arrays. *Applied Physics Letters*, *78*(7), 901–903.

Soto, M., Boyer, T. A., Biradar, S., Ge, L., Vajtai, R., Elías-Zúñiga, A., Ajayan, P. M., & Barrera, E. V. (2015). Effect of interwall interaction on the electronic structure of double-walled carbon nanotubes. *Nanotechnology*, *26*(16), 165201.

Špitalský, Z., Matějka, L., Šlouf, M., Konyushenko, E. N., Kovářová, J., Zemek, J., & Kotek, J. (2009). Modification of carbon nanotubes and its effect on properties of carbon nanotube/epoxy nanocomposites. *Polymer Composites*, *30*(10), 1378–1387.

Su, Y., & Zhang, Y. (2015). Carbon nanomaterials synthesized by arc discharge hot plasma. *Carbon*, *83*, 90–99.

Sun, Y., Zhang, J., Huang, T., Liu, Z., & Yu, A. (2013). Fe_2O_3/CNTs composites as anode materials for lithium-ion batteries. *Int. J. Electrochem. Sci*, *8*(2), 2919–2931.

Sun, Z., Qi, H., Chen, M., Guo, S., Huang, Z., Maganti, S., Murugadoss, V., Huang, M., & Guo, Z. (2021). Progress in cellulose/carbon nanotube composite flexible electrodes for supercapacitors. *Engineered Science*, *18*, 59–74.

Suryawanshi, P. L., Sonawane, S. H., Bhanvase, B. A., Ashokkumar, M., Pimplapure, M. S., & Gogate, P. R. (2018). Synthesis of iron oxide nanoparticles in a continuous flow spiral microreactor and Corning® advanced flow™ reactor. *Green Processing and Synthesis*, *7*(1), 1–11.

Švancara, I., Vytřas, K., Kalcher, K., Walcarius, A., & Wang, J. (2009). Carbon paste electrodes in facts, numbers, and notes: a review on the occasion of the 50-years jubilee of carbon paste in electrochemistry and electroanalysis. *Electroanalysis: An International Journal Devoted to Fundamental and Practical Aspects of Electroanalysis*, *21*(1), 7–28.

Szabó, A., Méhn, D., Kónya, Z., Fonseca, A., & Nagy, J. B. (2003). "Wash and go": sodium chloride as an easily removable catalyst support for the synthesis of carbon nanotubes. *PhysChemComm*, *6*(10), 40–41.

Szybowicz, M., Nowicka, A. B., & Dychalska, A. (2018). Characterization of carbon nanomaterials by Raman spectroscopy. In *Characterization of Nanomaterials*.

Elsevier, 1–36.

Takagi, D., Hibino, H., Suzuki, S., Kobayashi, Y., & Homma, Y. (2007). Carbon nanotube growth from semiconductor nanoparticles. *Nano Letters*, *7*(8), 2272–2275.

Takagi, D., Homma, Y., Hibino, H., Suzuki, S., & Kobayashi, Y. (2006). Single-walled carbon nanotube growth from highly activated metal nanoparticles. *Nano Letters*, *6*(12), 2642–2645.

Takagi, D., Kobayashi, Y., & Homma, Y. (2009). Carbon nanotube growth from diamond. *Journal of the American Chemical Society*, *131*(20), 6922–6923.

Talapatra, S., Kar, S., Pal, S. K., Vajtai, R., Ci, L., Victor, P., Shaijumon, M. M., Kaur, S., Nalamasu, O., & Ajayan, P. M. (2006). Direct growth of aligned carbon nanotubes on bulk metals. *Nature Nanotechnology*, *1*(2), 112–116.

Tasis, D., Tagmatarchis, N., Bianco, A., & Prato, M. (2006). Chemistry of carbon nanotubes. *Chemical Reviews*, *106*(3), 1105–1136.

Tasis, D., Tagmatarchis, N., Georgakilas, V., & Prato, M. (2003). Soluble carbon nanotubes. *Chemistry–A European Journal*, *9*(17), 4000–4008.

Tatarova, E., Dias, A., Henriques, J., Abrashev, M., Bundaleska, N., Kovacevic, E., Bundaleski, N., Cvelbar, U., Valcheva, E., & Arnaudov, B. (2017). Towards large-scale in free-standing graphene and N-graphene sheets. *Scientific Reports*, *7*(1), 1–16.

Teo, K. B. K., Singh, C., Chhowalla, M., & Milne, W. I. (2003). Catalytic synthesis of carbon nanotubes and nanofibers. *Encyclopedia of Nanoscience and Nanotechnology*, *10*(1).

Terrado, E., Redrado, M., Muñoz, E., Maser, W. K., Benito, A. M., & Martínez, M. T. (2006). Aligned carbon nanotubes grown on alumina and quartz substrates by a simple thermal CVD process. *Diamond and Related Materials*, *15*(4–8), 1059–1063.

Terrones, M. (2003). Science and technology of the twenty-first century: synthesis,

properties, and applications of carbon nanotubes. *Annual Review of Materials Research*, *33*(1), 419–501.

Thevenot, D. R., Toth, K., Durst, R. A., & Wilson, G. S. (1999). Electrochemical biosensors: recommended definitions and classification. *Pure and Applied Chemistry*, *71*(12), 2333–2348.

Thévenot, D. R., Toth, K., Durst, R. A., & Wilson, G. S. (2001). Electrochemical biosensors: recommended definitions and classification. *Biosensors and Bioelectronics*, *16*(1–2), 121–131.

Thostenson, E. T., Ren, Z., & Chou, T.-W. (2001). Advances in the science and technology of carbon nanotubes and their composites: a review. *Composites Science and Technology*, *61*(13), 1899–1912.

Tîlmaciu, C.-M., & Morris, M. C. (2015). Carbon nanotube biosensors. *Frontiers in Chemistry*, *3*, 59.

Tingaev, M. I., & Belenkov, E. A. (2017). Hybrid sp^2+ sp^3 carbon phases created from carbon nanotubes. *Journal of Physics: Conference Series* (Vol. 917). IOP Publishing, 32013.

Todankar, B., Desai, P., Ranade, A. K., Narayanan, T. N., Tanemura, M., & Kalita, G. (2021). Trifunctional electrocatalytic activities of nitrogen-doped graphitic carbon nanofibers synthesized by chemical vapor deposition. *ChemistrySelect*, *6*(20), 4867–4873.

Tritsch, N. X., Granger, A. J., & Sabatini, B. L. (2016). Mechanisms and functions of GABA co-release. *Nature Reviews Neuroscience*, *17*(3), 139–145.

Tsai, M. H., Sun, S. C., Chiu, H.-T., Tsai, C. E., & Chuang, S. H. (1995). Metalorganic chemical vapor deposition of tantalum nitride by tertbutylimidotris (diethylamido) tantalum for advanced metallization. *Applied Physics Letters*, *67*(8), 1128–1130.

Ţucureanu, V., Matei, A., & Avram, A. M. (2016). FTIR spectroscopy for carbon family study. *Critical Reviews in Analytical Chemistry*, *46*(6), 502–520.

Tuncel, D. (2011). Non-covalent interactions between carbon nanotubes and

conjugated polymers. *Nanoscale*, *3*(9), 3545–3554.

Turner, A., Karube, I., & Wilson, G. S. (1987). *Biosensors: fundamentals and applications*. Oxford university press.

Turner, A. P. F. (2013). Biosensors: sense and sensibility. *Chemical Society Reviews*, *42*(8), 3184–3196.

Unalan, H. E., & Chhowalla, M. (2005). Investigation of single-walled carbon nanotube growth parameters using alcohol catalytic chemical vapour deposition. *Nanotechnology*, *16*(10), 2153.

Unwin, P. R., Guell, A. G., & Zhang, G. (2016). Nanoscale electrochemistry of sp2 carbon materials: from graphite and graphene to carbon nanotubes. *Accounts of Chemical Research*, *49*(9), 2041–2048.

Updike, S. J., & Hicks, G. P. (1967). The enzyme electrode. *Nature*, *214*(5092), 986–988.

Vahlas, C., Caussat, B., Serp, P., & Angelopoulos, G. N. (2006). Principles and applications of CVD powder technology. *Materials Science and Engineering: R: Reports*, *53*(1–2), 1–72.

Vajtai, R. (2013). *Springer handbook of nanomaterials*. Springer Science & Business Media.

Valentini, L., Kenny, J. M., Lozzi, L., & Santucci, S. (2002). Formation of carbon nanotubes by plasma enhanced chemical vapor deposition: role of nitrogen and catalyst layer thickness. *Journal of applied physics*, *92*(10), 6188–6194.

Van der Heide, P. (2011). *X-ray photoelectron spectroscopy: an introduction to principles and practices*. John Wiley & Sons.

Veronese, G. P., Rizzoli, R., Angelucci, R., Cuffiani, M., Malferrari, L., Montanari, A., & Odorici, F. (2007). Effects of Ni catalyst–substrate interaction on carbon nanotubes growth by CVD. *Physica E: Low-dimensional Systems and Nanostructures*, *37*(1–2), 21–25.

Vestergaard, M. C., & Tamiya, E. (2015). Nanobiosensors and Nanobioanalyses: A

Review. *Nanobiosensors and Nanobioanalyses*, 3–20.

Vicentini, R., Nunes, W., Freitas, B. G. A., Da Silva, L. M., Soares, D. M., Cesar, R., Rodella, C. B., & Zanin, H. (2019). Niobium pentoxide nanoparticles@ multi-walled carbon nanotubes and activated carbon composite material as electrodes for electrochemical capacitors. *Energy Storage Materials*, *22*, 311–322.

Vivekchand, S. R. C., Cele, L. M., Deepak, F. L., Raju, A. R., & Govindaraj, A. (2004). Carbon nanotubes by nebulized spray pyrolysis. *Chemical Physics Letters*, *386*(4–6), 313–318.

Walker, N. L., Roshkolaeva, A. B., Chapoval, A. I., & Dick, J. E. (2021). Recent advances in potentiometric biosensing. *Current Opinion in Electrochemistry*, *28*, 100735.

Wan, X., Dong, J., & Xing, D. Y. (1998). Optical properties of carbon nanotubes. *Physical Review B*, *58*(11), 6756.

Wang, A., Ye, J., Humphrey, M. G., & Zhang, C. (2018). Graphene and Carbon-Nanotube Nanohybrids Covalently Functionalized by Porphyrins and Phthalocyanines for Optoelectronic Properties. *Advanced Materials*, *30*(17), 1705704.

Wang, H., Zhou, A., Peng, F., Yu, H., & Yang, J. (2007). Mechanism study on adsorption of acidified multiwalled carbon nanotubes to Pb (II). *Journal of Colloid and Interface Science*, *316*(2), 277–283.

Wang, Jiajun, Yin, G., Shao, Y., Wang, Z., & Gao, Y. (2008). Investigation of further improvement of platinum catalyst durability with highly graphitized carbon nanotubes support. *The Journal of Physical Chemistry C*, *112*(15), 5784–5789.

Wang, Jingfang, Yang, S., Guo, D., Yu, P., Li, D., Ye, J., & Mao, L. (2009). Comparative studies on electrochemical activity of graphene nanosheets and carbon nanotubes. *Electrochemistry Communications*, *11*(10), 1892–1895.

Wang, Qi, Zheng, Y., Zhou, C., Chan, M., & Yang, C. Y. (2021). Low-temperature grown vertically aligned carbon nanotube array for an optimal infrared bolometer. *Nanotechnology*, *32*(50), 505719.

Wang, Qiong, Wang, J., Huang, Y., Du, Y., Zhang, Y., Cui, Y., & Kong, D. (2022). Development of the DNA-based biosensors for high performance in detection of molecular biomarkers: More rapid, sensitive, and universal. *Biosensors and Bioelectronics*, *197*, 113739.

Wang, Shangshang, Zhang, J., Gharbi, O., Vivier, V., Gao, M., & Orazem, M. E. (2021). Electrochemical impedance spectroscopy. *Nature Reviews Methods Primers*, *1*(1), 1–21.

Wang, Songyan, Cao, K., Xu, L., Zhao, D., & Tong, Y. (2022). Carbon nanotubes/reduced graphene oxide composites as electrode materials for supercapacitors. *Applied Physics A*, *128*(1), 1–10.

Wang, X.-D., Vinodgopal, K., & Dai, G.-P. (2019). Synthesis of carbon nanotubes by catalytic chemical vapor deposition. *Perspective of Carbon Nanotubes*, 13–32.

Wang, X., Xu, B., Liu, X., Guo, J., & Ichinose, H. (2006). Synthesis of Fe-included onion-like fullerenes by chemical vapor deposition. *Diamond and Related materials*, *15*(1), 147–150.

Wang, Y., Yang, P., Zheng, L., Shi, X., & Zheng, H. (2020). Carbon nanomaterials with sp2 or/and sp hybridization in energy conversion and storage applications: A review. *Energy Storage Materials*, *26*, 349–370.

Ward, J. W., Wei, B. Q., & Ajayan, P. M. (2003). Substrate effects on the growth of carbon nanotubes by thermal decomposition of methane. *Chemical Physics Letters*, *376*(5–6), 717–725.

Warheit, D. B., Laurence, B. R., Reed, K. L., Roach, D. H., Reynolds, G. A. M., & Webb, T. R. (2004). Comparative pulmonary toxicity assessment of single-wall carbon nanotubes in rats. *Toxicological sciences*, *77*(1), 117–125.

Wartman, F. S., Baker, D. H., Nettle, J. R., & Homme, V. E. (1954). Some observations on the Kroll process for titanium. *Journal of the Electrochemical Society*, *101*(10), 507.

Wilder, J. W. G., Venema, L. C., Rinzler, A. G., Smalley, R. E., & Dekker, C. (1998). Electronic structure of atomically resolved carbon nanotubes. *Nature*, *391*(6662),

59–62.

Willems, I., Kónya, Z., Colomer, J.-F., Van Tendeloo, G., Nagaraju, N., Fonseca, A., & Nagy, J. B. (2000). Control of the outer diameter of thin carbon nanotubes synthesized by catalytic decomposition of hydrocarbons. *Chemical Physics Letters*, *317*(1–2), 71–76.

Wong, Y. M., Wei, S., Kang, W. P., Davidson, J. L., Hofmeister, W., Huang, J. H., & Cui, Y. (2004). Carbon nanotubes field emission devices grown by thermal CVD with palladium as catalysts. *Diamond and related materials*, *13*(11–12), 2105–2112.

Wood, P. J. (2006). *Understanding immunology*. Pearson Education.

Wooten, M., Karra, S., Zhang, M., & Gorski, W. (2014). On the direct electron transfer, sensing, and enzyme activity in the glucose oxidase/carbon nanotubes system. *Analytical chemistry*, *86*(1), 752–757.

Wu, F., Wang, C., Hu, H.-Y., Pan, M., Li, H.-F., Xie, N., Zeng, Z., Deng, S., Wu, M. H., & Vinodgopal, K. (2019). One-step synthesis of hierarchical metal oxide nanosheet/carbon nanotube composites by chemical vapor deposition. *Journal of materials science*, *54*(2), 1291–1303.

Wu, Q., Zhang, H., Ma, C., Li, D., Xin, L., Zhang, X., Zhao, N., & He, M. (2021). SiO2-promoted growth of single-walled carbon nanotubes on an alumina supported catalyst. *Carbon*, *176*, 367–373.

Xie, Q.-Z., Lin, M.-W., Hsu, W.-E., & Lin, C.-T. (2020). Advancements of Nanoscale Structures and Materials in Impedimetric Biosensing Technologies. *ECS Journal of Solid State Science and Technology*, *9*(11), 115027.

Yabe, Y., Ohtake, Y., Ishitobi, T., Show, Y., Izumi, T., & Yamauchi, H. (2004). Synthesis of well-aligned carbon nanotubes by radio frequency plasma enhanced CVD method. *Diamond and Related Materials*, *13*(4–8), 1292–1295.

Yadav, H. M., Park, J.-D., Kang, H.-C., & Lee, J.-J. (2021). Recent development in nanomaterial-based electrochemical sensors for cholesterol detection. *Chemosensors*, *9*(5), 98.

Yahyazadeh, A., & Khoshandam, B. (2017). Carbon nanotube synthesis via the catalytic chemical vapor deposition of methane in the presence of iron, molybdenum, and iron–molybdenum alloy thin layer catalysts. *Results in physics*, *7*, 3826–3837.

Yakobson, B I. (1998). Mechanical relaxation and “intramolecular plasticity” in carbon nanotubes. *Applied Physics Letters*, *72*(8), 918–920.

Yakobson, B I, Samsonidze, G., & Samsonidze, G. G. (2000). Atomistic theory of mechanical relaxation in fullerene nanotubes. *Carbon*, *38*(11–12), 1675–1680.

Yakobson, Boris I, Brabec, C. J., & Bernholc, J. (1996). Nanomechanics of carbon tubes: instabilities beyond linear response. *Physical review letters*, *76*(14), 2511.

Yan, H., Guo, S., Wu, F., Yu, P., Liu, H., Li, Y., & Mao, L. (2018). Carbon atom hybridization matters: ultrafast humidity response of graphdiyne oxides. *Angewandte Chemie International Edition*, *57*(15), 3922–3926.

Yanase, T., Miura, T., Shiratori, T., Weng, M., Nagahama, T., & Shimada, T. (2019). Synthesis of carbon nanotubes by plasma-enhanced chemical vapor deposition using Fe1− xMnxO nanoparticles as catalysts: How does the catalytic activity of graphitization affect the yields and morphology? *C*, *5*(3), 46.

Yang, G., Kang, Z., Ye, X., Wu, T., & Zhu, Q. (2012). Molecular simulation of flavin adenine dinucleotide immobilized on charged single-walled carbon nanotubes for biosensor applications. *Biomaterials*, *33*(34), 8757–8770.

Yang, N., Chen, X., Ren, T., Zhang, P., & Yang, D. (2015). Carbon nanotube based biosensors. *Sensors and Actuators B: Chemical*, *207*, 690–715.

Yang, W.-C., Yang, T.-Y., & Yew, T.-R. (2007). Growth of self-aligned carbon nanotube for use as a field-effect transistor using cobalt silicide as a catalyst. *Carbon*, *45*(8), 1679–1685.

Yang, W., Ratinac, K. R., Ringer, S. P., Thordarson, P., Gooding, J. J., & Braet, F. (2010). Carbon nanomaterials in biosensors: should you use nanotubes or graphene? *Angewandte Chemie International Edition*, *49*(12), 2114–2138.

Yang, X., Zou, T., Shi, C., Liu, E., He, C., & Zhao, N. (2016). Effect of carbon nanotube (CNT) content on the properties of in-situ synthesis CNT reinforced Al composites. *Materials Science and Engineering: A*, *660*, 11–18.

Yao, X., Zhang, Y., Jin, W., Hu, Y., & Cui, Y. (2021). Carbon nanotube field-effect transistor-based chemical and biological sensors. *Sensors*, *21*(3), 995.

Yao, Y., Falk, L. K. L., Morjan, R. E., Nerushev, O. A., & Campbell, E. E. B. (2004). Synthesis of carbon nanotube films by thermal CVD in the presence of supported catalyst particles. Part II: the nanotube film. *Journal of Materials Science: Materials in Electronics*, *15*(9), 583–594.

Yasuda, S., Hiraoka, T., Futaba, D. N., Yamada, T., Yumura, M., & Hata, K. (2009). Existence and kinetics of graphitic carbonaceous impurities in carbon nanotube forests to assess the absolute purity. *Nano letters*, *9*(2), 769–773.

Yazyev, O. V, & Pasquarello, A. (2008). Carbon diffusion in CVD growth of carbon nanotubes on metal nanoparticles. *physica status solidi (b)*, *245*(10), 2185–2188.

Yilmaz, M., Raina, S., Hsu, S. H., & Kang, W. P. (2017). Growing micropatterned CNT arrays on aluminum substrates using hot-filament CVD process. *Materials Letters*, *209*, 376–378.

Yogeswaran, U., & Chen, S. (2008). Recent trends in the application of carbon nanotubes–polymer composite modified electrodes for biosensors: A review. *Analytical Letters*, *41*(2), 210–243.

Yoon, Y. J., & Baik, H. K. (2001). Catalytic growth mechanism of carbon nanofibers through chemical vapor deposition. *Diamond and related materials*, *10*(3–7), 1214–1217.

Yu, G., Gong, J., Wang, S., Zhu, D., He, S., & Zhu, Z. (2006). Etching effects of ethanol on multi-walled carbon nanotubes. *Carbon*, *44*(7), 1218–1224.

Yue, B., Zhang, X., Wang, X., Lian, L., Gao, W., Zhang, H., Hou, S., & Lou, D. (2022). A Needle Extraction Device Packed with Molecularly Imprinted Polymer Functionalized Fiber for the Determination of Polycyclic Aromatic Hydrocarbon in Water. *Water, Air, & Soil Pollution*, *233*(1), 1–12.

Yun, S.-M., Kim, J.-W., Jung, M.-J., Nho, Y.-C., Kang, P.-H., & Lee, Y.-S. (2007). An XPS study of oxyfluorinated multiwalled carbon nano tubes. *Carbon letters*, *8*(4), 292–298.

Yun, Y., Shanov, V., Tu, Y., Subramaniam, S., & Schulz, M. J. (2006). Growth mechanism of long aligned multiwall carbon nanotube arrays by water-assisted chemical vapor deposition. *The journal of physical chemistry B*, *110*(47), 23920–23925.

Zaytseva, O., & Neumann, G. (2016). Carbon nanomaterials: production, impact on plant development, agricultural and environmental applications. *Chemical and Biological Technologies in Agriculture*, *3*(1), 1–26.

Zhang, C., Li, J., Shi, C., Liu, E., Du, X., Feng, W., & Zhao, N. (2011). The efficient synthesis of carbon nano-onions using chemical vapor deposition on an unsupported Ni–Fe alloy catalyst. *Carbon*, *49*(4), 1151–1158.

Zhang, G., Mann, D., Zhang, L., Javey, A., Li, Y., Yenilmez, E., Wang, Q., McVittie, J. P., Nishi, Y., & Gibbons, J. (2005). Ultra-high-yield growth of vertical single-walled carbon nanotubes: Hidden roles of hydrogen and oxygen. *Proceedings of the National Academy of Sciences*, *102*(45), 16141–16145.

Zhang, J., Tu, R., & Goto, T. (2011). Preparation of carbon nanotube by rotary CVD on Ni nano-particle precipitated cBN using nickelocene as a precursor. *Materials letters*, *65*(2), 367–370.

Zhang, N., Wei, X., Fan, Y., Zhou, X., & Liu, Y. (2020). Recent advances in development of biosensors for taste-related analyses. *TrAC Trends in Analytical Chemistry*, *129*, 115925.

Zhang, Qiang, Huang, J., Zhao, M., Qian, W., & Wei, F. (2011). Carbon nanotube mass production: principles and processes. *ChemSusChem*, *4*(7), 864–889.

Zhang, Qiang, Wei, N., Laiho, P., & Kauppinen, E. I. (2019). Recent developments in single-walled carbon nanotube thin films fabricated by dry floating catalyst chemical vapor deposition. *Single-Walled Carbon Nanotubes*, 99–128.

Zhang, Qing, Chen, G., Yoon, S. F., Ahn, J., Wang, S. G., Zhou, Q., Wang, Q., & Li,

J. Q. (2002). Thermal conductivity of multiwalled carbon nanotubes. *Physical Review B*, *66*(16), 165440.

Zhang, S., Pang, J., Li, Y., Yang, F., Gemming, T., Wang, K., Wang, X., Peng, S., Liu, X., & Chang, B. (2022). Emerging Internet of Things driven carbon nanotubes-based devices. *Nano Research*, 1–25.

Zhang, X., Wang, L., Xin, J., Yakobson, B. I., & Ding, F. (2014). Role of hydrogen in graphene chemical vapor deposition growth on a copper surface. *Journal of the American Chemical Society*, *136*(8), 3040–3047.

Zhang, Y. I., Zhang, L., & Zhou, C. (2013). Review of chemical vapor deposition of graphene and related applications. *Accounts of chemical research*, *46*(10), 2329.

Zhang, Yi, Bai, Y., & Yan, B. (2010). Functionalized carbon nanotubes for potential medicinal applications. *Drug discovery today*, *15*(11–12), 428–435.

Zhang, Yuanyuan, Cao, Q., Zhu, F., Xu, H., Zhang, Y., Xu, W., & Liao, X. (2020). An Amperometric hydrogen peroxide sensor based on reduced graphene Oxide/Carbon nanotubes/Pt NPs modified glassy carbon electrode. *Int. J. Electrochem. Sci*, *15*, 8771–8785.

Zhang, Yuyan, & Tadigadapa, S. (2004). Calorimetric biosensors with integrated microfluidic channels. *Biosensors and Bioelectronics*, *19*(12), 1733–1743.

Zhao, B., Sivasankar, V. S., Dasgupta, A., & Das, S. (2021). Ultrathin and ultrasensitive printed carbon nanotube-based temperature sensors capable of repeated uses on surfaces of widely varying curvatures and wettabilities. *ACS Applied Materials & Interfaces*, *13*(8), 10257–10270.

Zhao, N., Wu, Q., Zhang, X., Yang, T., Li, D., Zhang, X., Ma, C., Liu, R., Xin, L., & He, M. (2022). Chemical vapor deposition growth of single-walled carbon nanotubes from plastic polymers. *Carbon*, *187*, 29–34.

Zhao, X., Zhang, X., Liu, Q., Zhang, Z., & Li, Y. (2021). Growth of single-walled carbon nanotubes on substrates using carbon monoxide as carbon source. *Chemical Research in Chinese Universities*, *37*(5), 1125–1129.

Zhao, Y.-L., & Stoddart, J. F. (2009). Noncovalent functionalization of single-walled carbon nanotubes. *Accounts of chemical research*, *42*(8), 1161–1171.

Zhao, Y., Choi, J., Kim, P., Fei, W., & Lee, C. J. (2015). Large-scale synthesis and characterization of super-bundle single-walled carbon nanotubes by water-assisted chemical vapor deposition. *RSC Advances*, *5*(39), 30564–30569.

Zhou, C., Kong, J., & Dai, H. (2000). Intrinsic electrical properties of individual single-walled carbon nanotubes with small band gaps. *Physical Review Letters*, *84*(24), 5604.

Zhou, Y., Fang, Y., & Ramasamy, R. P. (2019). Non-covalent functionalization of carbon nanotubes for electrochemical biosensor development. *Sensors*, *19*(2), 392.

Zhu, L., Xiu, Y., Hess, D. W., & Wong, C.-P. (2005). Aligned carbon nanotube stacks by water-assisted selective etching. *Nano letters*, *5*(12), 2641–2645.

Zhu, S., & Ni, J. (2022). The Critical Role of Carbon Nanotubes in Bridging Academic Research to Commercialization of Lithium Batteries. *The Chemical Record*, e202200125.

Zhu, Y., Lin, T., Liu, Q., Chen, Y., Zhang, G., Xiong, H., & Zhang, H. (2006). The effect of nickel content of composite catalysts synthesized by hydrothermal method on the preparation of carbon nanotubes. *Materials Science and Engineering: B*, *127*(2–3), 198–202.